8-1-1979

Laboratory Study Of Flow And Thermal Structures In Heated And/Or Cooled Layers Of Water

M. Behnia

R. Viskanta

Behnia, M. and Viskanta, R., "Laboratory Study Of Flow And Thermal Structures In Heated And/Or Cooled Layers Of Water" (1979). *IWRRC Technical Reports.* Paper 123.
http://docs.lib.purdue.edu/watertech/123

TECHNICAL REPORT NO. 123

LABORATORY STUDY OF FLOW AND THERMAL STRUCTURES IN HEATED AND/OR COOLED LAYERS OF WATER

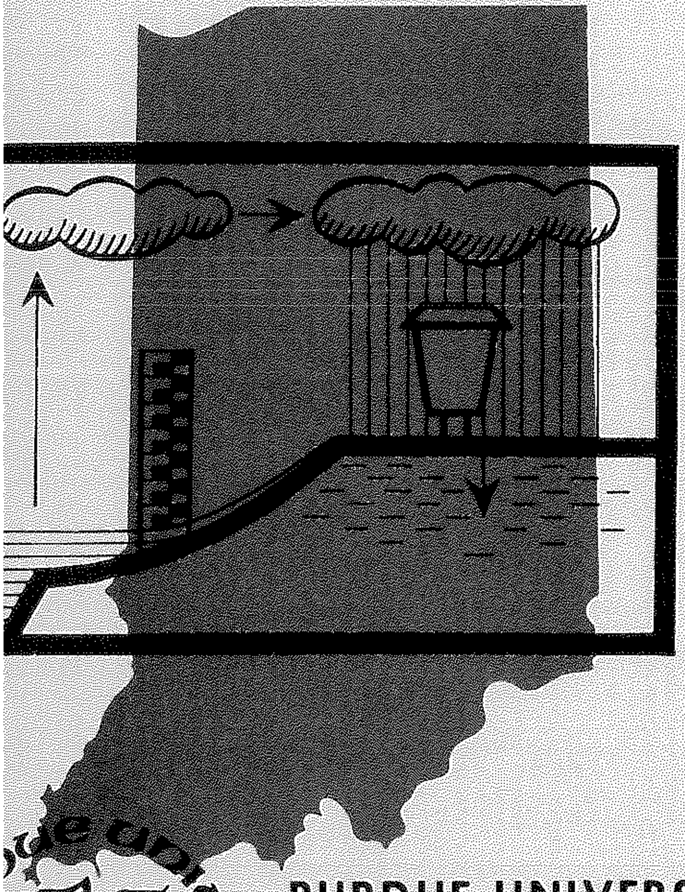

by

M. Behnia

R. Viskanta

August 1979

PURDUE UNIVERSITY
WATER RESOURCES RESEARCH CENTER
WEST LAFAYETTE, INDIANA

Water Resources Research Center
Purdue University
West Lafayette, Indiana 47907

LABORATORY STUDY OF FLOW AND THERMAL STRUCTURES IN HEATED AND/OR COOLED LAYERS OF WATER

by

M. Behnia
R. Viskanta

The work upon which this report is based was supported in part by funds provided by the United States Department of the Interior, Office of Water Research and Technology, as authorized by the Water Resources Research Act of 1978 (PL 95-467).

Completion Report for Matching Grant Project OWRT B-077-IND
Agreement No. 14-34-0001-6075

Purdue University Water Resources Research Center
Technical Report No. 123

August 1979

ACKNOWLEDGMENTS

This research was supported in part by the United States Department of Interior, Office of Water Research and Technology. This temination report is being submitted in fulfillment of Matching Grant Project OWRT B-077-IND. Other publications which have resulted from the work performed under the grant are listed at the end of the report.

Except for minor changes, this report constitutes the doctoral dissertation of M. Behnia which was submitted to the Faculty of Purdue University in partial fulfillment of the degree of Doctor of Philosophy. Professor R. Viskanta acted as the research advisor and principal investigator of the project.

The authors wish to express their thanks to Dr. Dan Wiersma, Director of the Water Resources Research Center for his assistance in the administration of the project.

The authors also wish to acknowledge fruitful discussions with Prof. D. B. Spalding regarding modeling of turbulence and use of the GENMIX computer program.

The authors would like to express their appreciation to other graduate students, Messrs. R. Bleikamp, A. Karalis, W. T. Lewis, and J. R. Parkin, who were associated with the project for their assistance and the exchange of ideas during the period of the investigation.

A final thanks belong to Ms. S. Broadstreet for her expert typing of this report.

ABSTRACT

The purpose of this work was to gain improved understanding of the basic internal transport processes in natural waters and the interactions at the air-water interface. To this end, thermal and flow structure in a stratified layer of water heated by a radiation source and/or cooled by forced air flow over the surface was studied in the laboratory. Accurate temperature measurements were obtained using a Mach-Zehnder interferometer which did not disturb or distort the temperature, radiation and flow fields. The flow structure was studied qualitatively by visualizing the patterns with dye injection, particle tracing ("fish scales") and shadowgraph techniques. Temperature fluctuations and thermal plume activities were detected by a thermistor.

The transport processes occurring in impounded waters such as lakes, ponds and reservoirs were simulated in a laboratory test cell 33 cm deep, 25 cm wide, and 10 cm thick filled with distilled water. Thermal stratification was induced by high temperature tungsten filament lamps in parabolic reflectors which produced collimated radiation flux of known spectral characteristics. At the surface, the water was cooled by forcing air through a 10 cm square air-channel which was assembled onto the test cell. A 20 cm deep test cell was also used to study the effects of the bottom on the deposition of solar energy in shallow waters. The test cell had provisions for cooling or heating the bottom by circulating coolant through serpentine tubing soldered onto it.

The experimental observations during thermal stratification of a shallow layer of water indicated that if sufficient radiant energy is absorbed at and near the bottom instabilities will occur. The spectral radiation flux incident on the water and the radiation characteristics of the bottom had a decisive influence on the temperature distribution. Numerical results based on a transient, one-dimensional energy transfer model showed good agreement with experimental measurements.

Heating from below of a nonuniformly stratified layer of water was studied to obtain understanding of turbulent mixing processes in an inherently unstable situation. Departure of warmer parcels (thermals) of water emanating from the immediate vicinity of the cell bottom was observed. The thermal plume activity near the bottom created a mixed (nearly uniform temperature) layer above the heated surface. A simple thermal model based on the energy equation was used to predict the dynamics of the mixed layer. The predictions from the thermal model as well as those from a more sophisticated energy model in which turbulence was accounted for agreed very well with the experimental data for the mixed layer height and temperature.

Experimental observations during forced cooling of a layer of water undergoing thermal stratification by radiation indicated a very complex thermal and flow structure. In a thermally stratified water being cooled, the flow is confined to a layer in which turbulent mixing is an important transport process. In the mixed layer random temperature fluctuations were detected shortly after cooling by forced air flow was initiated. Restratification by radiation of a layer of water undergoing cooling and mixing proved that the deposition of radiant energy in the surface layer influences strongly the persistence of turbulence. A model based on the conservation principles and $K-\varepsilon$ turbulence model was developed. The numerical results obtained were compared to experimental data obtained in controlled laboratory experiments. The data and predictions were consistent and agreed reasonably well with each other.

TABLE OF CONTENTS

LIST OF TABLES

LIST OF FIGURES

Appendix
Figure

LIST OF SYMBOLS

B	buoyancy parameter defined by Eq. (3.21)
c	specific heat
C_μ	constant in turbulence model
C_t'	constant in turbulence model
$C_{1\varepsilon}$	constant in turbulence model
$C_{2\varepsilon}$	constant in turbulence model
$C_{3\varepsilon}$	constant in turbulence model
D	depth of water layer
E_n	exponential integral function defined by Eq. (3.13)
f	Coriolis parameter
F	total radiative flux
F_{inc}	total incident radiative flux
g	acceleration due to gravity
h	mixed layer thickness (depth)
H	total volumetric absorption rate of radiant energy defined by Eq. (3.8) or heat flux due to molecular and turbulent diffusion defined in Eq. (5.2)
H^*	dimensionless heat flux, $H/\rho c(g\beta\alpha^2/\nu)^{1/3}(T_f - T_{fo})^{4/3}$
I_λ	spectral intensity of radiation
k	thermal conductivity
k_{eff}	effective thermal conductivity
K	turbulent kinetic energy, $(\overline{u'^2} + \overline{v'^2} + \overline{w'^2})/2$
ℓ	turbulent mixing length scale
p	pressure
Pr	Prandtl number, $\mu c/k$
Pr_{eff}	effective Prandtl number defined in Eq. (3.4)
Pr_t	turbulent Prandtl number defined in Eq. (3.20)
q	heat flux
r	relative humidity

t	time
T	temperature
T'	fluctuating temperature
T_2	exponential transmission function defined in Eq. (3.14)
T_3	exponential transmission function defined in Eq. (3.15)
T_f	average coolant temperature
u	velocity component in x-direction
v	velocity component in y-direction
w'	fluctuating vertical velocity component
$\rho c\overline{w'T'}$	turbulent heat flux
x, y	horizontal coordinates
z	vertical coordinate
α	thermal diffusivity of fluid, $k/\rho c$ or absorptivity
α_b	absorptance of bottom
β	thermal expansion coefficient
γ	temperature gradient $(\partial T/\partial z)$ in the stable region
Γ	normalized temperature gradient in the stable region, γ/γ_o
$\Delta\tau$	dimensionless time step
ε	dissipation of turbulent kinetic energy or emissivity
η	dimensionless mixed layer height, $\gamma_o h/(T_f - T_{fo})$
θ	angle between normal and pencil of radiation or dimensionless temperature defined by Eq. (4.6)
Θ	dimensionless mixed layer temperature, $(T_m - T_{mo})/(T_f - T_{fo})$
κ	proportionality factor defined by Eq. (5.4) or von Karman's constant
κ_λ	spectral absorption coefficient
λ	wavelength
μ	dynamic viscosity or direction cosine in water, $\mu = \cos\theta$
μ_{eff}	effective viscosity defined by Eq. (3.3)
μ°	direction cosine in air, $\mu^\circ = \cos\theta^\circ$
ν	kinematic viscosity, μ/ρ
ξ	dimensionless vertical coordinate, z/D
ρ	density
ρ_s	surface reflectance

σ	Stefan-Boltzmann constant
σ_K	turbulent kinetic energy Prandtl number
σ_ε	turbulent kinetic energy dissipation Prandtl number
τ	dimensionless time defined as $(g\beta\alpha^2/\nu)^{1/3}\gamma_o(T_f - T_{fo})^{-2/3}$ $(t - t_{ref})$
τ_s	surface shear stress
τ_λ	spectral optical depth
$\tau_{D\lambda}$	spectral optical thickness
ϕ	azimuthal angle, constant in turbulence model or dimensionless radiative flux defined by Eq. (4.6)
ϕ_t	constant in turbulence model
ϕ_t'	constant in turbulence model
ψ	parameter defined in Eq. (4.3)
Ω	solid angle

Subscripts

b	refers to the bottom
eff	refers to effective
h	refers to the top of the mixed layer
i	refers to grid space
j	refers to time step
ℓ	refers to laminar
m	refers to the mixed layer
o	refers to initial conditions
ref	refers to reference
s	refers to the surface
t	refers to turbulent
λ	refers to wavelength
0	refers to space coordinate origin ($z = 0$)

1. INTRODUCTION

1.1 Discussion of Problem

For time immemorial man has been interested in understanding and harnessing his physical environment. The life-sustaining atmosphere and the oceans of water upon which depend so many living organisms including man have been of particular concern to him. With the personal and collective demand in harnessing the maximum amount of energy to produce goods and machinery to serve him, man has been inadvertently modifying his surroundings. Historically, scientists such as meteorologists, oceanologists, geologists and others have contributed to man's understanding of his physical environment, but more recently ecologists, environmentalists, engineers and others have come to share their specialized training in the task of solving the variety of problems associated with the modification, monitoring, purification and overall management of air and water resources.

The physical processes of fluid motion, energy and mass transfer in natural waterbodies are very complex. Figure 1.1 illustrates schematically some of the transport processes which occur in the vicinity of the air-water interface. The ultimate energy source of the atmosphere-hydrosphere system is the sun which "drives" the system. Turbulent exchange of momentum, heat and mass is controlling the transport processes on large and small scales, and molecular diffusion is important only on very small scales. The internal transport processes as well as the interactions which occur at the air-water interface are responsible for the thermal structure of water as well as for the heat and mass transfer at the surface. As expected, two different levels of detail in understanding are required for predicting the heat and mass exchange at the surface and

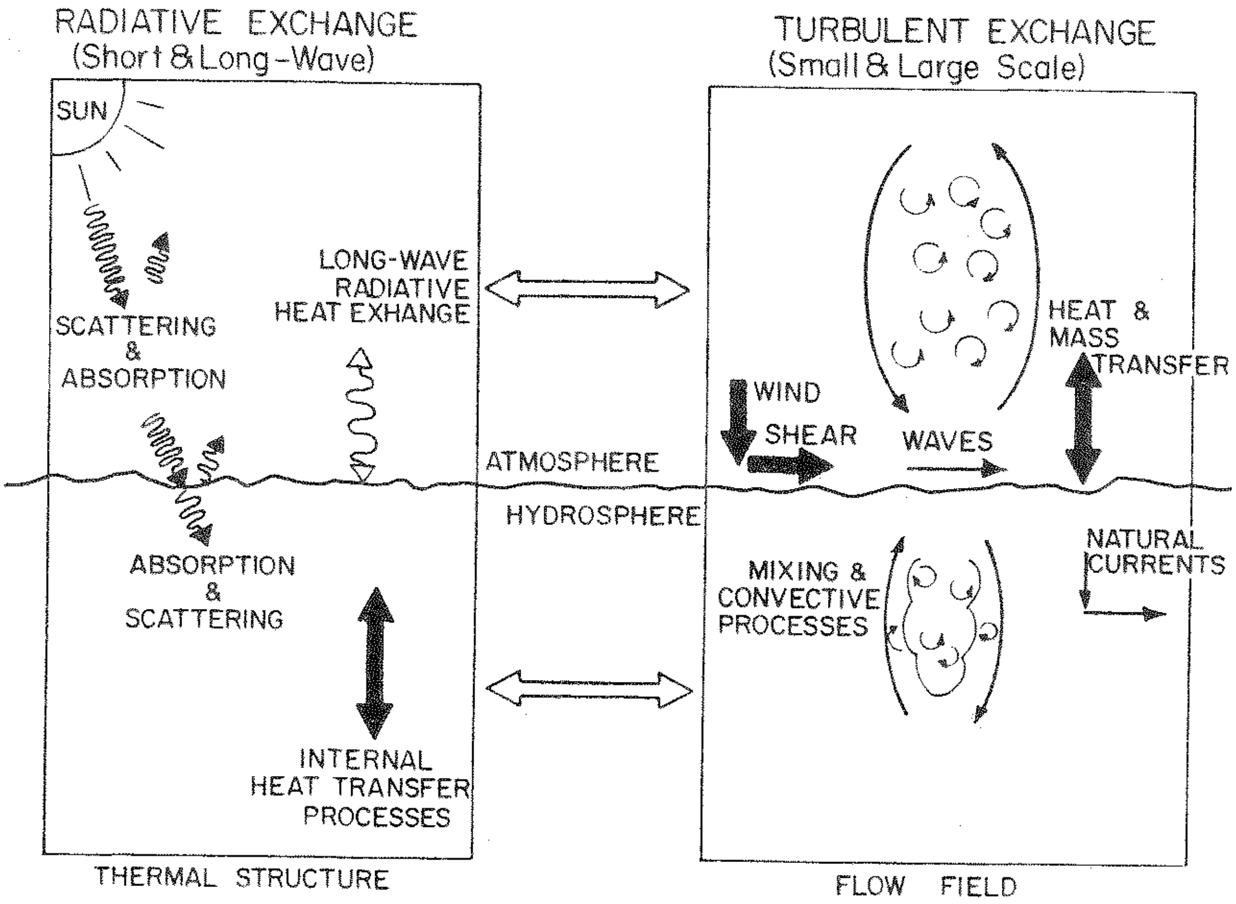

Figure 1.1 Physical processes in the atmosphere-hydrosphere system

temperature structure in a body of water.

In general, the physical, chemical and biological processes in waters is of interest, to scientists (Hutchinson, 1957; Hill, 1962; Mamayev, 1975), environmentalists (Annonymous, 1969; Eskinazi, 1975) and engineers (Parker and Krenkel, 1969, 1970; Harleman, 1972; Zaric, 1977) for many reasons. For example, the vertical temperature (density) variations in a water body have important effects on chemical and physical properties, dissolved oxygen, biological and chemical oxygen demand, aquatic life, chemical and thermal pollution, ecology and mixing processes in water. The thermal structure influences the plant and animal life and affects the status of the water resources. Data on thermal and flow structure, energy transfer and mixing often provide the basic information that leads to better understanding of complex hydraulic phenomena. Such data are invaluable as input to those concerned with water quality, ecology, thermal impacts of large heat sources and hydroscience in general. For example, the transport processes governing the vertical distribution of mass and energy in impounded waters (lakes, reservoirs, and ponds) play a critical role in various other basic and applied studies of current interest: in the dispersal of material pollutants (Hamelnik and Waybrant, 1973; Eddington and Robbins, 1973), in the transport of nutrients and biota (Schindler and Fee, 1973; Holm-Hansen et al., 1976), on the dispersal of thermal effluents (Harleman and Stolzenbach, 1972; Zaric, 1977), and seasonal thermal energy storage in artificial lakes (Schöll, 1974).

Because of the complex nature of the physical processes governing the hydrodynamics and thermodynamics of waterbodies and the difficulties in experimental and theoretical scaling of natural processes, most of the present state-of-knowledge concerning waters has been acquired by measurements. The methodologies employed have included large and small scale field experiments and laboratory tests. A great store of useful empirical knowledge has been obtained. The belief that natural phenomena were too complex to be modeled mathematically using the basic conservation principles and laws and too complex to be realistically simulated in the laboratory has led to the approach (Parker and Krenkel, 1970). Empirical relations developed from the field data have limited usefulness and can only be applied to situations approximating those for which the original field data were obtained. Unfortunately, the fundamental difficulty with these approaches is that field and laboratory data alone cannot predict what will happen in the future in a body of water, for example, if it is subjected to large thermal loads, say, from an electric power generating plant. For this purpose predictive mathematical models are needed. Before these type of models can be developed, a more detailed understanding not only of the internal physical processes governing fluid flow, mixing and energy processes but also of the interactions at the air-water interface must be obtained. Only then can mathematical models governing the complex phenomena be developed with some confidence and verified experimentally using data obtained from small scale laboratory tests or from field data.

Models for predicting heat dissipation from the water surface and the thermal structure in waters are needed, for example, by electric power plant designers, electric utilities, local and federal water pollution control agencies responsible for determining if the thermal pollution standards are met. Also, models provide better understanding of complex hydraulic phenomena in natural waters and such information is invaluable to those concerned with water quality and ecology.

This work is concerned with fundamental understanding of the internal radiation, mixing and energy transfer processes in quiescent water. To this end, the detailed mixing and energy transfer processes in thermally stratified, heated and/or cooled water are studied by performing laboratory experiments under carefully controlled environmental conditions simulating as closely as possible the conditions existing in impounded waters.

1.2 Background

The physical processes governing the internal dynamics and thermal structure of impounded waterbodies without and with thermal discharges are very complex. The subject covers a wide range of physical phenomena and a great deal of field data and empirical information has been acquired. The interest in data collection and modeling of fluid-thermal dynamics in natural and impounded waters has been intense during the last two decades and is evidenced by a number of short courses, seminars and conferences (Harleman, 1972; Abraham, 1975; Spalding and Afgan, 1977; Zaric, 1977; Lee and Sengupta, 1977, 1979), to mention just a few, that have been held.

The need for modeling of the fluid-thermal dynamics in natural waters has been discussed in some detail (Tichenor and Cawley, 1970; Parker and Krenkel, 1970) and there is no need to summarize the recommendations here. In brief, mathematical models are used for design and predictive (forecasting) purposes of hydraulic and thermal phenomena in waterbodies. The models are only as good as the physical approximations made in their development. Reliable predictive models can be constructed if the internal physical processes in the water and the interactions at the air-water interface are realistically accounted for. According to Figure 1.1 the internal processes include radiation, advection, shear and buoyancy generated turbulence and mixing and their interactions together with convection, latent energy transport, evaporation (condensation), shear and wave generation at the air-water interface. Currents, inflows-outflows of water and possibly discharge of thermal effluents must also be considered. The principal difficulties in modeling fluid flow and energy transfer in natural waters are the lack of knowledge of the internal physical processes, the interactions at the air-water interface as well as the solution of a set of conservation equations governing the phenomena. Several energy transport processes, for example, must be taken into account simultaneously and the sources and sinks of energy are not obvious. An array of mixing phenomena which are relevant to large waterbodies has been reviewed by Turner (1973). However, pertinent quantitative data are lacking to understand detailed physical processes of stratification, shear and buoyancy generated mixing, restratification of water which is undergoing mixing, wind-shear produced mixing in thermally stratified and unstratified natural waters and others.

Because of the very broad subject matter, the discussion here will of necessity be limited to the topics directly relevant to this work. Specific attention in this section is focused on the basic internal transport processes in the water such as radiation, buoyancy generated flow and mixing, turbulence, interactions at the air-water interface and mathematical description of laboratory experiments.

1.2.1 Radiation Transfer

The primary energy source in natural waters is solar radiation, and available experimental evidence (Turner, 1973; Ryan, 1972) indicates that natural thermal stratification in waters is primarily determined by the net radiation transfer, except the upper 1 to 2 m deep layer of water which responds to daily changes in insolation. Turbulence generated by wind and currents and aided by buoyancy induced natural convection creates a mixed surface layer. Only relatively quiescent, sheltered waterbodies have significant thermal stratification in the upper 10 m during the days with a positive net (downward) heat flux in the surface layers.

Prediction of temperature structure in surface layers or of thermal stratification in impounded waters requires models for short-wave (solar) radiation transfer. The assumption that solar radiation is totally absorbed at the surface (Parker and Krenkel, 1970) has no physical justification, except possibly in the limiting case of very turbid waters. Another approach of those who have accounted for internal absorption of solar radiation has been to approximate field data using exponential functions (Kraus and Roth, 1968; Dake and Harleman, 1969; Denman, 1973; Denman and Miyake, 1973). A fundamentally more sound approach (Viskanta and Toor, 1972, 1973, 1978; Jerlov, 1976; Daniel et al., 1979) is to use radiative transfer theory. Attenuation (absorption and scattering) and multiple scattering by water can be accounted for and reflection as well as transmission of incident solar radiation can be included. Nonisotropic multiple scattering of radiation by water increases the complexity of the analysis (Viskanta and Toor, 1973; Daniel et al., 1979), but flux approximations (Daniel et al., 1979) can be developed which do not increase the complexity of the problem greatly beyond that which is inherent to the forward scattering model (Viskanta and Toor, 1972).

A comparison of some approaches for predicting radiative transfer in waters is available (Viskanta and Toor, 1978). The results show that neither the assumption of mean-gray absorption coefficient (Dake and Harleman, 1969) nor semiempirical equations used (Rabl and Nielson, 1975) are completely satisfactory. The comparison indicates that generally for accurate prediction of the volumetric rate of short-wave energy absorption within water, the spectral distribution of the incident solar radiation flux, the spectral absorption coefficient as well as the radiative effects of the bottom must be accounted for. Temperature distribution in a quiescent layer of water being stratified by radiant heating in a laboratory tank has been measured, and the good agreement between data and predictions (Snider and Viskanta, 1974; Bloss and Grigull, 1978) provides an indirect confirmation of the validity of the phenomological radiation transfer models and gives some confidence in the approach used. It should be emphasized that the models (Snider and Viskanta, 1974; Dake and Harleman, 1969) do not account for fluid motion, turbulence or surface shear due to wind.

1.2.2 Buoyancy Generated Flow and Mixing

Buoyancy generated natural convection flows are common geophysical problems and an excellent review of the phenomenon is available (Turner, 1973). The bulk of the work in the past has been devoted to thermal convection between parallel plates uniformly heated from below and cooled from above (Deardorff and Willis, 1967a, b; Willis and Deardorff, 1967a, b; Goldstein and Chu, 1969; Carroll, 1971; Chu and Goldstein, 1973; and Fitzjarrald, 1976). Natural convection in water cooled from the free surface has been studied (Spangenberg and Rowland, 1961; Foster, 1965; Viskanta et al., 1977, 1978; Katsaros et al., 1977). A review of cellular convection in evaporating shallow liquids is given by Berg et al. (1966), and the effects of surface tension, surfactants and the depth of fluid are discussed. In many experiments of this type the mean temperature profiles within the fluid were obtained (Deardorff et al., 1969; Viskanta et al., 1977, 1978; Katsaros et al., 1977). An excellent review of the relevant literature is available (Katsaros et al., 1977) and will not be repeated here.

Laboratory studies modeling atmospheric penetrative convection in a tank of water which was continuously and uniformly stratified has been performed by Deardorff et al. (1969) and Heidt (1977). In both studies the water was heated from the bottom by imposing a constant temperature boundary condition. The dynamics of the convective layer were observed and simple mathematical models developed. The cooling of a nonuniformly thermally stratified layer of water from the free surface in the absence of shear has been investigated (Behnia and Viskanta, 1979). The dynamics of the mixed layer was observed, detailed temperature distributions were measured and a simple thermal model was developed for predicting the dynamics of the mixed layer. The interaction of motion generated by wind shear with buoyancy produced natural convection in a thermally stratified water layer does not appear to have been studied in the laboratory. This is an important problem which arises in nature.

1.2.3 Turbulence

The turbulent transport processes below the water surface are very complex indeed (Coantic, 1978). The complexity arises as a result of lack of understanding of turbulent structure generated by several different sources. In fact, this has been one of the main drawbacks in the modeling of transport processes in waters. Buoyancy resulting from unstable stratification is one of the sources of turbulence. Since short-wave radiation absorption causes stratification, the modeling of thermal structure in the upper layers of water is further complicated by the interaction of turbulence and radiation transfer. Another important factor is that data are lacking because the direct experimental determination of turbulent parameters in natural waters is difficult under field conditions. Turbulence has been receiving and continues to receive considerable attention (Parker and Krenkel, 1970; Fischer, 1973 and 1976; Spalding and Svensson, 1977). Therefore, in order to predict temperature distribution in the water either assumptions must be made to by-pass the modeling of turbulence or turbulent quantities (e.g. eddy diffusivities) must be determined. An up to date review of different one-dimensional approaches to the problem is given by Niiler and Kraus (1977) and will not be repeated here. This topic will be discussed in greater detail in a later section.

The modeling of turbulence or its by-passing is determined by the type of analytical models constructed. The models which have been used can be divided into three groups: 1) mixed layer models that assume the existence of a completely mixed layer, 2) models that emphasize mixing due to unstable stratification and neglect the effect of wind and 3) models that take into account the turbulence by employing turbulent transport coefficients. The models developed which belong to the first two groups are the simplest and most widely used. The first model of this kind was developed by Kraus and Turner (1967). Examples of more recent models for the atmosphere are those of Tennekes (1973), Carson and Smith (1974), Mahrt and Lenschow (1976) and in waters are those of Deardorff et al. (1969), Moore and Jaluria (1972), Denman (1973), Heidt (1977), and Behnia and Viskanta (1979). The models developed by Sundaram and Rehm (1973) and Spalding and Svensson (1977) are typical of those in the third group. Sundaram and Rehm (1973) used an algebraic equation for turbulent exchange coefficient of heat and solved the energy equation to predict the temperature distribution. The model of Spalding and Svensson (1977) relates the eddy diffusivity to the turbulent kinetic energy and dissipation.

1.2.4 Interactions at the Air-Water Interface

Interaction between the atmosphere and hydrosphere manifests itself most strongly at the air-water interface and plays a very important role in the dynamic processes within water and in the establishment of the temperature structure not only near the interface but also to a considerable distance below the water surface (Coantic, 1978). For example, water surface temperature has key importance to both heat (convective, latent and radiative) exchange and mass (evaporation and condensation) transfer. Mechanical and thermal energy are transported by several different mechanisms, Figure 1.1, and the presence of turbulence in the air and water on a very wide range of scales which complicates the understanding and modeling of the interaction at the interface. A very thorough review of interactions on micro and macro scales are given by Kraus (1972) and Coantic (1978).

At the air-water interface there exists the reflection and transmission of short-wave solar radiation incident on the interface. Long-wave radiation exchange between the surface and the environment, and transport of sensible and latent heat to or from the interface are controlling in the absence of solar radiation. The transport of mechanical energy as a result of momentum exchange between the surface and wind as well as wave generation and breakage are also very important. A two-dimensional boundary layer model has been used by several investigators (Weisman and Brutsaert, 1973; Brutsaert, 1975; Shaw and Lee, 1976) to simulate the interaction, and the effect of several parameters on the wind velocity profile. The processes at the air-water interface are usually described by semiempirical correlations both for the momentum and thermal energy transfers. Equations of this type are widely adopted by investigators either in laboratory or field experiments. Studies by Dunchel et al., 1974; Ryan et al., 1974; Weisman, 1975; Shaw and Lee, 1976; Hicks and Hess, 1977; Lai, 1977; Ginzburg and Fedorov, 1978 are only a few that can be mentioned. In some studies the effects of waves and wavy air-water interface on the thermal and mechanical energy transports are studied and correlated (Mangarella et al., 1971, 1973). No laboratory studies in water layers dealing with combined radiation transfer, turbulence, mixing due to buoyancy and wind shear and their interactions appear to have been reported in the literature.

1.3 Objectives and Scope

The primary objective of this investigation is to obtain improved understanding of radiation transfer, mixing in stratified water due to buoyancy and wind shear and their interactions. The emphasis is placed on laboratory modeling of these processes in experiments under carefully controlled laboratory conditions. More specifically, the tasks were the following:

1. Study stratification (heating by radiation) of shallow water layers.
2. Investigate the mixing of nonuniformly stratified water due to heating from below or cooling from above.
3. Study the mixing of a layer of water due to cooling and wind shear at the water surface.
4. Investigate the restratification (reheating by radiation) of a layer of water which is undergoing mixing due to cooling and wind shear at the surface.

Experimentally, emphasis is on developing apparatus and procedure for obtaining accurate data with well defined conditions in the laboratory. The details of experimental apparatus and procedure are described in Chapter 2. The experimental data obtained are used to check the validity of the mathematical models discussed in Chapter 3. A one-dimensional energy model based on radiative transfer analysis of Viskanta and Toor (1978) is developed for predicting temperature distribution in a shallow layer of water undergoing thermal stratification, and the results obtained are presented in Chapter 4. The dynamics of an initially stably stratified layer of water heated from below is mathematically modeled and discussed in Chapter 5. Shear and buoyancy induced turbulent flow is modeled using the K-ε turbulence model of Launder and Spalding (1972) and the experimental and numerical results obtained are described and compared in Chapter 6. The conclusions are summarized in Chapter 7.

2. EXPERIMENTS

2.1 Introduction

The purpose of the experimental part of this study is to simulate in the laboratory the basic energy transport and mixing processes occurring in natural waterbodies such as ponds, lakes or reservoirs. Experimental data are needed to gain understanding of internal energy transport processes in waters cooled and/or heated from the surface. The effects of wind shear, incident short- and long-wave radiation, and surface heat flux on the mixing processes in the water are not completely understood. Quantitative data are also required to verify analytical models which have been developed for predicting unsteady temperature distribution and flow characteristics of complex hydraulic systems. The general objectives of the experimental phase of this work are:

- Simulate in the laboratory the internal energy transfer and mixing processes in a shallow quiescent body of water.
- Simulate the effects of wind shear in a stagnant waterbody and study the energy transfer processes near the air-water interface.

To this end, experimental apparatus was designed and constructed to simulate in the laboratory under carefully controlled conditions the different physical transport processes occurring in natural waters.

Thermal stratification was accomplished using tungsten filament lamps within parabolic reflectors which produced collimated radiation and simulated solar irradiation. The water was cooled or heated from the surface by heat exchange with ambient air and surroundings. A Mach-Zehnder interferometer was used as a diagnostic tool for optical measurement of unsteady temperature distribution and flow visualization within the water. For visualization of flow field, several optical, particle tracing, and dye techniques were suitable for the present study and included shadowgraph (optical), fish scales (particle tracing), and blue-black dye techniques.

2.2 Test Cells

The complexity of realistic modeling in a laboratory of natural waterbodies such as ponds, lakes and reservoirs is fully recognized. A large test cell was desirable to minimize the edge effects. Unfortunately, a width limit for uniform heating was imposed by the length of the solar simulators. Also, a width limit in the direction of the optical path was imposed by the interferometer. Interference fringe shifts are directly related to the width of the test cell along the optical path. Too wide of a test cell along the optical path produces a fringe shift pattern which is too dense for interpretation.

Two test cells were designed and constructed. Test cell A was intended to model a shallow layer of quiescent water in which a significant fraction of the incident solar radiation penetrates to the bottom of the layer and interacts with it. Test cell B was designed to model a deeper layer of water in which there is relatively little interaction of solar radiation with the bottom.

2.2.1 Test Cell A

The depth of this test cell chosen was based on a compromise between radiant heating of the water which would cause sufficient interaction of radiation with the bottom and the free convection circulation considerations. Both of these factors were important for choosing a depth of the tank. Penetration of radiant energy into the water depends on several factors of which the most important ones are, magnitude and spectral distribution of the incident radiative flux and the radiation characteristics of the water. The results obtained (Snider and Viskanta, 1975; Viskanta et al., 1975; Viskanta et al., 1977 and 1978) using tungsten filament lamps in parabolic reflectors operating at temperatures in excess of 2500 K resulted in penetration of radiation to about 15 cm, depending on the effective temperature of the radiation source. Consequently, absorption of radiation by the bottom produces heating which in an unstable situation induces natural convection motion. Hence, to model and study a shallow layer of water realistically, the depth of the test cell should be sufficiently deep for the circulation convection mixing not to penetrate to the surface in the presence of thermal stratification. Based on the experimental results available (Viskanta et al., 1977 and 1978) for cooling of a layer of water from the surface, the penetrative convection is confined to a depth of about 10 to 15 cm. For these reasons, the depth of test cell A was chosen to be 20 cm.

Figure 2.1 shows a photograph of the test cell A. The inside dimensions were 10 cm along the optical path, 25 cm wide and 20 cm deep. The walls of the test cell were made of 2.5 cm thick plexiglass. The optical quality glass windows, 15 cm wide and 1.5 cm thick, were installed and cemented into openings milled in the plexiglass walls. To insure that the windows were parallel and would not deform, the windows were further secured in place by brass clamps.

The bottom of this test cell was made from a 2.5 mm thick copper sheet with 50 mm diameter serpentine copper tubing soldered to the lower side of the copper plate. The bottom acted as a heat source/sink and was cooled or heated by circulating coolant from a LAUDA constant temperature bath (LAUDA-Thermostat Type NBSD 8/25) through the bottom copper tubing. The flow rate of coolant through the heat source/sink was controlled by means of a bypass and measured by a calibrated ball type water flow meter (Gilmont No. 15).

A calibrated Type-T thermocouple was installed in the center of the bottom plate. This thermocouple was the only means of measurement of the bottom plate average temperature. The inlet and outlet

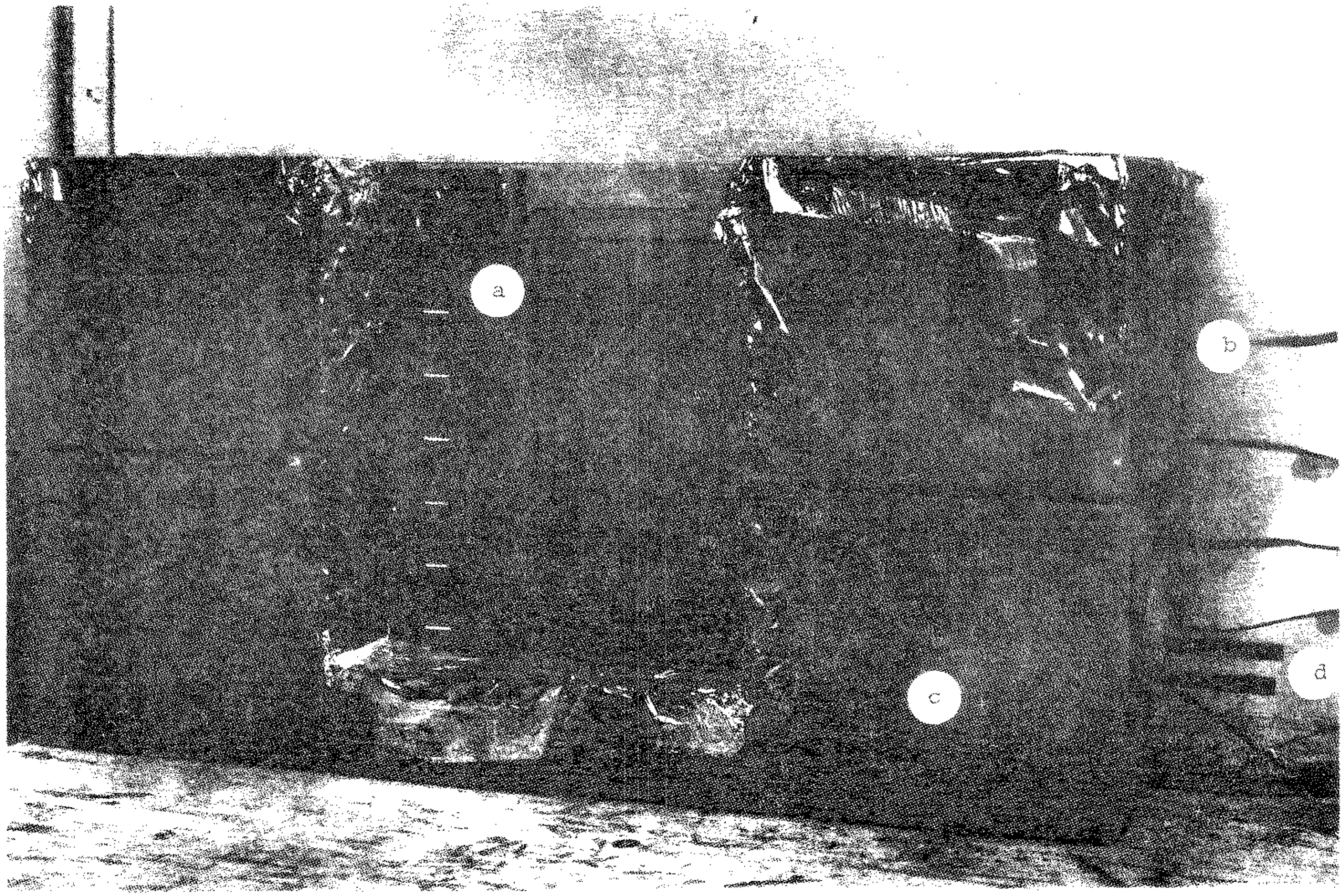

Figure 2.1 Photograph of test cell A: (a) optical window, (b) thermocouple, (c) styrofoam insulation, (d) coolant inlet-outlet

temperature of the coolant was measured by two calibrated Type-T thermocouples epoxyed into the two small holes drilled in the inlet and outlet tubes of the heat source/sink.

The test cell was assembled with the 2.5 cm thick plexiglass side walls and bottom copper plate placed between the two walls containing the optical windows. The plexiglass side walls and the bottom acted as spacers between the windows. To insure that the windows were parallel, the sides and the bottom of the test cell were machined together to 10 cm (± 0.015 cm) which assured a uniform test cell width. The sides of the test cell were secured by means of six screws placed into the side spacers on each side of the test cell. Clear silicon glue (General Electric No. GE2562-01DP) was used on the inside of the test cell to seal the sides and the bottom and insure no leakage of water.

Four holes were drilled in the plexiglass side of the test cell. The first hole was about 1.5 cm from the bottom and the rest of the holes were equally spaced 3 cm apart. Four calibrated Type-T thermocouples inserted in 1.2 mm thick, 20 cm long tubing were installed in the holes and glued in place, extending about 15 cm into the test cell. To insure no leaks through the brass sleeves, the tip of the tubes were epoxyed leaving only the tip of the thermocouples exposed to water. A calibrated 2 mm bead diameter thermistor (YSI 44201) was installed approximately 0.6 cm above the bottom plate to detect temperature fluctuations. The thermistor was inserted in a 2 mm diameter, 40 cm long "L" shape stainless steel tubing and was installed inside the test cell. The thermistor was used in a special circuit with two other resistors to insure a nearly linear variation of resistance with temperature. The maximum deviation of the thermistor from linearity in the range of interest was about ± 0.1°C. The thermistor circuit was placed in one arm of a four arm Ellis Bridge Amplifier (Model BAM-1) with a 4 volt bridge excitation voltage. The output of the bridge was recorded on a strip chart with variable output scale and speed (Honeywell Elektronik 19). The output of the thermistor was also recorded on a

Keithley DVM (Model 178). The calibration curve and the electric circuit of the thermistor are given in Appendix A.

The bottom of the test cell was painted with flat black Pyromark paint of known spectral radiation characteristics. A 0.5 mm thick sheet covered with a highly reflective aluminum foil metal could be placed in the bottom of the test cell to act as a reflective bottom. Styrofoam insulation, 3 cm thick, was covering the side walls. The test cell rested on a slab of plexiglass with a 2 cm thick layer of glass-wool between the bottom plate and plexiglass slab which was secured on a scissors-type laboratory jack. The height of the test cell was adjusted by means of this jack with a maximum travel of about 20 cm. Styrofoam insulation, 3 cm thick, also covered the optical windows. The insulation on the optical windows could be easily removed to take photographs of the interference fringe patterns.

The test cell rested on a large metal stand and each leg could be adjusted to the desired height. Since the instrument was very sensitive to vibrations, rubber pads were placed under each leg of the test stand to isolate the stand from sources of vibration. The experiments were performed late at night when the traffic was light, and all motors and compressors were turned off in the laboratory to eliminate vibrations.

2.2.2 Test Cell B

Imposition of wind at the water surface results in both cooling and stirring of water which induces a downward motion of fluid. Hence, to realistically model a deep layer of water, the cooler fluid moving downward should lose its thermal identity and become sufficiently damped before it reaches the bottom of the test cell. Experiments of Spangenberg and Rowland (1961) and of Foster (1965), both using test cells 10 cm deep, showed that the thermal plumes induced by buoyancy as a result of cooling from the surface descended to the bottom of the test cell. However, the 40 cm deep test cell used in this laboratory (Viskanta et al., 1975; 1977 and 1978) for similar investigations proved to be adequate. For this reason and the fact that high quality optical glass are very expensive and not readily available, the depth of test cell B was chosen to be about 33 cm. The width and thickness of test cell B was also imposed by the radiant heaters and was chosen to be 10 cm along the optical path and 25 cm wide. Figure 2.2 shows a photograph of the test cell assembled with the air channel.

In the design of test cell B special consideration had to be given to the air channel-test cell assembly. To insure a smooth transition of air flowing over the water surface and also to be able to observe and record the interference fringe patterns clearly, the optical sides of the test cell also acted as the side walls of the air channel. The nonoptical sides and the bottom were made of 2.5 cm thick plexiglass. The optical glass windows (45 x 30 cm) which also acted as walls were 2.5 cm thick.

The test cell was assembled with the 2.5 cm thick plexiglass side walls (35 x 10 cm) and bottom section (25 x 10 cm) placed between the optical windows. The plexiglass side walls and bottom acted as spacers between the windows. The sides and bottom the test cell were machined and milled together to 10 cm (± 0.015 cm) which insured a uniform width of the test cell B.

Aluminum frames were placed over the outside of the windows, and tightening nuts on threaded rods connecting the frames forced the windows tightly against the walls. The frames did not act as support for the windows but supplied only enough force to counter the hydrostatic pressure. Clear silicone rubber cement was used to seal the edges to prevent water leakage.

On the outside of the walls two 2.5 cm plexiglass cubes, spaced 4 cm apart, were glued 6 mm below the top edge. The cubes acted as supports for the bottom wall of the air tunnel. An 8 mm hole was drilled in the bottom of the cell and a copper tube inserted in it to act as the drain plug. A total of seven 8 mm holes were drilled and tapped on the side wall of the cell. The top hole was 2.5 cm

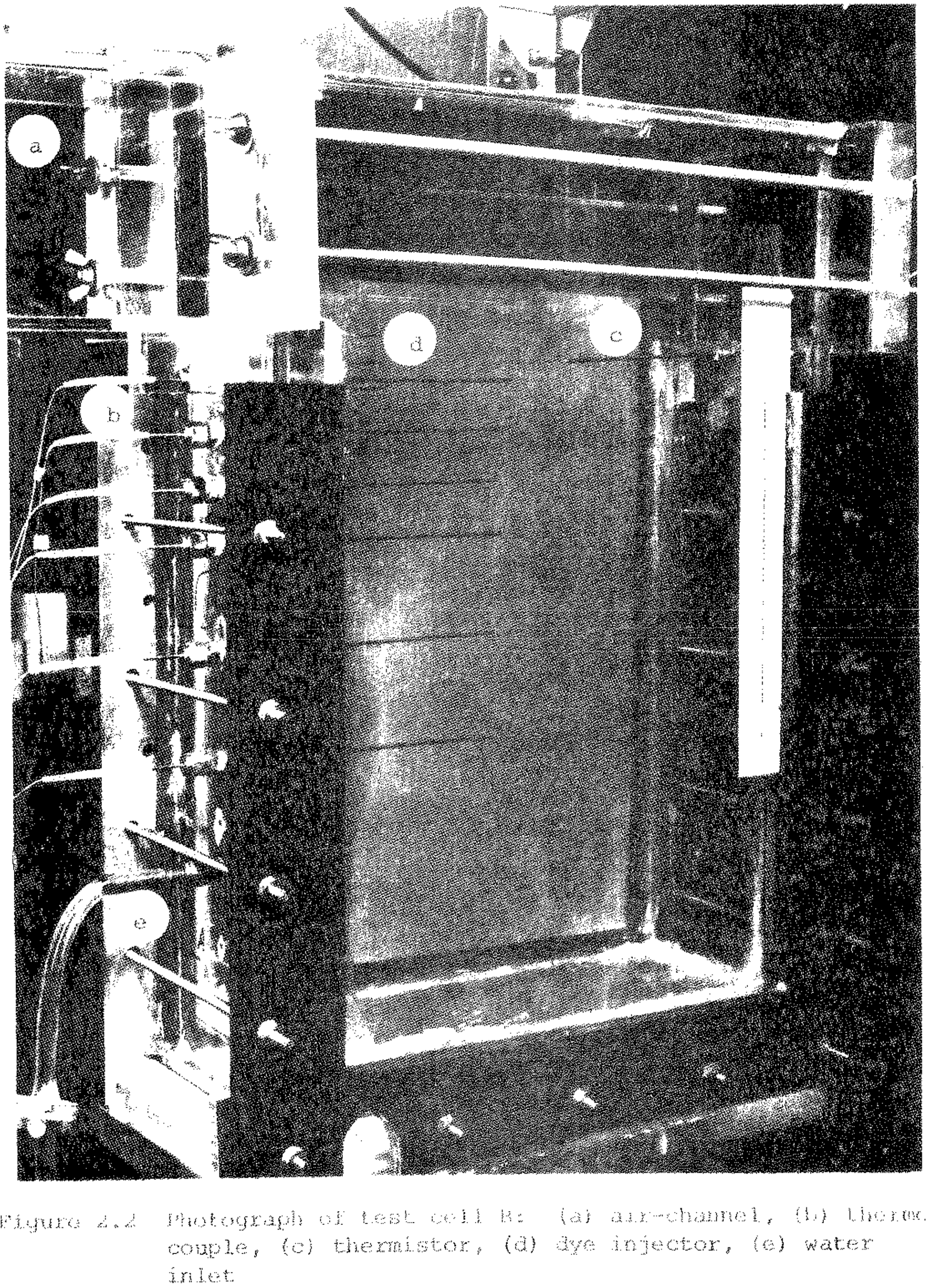

Figure 2.2 Photograph of test cell B: (a) air-channel, (b) thermocouple, (c) thermistor, (d) dye injector, (e) water inlet

below the surface, and the next three holes were equally spaced at 2.5 cm apart. The fifth hole from the top was 15 cm below the surface with the next two holes spaced 5 cm apart. The bottom hole acted as the inlet for filling the tank with distilled water from a container.

Six calibrated Type-T thermocouples each jacketed by a 25 cm long, 1.5 mm thick brass tubing were installed into a pipe thread fitting to be tightened in the tapped holes. The brass tubing was sealed inside the fitting by means of two rubber O rings. The tip of the thermocouples were located about 12 cm from the test cell side wall. In some of the experiments a Type-T thermocouple was inserted into the test cell from the top which could be placed about 1 or 2 mm below the water surface.

The same YSI44201 thermistor that was used in test cell A was also employed in test cell B (see Appendix A for electric circuit). The thermistor was inserted in a 3 mm hole drilled on the side of the test cell opposite to the thermocouple side. The top of the thermistor was located about 10 cm from the side wall and about 1 cm below the air-water interface. It was secured in place by filling up the hole with silicone glue. Styrofoam insulation, 2 cm thick, covered the sides of the test cell. The test cell rested on the same stand that was used for test cell A. The top of the test cell-air channel assembly was covered by a 6 mm thick layer of clear float glass which also acted as a part of the top wall of air tunnel.

2.3 Heat Sources and Heat Sink

The water was thermally stratified using two tungsten filament lamps (Quartz Infrared Lamp GE-QH1000T3/2CL/HT) within parabolic reflectors (Research Incorporated, Model 5305-10B) to simulate solar heating of the water. The reflectors were designed to produce collimated radiation within a 5 cm wide by 25 cm long rectangular region. Two lamps within two reflectors were used, and they were placed approximately 125 cm above the surface of the water.

A relationship between the filament temperature and voltage applied to the lamps was determined using an optical pyrometer (Instrument Development Laboratories Model Pyro 650). From the voltage versus temperature plot (see Appendix B), any filament temperature could be obtained by the adjustment of the voltage to the heaters. Power to the lamps was controlled with a variable transformer (Powerstat Variable Autotransformer Type 1256C) connected to a step-up transformer (Sorgel Type S) which could supply up to 500 volts at 15 amperes. The lamps had a maximum voltage rating of 480 volts which corresponded to a filament temperature of 3250 K; however, for prolonged operation of the lamps at 3250 K, a tungsten compound deposit formed on the inside of the quartz envelopes. For the experiments in which the spectral distribution of radiation from the lamps was not a determining factor, the lamps were operated at about 2800 K in order to prolong the operating life of the lamps. Special care was taken in the installation of new lamps in the reflectors housing. The reflectors were cleaned with a tissue soaked in alcohol after the old lamps were removed. Since operation of the lamps with fingerprints or grease on the surface caused devitrification of the quartz, the lamps were handled very carefully and wiped with a clean cloth dampened with alcohol.

The parabolic reflector housing was cooled by circulating cold tap water at a rate of few liters per minute. To assure safe operation of the parabolic reflectors a Type-K thermocouple was installed into the back side of the reflector housing. The output of this thermocouple was monitored in order to adjust the water flow rate through the housing. Aging of the lamps results in a decrease of the radiative flux of the heaters. This was due to formation of deposits on the inside of the quartz envelope. For this reason the total incident flux at the water surface was continuously decreasing. Therefore, the total radiation flux incident on the water surface was monitored during an experiment by means of an Eppley Radiometer (Model 8-48). The output voltage of the radiometer varied linearly [11.82×10^{-6} V/(W/m^2)] with the total incident flux.

A thin sheet metal shield covered with aluminum foil was placed approximately 30 cm above the test cell and covered the entire interferometer leg in which the test cell rested. A hole in the shield allowed only the water to be heated while the shield protected the other components from radiant heating and reduced free convection within the interferometer leg. For more complete protection from radiant heating the other components of the apparatus exposed to radiation were covered by aluminum foil.

As discussed earlier, a heat source/sink was installed into the bottom of the test cell A and was cooled or heated by circulating coolant from a constant temperature bath which could be set between 15°C to 50°C. The temperature of the source/sink was found to be quite uniform on the basis of measurements in preliminary experiments. In order to achieve a fast temperature response of the source/sink it was made from a relatively thin copper sheet to reduce its mass. About two minutes after the start of the circulation of the fluid through the copper tubing the surface temperature of the copper plate reached a constant and steady value.

2.4 Wind Channel

A wind channel was designed and constructed to produce shear at the air-water interface. For simulating shear stress at the surface of waterbodies generated by wind, a long, wide wind channel is needed to reduce entrance effects and to ensure nearly fully developed conditions. It is also desirable to have approximately one-dimensional air flow over the water surface as observed in natural waterbodies. In their experiments Shaw and Lee (1976) used a long wind tunnel (approximately 19 m). However, their test section was only 30 cm high above the water surface. In similar experiments Mangarella et al. (1973) employed a 14 m long tunnel which was about 97 cm high above the water surface.

Even though a large wind channel was desirable, the size constraint was imposed by the space available in the interferometer leg and one test cell. In fact, the length of the tunnel was optimized with respect to the space limitation between the two legs of the interferometer. It should be pointed out that other investigators have been primarily concerned with the air side of the interface. However, in this investigation the effect of wind on the thermal and flow structure in the water was of primary concern. In view of the optical diagnostics employed and objectives of the study, the size of the test cell-wind tunnel assembly was definitely a compromise.

Figure 2.3 shows a photograph of the air-channel assembled onto the test cell B. The channel consisted of five parts: a fan section, a fan entrance section with flow straighteners, a curved fan duct, a working section, and an entrance section with flow straighteners. The cross section of the channel was 10 cm by 10 cm square. The total length of the channel was approximately 2 m. All parts except the curved duct was made from 6 mm thick plexiglass. The curved duct was made from 1 mm thick sheet metal. To insure a uniform width and height of the channel, all the plexiglass sides were machined, milled and then glued together by a clear cement made from chloroform. The top and bottom sides served as spacers between the side walls.

The entrance flow section was 20 cm long and was packed with plastic straws 6 mm in diameter which acted as straighteners. Two square pieces of fine mesh wire screen held the two ends of the packed straws. This section was attached to the entrance section by means of brass screws passing through 20 holes drilled in a 2.5 cm plexiglass flange that was glued around the outside end of the section. The entrance section was 40 cm long and was flanged on both ends. In the middle of this section two 2 cm diameter holes were drilled opposite to each other on the top and bottom walls. A static pressure tap and a Pitot tube fitted into the two holes. The optical windows of the test cell B acted as the side walls of the

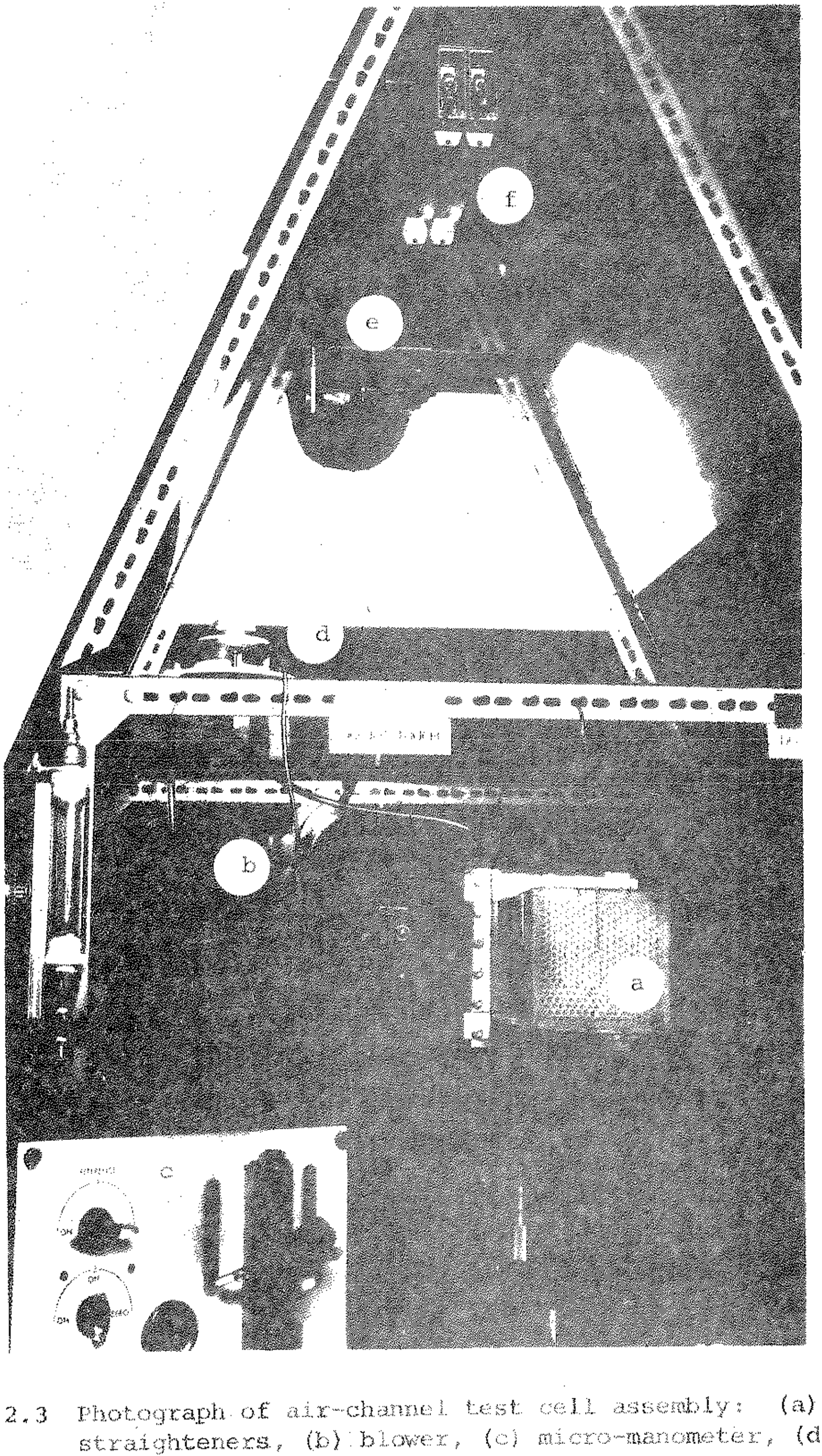

Figure 2.3 Photograph of air-channel test cell assembly: (a) flow straighteners, (b) blower, (c) micro-manometer, (d) radiometer, (e) multiple mirror scanner, (f) radiant heaters

working section. The top of the test section was covered with a 6 mm thick sheet of clear float glass which also acted as a filter for the long-wave infrared radiation emitted by the tungsten filament lamps in parabolic reflectors. A calibrated Type-T thermocouple, for measuring the air temperature, was inserted halfway into the channel from the top wall between the working and entrance sections.

The straight plexiglass duct beyond the test cell was 30 cm long and flanged at the end to be attached to the sheet metal duct. The two sections of the channel on the sides of the test cell were held in place and on to the test cell by means of four 6 mm threaded rods. On each side two rods were passed through holes drilled in 3 cm wide, 2 cm thick, plexiglass flanges cemented to the sides of the two sections of the air channel. Additional support was provided by a small plexiglass block secured on the sides of the test cell on which the two sections rested. The sheet metal duct was curved in order to clear the other leg of the interferometer.

The tunnel was operated as a suction channel with the fan located at the end sucking air through the test section. A "squirrel cage" fan (Lan Industries, model DD9-7R) with a 4-speed AC motor (Westinghouse FR-DT 42) was used. To insure uniformity of the suction velocity, a 20 cm long section of plexiglass duct similar to the entrance section was packed with straws held by screens and was attached to the suction end of the fan. The fan was secured on large and stable tripod. Because of the sensitivity of the interferometer to vibrations, the fan was isolated from the rest of the tunnel. Most of the experiments were performed by operating the fan at first or second setting which corresponded to speeds of about 3700 ±50 and 4200 ±50 RPM, respectively. After assembly of the air-tunnel, a smoke test was performed to check for possible air leakage. All the leaks discovered were sealed by clear silicone rubber cement.

Air velocity profile in the middle of the channel was measured by means of a traversing Pitot-type probe and a static pressure tap consisted of a flush 1 mm hole drilled in a 6 mm thick plexiglass disk, merging with a 6 mm diameter hole drilled from the outside. A brass tube, 6 mm in O.D. and about 2 cm long, was epoxyed in the hole allowing attachment of tygon tubing tubing. The disk was secured in the hole at the top of the air channel.

A traversing Pitot-type probe was designed and built for the measurement of stagnation pressure profile in the channel. Figure 2.4 shows a schematic diagram of the probe traversing mechanism. The mechanism was constructed primarily of brass, and consisted of a spring-loaded piston-cylinder assembly. A micrometer was mounted on the side of the cylinder which was used to measure the relative position of the probe. Distances of ± 0.01 mm could be measured on the micrometer scales. The probe was mounted in the piston via a snug fitting sleeve and held in position by an easily accessible set screw. The probe itself consisted of two parts, a 3 mm O.D., 20 cm long brass tube with a 0.5 mm I.D. hypodermic needle bent at 90° at the end. To insure smooth transition, the end of the brass tubing was tapered with the needle soldered in place at the end. The probe could be traversed as close as 0.6 mm from the walls of the channel. The traversing mechanism and probe was secured in the bottom wall of the channel by three brass screws. Much care was taken to insure a smooth transition between the inside walls, static pressure tap, and the traversing unit.

The local dynamic pressure in air was measured by connecting the traversing probe and static pressure tap to the two sides of a Micromanometer via 5 mm I.D. Tygon tubing. The manometer (CGS Scientific Corporation Model MM3) could accommodate a maximum pressure difference of 5 cm of N-Butyl Alcohol (specific gravity of 0.8076). The resolution of the manometer was ± 0.0025 mm of fluid with an estimated accuracy of about ± 0.005 mm of fluid. The manometer operated on a nulling principle and had a relatively slow time response. About five minutes of time were required to insure a steady reading of the manometer. The air velocity profile measured in the channel is included in Appendix C.

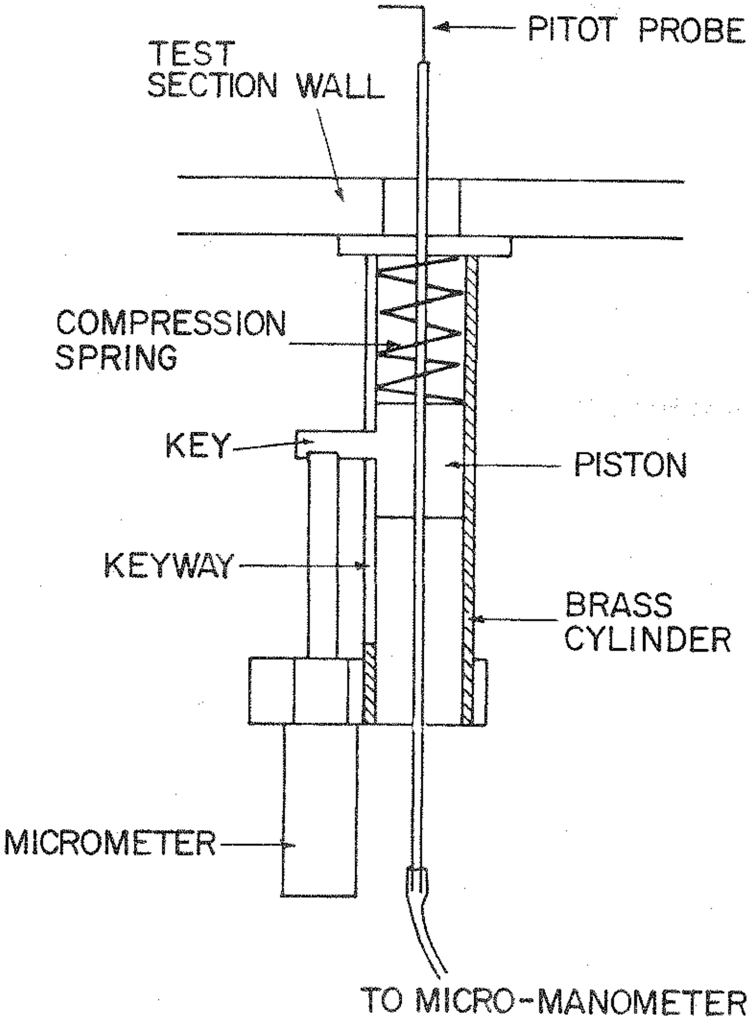

Figure 2.4 Schematic diagram of the Pitot probe traversing mechanism

2.5 Temperature Measurements

A Mach-Zehnder interferometer was selected as a diagnostic tool for measuring unsteady temperature distributions. It has advantages not available in other temperature measuring devices such as probes (thermocouples, thermistors, and other sensors) because probes of any kind disturb and distort the temperature field and if not carefully used can yield erroneous results. The interferometer is an ideal instrument to study two-dimensional transport phenomena. If it is possible to align the axis of symmetry of the phenomena studied along the optical axis, then an instantaneous two-dimensional distribution can be determined accurately without disturbing the field. The main advantages of the Mach-Zehnder interferometer system over other interferometers is the large displacement of the reference beam from the test beam. In this way the reference beam can pass through a uniform field. In addition, since the test beam passes through the disturbed region only once, the image is sharp and optical paths can be clearly defined. The Mach-Zehnder interferometer is considered to be the best system for obtaining quantitative temperature profiles (Hauf and Grigull, 1970). The details of the optics of Mach-Zehnder interferometers are discussed by Hauf and Grigull (1970) and Goldstein (1976).

The interferometer used in this study was of a typical rectangular design but consisted of large, 25 cm diameter optics. The reader is referred to Stevenson (1965) for a detailed description of the system. Figure 2.5 shows a schematic diagram of the interferometer light source and recording optics as used in this investigation.

A 10 milliwatt He-Ne laser (Spectra-Physics Stabilite Model 253A/123) served as the light source for the interferometer. The primary reason for using a laser light source was that it eliminated the need for compensation of the optical path in the reference leg of the interferometer. A microscope objective condensed the laser beam to a point source which then expanded onto a second lens. The

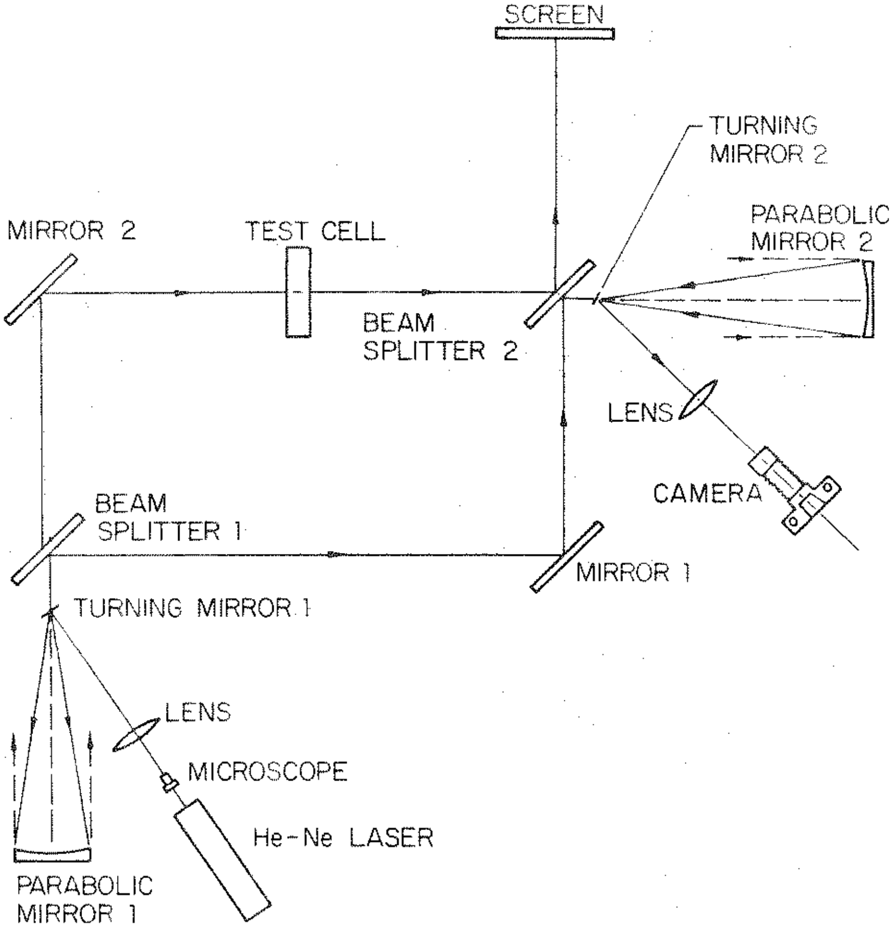

Figure 2.5 Schematic diagram of Mach-Zehnder interferometer

second lens provided a point source at the focal length of a 25 cm diameter parabolic mirror which in turn produced a collimated beam. A small turning mirror changed the direction of the beam, coming from the second lens, toward the parabolic mirror. In order to produce a uniform point source from the laser beam, the objective was placed in a pinhole-spatial filter assembly (Gaertner Scientific Corporation Model 20X).

A thermocouple was used as a temperature reference for interpreting interferograms. The interferometer optics could not accommodate the lower part of the test cell B and thermocouples in the lower region provided the only means of temperature measurement. All thermocouples used were Type-T (Copper-Constantan), 30 gauge. Before and after each experiment, the distance between a reference point and the reference thermocouple was measured using a cathetometer (Gaertner Scientific, serial number 840-A) which was accurate to 0.05 mm. A multi-channel, integrating voltmeter (Doric Scientific Corp., Model PS-100-PZA-F(53-1)-YW) with both printout (Matric Corporation) and visual display was used to record the output of the thermocouples. Interferograms in different experiments were photographed using different photographic techniques which will be discussed in Section 2.8. A photograph of the overall view of the interferometer and experimental apparatus is shown in Figure 2.6.

2.6 Interpretation of Interferograms

The deviation of an interference fringe from a reference position is produced by a change in optical path length. The fringe shift differences can be related to index of refraction change between a point within the test section (n) and a reference region (n_{ref}). Hauf and Grigull (1970) have derived the following relation between index of refraction and the fringe shift (ε),

$$S\lambda_o = (n_{ref} - n)\bar{z}_\ell = [(d\eta/\overline{dz})^2/12]n_{ref}\bar{z}_\ell \tag{2.1}$$

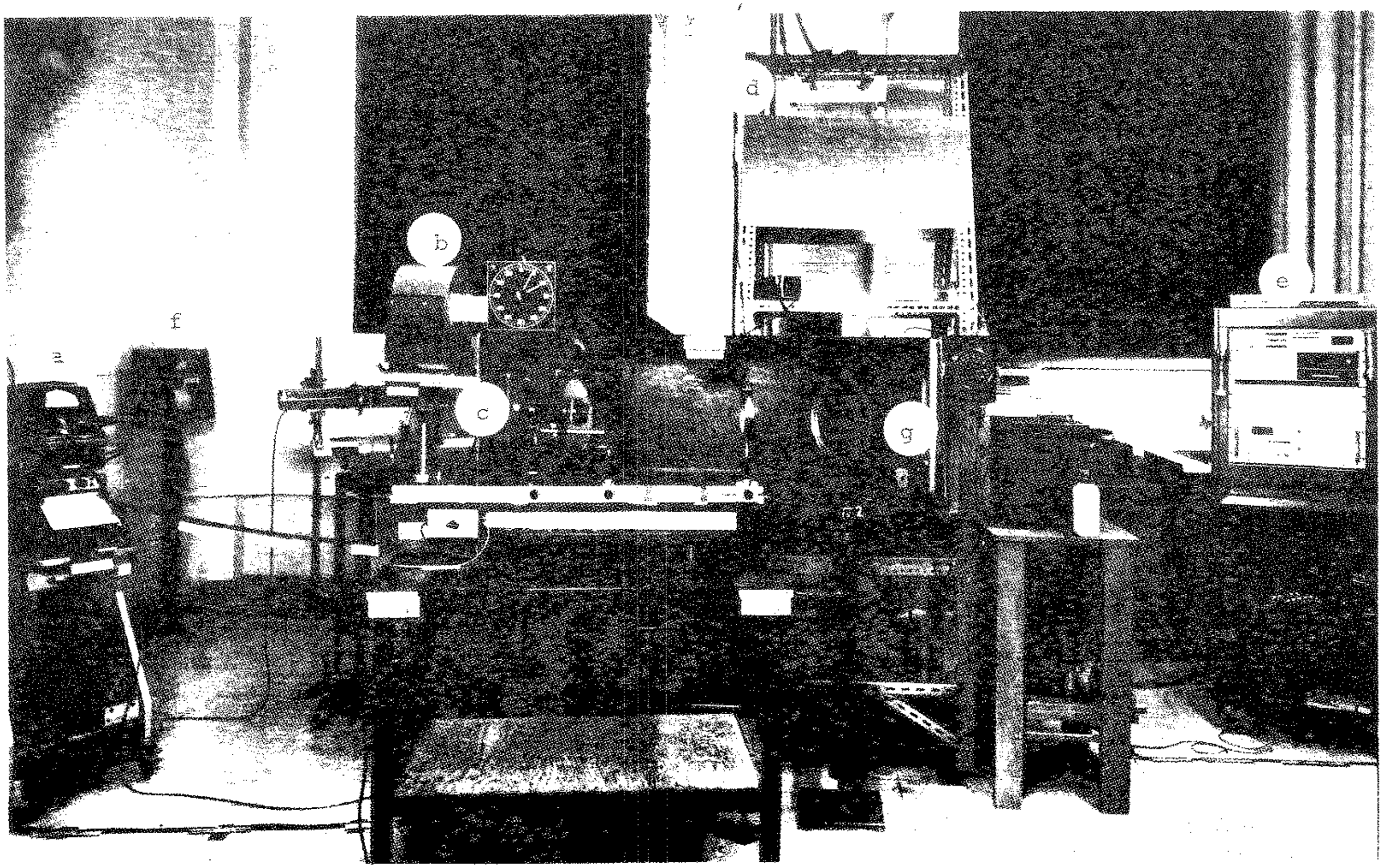

Figure 2.6 Photograph of overall view of experimental apparatus: (a) thermistor bridge and recorder, (b) blower, (c) camera, (d) radiant heaters, (e) multi-channel DVM, (f) parabolic mirror 1, (g) beam splitter 2

where

$S\lambda_o$ - path difference

$\bar{z}_\ell$ - dimensionless coordinate along the optical path

η - dimensionless coordinate perpendicular to optical path.

Equation (2.1) can be rearranged and simplified to yield,

$$n - n_{ref} = \varepsilon(\lambda_o/L) - n_{ref} b_1^2 L^2/12 \tag{2.2}$$

where

$$b_1 = \frac{\lambda_o}{n_{ref}} \frac{d\varepsilon}{dz}$$

λ_o - wavelength of the light source

L - distance along optical path length.

The above relation assumes a two-dimensional variation in index of refraction with no change along the optical path. Variations along the optical path produce an averaging effect. Both Eqs. (2.1) and (2.2) are only valid for rays entering the test section at about 90°. Since the fringe shift is fairly small, higher order terms in both Eqs. (2.1) and (2.2) have been neglected for simplifying the calculations. Also, Eqs. (2.1) and (2.2) are only valid when the optical system or camera is focused at the center of the test section.

The first term of Eq. (2.1) is the phase difference in ideal interferometry; the second term describes the deviation for a parabolic ray path. The first term in Eq. (2.2) represents the effect for an unrefracted ray while the second term accounts for the effects of the bending of light produced by the gradient of index of refraction. In this study, the bending of light introduced less than 1% maximum variation in the index of refraction in the maximum case and is neglected along with the higher order terms.

The index of refraction of water given in Eq. (2.2) can be found as a function of temperature. Tilton and Taylor (1938) have reported a precise empirical relation for index of refraction of water as a function of temperature for a mercury vapor light source ($\lambda = 0.5461\ \mu m$); however, the empirical relation can be modified for a He-Ne laser light source, but the relation is very complicated and involves some fifteen constants.

Chu (1972) has reported a simplified version of Tilton and Taylor's equation for a He-Ne laser light source ($\lambda = 0.6328\ \mu m$) as

$$n_{water}/n_{air} = n_{20} - \frac{B(T-20)^3 + A(T-20)^2 + C(T-20)}{(T+D) \cdot 10^7} \tag{2.3}$$

where T is in °C and

$n_{20} = 1.33174428$

$A = 2340.43473856$

$B = 6.36319314$

$C = 75453.63565991$

$D = 65.7081$

The relation is very precise, introducing an error of about 0.03%.

Combining Eqs. (2.2) and (2.3) yields a single equation for the temperature distribution, with temperature as the independent variable and fringe shift as the dependent variable. From this relation between temperature and fringe shift, the temperature distribution is determined.

A temperature at a known point (i.e., reference point) is measured with a thermocouple. Then, for each interferogram evaluated, fringe shifts were calculated for temperatures about the reference temperature using Eqs. (2.2) and (2.3). The calculated results were then used in a quadratic least square fit to obtain a relation between the fringe shift as the independent variable and temperature, as the dependent variable.

$$T(x,y) = A_0 + A_1\varepsilon_{ref} + A_2\varepsilon_{ref}^2 \tag{2.4}$$

The term ε_{ref} denotes the number of fringe shifts measured from the reference point. Since for each interferogram the reference temperature was different, the coefficients A_0, A_1, and A_2 had to be recalculated for each interferogram. The least square fit procedure involved an error of about 0.2% for the temperature ranges studied.

For a more convenient and accurate reduction of data a computer program was written to calculate temperature at every fringe shift for the measured reference temperature. Using the program a table of fringe shift versus temperature was prepared. The temperature at every fringe shift (up to 80 fringe shifts) was evaluated for temperatures in the range of interest in steps of 0.05°C.

Since the region of interest was near the surface of the water, in most experiments this region of the tank was photographed. Interferograms were analyzed using a measuring microscope (Precision Tool and Instruments, LTD Vernier Microscope Model Number 14). The coordinate microscope was accurate to ± 0.01 mm which corresponded to approximately ± 0.02 mm actual distance. For the experiments in which the fringe shift density was not very large, a densitometer with digital print out was used to interpret the interferograms. The densitometer was accurate to about ± 0.001 mm which corresponded to approximately ± 0.002 mm actual distance.

A scale factor was required to relate the distances measured from the interferograms to the actual distances. Two reference points visible in the interferograms were marked on the optical window (i.e., the side of the test cell), the actual distance between the two points was compared with the distance measured in the interferogram for the same two points, and a scale factor was determined. Because of the evaporation and convection from the surface, the precise position of the interface was often difficult to determine. This was caused by the meniscus and condensation of moist air on the optical windows; therefore, the scaled distances from reference points were used to accurately identify the interface.

2.7 Flow Visualization

Flow visualization has contributed much to the detailed understanding of fluid motion. It is an accepted fact that once a phenomenon is visualized, a large step has been taken toward physical comprehension and development of appropriate theory and experiments. There are numerous different types of flow visualization techniques available, but because of the experimental setup, fluid used, and type of flow field expected, only very few techniques can be used to yield satisfactory results. Merzkirch (1974) has an extensive review of different techniques available. Also, a detailed summary of flow visualization techniques in water has been given by Werlé (1973) and Powe et al. (1973).

Since water is a transparent medium, its motion remains invisible to the human eye during direct observation. In order to delineate this motion, one must therefore use a technique which renders the flow visible. Such methods have played an important role in developing an understanding of the nature of the convective motions. Visualization is an indirect method (i.e., the fluid motion is made visible indirectly), and to be used, the tracer particles or dye must have the following minimal characteristics:

1. They must be almost neutrally buoyant over a wide temperature range, and this characteristic must not change during the course of the experiment.
2. They must have a high apparent reflectivity in order to be visible and photographed.
3. They must not adhere to solid surfaces.
4. They must follow closely and indicate the actual physical flow phenomena.

After a thorough review of past work in the area of flow visualization only a few of the techniques were selected as possible candidates. A description of several suitable techniques is given in the next few subsections with specific details of the methods actually adopted in this study. The hydrogen-bubble technique

(Merzkirch, 1974), because of the rise of the bubbles (i.e., change in the drag coefficient), cannot be used for the present study because the bubble rise velocities are larger than the main flow.

Visualization of the velocity field by optical, dye production, and particle tracing techniques appeared to be promising for the special type of unsteady, buoyancy affected flow and were therefore successfully adopted.

2.7.1 Tellurium Method

This method allows one to mark certain fluid elements and to measure velocity profiles by means of an electrolytic reaction. The technique has been reported by Wortmann (1953) and later reviewed by Eichhorn (1961). The electrolytic conductivity of water can be increased by the addition of a small amount of KCl. Two electrodes are introduced into the fluid; the cathode is a thin wire of tellurium and is placed in the flow regime under study. With an external voltage applied between the electrodes, tellurium ions with a double negative charge are separated from the surface of the cathode. With oxygen present in the fluid, the tellurium ions are brought into a state of colloidal suspension that appears in the fluid in the form of a black dye.

If the cathode wire is oriented normal to the mean flow direction, with a short electric pulse applied, the marked fluid is a thin cylinder adjacent to the wire. The edge of the dye cylinder moves with the flow, and its position on a photograph represents the velocity profile of the flow which has passed the wire. Colloidal dye generated in this technique exhibits a low settling rate of the suspended particles. The settling velocity of these particles is about 0.1 mm/sec and a diffusion rate of less than 0.01 mm/sec. The tellurium wires which serve as the cathode are either drawn from metallic tellurium or tellurium is vaporized onto a thin steel wire. The tellurium wire has a limited lifetime and lasts only for a few experiments.

The suspension of the particles and difficulty of making wires from tellurium makes this method impractical for the present study.

2.7.2 Flash Photolysis

A technique for flow measurements by flash photolysis has been described by Popovich and Hummel (1967). The working fluid is a photoactive solution. By focusing the light from a flash tube onto a point in the fluid one initiates a photochemical reaction which yields a spot of blue dye within a few microseconds. In this way a tracer is introduced, without disturbing the flow, at the desired position and time. During later applications investigated by Iribarne et al. (1972), a pulsed ruby laser was used instead of the flash tube. This arrangement enables initiation of the photochemical dye production along the whole path of the laser beam through the fluid.

Two different test solutions can be used as the photoactive fluid. 0.1 wt% of 2-(2,4-dinitrobenzyl) pyridine dissolved in ethyl alcohol yields a fluid with a kinematic viscosity of 0.0169 cm^2/s at a temperature of 22°C. The second solution is 0.02 wt% of nitrospyran dissolved in kerosene with a reported value for kinematic viscosity of 0.0275 cm^2/s at 25°C. The solutions show aging effects and tend to decompose after long standing.

The specific properties of these solvent do not allow utilization of this fluid in a closed circuit flow tunnel. The other difficulty with this method is the fact that the kinematic viscosity of neither photoactive solutions are close to that of water ($\nu = 0.01006\ cm^2/s$ at 20°C); therefore, this method is not suitable for the experiments.

2.7.3 Thymol Blue Dye

The pH indicator technique described by Baker (1966) was used, with limited success, by Viskanta et al. (1977) and Behnia and Viskanta (1979) in similar studies to visualize the flow field. The technique is suitable for the measurement of the velocities in the range 0 to 5 cm/s and is applicable to aqueous solutions.

Viskanta et al. (1975; 1977) used four 0.0125 cm diameter platinum wires placed across the test cell filled with a solution of thymol blue (thymolsulphonephtalein) which has been titrated to the end point. One of the wires acted as the positive electrode with the others as negative electrodes. As a 6 volt potential was pulsed, a small cylinder of blue color solution was formed around the positive electrodes. The solution moved away from the wire with the fluid, forming a neutrally buoyant marker. The dye was generated as a consequence of proton transfer reaction near the wire. This process is discussed in detail by Gold (1956) and Noller (1957).

Although this method produces a neutrally buoyant dye, two factors made the technique unsuitable for the present study. The constant formation of bubbles on the electrodes which at time of departure obstructed the flow field and the production of the dye in the form of a horizontal streak made it difficult to trace the horizontal motion of the fluid.

2.7.4 Blue-Black Dye

One of the techniques adopted for flow visualization was injection of a dye solution into the test cell B. The dye solution was prepared by adding 0.5 gm of Calcoid Blue Black dye (Calco Chemical Company Serial # 85960-1 Ex-Cone) to 4 liters of distilled water. The density of the distilled water was measured before and after addition of the dye powder and no difference was observed. A special three outlet probe was designed and constructed for the injection of the dye into the test cell. The probe was made from 3 mm O.D. brass tube with two right angle bends by means of which it was rested on the top edge of the plexiglass side of the test cell.

The end of the brass tube was plugged. Right above the plug three 1.25 mm holes, 1.25 cm apart, were drilled. Three hypodermic needles were inserted in the holes and positioned to assure an even flow of dye. The needles were secured in place by epoxying them at the base where they were inserted into the brass tube. The dye was supplied by means of a 50 cc syringe with a long hypodermic needle which was connected to the brass tube. The plunger in the syringe was not used and instead the dye was injected by adjusting the height of the dye in the syringe at a constant level, just a few millimeters above the height of the top injector needle in the test cell. Care was exercised to insure that the exit velocity of the dye was approximately the same as the flow velocity in order to minimize the obstruction of the flow field by the dye jet. The top dye needle was approximately 5 mm below the water surface.

2.7.5 Particle Tracing

A tracer derived from the natural guanine of fish scales was used as another means of flow visualization. It consists of crystal platelets with an average face dimension of 6x30 μm and a density 1.6 times that of water (Matisse, 1974). The crystals become aligned with shear in the flow field and therefore reflect light according to the pattern of motion. Because of their small size and platelet shape, they remain in suspension for long periods of time even in quiescent water. Katsaros et al. (1977) used this technique rather successfully in free convection studies. Collimated white light from a conventional source penetrates to a distance within the water which depends on the crystal concentration. This type of light source is desirable to observe three dimensional motion. However, scattered light often makes the image unclear. For observation of motion in two dimensions it was necessary to produce a sheet of light.

An expanding sheet of light can be produced by passing a collimated beam through a cylindrical lens. However, good quality cylindrical lenses are expensive and not readily available. Therefore, a unique system for producing a sheet of light from a laser source was designed and constructed. The basic principle of the technique was to deflect the laser beam by means of a fast rotating multiple mirror scanner. Then if the reflected beam from the scanner was used to illuminate the test cell at the right angle, it would sweep a plane and therefore produce a sheet of light.

The multiple mirror scanner used was constructed from a solid piece of brass, 3 cm long, machined in the shape of a hexagon with 3 cm sides. Six optical quality mirrors, 3x3 cm, were epoxyed on the faces of the machined brass. A steel shaft was inserted and secured in a hole drilled through the center of the brass block. A pulley at the end of the shaft rotated the mirrors by means of a belt driven by an AC motor with variable speed. The scanner was usually rotated at about 1500 RPM. The motor and scanner were bolted onto a square piece of aluminum which was in turn bolted to the test cell stand about 1 m above the test cell (see Figure 2.3). A 5 milliwatt He-Ne laser (Spectra-Physics Stabilite Model 120) acted as the light source. The laser was positioned horizontally and the beam was deflected onto the multiple mirror scanner by means of a small turning mirror attached to the aperture of the laser. This technique produced a vertical sheet of light about two millimeters in thickness right in the middle of the test cell.

One cm^3 of AQ-1000 Rheoscopic concentrate solution (Kalliroscope Corporation KA-11110) per liter of distilled water was used. The concentrate solution was injected into the supply water line of the test cell by a hypodermic needle. A special photographic setup was used and is discussed in Section 2.8. It should be pointed out that this technique is mainly qualitative since individual crystals do not necessarily remain aligned with the shear and may move into or out of the plane of light during the time of exposure, precluding streak photography for determination of particle velocity. However, time lapse sequences with time exposure provide estimates of relative velocities, the movement and persistence of recognizable features.

One of the main advantages of this technique was instantaneous visualization of the entire flow field. The test cell had to be drained after each experiment and flushed with distilled water to prevent deposition of the particles on the optical windows and the sides of the test cell.

2.7.6 Shadowgraph

The flow field induced by density differences as a result of heat transfer in water layers (heating from below or cooling from above) can be visualized by the shadowgraph technique. In a shadowgraph system the linear displacement of the perturbed collimated light beam passing through a test section is measured. When a collimated light beam enters a test section, as a result of density differences, the beam is deflected at different angles depending on the local temperature gradients in the test cell. The shadowgraph, like the interferometer method, can only be utilized for two-dimensional studies and there is an averaging effect along the beam.

The interferometer was very easily made into a shadowgraph system by covering the reference beam of the interferometer. The details of shadowgraph setups are given by Hauf and Grigull (1970) and Goldstein (1976).

2.8 Photography

The special experimental setups for experiments required several different techniques of photography. The interferograms were recorded by two different cameras. A 35 mm Fikon F2AS camera with an MD-3 motor drive and bellows attachment was used to photograph the beam reflected from the parabolic mirror (see Figure 2.6). An additional lens was used to focus the photographic system at the center of the test cell. Either Kodak Plus-X or Tri-X film was used with this camera. The films were developed in Kodak high contrast developer (HC-110) for good fringe contrast.

Large negatives of the interferograms were desirable for clear image of the interference fringe patterns near the air-water interface. Therefore, a Graflex Box Camera (Serial # 470022) with a plane-shutter without a lens was placed in front of the screen (see Figure 2.5). A large, Type 55 Positive-Negative Polaroid film (9x11.5 cm negatives) was used in a Type 545 Polaroid Land film holder which was attached to the back of the camera. Very clear and sharp negatives were produced by this setup which were later treated in Sodium Sulfite solution (anhydrous/desiccated).

The dye visualization technique was photographed by a Zenza Bronica EC-TL camera which was placed in front of the test cell. In order to get good contrast between the water and the blue dye a yellow filter was placed in front of the camera lens and Kodak Plus-X Pan Professional-120 black and white film was used. The film was developed in Kodak HC-110 developer. An electronic flash (Nikon SB-10) was used behind the test cell as the light source. In order to eliminate nonuniformity in lighting and "hot-spots" by the flash a large sheet of ground glass covered the back of the test cell. Several small pieces of the same type of glass also covered the flash unit. The electronic flash was synchronized to the camera shutter and was activated by the camera's release button. Similar photographic setup was used for taking pictures of the tracer visualization. However, the laser beam itself acted as the only light source. Because of scattering of the laser beam by the platelet shape particles the lighting conditions were inadequate for high speed photography. A 4 second exposure time for very fast film (Kodak Royal-X Pan-120 film, 1250 ASA) was used. The film was developed in Kodak HC-110 chemical with developing times extending more than twice as long recommended by the manufacturer were used.

Shadowgraphs were also photographed by the Graflex camera placed in front of the interferometer screen. Because of special photographic setup required and interference with the interferometer beam it was not possible to employ the interferometer simultaneously with the flow visualization techniques.

3. UNSTEADY ONE-DIMENSIONAL TRANSPORT MODEL

3.1 Discussion of the Problem

The processes of fluid motion, mixing and energy transport in natural waters are very complicated and encompass varied physical mechanisms as well as space and time scales. To compound matters there is strong interaction between the hydrosphere and atmosphere which manifests itself most strongly at the air-water interface. The occurrence of turbulence in both the atmosphere and hydrosphere at a very wide range of scales further complicates the understanding and modeling of the interaction at the air-water interface and the internal energy transport processes in waters. Both large and small scale interactions are discussed in the literature and there is no need to repeat these excellent reviews (Kraus, 1972; Coantic, 1978).

The main energy transport processes which control the thermal structure in waters are summarized in Figure 3.1. The long range process of "short-wave" ($0.1 < \lambda < 3$ μm) radiation of solar origin and "long-wave" ($3 < \lambda < 100$ μm) radiation of terrestial origin are the basic energy "sources" that drive the entire hydrosphere-atmosphere system. A large fraction of the incoming solar radiation is absorbed within the upper layers of water causing a temperature increase. In the long-wave infrared part of the spectrum there is radiative heat exchange between the water surface and the atmospheric constituents. The exchange of heat between the air and the water at the interface occurs by turbulent transfer of sensible and latent heat as well as of mechanical energy. When air moves over water, it is not brought to rest at the interface as at a rigid surface. It is slowed down, however, enough to cause strong shear flow immediately above. The work of the Reynolds stress on this shear flow generates waves, wind driven currents and mixing motions (Kraus,

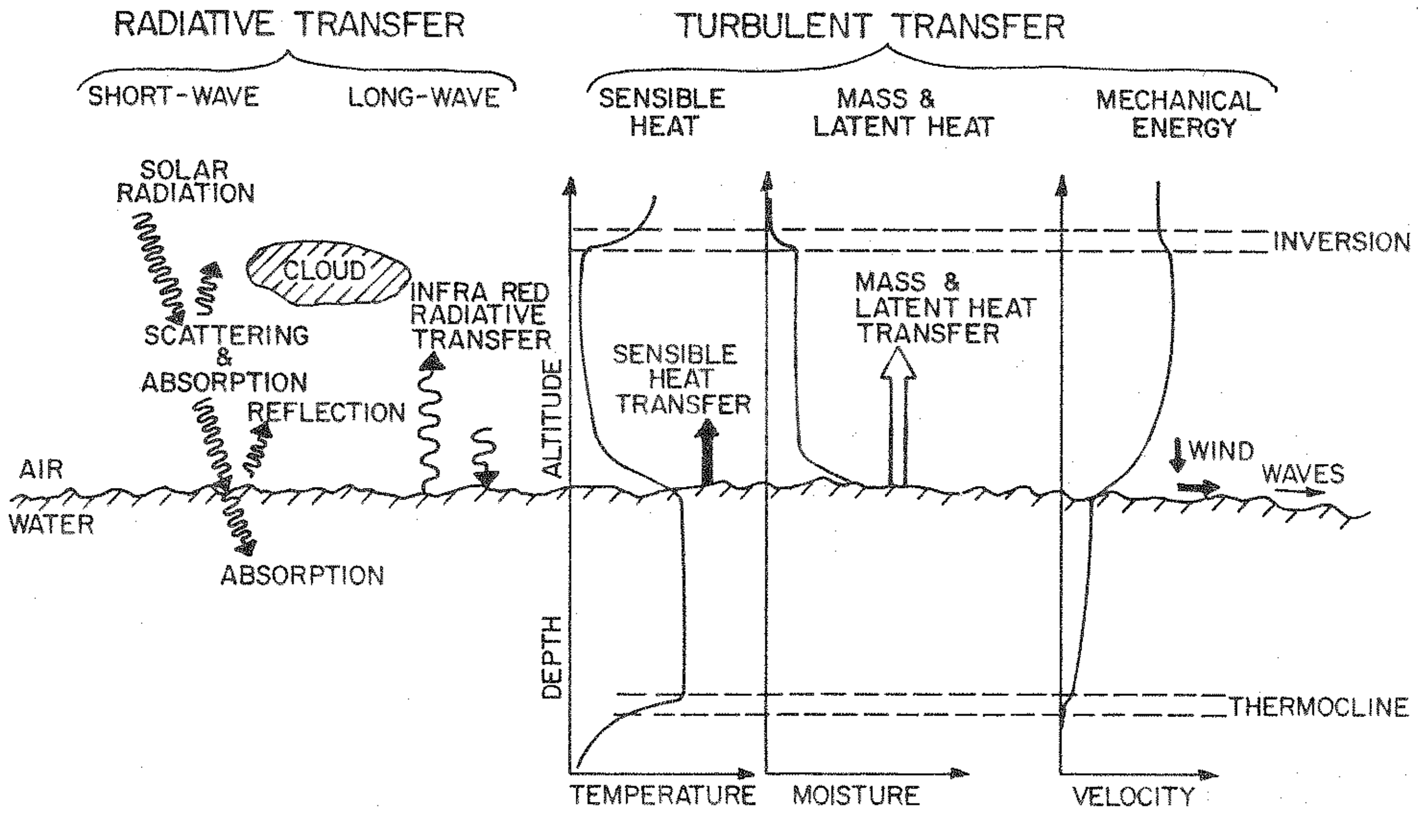

Figure 3.1 Main energy transport processes controlling thermal structure in bodies of water (after Coantic, 1978)

1972; Coantic, 1978). The water surface tends to be cooler than the region located immediately below; and energy transport has to be established in order to carry the sensible energy from the deeper water layers to the surface. Molecular diffusion alone is quite inefficient, and only turbulent transfer is able to maintain significant energy fluxes.

The primary objective of this part of the study is to model on a phenomenlogical level the basic energy transfer processes in natural waterbodies. However, as discussed in the preceeding paragraphs, the complexity of the physical phenomenon in natural waters demands a much more modest goal as a first step. That goal is to model mathematically the interaction of radiation and turbulence, driven by buoyancy and wind shear at the air-water interface, in establishing the unsteady temperature structure in a layer of water. It should be emphasized that turbulent processes in geophysical problems occur over a very wide range of scales which are very difficult to model in the laboratory. Therefore, as with the experiments, the analysis is restricted to modeling of energy transport processes which occur on a small scale in a shallow stratified layer of water or in the vicinity of the air-water interface.

3.2 Physical Model and Equations

Mathematical modeling of the complex problems which occur in nature requires a number of simplifying assumptions to make it tractable. The basic assumptions made in the analysis are the following:

- Energy transport in the layer of water is considered to be one-dimensional, i.e. horizontal advection is neglected.
- The mean velocity in the vertical direction is negligible in comparison to the horizontal components.
- Internal waves and natural currents are absent.
- There is no variation in the horizontal distribution of heat and momentum fluxes at the air-water interface.

- All physical properties are independent of temperature, except density in the buoyancy term.
- Boussinesq approximation is valid.

These assumptions are similar to those introduced when constructing unsteady, one-dimensional models describing geophysical transport processes (Coantic, 1978). Most importantly, neglect of advection is consistent with the assumption of horizontal homogeneity, e.g. absence of drift currents. Field data also indicate that assuming a lake, pond or reservoir as one-dimensional is a reasonable approximation, provided inflows and outflows are not considered and horizontal natural currents are light (Denman and Miyake, 1973).

A detailed discussion of the basic transport processes and interactions at the air-water interface are available in the literature (Kraus, 1972; Coantic, 1978). The general equations which describe the dynamics and thermodynamics of water have also been derived (Phillips, 1966; Kraus, 1972 and Coantic, 1978). Here, only the final forms of the model equations used in the analysis are presented.

3.2.1 Conservation of Energy Equation

With the assumptions discussed earlier, the one-dimensional (see Figure 3.2 for coordinate system) conservation of energy equation (i.e., the First Law of Thermodynamics) reduces to

$$\frac{\partial}{\partial t}(\rho c T) = \frac{\partial}{\partial z}\left[\frac{\mu}{\rho \Pr}\frac{\partial}{\partial z}(\rho c T)\right] - \frac{\partial}{\partial z}(\rho c \overline{w'T'}) + \frac{\partial F}{\partial z} \tag{3.1}$$

where T and T' are the mean and fluctuating temperatures, respectively. The fluctuating velocity component in the vertical direction is denoted by w'. The total radiative flux is represented by F. In the Cartesian coordinate used, z is the vertical coordinate, positive upward (see Figure 3.2). The three terms on the right-hand-side of Eq. (3.1) account for molecular diffusion of heat, turbulent diffusion of heat, and transport of radiant energy, respectively.

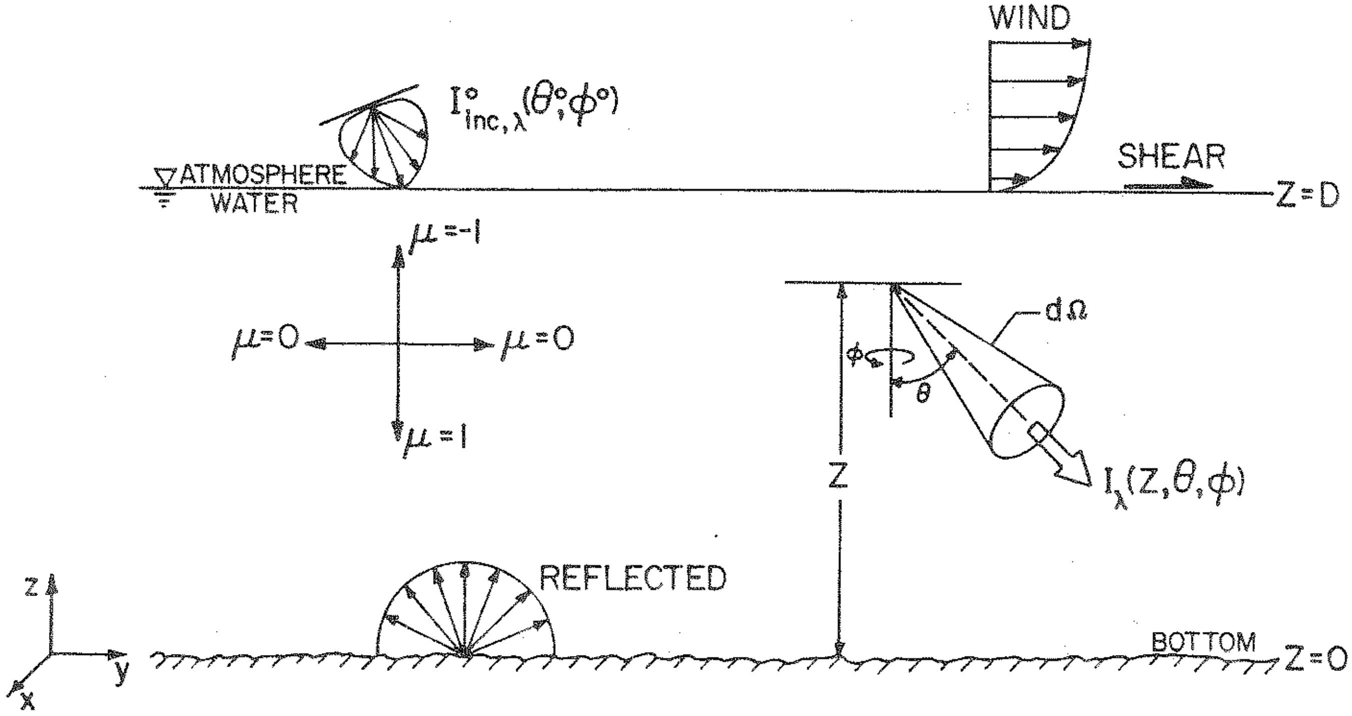

Figure 3.2 Physical model and coordinate system

The turbulent diffusion term in the energy equation can be expressed by defining a turublent exchange coefficient (Patankar and Spalding, 1970)

$$\rho c \overline{w'T'} = - \frac{c\mu_t}{Pr_t} \frac{\partial T}{\partial z} \tag{3.2}$$

where μ_t is the turbulent eddy viscosity and Pr_t is the turbulent Prandtl number. Introducing an effective viscosity and effective Prandtl number as follows (Patankar and Spalding, 1970)

$$\mu_{eff} = \mu + \mu_t, \tag{3.3}$$

and

$$\frac{\mu_{eff}}{Pr_{eff}} = \frac{\mu}{Pr} + \frac{\mu_t}{Pr_t} , \tag{3.4}$$

the energy equation, Eq. (3.1), can be rewritten as

$$\frac{\partial}{\partial t}(\rho cT) = \frac{\partial}{\partial z}[\frac{\mu_{eff}}{\rho Pr_{eff}} \frac{\partial}{\partial z}(\rho cT)] + \frac{\partial F}{\partial z} \tag{3.5}$$

The radiative flux divergence, $\partial F/\partial z$, can be considered as a heat source term and will be discussed in detail in the later sub-sections.

3.2.2 Conservation of Momentum Equations

With the assumptions discussed earlier and the turbulent exchange coefficients introduced in the previous sub-section, the conservation of momentum equations become,

x-direction:

$$\frac{\partial}{\partial t}(\rho u) = \frac{\partial}{\partial z}[\frac{\mu_{eff}}{\rho} \frac{\partial}{\partial z}(\rho u)] - \frac{\partial p}{\partial x} + f\rho v , \tag{3.6}$$

y-direction:

$$\frac{\partial}{\partial t}(\rho v) = \frac{\partial}{\partial z}[\frac{\mu_{eff}}{\rho} \frac{\partial}{\partial z}(\rho v)] - \frac{\partial p}{\partial y} - f\rho u \ , \qquad (3.7)$$

where u and v are components of the velocity in x and y directions, respectively. The last two terms in Eqs. (3.6) and (3.7) can be considered as the source terms which produce the fluid motions and include both the pressure and Coriolis forces. From inspection of the two source terms, it is evident that the two momentum equations are coupled. The effect of the rotation of the earth (i.e., Coriolis term) is significantly important for large bodies of water. The pressure forces are usually neglected due to the complexity encountered in the shape of the surface due to the tilt. However, the shear imposed at the surface introduces a curvature that in turn creates pressure forces which are important in producing circulation in natural waters. The shape of the surface is a function of numerous parameters which creates difficulties in the treatment of pressure effects.

The basic requirement for the pressure gradient models is to satisfy the conservation of mass equation. This is important because the flow induced by the pressure forces is in the opposite direction to that generated by the wind. A simple model for the evaluation of pressure gradients has been reported by Spalding and Svensson (1977).

3.2.3 Radiative Transfer

Accurate determination of temperature distribution in a layer of water being heated by solar radiation requires prediction of the volumetric rate of absorption of solar radiation. This in turn is dependent upon time of day, season, latitude, atmospheric conditions, surface and bottom radiation characteristics and the spectral and absorption characteristics of water. The air-water interface is assumed to be plane. Although in nature, the interface is tilted due to the surface waves generated by wind shear; however, the complexity of a random interface (Preisendorfer, 1971) does not warrant inclusion of such detailed analysis at present time. Justification of this assumption is found in the observations of Payne (1972) who noted little effect on the reflectance of the water surface at moderate wind speeds.

If the internal emission of radiation by the water is neglected, the conservation of radiant energy equation becomes (Viskanta and Toor, 1972; 1978)

$$H(z) = \frac{dF}{dz} = \int_0^\infty \kappa_\lambda [\int_0^{2\pi}\int_0^{\pi/2} I_\lambda(z,\theta,\phi)\sin\theta d\theta d\phi] d\lambda \qquad (3.8)$$

where λ is the wavelength, κ_λ is the spectral absorption coefficient of water and $I_\lambda(z,\theta,\phi)$ is the spectral intensity of radiation in direction θ,ϕ (polar angle θ and azimuthal angle ϕ)(see Figure 3.2). The right-hand-side of Eq. (3.8) represents the local rate of absorption of radiation per unit volume in the absence of internal emission. Neglect of internal emission is well justified since the water is relatively opaque to radiation for wavelengths greater than ~ 2 μm; and a blackbody at 300 K (approximate temperature of water) contains 99.9% of its energy in the range greater than 3 μm.

Using a forward scattering approximation and omitting the mathematical details, it can be shown that the total radiative flux F and the volumetric heating rate H can be expressed as

$$F(z) = 2\int_0^\infty \{\frac{1}{2}\mu^\circ[1 - \rho_{s\lambda}(\mu^\circ)]F_{b\lambda}e^{-(\tau_{D\lambda}-\tau_\lambda)/\mu}/\beta(\tau_{D\lambda},|\mu|)$$

$$+ F_{d\lambda}T_3(\tau_{D\lambda}-\tau_\lambda) - F_{b\lambda}E_3(\tau_\lambda)\}d\lambda \qquad (3.9)$$

and

$$H(z) = \frac{\partial F}{\partial z} = \int_0^\infty 2\kappa_\lambda \{ \frac{1}{2} (\mu^\circ/\mu) [1 - \rho_{s\lambda}(\mu^\circ)] F_{b\lambda} e^{-(\tau_{D\lambda} - \tau_\lambda)/\mu} /$$

$$\beta(\tau_{D\lambda}, |\mu|) + F_{d\lambda}(\tau_{D\lambda} - \tau_\lambda) + \tilde{F}_{b\lambda} E_2(\tau_\lambda) \} d\lambda \tag{3.10}$$

where $\rho_{s\lambda}$ is the spectral reflectivity of the air-water interface. It should be noted that the radiation flux indicent on the water surface is approximated by a sum of a direct (beam), $F_{b\lambda}$, and scattered (diffuse), $F_{d\lambda}$, components. The upward spectral radiative flux leaving the bottom is given by

$$\tilde{F}_{b\lambda} = 2\rho_{b\lambda} \{ \frac{1}{2} \mu^\circ [1 - \rho_{s\lambda}(\mu^\circ)] F_{b\lambda} e^{-\tau_{D\lambda}/\mu} / \beta(\tau_{D\lambda}, |\mu|)$$

$$+ F_{d\lambda} T_3(\tau_{D\lambda}) \} . \tag{3.11}$$

The optical depth τ_λ and the optical thickness $\tau_{D\lambda}$ are defined as

$$\tau_\lambda = \int_0^z \kappa_\lambda dz' \text{ and } \tau_{D\lambda} = \int_0^{z=D} \kappa_\lambda dz' \tag{3.12}$$

The exponential and transmission integral functions $E_n(\chi)$, $T_2(\chi)$ and $T_3(\chi)$, respectively, are defined as

$$E_n(\chi) = \int_0^1 e^{-\chi/\mu} \mu^{n-2} d\mu \tag{3.13}$$

$$T_2(\chi) = \int_0^1 [1 - \rho_s(\mu')] e^{-\chi/\mu} (\mu'/\mu) d\mu' / \beta(\tau_D, |\mu|) \tag{3.14}$$

$$T_3(\chi) = \int_0^1 [1 - \rho_s(\mu')] e^{-\chi/\mu} \mu' d\mu' / \beta(\tau_D, |\mu|) \tag{3.15}$$

The factor $\beta(\tau_D, |\mu|)$ which accounts for interreflections between bottom and interface is defined by

$$\beta(\tau_D, |\mu|) = 1 - \rho_b \rho(\mu) \exp(-2\tau_D/|\mu|) \tag{3.16}$$

The first and second term on the right-hand-side of Eq. (3.9) represent the contributions of the beam and diffuse components of the incident solar flux, respectively. The third term denotes the contribution to the flux due to the reflection from the bottom.

As discussed earlier, these equations have been developed by Viskanta and Toor (1972, 1978) and have been verified indirectly in the laboratory by Snider and Viskanta (1975). Equations (3.9) and (3.10) also yield realistic estimates of radiative transfer in natural waters and detailed calculations are presented by Viskanta and Toor (1973 and 1978). Therefore, if the depth, bottom surface properties, spectral optical properties of water and spectral incident radiation flux are known, the local radiative flux and the local rate of internal absorption of radiant energy in the water can be calculated.

3.2.4 Turbulence Model

Solution of the momentum and energy equations, Eqs. (3.5), (3.6) and (3.7) requires a knowledge of the fluctuating components of velocity and temperature. Equations have been derived for determining the fluctuating components (Coantic, 1978); however, the difficulties with closure, incompleteness of experimental data needed to evaluate parameters that arise in model equations and computational problems are just a few of the reasons for the lack of a more widespread adoption of this method for predicting turbulence. For example, accurate prediction of the fluctuations necessitates using a very fine grid spacing (i.e., grids of a size smaller than the micro-scale eddies). This in turn requires unrealistic computer core memory storage. Although introducing turbulent exchange coefficients (e.g. turbulent eddy diffusivities) simplifies the form of the conservation equations yet a knowledge of these coefficients is required for the solution of the conservation equations.

There are several different levels of sophistication in modeling turbulence (Launder and Spalding, 1972). The method adopted in this work is based on the two differential equation model for predicting the turbulent exchange coefficients, i.e. turbulent conductivity as defined by Eq. (3.2). The detailed development of the model equations is given by Launder and Spalding (1972) and will not be repeated here. One of the main reasons for using the model is that it is capable of accounting for both the buoyancy and shear generated turbulence in a horizontal layer of fluid.

The turbulent exchange coefficients can be related to the turbulent kinetic energy K and some length scale ℓ by the Prandtl's formula

$$\mu_t = \rho \ell \sqrt{K} \qquad (3.17)$$

The length scale ℓ is defined in terms of the turbulent kinetic energy dissipation ε (Launder and Spalding, 1972) such that

$$\ell = C_\mu K^{3/2}/\varepsilon \qquad (3.18)$$

Elimination of the mixing length ℓ between Eqs. (3.17) and (3.18) yields

$$\mu_t = \rho C_\mu K^2/\varepsilon \qquad (3.19)$$

The turbulent Prandtl number Pr_t is defined by the following expression

$$Pr_t = \left(\frac{\phi}{\phi_t}\right)\left[\frac{1 + \phi_t'(C_t' - \phi_t)B}{1 + B\phi\,\phi_t}\right] \qquad (3.20)$$

where ϕ, ϕ_t, ϕ_t', C_t' are constants. Their values are determined on the basis of experimental data and/or empirical information, and the specific values used in the model will be presented later. The buoyancy parameter B is defined as

$$B = g\beta (\frac{K}{\varepsilon})^2 \frac{\partial T}{\partial z} \tag{3.21}$$

Mathematical models have been constructed for the two quantities, turbulent kinetic energy K and the turbulent kinetic energy dissipation ε, which define the turbulent exchange coefficient defined by Eq. (3.17). The details of the derivation of the K-ε turbulence model can be found in the literature (Launder and Spalding, 1972; Launder, 1975; Spalding and Svensson, 1977).

The differential equation for the turbulent kinetic energy K is given by

$$\frac{\partial K}{\partial t} = \frac{1}{\rho}\frac{\partial}{\partial z}(\frac{\mu_{eff}}{\sigma_K}\frac{\partial K}{\partial z}) + \frac{\mu_t}{\rho}[(\frac{\partial u}{\partial z})^2 + (\frac{\partial v}{\partial z})^2]$$

$$- \frac{\mu_t}{\rho}\frac{g\beta}{Pr_t}\frac{\partial T}{\partial z} - \varepsilon \tag{3.22}$$

The first term on the right-hand-side of Eq. (3.22) represents diffusion of turbulent kinetic energy; the second term denotes production of kinetic energy; the third term signifies production or dissipation of kinetic energy by density (temperature) gradients; and the fourth term represents dissipation of turbulent kinetic energy. In Eq. (3.22) σ_K is the turbulent kinetic energy Prandtl number.

The differential equation for the turbulent kinetic energy dissipation ε is

$$\frac{\partial \varepsilon}{\partial t} = \frac{1}{\rho}\frac{\partial}{\partial z}(\frac{\mu_{eff}}{\sigma_\varepsilon}\frac{\partial \varepsilon}{\partial z}) + C_{1\varepsilon}\frac{\mu_t}{\rho}\frac{\varepsilon}{K}[(\frac{\partial u}{\partial z})^2 + (\frac{\partial v}{\partial z})^2]$$

$$- C_{3\varepsilon}\frac{\mu_t}{\rho}\frac{\varepsilon}{K}\frac{g\beta}{Pr_t}\frac{\partial T}{\partial z} - C_{2\varepsilon}\frac{\varepsilon^2}{K} \tag{3.23}$$

The physical meaning of the terms on the right-hand-side of Eq. (3.23) is analogous to that of Eq. (3.22). In Eq. (3.23) $C_{1\varepsilon}$, $C_{2\varepsilon}$ and $C_{3\varepsilon}$ are semiempirical constants. Values for these and other constants appearing in the two differential model of turbulence have been given by Launder and Spalding (1972) and are summarized in Table 3.1.

Table 3.1 Values of the turbulence model constants (Launder and Spalding, 1972)

Constant	Value
ϕ	0.2
ϕ_t	0.31
ϕ_t'	0.155
σ_K	1.0
σ_ε	1.3
$C_{1\varepsilon}$	1.44
$C_{2\varepsilon}$	1.92
$C_{3\varepsilon}$	0.0
C_μ	0.09
C_t'	1.6

The original values of the constants reported have been substantiated by other investigators (Plumb and Kennedy, 1977; Spalding and Svensson, 1977). As it is indicated in Table 3.1 constant $C_{3\varepsilon}$ has a reported value of 0 which implies that stratification does not influence the development of turbulence, Eq. (3.23). This value has been reported by Launder (1975), Gibson and Launder (1976) and Hossain and Rodi (1976) for horizontal unstratified shear flows. However, for a stratified fluid this value is unrealistic. Experimental results indicate that even in the absence of surface shear turbulence is generated by buoyancy forces. Therefore, it is believed that a non-zero value of $C_{3\varepsilon}$ must be used since the buoyancy term in the turbulent kinetic energy dissipation equation, Eq. (3.23), is an important term in that equation.

The K-ε turbulence model formulated here is a simple version of a more general turbulence model discussed by Launder and Spalding (1972), as well as Launder (1975) and later adopted by Spalding and Svensson (1977). Note that once the K-ε equations are solved the instantaneous, local turbulent eddy viscosity can be determined from Eq. (3.19).

3.2.5 Boundary and Initial Conditions

The initial conditions for an initially stagnant body of water are assumed to be

$$\begin{aligned} T(z,0) &= T_o(z) \\ u(z) &= v(z) = 0 \end{aligned} \tag{3.24}$$

The boundary conditions for a layer of water with a free surface (i.e. air-water interface) can be expressed as

$$\begin{aligned} k_{eff} \left.\frac{\partial T}{\partial z}\right|_{z=D} &= q_s \\ k_{eff} \left.\frac{\partial T}{\partial z}\right|_{z=0} &= q_b \\ \tau_{sx} &= \mu_{eff} \left.\frac{\partial u}{\partial z}\right|_{z=0} \\ \tau_{sy} &= \mu_{eff} \left.\frac{\partial v}{\partial z}\right|_{z=0} \end{aligned} \tag{3.25}$$

where k_{eff} is the effective thermal conductivity, q_s is the total heat flux at the surface and q_b is the total heat flux at the bottom. The shear stresses at the surface in the x and y directions are denoted by τ_{sx} and τ_{sy}, respectively.

The initial conditions for the turbulence model are evaluated by assuming negligible initial turbulence level in the water and can be represented as

$$\begin{aligned} \mu_t(z,0) &= 0 \\ \varepsilon(z,0) &= 0 \qquad (3.26) \\ K(z,0) &= 0 \end{aligned}$$

The boundary conditions for the turbulent quantities at the free surface (i.e. $z = D$) and the solid wall (i.e. $z = 0$) in the finite difference form are discussed by Launder and Spalding (1972).

3.3 Numerical Solution of the Model Equations

The momentum, energy and turbulence model equations need to be solved to yield the temperature distribution in the water. However, a closed form analytical solution of these equations does not appear possible. Therefore, a recourse to numerical schemes must be taken in order to integrate the differential equations.

Using finite difference methods, the nonlinear governing equations with appropriate boundary conditions and internal radiant energy absorption can be solved. This section deals with the formulation of the finite difference equations and boundary conditions. Raithby (1976) has discussed several ways of deriving the finite difference approximations of the differential equations. The form adopted here was obtained by Patankar and Spalding (1970) and Spalding (1977). This was accomplished by integrating the finite difference forms of the equations over a differential control volume. Since the detailed derivation of these equations is presented elsewhere (Patankar and Spalding, 1970; Spalding, 1977) only the grid arrangement and the general form of the equations are included here.

The momentum, energy and K-ε differential equations can be written in the general form,

$$\frac{\partial \Phi}{\partial t} = \frac{\partial}{\partial z} (\Gamma_\Phi \frac{\partial \Phi}{\partial z}) + S_\Phi \qquad (3.27)$$

where Φ stands for ρu when x-direction momentum is considered, ρcT when thermal energy equation is considered, etc. The symbol S_Φ denotes the source term for the variable Φ, and Γ_Φ is a transport coefficient. This general equation is to be integrated over the control volume denoted by index i (see Figure 3.3). The time is represented by index j, and N is the number of grid lines along the vertical direction. The upstream (in time) is denoted by t^+ and the downstream by t^-.

Term by term integration of Eq. (3.27) over the control volume yields the final form of the equations to be solved:

$$D(i)\Phi^+(i) = A(i)\Phi^+(i+1) + B(i)\Phi^+(i-1) + C(i) \qquad (3.28)$$

where:

$$A(i) = \Gamma_\Phi(i+\tfrac{1}{2})/\Delta z(i+\tfrac{1}{2}) \qquad (3.29)$$

$$B(i) = \Gamma_\Phi(i-\tfrac{1}{2})/\Delta z(i-\tfrac{1}{2}) \qquad (3.30)$$

$$C(i) = \Phi^-(i)\Delta z(i)/\Delta t + \Delta z(i)S(i) \qquad (3.31)$$

$$D(i) = A(i) + B(i) + \Delta z(i)/\Delta t - \Delta z(i)S'(i) \qquad (3.32)$$

The source term in Eq. (3.27) has been divided into two parts, one of which contains the variable itself:

$$S_\Phi = S(i) + S'(i)\Phi^+ \qquad (3.33)$$

Equation (3.28) can be written in a form of a tri-diagonal matrix which can be solved by a special algorithm. In writing the energy equation, Eq. (3.5) expressed in the general form Eq. (3.27), it has been assumed that the volumetric rate of radiant energy absorption is a known function of time and position. In other words, the radiative transfer is determined independently of the energy equation for the volumetric heating rate (Viskanta and Toor, 1978), and the results are used in the form of a known source term. The

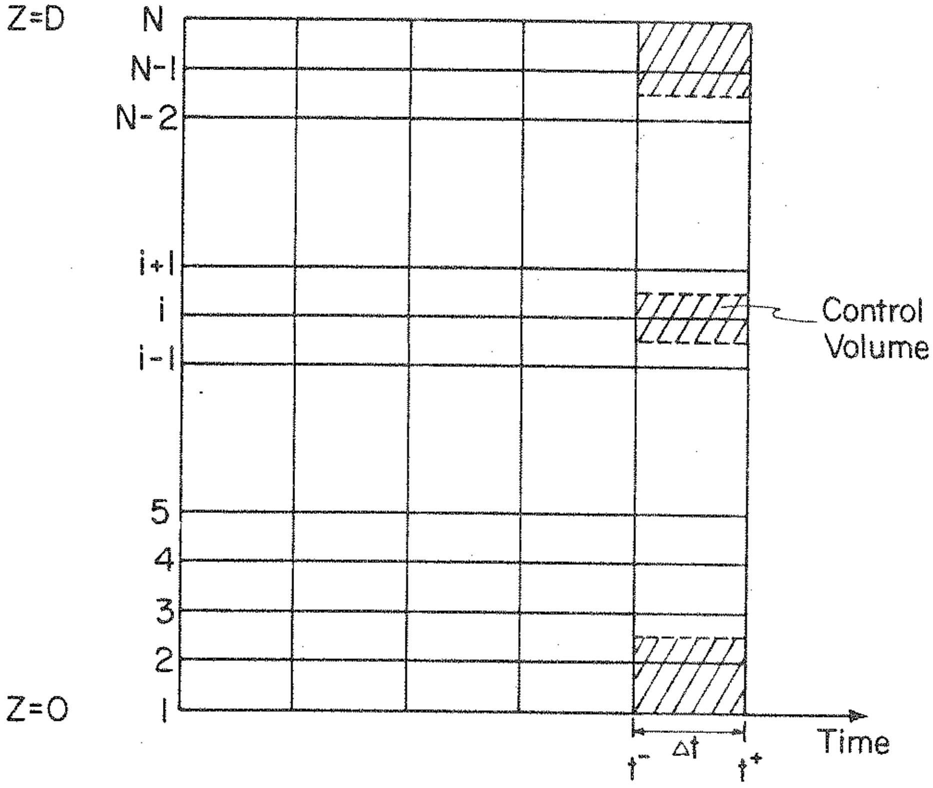

Figure 3.3 Schematic diagram of grid spacings

finite difference equations were solved using the GENMIX computer program (Spalding, 1977) for the two-dimensional parabolic equations. The modified computer program was a simplified version of the general GENMIX program (Spalding and Svensson, 1977). The extensive documentation of the GENMIX computer program is given by Patankar and Spalding (1970) and Spalding (1977).

The boundary conditions used were:

$$q_s = q_{conv} + q_{evap} + q_{rad} \tag{3.34}$$

$$q_b = q_{cond} + q_{rad} \tag{3.35}$$

where q_s and q_b are the total heat fluxes at the surface and bottom, respectively. Numerous semiempirical relations are available in the literature for predicting energy and momentum transfer across the air-water interface of natural waters (Wieringa, 1974; Dunchel et al., 1974; Weisman, 1975; Davies et al., 1975 and Reed, 1977). An extensive review of correlations reported in the literature is given by Paily et al. (1974). Determination of surface energy transfer for the body of water in the laboratory situation does not contain as many variables and is not as complex as in natural water; however, empirical and semiempirical relations must still be employed.

The net radiative flux at the water surface consists of radiation flux emitted by the heaters which reaches the surface in the part of the spectrum where water is effectively opaque to radiation and is absorbed there, and net radiation exchange between the water surface and the surroundings. The radiation flux from the radiant heaters, absorbed at the surface, can be expressed as

$$F_0 = \int_{\lambda_{opaque}} \alpha_\lambda F_{inc,\lambda} d\lambda \tag{3.36}$$

where α_λ is the spectral absorptivity of the water and $F_{inc,\lambda}$ is the spectral incident flux which is emitted from the heaters and reaches the water surface after transmission by glass plates. The radiation flux incident on the water surface can be approximated by

$$F_{inc,\lambda} = \tau_{g,} \varepsilon_{lamp,\lambda} E_{b\lambda}(T_{lamp}) A_{filament} A_{test\ cell}/\pi d^2 \qquad (3.37)$$

where $\tau_{g,\lambda}$ is the spectral transmittance of glass plate(s) above the water surface, $A_{test\ cell}$ is the cross-sectional area of the test cell parallel to the heater strips, $\varepsilon_{lamp,\lambda}$ is the effective emissivity of the heater filament per unit area of the filament, $E_{b\lambda}$ is the Planck's function and $A_{filament}$ is the effective emitting area of the heater filament.

The water surface exchanges heat by radiation with the surroundings and primarily with the glass plate(s) above the water surface. Assuming that the plate(s) is at the ambient temperature, the net infrared radiant heat transfer can be approximated by

$$q_{rad} = - F_0 + \frac{\sigma(T_s^{\ 4} - T_{amb}^{\ \ 4})}{\frac{1}{\varepsilon_s} + \frac{1}{\varepsilon_g} - 1} \qquad (3.38)$$

where ε_s is the emissivity of the water surface in the long-wave part of the spectrum and ε_g is the emissivity of the glass plate.

In the presence of air flow heat is also transported by convection and latent energy transport. Using semiempirical relation given by Ginzburg and Fedorov (1978) obtained in laboratory experiments, the sum of the convective and evaporative heat fluxes at the water surface can be expressed as

$$\begin{aligned} q_{conv} + q_{evap} &= h_c(T_{surface} - T_a) + h_m(p_{v0} - p_{va})h_{fg} \\ &= C_m \rho_a c_{pa}(T_{surface} - T_a)U_a + \qquad (3.39) \\ &\quad C_m \rho_a h_{fg}\left(\frac{0.622}{p}\right)(p_{s0} - p_{va})U_a \end{aligned}$$

where subscript a denotes air, h_{fg} is the latent heat of vaporization of water, U_a is the air velocity and p is the ambient pressure in mb. The saturation pressure at surface temperature is p_{s0}, and

p_{va} is the partial pressure of water vapor at the ambient temperature. The proportionality coefficient C_m is a measure of mass transfer and is determined empirically. The water vapor saturation pressure at temperature T can be evaluated from the accurate expression given by Paily et al. (1974),

$$p_s = 23.38\exp(18.1 - \frac{5303.3}{T}) \tag{3.40}$$

where p_s is in mb and T is in Kelvins. The vapor pressure of water in air, p_{va}, can be calculated from the definition

$$p_{va} = rp_{sa} \tag{3.41}$$

where r is the relative humidity of air.

The boundary conditions for the turbulence model equations can be obtained from the fixed rigid boundary (bottom) and free surface (water) relations (Launder and Spalding, 1972). At a solid boundary the turbulent kinetic energy is specified by assuming equilibrium condition (i.e. generation equals dissipation close to a rigid boundary) which results in

$$K = [(\frac{\tau_w}{\rho\sqrt{C_\mu}})^{3/2} + \frac{q_w\kappa\Delta z\beta g}{\rho c C_\mu^{3/4}}]^{2/3} \tag{3.42}$$

where q_w is the heat flux and τ_w is the shear stress at the rigid boundary, respectively, and are expressed as

$$q_w = c\,\frac{\mu_t}{Pr_t}\frac{\partial T}{\partial z} \tag{3.43}$$

$$\tau_w = \mu_t\frac{\partial u}{\partial z} \tag{3.44}$$

In Eq. (3.42) κ is the von Karman's constant and Δz is the grid spacing near the solid wall. Dissipation of turbulent kinetic energy is specified from the requirement that

$$\varepsilon = C_\mu K^{3/2}/\ell \tag{3.44}$$

where ℓ is the length scale and near a solid wall is evaluated from (Launder and Spalding, 1972):

$$\ell = C_\mu^{1/4} \kappa \Delta z \tag{3.45}$$

Substitution of Eq. (3.45) into Eq. (3.44) yields the dissipation of turbulent kinetic energy near a solid wall,

$$\varepsilon = C_\mu^{3/4} K^{3/2}/\kappa \Delta z \ . \tag{3.46}$$

At a free surface, in the absence of shear stress and heat flux, the boundary can be treated as a symmetry plane (Hossain and Rodi, 1976),

$$\begin{aligned} \frac{\partial K}{\partial z} &= 0 \\ \frac{\partial \varepsilon}{\partial z} &= 0 \end{aligned} \tag{3.47}$$

At a free surface in the presence of shear stress and/or heat flux, the boundary can be treated as a fixed rigid one. If the fluid is assumed quiescent, the interface can be treated as a moving wall, and the boundary conditions can be expressed (Spalding, 1975) as

$$K = [(\frac{\tau_w}{\rho\sqrt{C_\mu}})^{3/2} + \frac{q_w \kappa \Delta z g \beta}{\rho c C_\mu^{3/4}}]^{2/3} \tag{3.48}$$

$$\varepsilon = C_\mu^{3/4} K^{3/2}/\kappa \Delta z \tag{3.49}$$

It should be noted that, although these equations are very similar to those for a fixed rigid boundary [Eqs. (3.42) and (3.44)], in these expressions τ_w and q_w are the imposed shear stress and heat flux, respectively.

Before discussing different turbulence model constants and their importance, it is appropriate to mention the numerical technique adopted by the GENMIX computer code. In approximating differential equations using finite difference schemes much care should be given to the stability of the finite difference equations. Oscillation of the approximate solution is a direct manifestation of instability in the finite difference scheme (Carnahan et al., 1969). Although stability of the finite difference equations presented earlier has been optimized (Spalding, 1977); however, the scheme is not unconditionally stable. Therefore, a stability and accuracy test must be performed to insure meaningful results. Both the accuracy and stability of a given finite difference scheme mainly depend on the spatial grid spacing and time step. On the one hand, both a small grid and time step is desired for accuracy, but on the other hand, too small time step may produce instability and may require unreasonable computer core-space and execution time. Therefore, the grid spacing and time step is usually a compromise.

A time step and grid space halving technique was used as a check for accuracy and stability. This was achieved by halving the grid size using a fixed time step until the solution became independent of the number of grid points. Using the selected grid size, the same procedure was repeated by halving the time step until the solution became independent of the time step. For most of the problems studied a total number of 100 grids and a time step of about 0.5 sec proved to be more than adequate for insuring accuracy and stability of the numerical results.

3.4 Sensitivity of K-ε Model to Different Turbulence Constants

In this section the sensitivity of the turbulence model to different constants and parameters is examined. A set of constants for the problem of heating from below of a stably stratified layer of water is determined by comparison of laboratory results with model predictions.

As discussed earlier, no universality in the actual values of turbulence model constants are claimed. In fact, it is believed that some of the constants and parameters are dependent on the particular physical situation and experimental conditions to which the model is applied (Spalding and Svensson, 1977). Values of these constants have been established for different problems (Launder and Spalding, 1972; Jones and Launder, 1972; Plumb and Kennedy, 1977); however, examination of the model equations and the constants presented in Table 3.1 shows that a zero value for $C_{3\varepsilon}$, which has been reported by Hossain and Rodi (1976), is unrealistic. Inspection of ε equation, Eq. (3.23), indicates that $C_{3\varepsilon} = 0$ means that the dissipation of turbulent kinetic energy is unaffected by thermal stratification. In the absence of wind stress but reasonable heat loss at the surface the fluid layer will be unstable near the surface and this will generate turbulence. Therefore, a nonzero value of $C_{3\varepsilon}$ is essential for the buoyancy affected turbulence problems.

The results of Deardorff et al. (1969) are used to establish the values of the turbulence model constants. In the particular experiments of Deardorff et al. a stably stratified layer of water was heated from below which resulted in instability near the bottom. Therefore, the convective turbulent motion was driven by buoyancy which makes it ideal for evaluation of $C_{3\varepsilon}$. Using data from Deardorff's experiment A, the energy equation with K-ε turbulence equations were solved for several values of the constant $C_{3\varepsilon}$ (for the values of other constants, see Table 3.1). It was found that $C_{3\varepsilon} = 0.8$ yields the best all around agreement between predicted temperature profiles and experimental results (see Figure 3.4). No measurements of the effective viscosities have been reported and the validity of the turbulence model cannot be checked directly. However, since the predicted temperature is in good

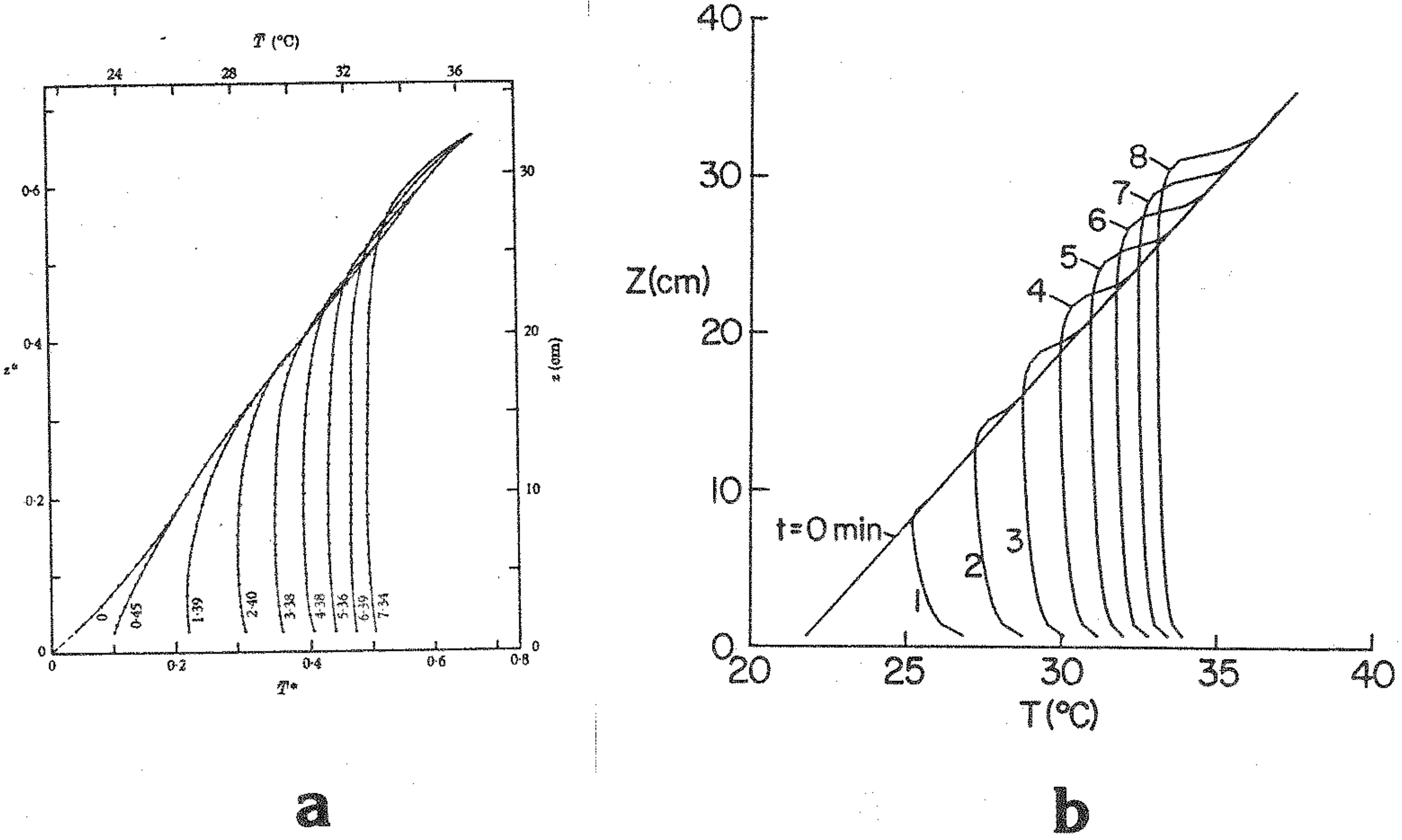

Figure 3.4 Comparison of measured and predicted temperature distribution during heating of uniformly stratified water from the bottom: (a) measured (Deardorff et al., 1969), (b) predicted

agreement with the data, it is believed that the results presented in Figure 3.5 represent the general trends and relative order magnitude of the effective viscosity profiles.

Figure 3.6 shows the sensitivity of the model equations to the value of constant $C_{3\varepsilon}$. The temperature profiles shown are the predictions at 5 minutes. The corresponding predicted effective viscosity profiles are presented in Figure 3.7. Note that a zero value for $C_{3\varepsilon}$ overpredicts both the mixed layer height and temperature. This is due to the fact that smaller value of $C_{3\varepsilon}$ indicates less dissipation of the turbulent kinetic energy, see Eq. (3.23), and therefore results in a higher value of the effective viscosity. Using a value of 1.6 for $C_{3\varepsilon}$, which is twice the adopted value, results in an underestimation of both the mixed layer height and temperature in comparison to measurements (Deardorff et al. 1969). This is due to an increase in the dissipation of the turbulent kinetic energy which in turn yields a decrease in the level of turbulence. It is interesting to note that the peak of the dimensionless effective viscosity after 5 minutes changes from 140 ($C_{3\varepsilon} = 1.6$) to 670 ($C_{3\varepsilon} = 0.0$). This indicates that the model equations are very sensitive to the constant $C_{3\varepsilon}$, at least for the particular physical problem considered here. However, the temperature distribution is not as sensitive to the constant. There is little difference between the predicted temperature profiles for $C_{3\varepsilon} = 0$ and 0.8, Figure 3.6.

Examination of the ε-equation, Eq. (3.23), indicates that in the absence of large velocity gradients (i.e. no applied wind shear) $C_{2\varepsilon}$ is an important parameter in predicting turbulence. Therefore, it is worthwhile to examine the sensitivity of the model equation to this constant ($C_{2\varepsilon}$). The temperature distribution after 5 minutes for three different values of this constant are presented in Figure 3.8, and the corresponding effective viscosity profiles are shown in Figure 3.9. It is evident that using a $C_{2\varepsilon}$ which is half of the suggested value (see Table 3.1) results in an underprediction of both the mixed layer height and temperature compared

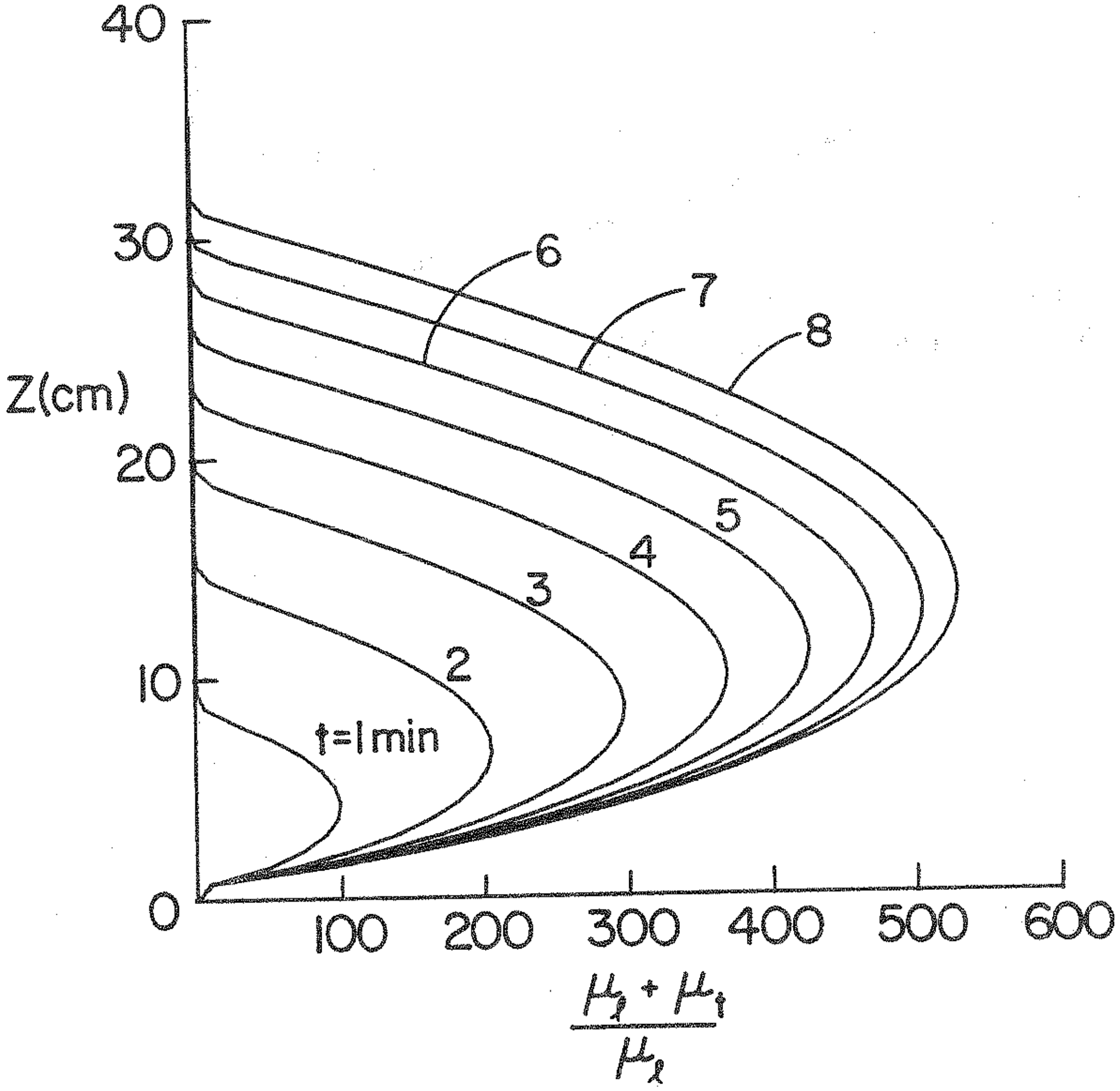

Figure 3.5 Predicted effective viscosity distribution for Experiment A of Deardorff et al. (1969)

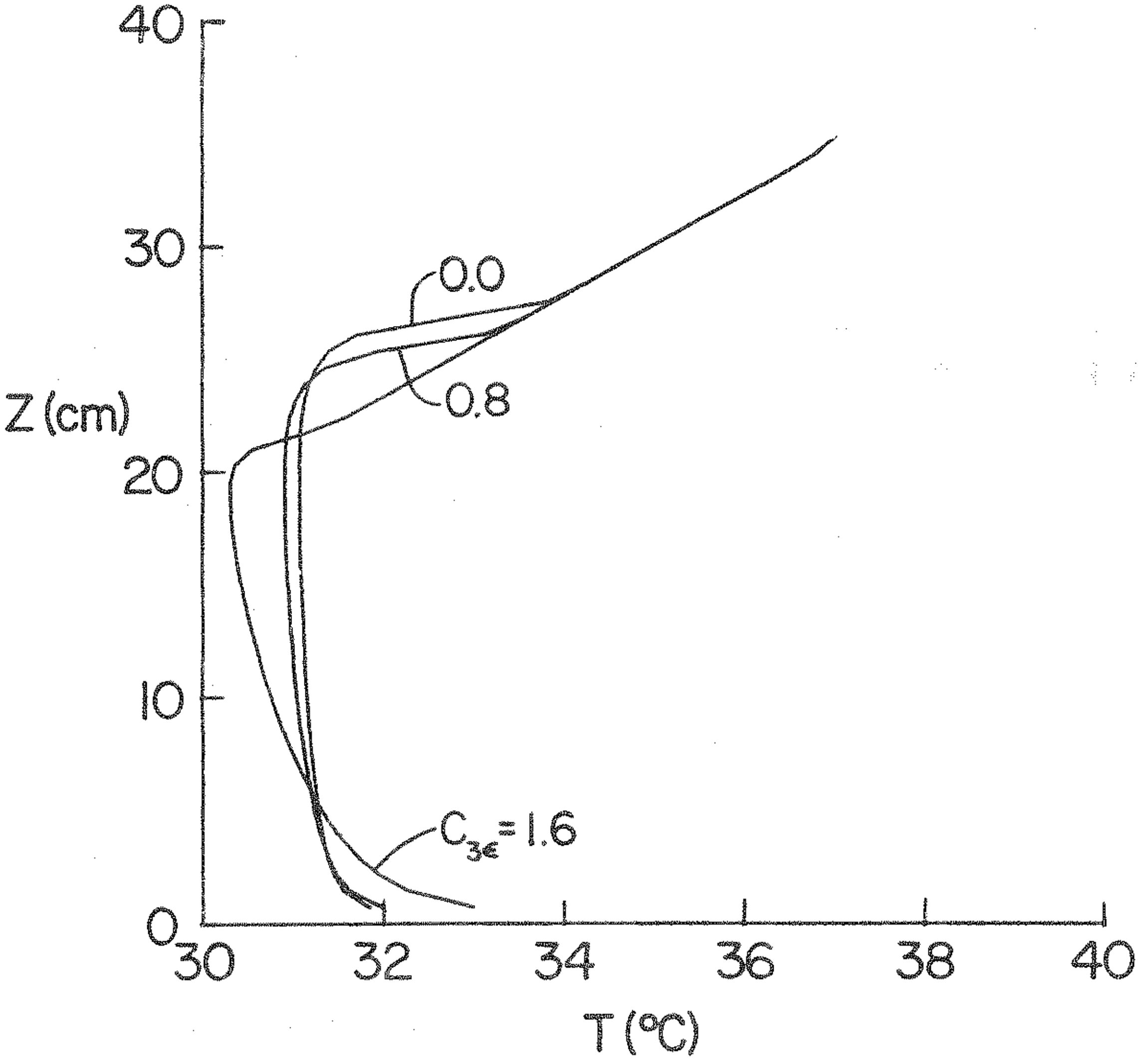

Figure 3.6 Effect of constant $C_{3\varepsilon}$ on the predicted temperature distribution at t = 5 min

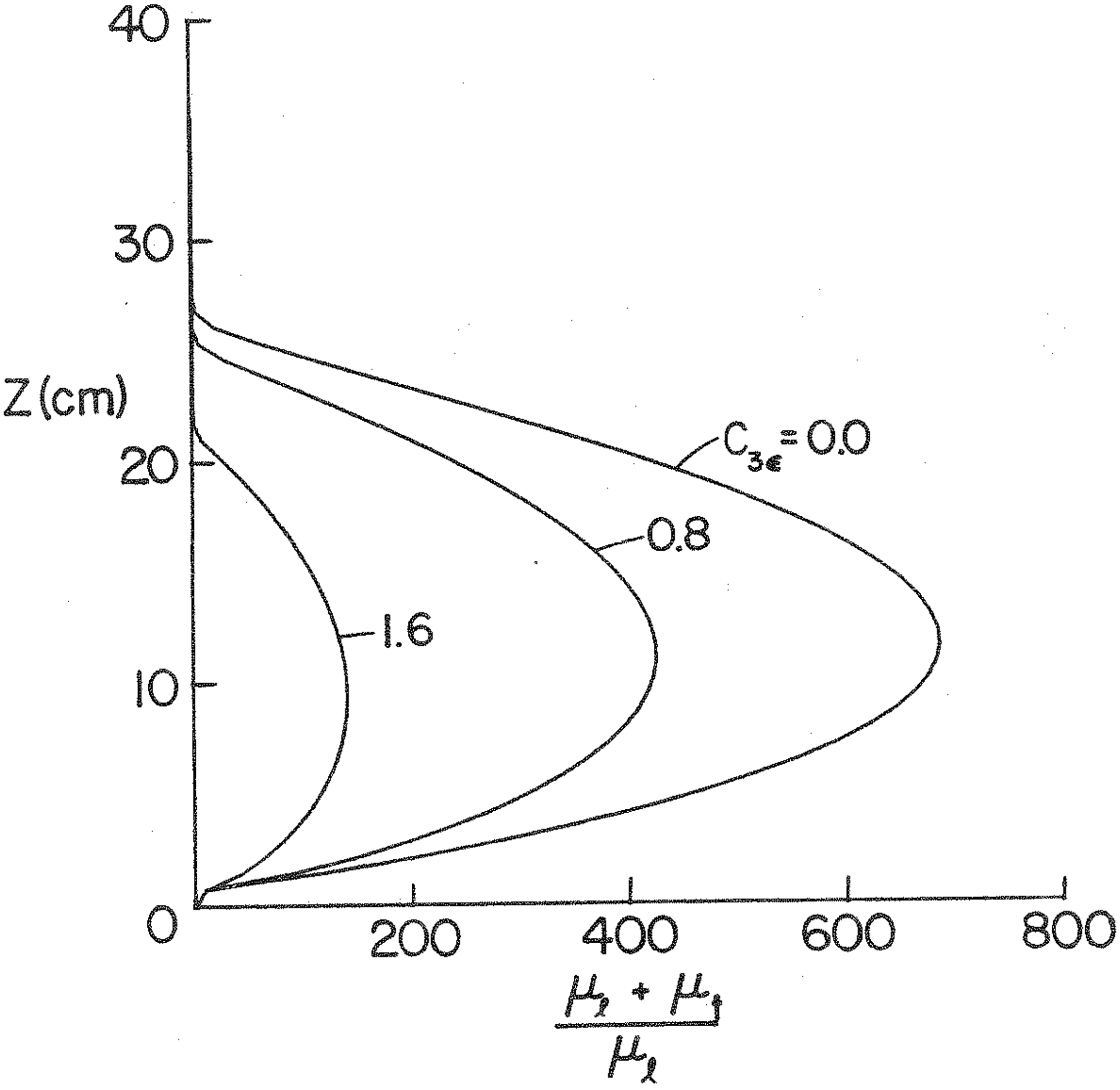

Figure 3.7 Effect of constant $C_{3\varepsilon}$ on the predicted dimensionless effective viscosity distribution at t = 5 min

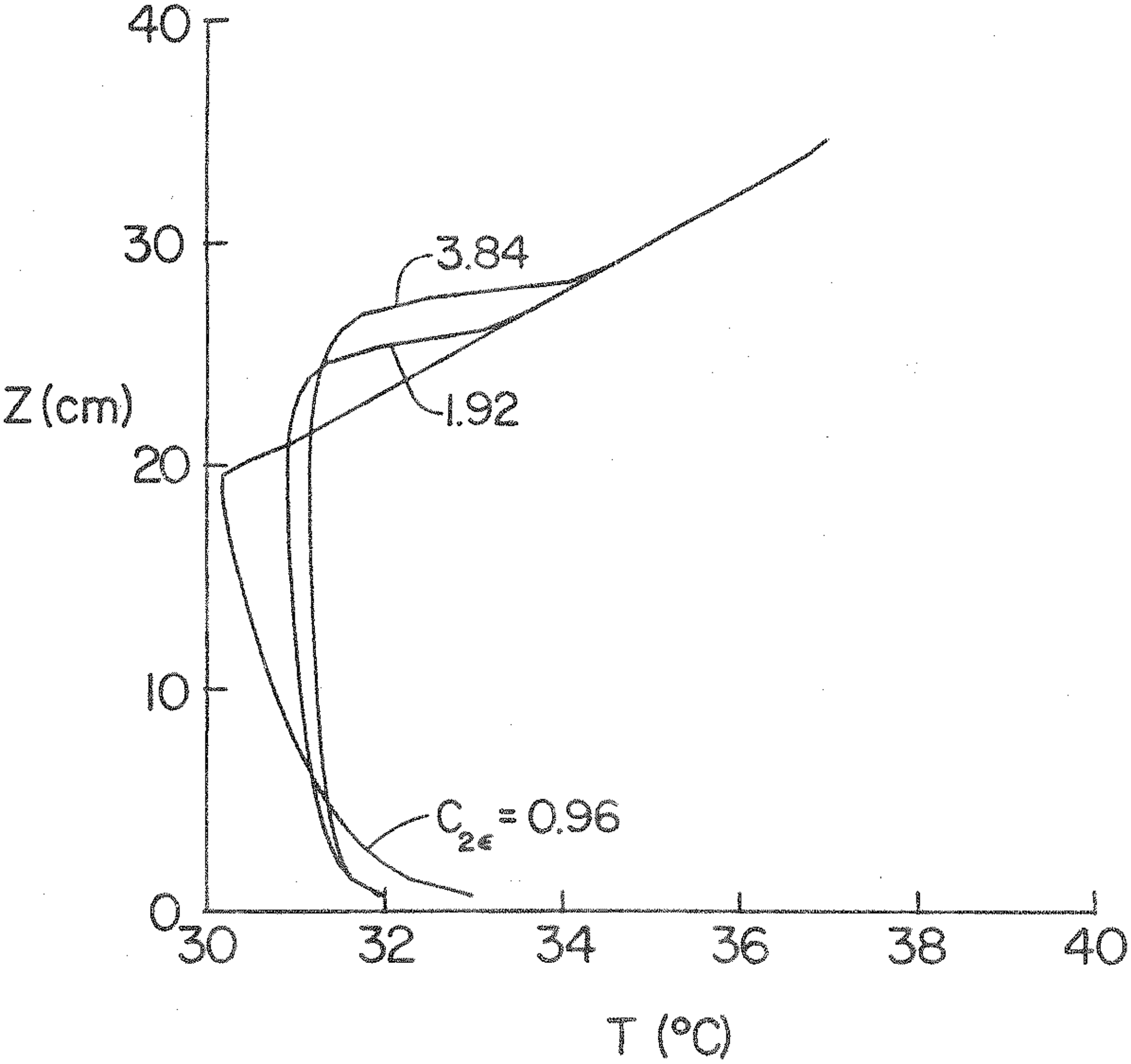

Figure 3.8 Effect of constant $C_{2\varepsilon}$ on the predicted temperature distribution at t = 5 min

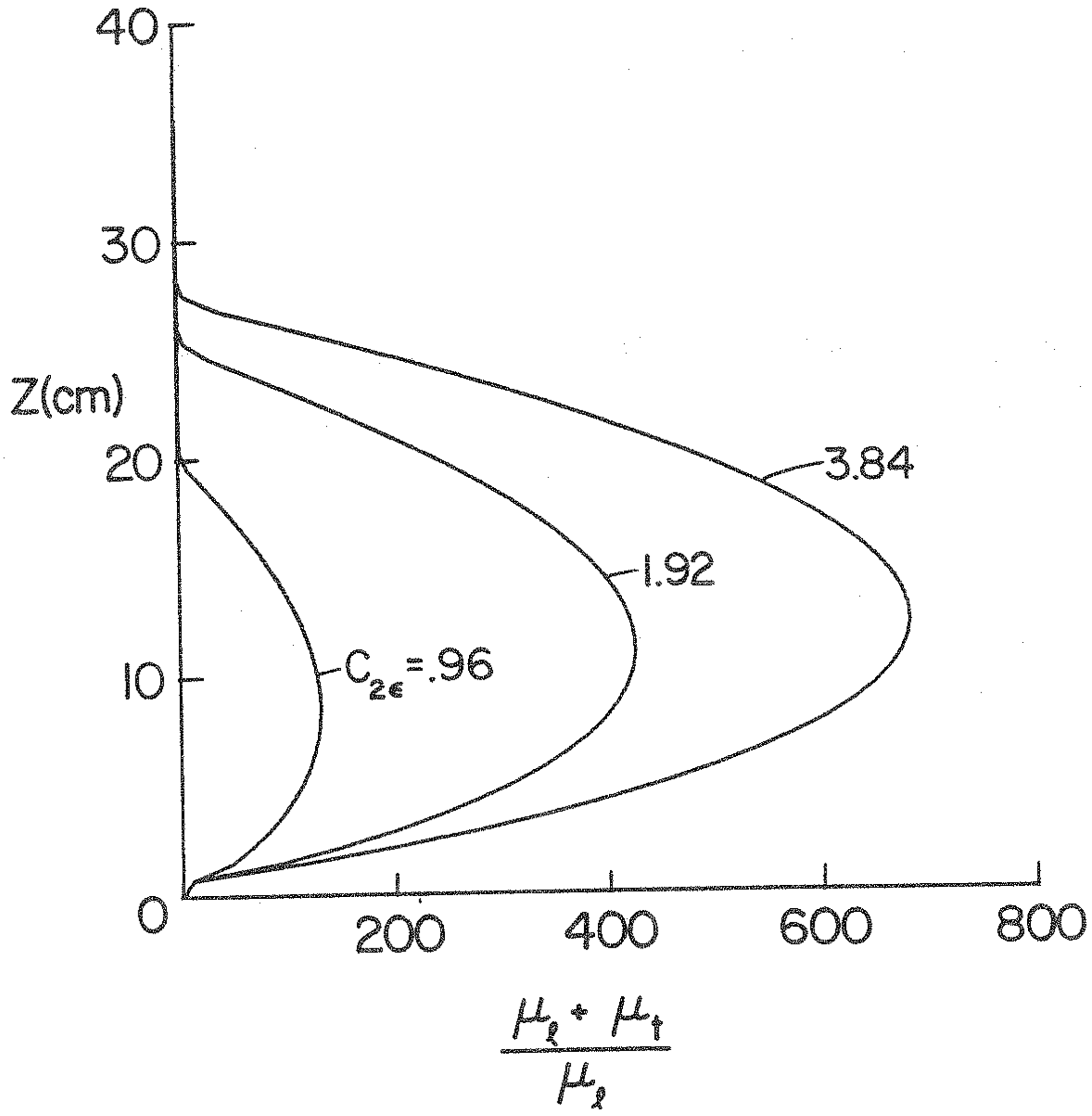

Figure 3.9 Effect of constant $C_{2\varepsilon}$ on the predicted dimensionless effective viscosity distribution at t = 5 min

to observations (Deardorff et al., 1969). This is due to an increase in the rate of dissipation of turbulent kinetic energy, as is evident from the ε-equation. A smaller value of $C_{2\varepsilon}$ results in a decrease in the peak value of effective viscosity, see Figure 3.9, and in turn produces less mixing (note the shape of the temperature profile for $C_{2\varepsilon} = 0.96$ in Figure 3.8). A value of $C_{2\varepsilon} = 3.84$ causes an increase in both the mixed layer height and temperature, although the general shape of the temperature profile is not significantly altered from that of $C_{2\varepsilon} = 1.92$. However, it should be noted that in the case of $C_{2\varepsilon} = 3.84$ a more distinct overshoot is obtained (see Figure 3.8) that has been observed experimentally. This is due to the fact that the peak value of dimensionless effective viscosity is about 670 which is about 75% larger than the peak value for $C_{2\varepsilon} = 1.92$.

It should be emphasized that the values established here for the constants are primarily for buoyancy driven turbulent flows and could be different for combined shear and buoyancy affected flows.

In all of the calculations presented in this section a 40 grid point and 0.5 second time step was used which was tested and proved to be satisfactory.

4. STRATIFICATION OF A SHALLOW LAYER OF WATER

4.1 Introduction

In a deep layer of water, the effect of the bottom on the radiation transfer and the temperature distribution is not expected to be significant. This is due to the penetration of the short-wave solar radiation to a finite depth. For example, the percentage of surface irradiance reaching different depths of various types of ocean waters has been reported by Jerlov (1976). For clean oceanic water, less than 90% of the incident solar energy is absorbed within the first 30 meters, while for very turbid coastal water more than 99% is absorbed over the first 6 meters. The volumetric heating rates, and therefore the turbulent structures, will as a consequence be appreciably different in both cases.

It is expected that for shallow waters such as lakes, ponds, reservoirs and coastal waters radiative transfer will be affected by the bottom. For a given depth of water and bottom reflectance, the local volumetric heating rate will be greater for turbid than for clear waters. However, penetration of a large fraction of short-wave solar radiation in clear waters will result in the heating of the bottom (Viskanta and Toor, 1978). In turn, this heating may produce an unstable situation which may develop into natural convection layer between the bottom and stably stratified region above. Radiation transfer in shallow waters does not appear to have received much experimental or analytical attention. Particularly, the thermal aspects of absorption of short-wave solar radiation by the bottom or by the water in the vicinity of the bottom have not been studied. Yet natural convection mixing processes resulting from deposition of energy near or at the bottom may have an important bearing on the transport of nutrients, pollutants, and sediments in this part of the layer.

In this phase of the investigation thermal structure of a shallow water layer was studied during heating by radiation. Carefully controlled laboratory experiments were performed using test cell A which was built to model a shallow layer of water with known bottom radiation characteristics.

The interferometer was used to visualize and measure the unsteady temperature profile in the water during heating. A thermistor located near the bottom was used to detect instabilities (if any) produced as a result of heating of the bottom layer due to absorption of radiation by the bottom or the water in its vicinity.

A model based on the unsteady one-dimensional energy transfer by conduction and radiation is used for predicting the temperature distribution in the water. Using the model, the effects of the layer depth, bottom and surface radiation characteristics on the temperature distribution are studied to gain improved understanding of the phenomena. Experimental data and numerical results obtained are discussed and compared.

4.2 Experimental Procedure

Test cell A was cleaned and then filled with distilled water, covered, and left undisturbed for some time to eliminate all convective currents which are normally present and to attain a uniform ambient room temperature. After it had been determined that convective currents in the test cell were absent, all the motors and compressors in the laboratory were turned off and the interferometer was adjusted to an infinite fringe (a single all-light or all-dark fringe). In these series of experiments a thin sheet metal shield covered with aluminum foil was placed approximately 30 cm above the test cell and covered the entire interferometer leg in which the test cell rested. A hole in the shield protected other components from radiant heating and reduced free convection currents within the interferometer leg.

After the interferometer was aligned to the infinite fringe the optical windows of the test cell were covered with styrofoam insulation to prevent cooling from the sides during heating. A few sheets of glass were placed directly above the test cell surface to attenuate the incident infrared radiation. The thermistor located a few millimeters above the bottom of the test cell was used to detect temperature fluctuations near the bottom. The output voltage of the thermistor bridge was nulled just before the heating of the water was started. After the thermistor bridge was adjusted, the heating lamps were set at a predetermined voltage to give a desired filament temperature, and then the heating of the water with the radiant heaters simulating the solar irradiation was initiated.

At prescribed time intervals, the optical window covers were removed, and the interference fringe patterns were photographed and the thermocouple emf readings simultaneously recorded. The photographs were recorded by the Nikon F2-AS camera on Kodak Plus-X 125 ASA film. The distances between the water surface and the reference thermocouple needed for data reduction were measured before and after each experiment using the cathetometer. The incident radiative flux was measured at the start and the end of each experiment using the Eppley radiometer.

4.3 Mathematical Formulation

4.3.1 Statement of the Problem

The objective of this analysis is to model a shallow, quiescent body of water, such as a pond or lake, which is heated by solar radiation and to determine the effect of the depth and bottom characteristics on radiation transfer and the temperature structure near the bottom of the water body. Simplifying assumptions are required to make the problem mathematically and computationally tractable. Therefore, inclusion of realistic boundary and initial conditions as well as turbulence processes discussed in the previous chapter does not appear to be warranted at this time.

4.3.2 Basic Equations

The layer of water is considered to be one-dimensional of constant depth D and infinite lateral extent (see Figure 3.2 for physical model), i.e., the effects of the edges are neglected. For unsteady, stagnant, constant property incompressible fluid under the hydrostatic equilibrium the energy equation, Eq. (3.1), reduces to:

$$\rho c\frac{\partial T}{\partial t} = k\frac{\partial^2 T}{\partial z^2} - \frac{\partial F}{\partial z} \tag{4.1}$$

where T is the local temperature of water and F is the total local radiative flux. It should be noted that in all the equations presented in this chapter z is the vertical coordinate measured from the air-water interface and is positive downward.

As discussed in the previous chapter the radiative transfer equation, Eq. (3.8), needs to be solved along with the energy equation, Eq. (4.1), to yield the temperature distribution. Since the radiative transfer model and assumptions are discussed in detail in Chapter 3 they will not be repeated here. The boundary conditions at the water surface (z = 0) and the bottom (z = D) are taken to be

$$-k\frac{\partial T}{\partial z}\bigg|_{z=0} = \psi F_{inc} \quad \text{at} \quad z = 0 \tag{4.2}$$

and

$$k\frac{\partial T}{\partial z}\bigg|_{z=D} = \alpha_b F_D^+ \quad \text{at} \quad z = D \tag{4.3}$$

where ψ is the fraction of the total incident flux absorbed at the surface, α_b is the total absorptance of the bottom and F_D^+ is the total downward directed (e.g. in the positive z direction) radiative flux at the bottom. The two equations represent instantaneous energy balances between conductive flux in the water and the absorbed radiative flux at the two boundaries. The initial condition for the temperature (i.e., temperature distribution prior to stratification) is taken as

$$T(z,0) = T_o \quad \text{at } t = 0 \tag{4.4}$$

The energy equation, Eq. (4.1), can be rearranged into a dimensionless form as follows,

$$\frac{\partial \theta}{\partial \tau} = \frac{\partial^2 \theta}{\partial \xi^2} - \frac{\partial \phi}{\partial \xi} \tag{4.5}$$

where dimensionless variables ξ, τ, θ, and ϕ are defined as

$$\begin{aligned} \xi &= z/D \ , \\ \tau &= kt/(\rho c D^2) \ , \\ \theta &= k(T - T_o)F_{inc}D \\ \phi &= F/F_{inc} \end{aligned} \tag{4.6}$$

where D is the depth of the layer, T_o is the initial (uniform) temperature of the water prior to heating, and F_{inc} is the total radiative flux incident on the surface of the water. The boundary conditions in the dimensionless form are expressed as

$$-\left.\frac{\partial \theta}{\partial \xi}\right|_{\xi=0} = \psi \text{ at } \xi = 0 \tag{4.7}$$

$$\left.\frac{\partial \theta}{\partial \xi}\right|_{\xi=1} = \alpha_b \phi^+_{(\xi=1)} \text{ at } \xi = 1 \tag{4.8}$$

In dimensionless form the initial condition is represented by

$$\theta(\xi,0) = 0 \text{ at } \tau = 0 \tag{4.9}$$

4.3.3 Numerical Solution of the Energy Equation

The energy equation along with the radiative energy transfer equation do not render a closed form analytical solution. Therefore, a numerical scheme was developed to solve the equations. There are several different ways of deriving the finite difference equations for problems of this type (Raithby, 1976). However, an explicit method used by Snider and Viskanta (1974) for a similar problem required a careful choice of both the time step and grid size for stable and accurate results. Although explicit methods enjoy the ease of formulation and computation, they suffer from the disadvantages of instability in the computation. For this reason an implicit Crank-Nicolson method (Roache, 1976) was adopted for the finite-difference formulation of the energy equation. Since the local volumetric rate of radiant energy absorption decreases very sharply near the air-water interface (Viskanta and Toor, 1978) a very fine mesh was desirable near the surface. However, using a fine mesh throughout the layer of water would result in an unnecessary high resolution away from the surface at the expense of computer core memory storage and execution time. Therefore, the implicit Crank-Nicolson scheme was modified and a variable grid size was adopted (Figure 4.1). Again, as discussed in Chapter 3, it has been assumed that the volumetric rate of radiant energy absorption is known and is determined independently of the energy equation (Viskanta and Toor, 1978) with the results used in the form of a known scource term.

The difficulty in derivation of variable grid size finite-difference scheme for a second order partial differential equation arises in the truncation errors having different order magnitudes for the first and second order derivatives. Therefore, much care must be taken to derive approximations for all terms in the equation such that small truncation errors are of the same order magnitude (Roache, 1976).

Using i for space coordinate and j for time, the implicit finite difference analogs for the terms in the dimensionless form

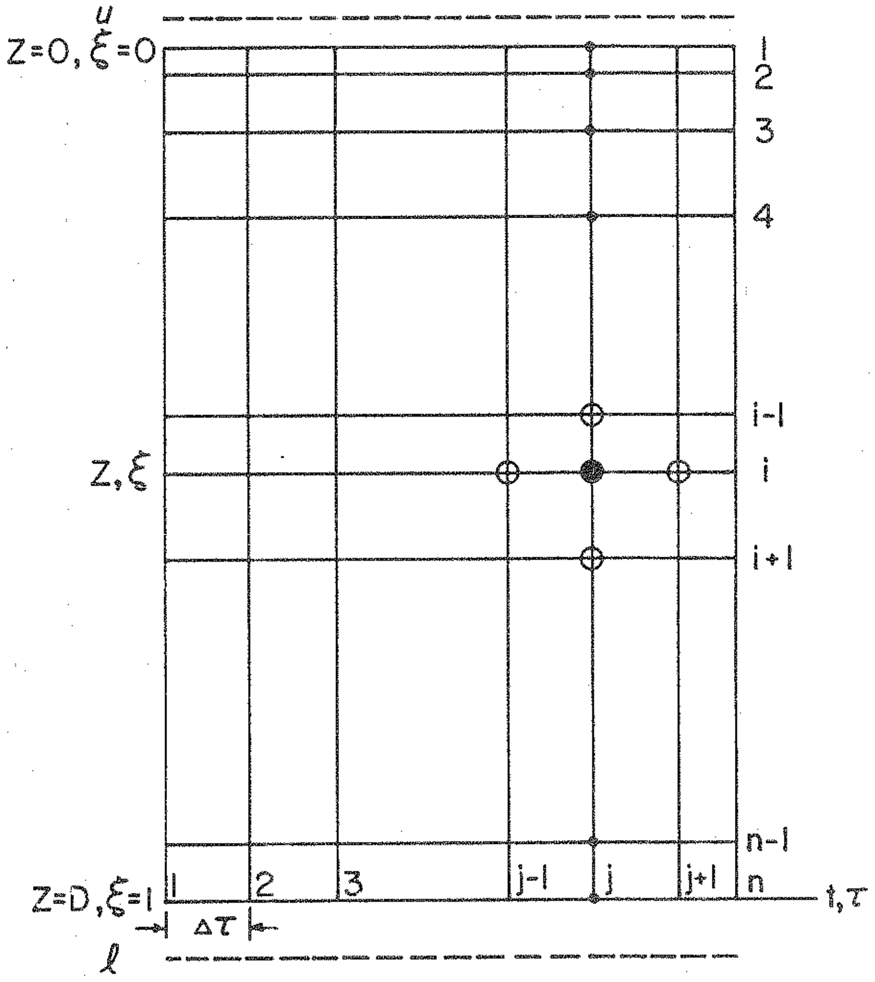

Figure 4.1 Illustration of variable space grid for finite-difference scheme

of the energy equation, Eq. (4.5), can be written as

$$\left.\frac{\partial\theta}{\partial\tau}\right|_i = \frac{\theta_i^{j+1} - \theta_i^j}{\Delta\tau} \tag{4.10}$$

and

$$\left.\frac{\partial^2\theta}{\partial\xi^2}\right|_i = \frac{s_i\theta_{i+1}^j - (1+s_i)\theta_i^j + \theta_{i-1}^j + s_i\theta_{i+1}^{j+1} - (1+s_i)\theta_i^{j+1} + \theta_{i-1}^{j+1}}{s_i(s_i+1)(\xi_{i+1}-\xi_i)^2} \tag{4.11}$$

respectively, where s_i is the ratio of two adjacent grid spacing defined as:

$$s_i = \frac{\xi_{i+1} - \xi_i}{\xi_i - \xi_{i-1}} \tag{4.12}$$

The expression for the second order partial derivative with respect to space coordinate, Eq. (4.11), was derived by fitting a parabola through (i-1), i, and (i+1) points and differentiating the resulting function (Salvadori and Baron, 1961). The scheme is second order in space coordinate (good accuracy) and first order in time and avoids oscillation problems which often beset second order time schemes (Roache, 1976). The scheme also enjoys the advantage of being unconditionally stable.

The finite difference analogs for the upper and lower boundary conditions (represented by u and ℓ, respectively; Figure 4.1) can also be derived from Eqs. (4.6) and (4.7);

$$-\frac{1}{4}\left[\frac{(\theta_2^j - \theta_u^j) + (\theta_2^{j+1} - \theta_u^{j+1})}{(\xi_2 - \xi_1)}\right] = \psi \tag{4.13}$$

$$\frac{1}{4}\left[\frac{(\theta_\ell^j - \theta_{n-1}^j) + (\theta_\ell^{j+1} - \theta_{n-1}^{j+1})}{(\xi_n - \xi_{n-1})}\right] = \alpha_b\phi^+_{(\xi=1)} \tag{4.14}$$

where θ_ℓ and θ_n are dimensionless temperatures beyond the boundaries at the imaginary grid points u and ℓ (see Figure 4.1). These unknowns can be eliminated by employing the finite difference approximation of the energy equation at the boundaries. Substitution of Eqs. (4.10) and (4.11) into Eq. (4.4) and elimination of θ_ℓ and θ_u by the use of Eqs. (4.13) and (4.14) results in

$$\left[\frac{1}{\Delta\tau} + \frac{1}{(\xi_2 - \xi_1)^2}\right]\theta_1^{j+1} - \left[\frac{1}{(\xi_2 - \xi_1)^2}\right]\theta_2^{j+1} =$$

$$\left[\frac{1}{\Delta\tau} - \frac{1}{(\xi_2 - \xi_1)^2}\right]\theta_1^{j} + \left[\frac{1}{(\xi_2 - \xi_1)^2}\right]\theta_2^{j} + \frac{2\psi}{(\xi_2 - \xi_1)} - \phi_1^{*} \,,$$

$$\text{for } i = 1 \qquad (4.15)$$

$$\left[\frac{-1}{s_i(s_i+1)(\xi_{i+1}-\xi_i)^2}\right]\theta_{i-1}^{j+1} + \left[\frac{1}{\Delta\tau} + \frac{1}{s_i(\xi_{i+1}-\xi_i)^2}\right]\theta_i^{j+1} +$$

$$\left[\frac{-1}{(s_i+1)(\xi_{i+1}-\xi_i)^2}\right]\theta_{i+1}^{j+1} = \left[\frac{1}{s_i(s_i+1)(\xi_{i+1}-\xi_i)^2}\right]\theta_{i-1}^{j} +$$

$$\left[\frac{1}{\Delta\tau} - \frac{1}{s_i(\xi_{i+1}-\xi_i)^2}\right]\theta_i^{j} + \left[\frac{1}{(s_i+1)(\xi_{i+1}-\xi_i)^2}\right]\theta_{i+1}^{j} - \phi_i^{*} \,,$$

$$\text{for } i = 2, \ldots n - 1 \qquad (4.16)$$

and

$$\left[\frac{-1}{(\xi_n-\xi_{n-1})^2}\right]\theta_{n-1}^{j+1} + \left[\frac{1}{\Delta\tau} + \frac{1}{(\xi_n-\xi_{n-1})^2}\right]\theta_n^{j+1} =$$

$$\left[\frac{1}{(\xi_n-\xi_{n-1})^2}\right]\theta_{n-1}^{j} + \left[\frac{1}{\Delta\tau} - \frac{1}{(\xi_n-\xi_{n-1})^2}\right]\theta_n^{j} + \frac{2\alpha_b\phi^{+}(\xi=1)}{(\xi_n-\xi_{n-1})} - \phi_n^{*} \,,$$

$$\text{for } i = n \qquad (4.17)$$

where ϕ_i^* is the dimensionless local volumetric rate of radiant energy absorption (i.e. $\left.\frac{d\phi}{d\xi}\right|_i$) at grid point i. Examination of

Eqs. (4.15) through (4.17) indicates that once the dimensionless temperature distribution at time j is known (i.e., the right hand side of these equations) the temperature distribution at time j+1 can be obtained by solving the system of n-linear equations, Eqs. (4.15) through (4.17), of the form of a tri-diagonal matrix.

The tri-diagonal matrix is solved by the well-known, efficient Thomas algorithm (Gerald, 1978) which requires minimum possible core memory storage and execution time. A 24 grid point mesh with high resolution near the surface and coarse spacing near the bottom was selected. For an accurate computation a small time step of the order of about 0.1 sec (in real time) was used. Both the grid spacing and time step were checked for accuracy of the solution by the halving technique described in Chapter 3.

It should be noted that the system of Eqs. (4.15) through (4.17) were derived for the idealized boundary conditions described. However, any other possible boundary conditions can be employed and formulated in the same manner.

4.4 Results and Discussion

Some experimental observations during stratification of a shallow layer of water will be discussed in this section. In the analysis presented the important parameters are identified and their effect on the temperature distribution is investigated. At the end, the experimental data are compared with analytical predictions.

4.4.1 Some Observational Data

An initially uniform layer of water was thermally stratified by irradiating the layer with radiation emitted from the tungsten filament radiant lamps. Some selected photographs of the interference fringe pattern illustrating the heating of an initally uniform water are shown in Figure 4.2 (the small square dark image is the turning mirror 1, see Fig. 2.5). In this particular experiment the bottom was coated with a "black" paint, $\alpha_b = 0.92$. Photograph 4.2a shows the fringe pattern before the heating was initiated.

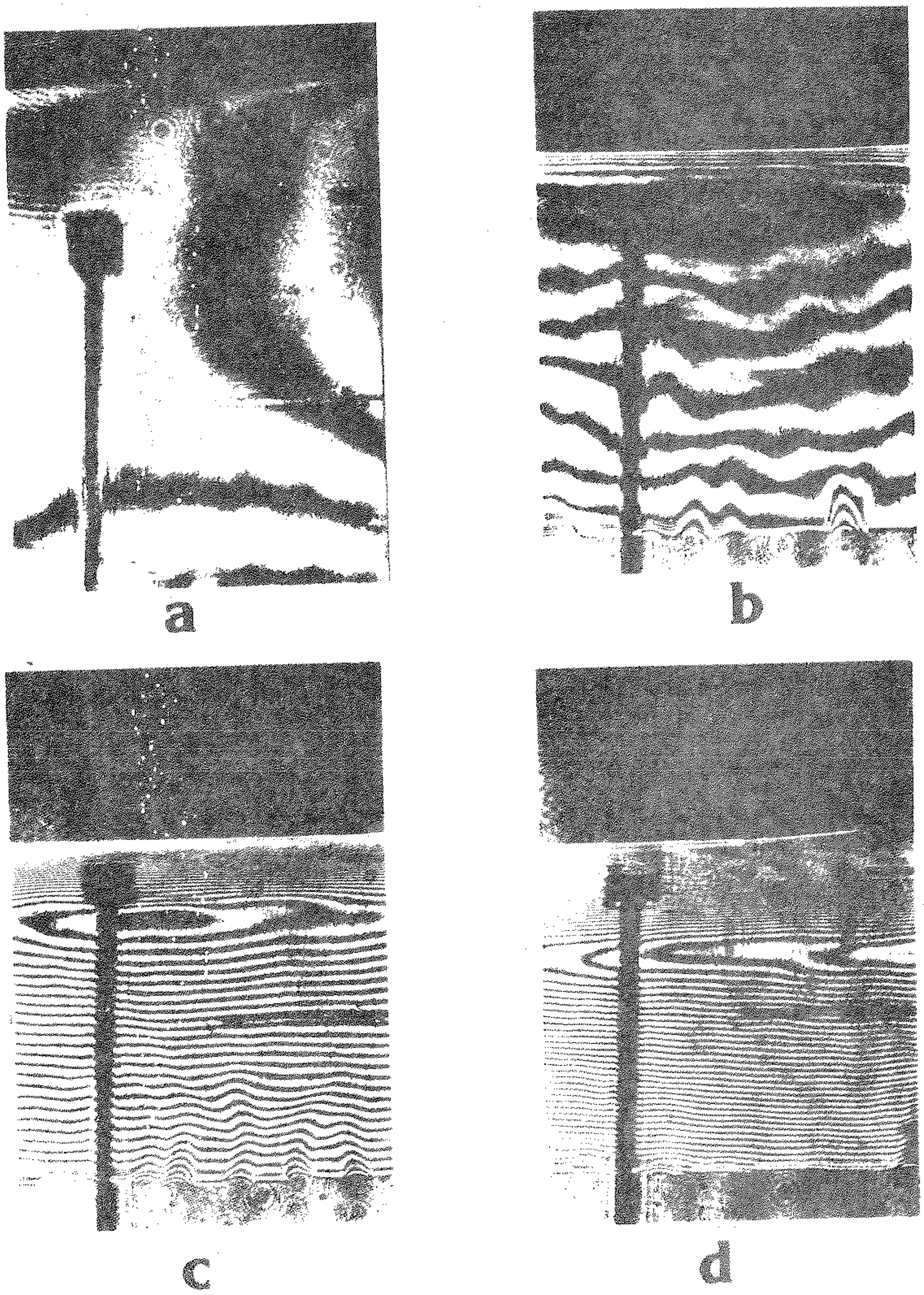

Figure 4.2 Selected interferograms during thermal stratification of an initially uniform layer of water, $D = 10$ cm, $\alpha_b = 0.92$, $T_o = 20$°C: (a) $t = 0$ min, (b) 6 min, (c) 30 min, (d) 60 min

The reference thermocouple seen in this photograph is about 3.5 cm above the bottom of the test cell. The diagonal fringes in photograph 4.2a are the interference fringe pattern in the air right above the water surface. The dark gray area at the top of photograph 4.2b is due to intense heating of the water. The very large fringe density that has resulted makes it impossible to distinguish the fringes from one another in this particular region. Prior to this experiment a new set of radiant lamps was installed in the housing and were operated at about 3000 K which resulted in a large radiation flux incident on the water surface.

In Figure 4.2b (and also 4.2c and 4.2d) two clearly distinct regions can be distinguished. An intensely stratified region near the interface indicates that the surface is being heated, and the temperature decreases with depth in this region. Near the bottom of the test cell fringes are some distance apart indicating not as intense heating of this layer. The fringes are more closely spaced near the bottom than the overlying region (see Figure 4.2c and 4.2d). The overall interference fringe pattern can be explained by the fact that a large fraction of the incident radiation transmitted into the water is absorbed near the surface which results in a decreasing local temperature with depth. As the radiation propagates through the water, it is partially attenuated. Upon reaching the bottom of the test cell the radiation is mostly absorbed by the nearly black coated bottom. Therefore, the bottom is heated and its temperature raised which in turn causes an increase in the local temperature above the bottom. The particular shape of temperature profile near the bottom is also partially due to the reflected portion of the radiation reaching the bottom which is absorbed as it propagates upward (i.e. in the opposite direction of the incident beam). The heating of the bottom of the test cell was clearly observed by a continuous increase in the emf output of the thermocouple installed into the bottom plate.

Photographs 4.2c and 4.2d indicate a small region of relatively uniform temperature water about 6 cm above the bottom plate. In this region the fringes are reversed indicating a reversal in the temperature gradient. This particular profile indicates that temperature decreases with depth (negative gradient) above the reversal and temperature increases with depth (positive gradient) below it. Interferograms recorded at different times suggested that the location of this temperature reversal layer was nearly fixed once it was established.

Absorption of radiation by the bottom of the test cell results in the heating of the water adjacent to the bottom and results in natural convection motion if critical conditions are reached. Figure 4.2c provides evidence that thermal plumes are formed right above the bottom of the test cell. The temperature fluctuations near the bottom were detected by the thermistor and recorded on a strip chart. Figure 4.3 presents a sample of strip chart output of the thermistor for this experiment. The chart indicates that the average temperature of the water at the location of the thermistor (about 6 mm above the bottom) increases with time. Also, fluctuations of about 0.15°C are detected. The temperature of a plume was approximately 0.15°C higher than the bulk temperature of the surrounding fluid. The temporal frequency of the plume generation is not fixed. However, for this particular experiment in average time period of one minute output voltage peaks 2.6 times (see Figure 4.3). This corresponds to an average plume departure frequency of about 2.6 $(\text{min})^{-1}$. Shadowgraph observations of instabilities and plume activity could not be recorded photographically even though they were observed visually. This was due to small density differences and the averaging effect along the beam as it traversed the test cell.

Some typical photographs of the interference fringe patterns for a different experiment are shown in Figure 4.4. In this experiment the bottom of the test cell was covered with a thin aluminum foil which fitted right into the test cell. The interferograms presented in this figure do not cover the entire depth of the water layer and only show the region of primary interest near the bottom.

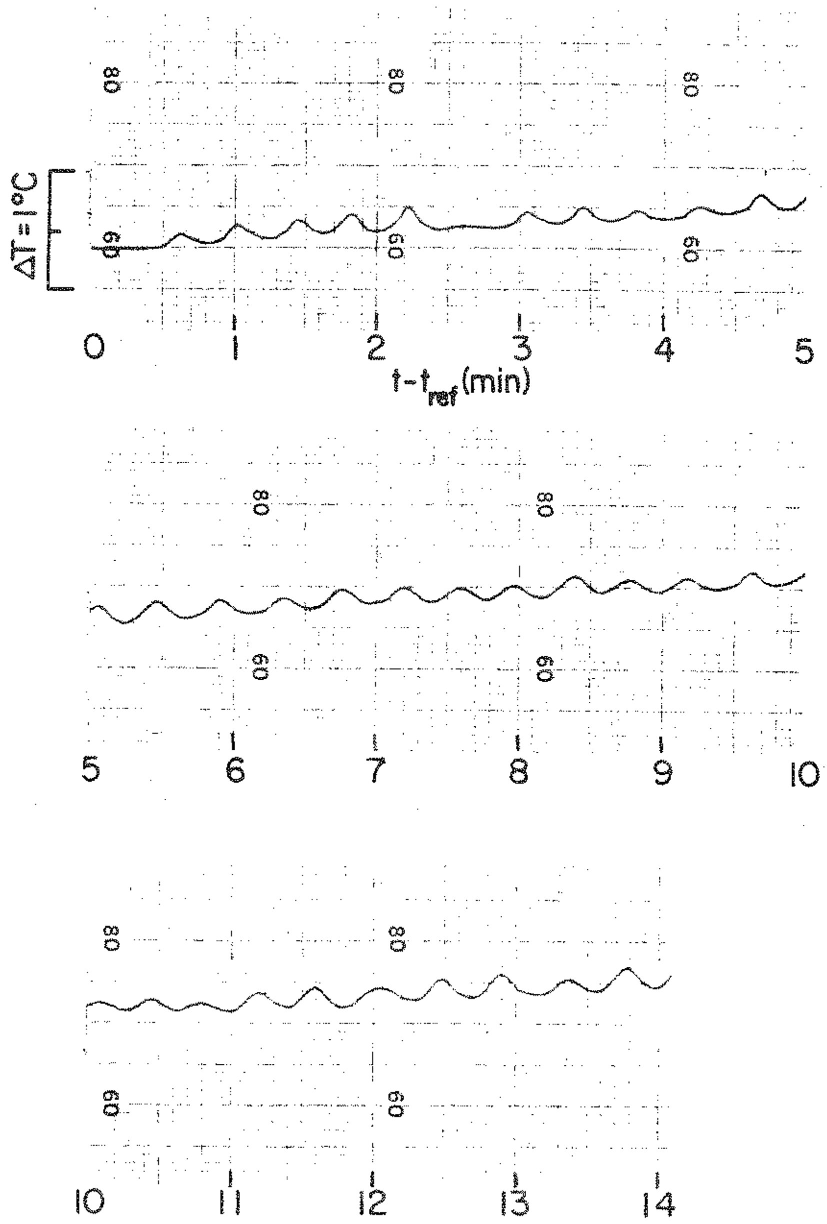

Figure 4.3 Thermistor output for experiment described in Figure 4.2

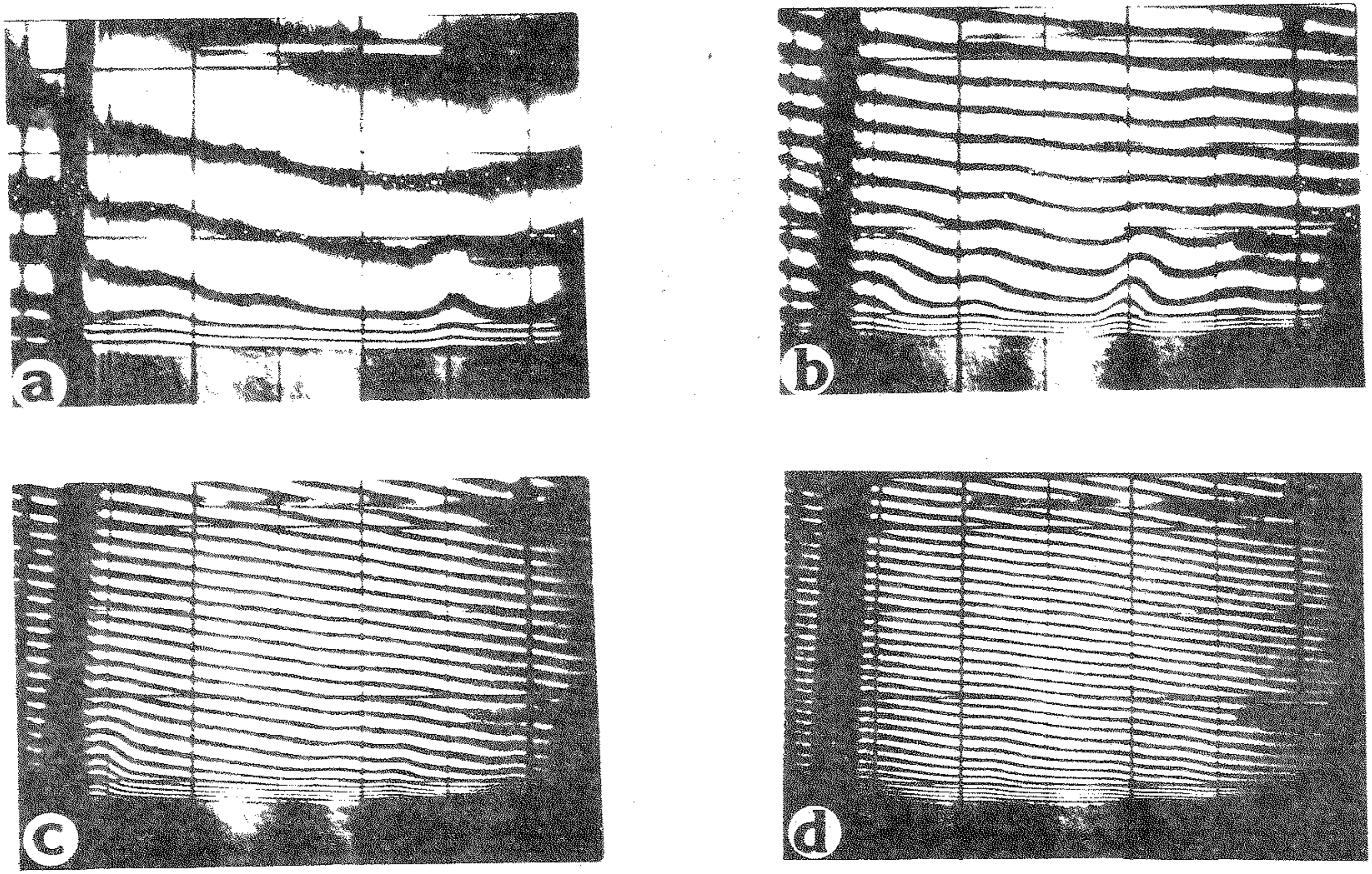

Figure 4.4 Selected interferograms during thermal stratification of an initially uniform layer of water, D = 10 cm, α_b = 0.08, T_o = 22.5°C: (a) t = 5 min, (b) 20 min, (c) 30 min, (d) 45 min

In the photographs the squares seen in the background are 1 × 1 cm. It is evident from Figure 4.4 that the water is being thermally stratified near the bottom as the heating continues. This is obvious from the increase in the number of fringes near the bottom at later times and the greater distance between fringes in the overlying region. From comparison of Figures 4.2 and 4.4 it is evident that the stratification near the bottom of the test cell for the experiment with the black painted bottom is more intense than the highly reflective one. This is due to the larger absorption of radiant energy by the black bottom. The temperature reversal described earlier was also observed in the experiment with the highly reflecting coating. However, this is not seen in Figure 4.4 since these photographs do not show the entire layer of water.

4.4.2 Analytical Predictions and Effect of Parameters

From the dimensionless form of the one-dimensional energy equation, Eq. (4.5), and related boundary conditions, Eqs. (4.7) and (4.8), it is evident that there are several important parameters which determine the temperature distribution. In this subsection the effect of these parameters on the predicted temperature distributions is presented and discussed.

Although the total incident flux (i.e., F_{inc}) does not directly appear in the dimensionless governing equations, the spectral distribution of the incident flux has important bearing on the temperature distribution through the functions $\phi(\xi)$ and ϕ^+ as well as parameters ψ and α_b. The local volumetric rate of radiant energy absorption and the radiant flux reaching the bottom and absorbed at the surface depend on the spectral distribution of $F_{inc,\lambda}$ (Snider and Viskanta, 1974). However, since the magnitude and the spectral effects of the incident radiation flux are well documented (Viskanta and Toor, 1978; Snider and Viskanta, 1974), this parameter will be held constant. In all the calculations reported here, the incident flux was determined for a Planckian radiator operating at an effective temperature of 3000 K. This approximates the operating conditions of the radiant heaters.

Figures 4.5, 4.6, and 4.7 present the predicted dimensionless temperature for depths of 5, 10, and 15 cm, respectively. The bottom was considered to be highly absorbing (black paint) with a total absorptivity of 0.92. The parameter ψ was taken as 0.25 (Snider and Viskanta, 1974). Since the depth of the layer D appears both in the dimensionless time τ and temperature θ, for ease of comparison the results presented in the figures correspond to the same real time of one, two, and three hours, respectively. Figure 4.8 shows similar predictions for a layer of water 10 cm deep with a highly reflective bottom having an absorptivity of 0.08. A summary highlighting the important features of the results presented in these figures is given in Table 4.1.

Table 4.1 Dimensionless temperatures for different times

	t = 60 min			t = 120 min			t = 180 min		
Figure	τ	θ_s	θ_b	τ	θ_s	θ_b	τ	θ_s	θ_b
4.5	0.2	.40	.28	0.4	.66	.55	0.6	.92	.78
4.6	0.05	.19	.09	0.1	.29	.14	0.15	.37	.20
4.7	0.023	.13	.06	0.046	.19	.08	0.068	.23	.10
4.8	0.05	.19	.02	0.1	.29	.04	0.15	.37	.07

Comparison of Figures 4.5, 4.6, and 4.7 indicates that the dimensionless temperature is more nonuniform for the deeper layers. This is due to the fact that at a given dimensionless depth, ξ, the local volumetric rate of radiant energy absorption, $\phi(\xi)$, is smaller for the deeper layers. However, for early times the temperature and temperature gradient (i.e., T and $\partial T/\partial z$) at the surface for all three cases is nearly the same. This is explained by the fact that very close to the surface $\phi(\xi)$ is independent of the depth

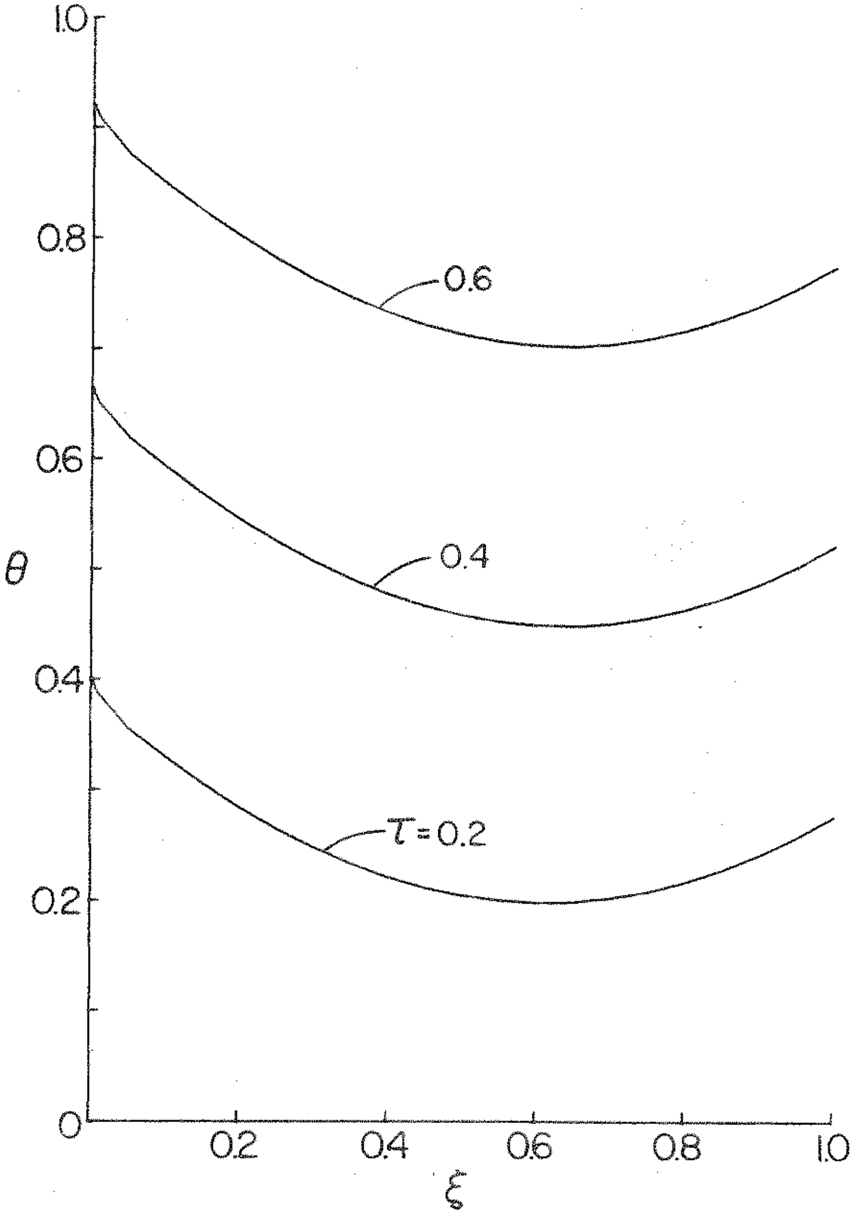

Figure 4.5 Predicted dimensionless temperature distribution during thermal stratification (insulated bottom), D = 5 cm, $\alpha_b = 0.92$, $\psi = 0.25$

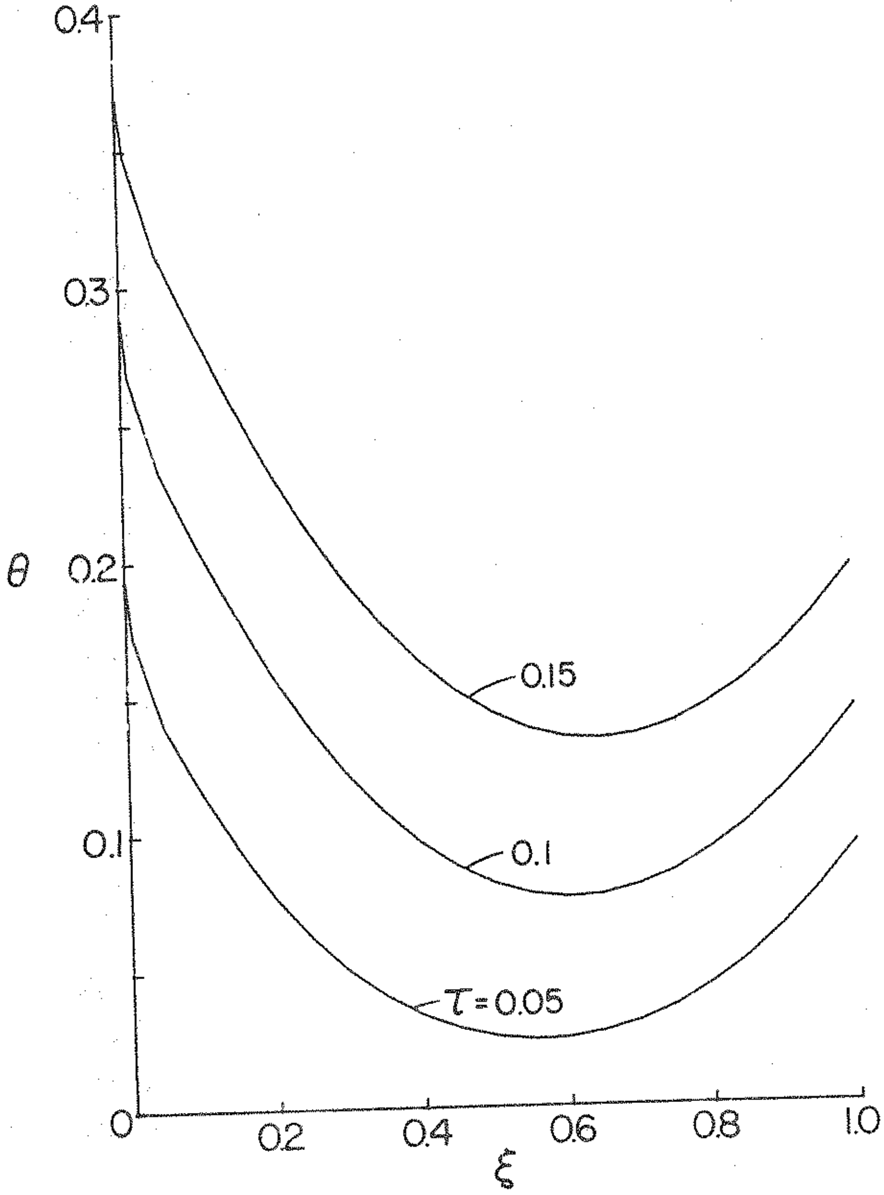

Figure 4.6 Predicted dimensionless temperature distribution during thermal stratification (insulated bottom), $D = 10$ cm, $\alpha_D = 0.92$, $\psi = 0.25$

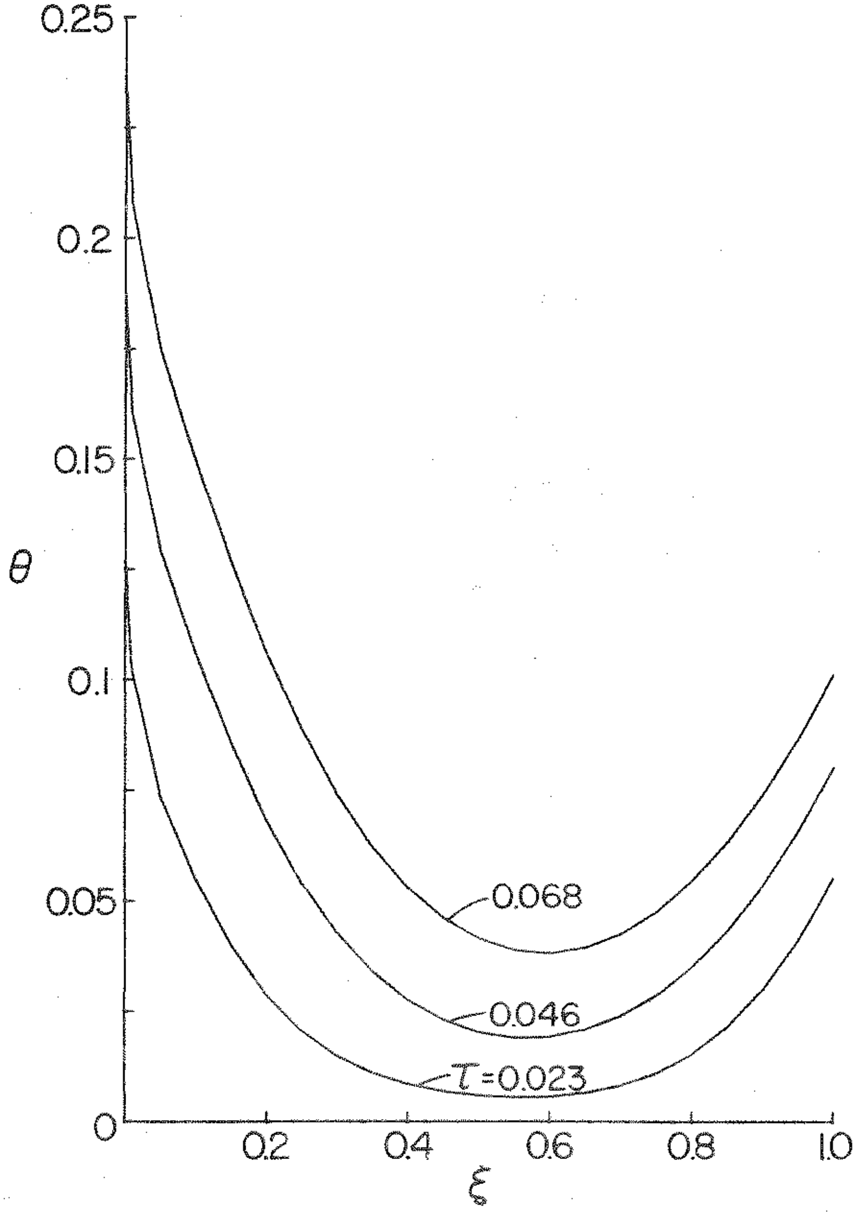

Figure 4.7 Predicted dimensionless temperature distribution during thermal stratification (insulated bottom), D = 15 cm, $\alpha_b = 0.92$, $\psi = 0.25$

of the layer (Viskanta and Toor, 1978), and heat diffusion is not as important as absorption of radiation. Note that the dimensionless temperature is smaller for deeper layers because it is inversely proportional to the depth of the layer.

Examination of Table 4.1 indicates that at all times the dimensionless temperature at the bottom (i.e., θ_b, bottom is denoted by b and surface by s) is smaller for a deeper layer even though the bottom characteristics are the same. This is a direct result of smaller volumetric rate of radiant energy absorption by deeper layers which is also clearly evident from the values of θ_b^+ listed in the figure captions. For a deeper layer there is less radiant energy incident on the bottom which results in a lower temperature.

Results presented in Figure 4.8 for a highly reflecting (α_b = 0.08) bottom indicate that the dimensionless temperature near the bottom is considerably smaller than that of Figure 4.6 with a highly absorbing bottom. However, the temperatures in the surface region are practically the same. This is because for $\alpha_b = 0.08$ only a small fraction of the radiation flux incident on the bottom is absorbed there, and the reflected ($1 - \alpha_b = 0.92$) fraction of the incident radiation does not affect the temperature near the surface. In fact, the results in the two figures show that the dimensionless temperature profiles at $\tau = 0.05$ are the same up to dimensionless depth of $\xi = 0.5$. However, at this time the dimensionless temperature at the bottom for $\alpha_b = 0.92$ is 4.5 times larger than for α_b = 0.08. It should be noted from Figure 4.8 that for the highly reflecting bottom there is still a temperature gradient reversal near $\xi = 1$.

The effect of the parameter ψ on the dimensionless temperature was studied and showed that the temperature distribution was insensitive to this parameter. This is evident from the examination of the finite difference equations, Eq. (4.15). In this equation, for the very fine grid selected near the surface, the magnitude of the term including ψ is much smaller than the other terms appearing in

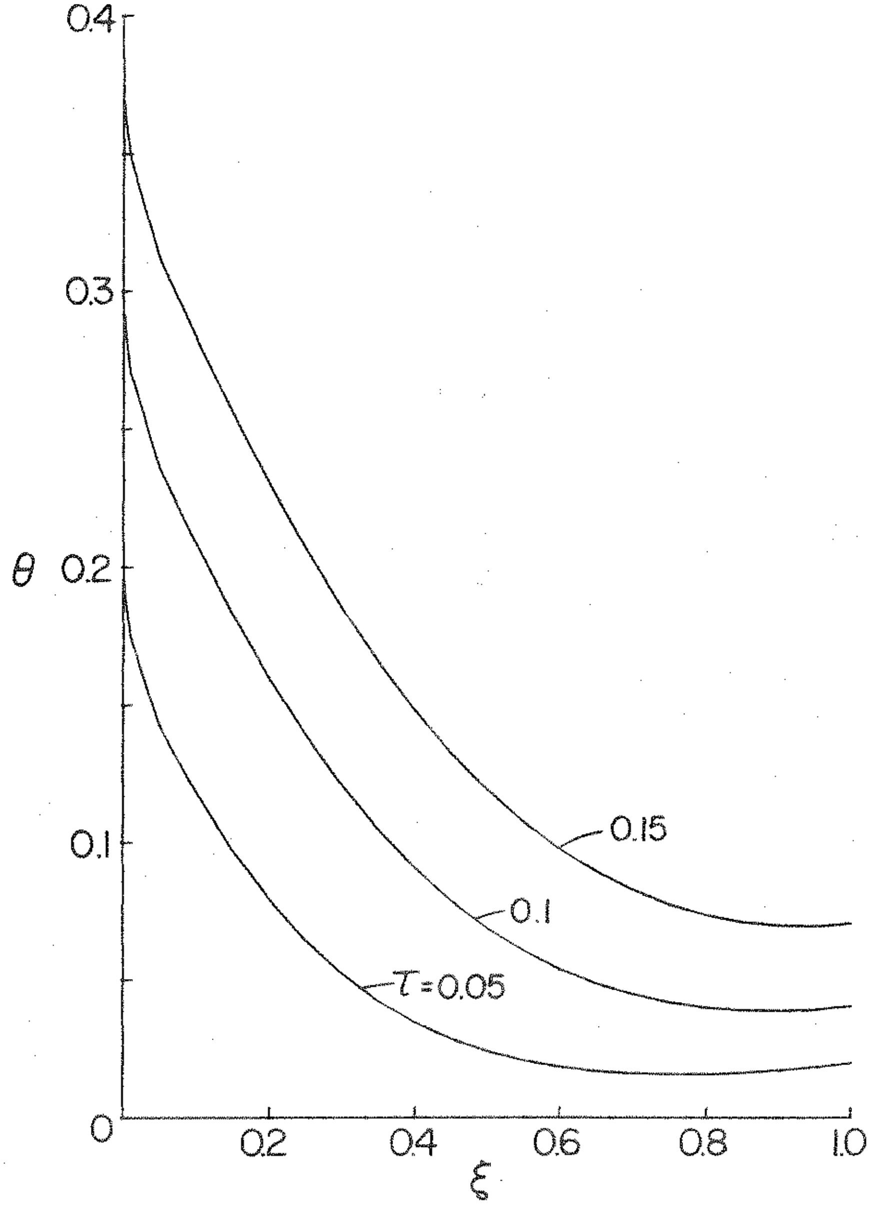

Figure 4.8 Predicted dimensionless temperature distribution during thermal stratification (insulated bottom), D = 10 cm, α_b = 0.08, ψ = 0.25

the equation. Since the value of the parameter ψ had such a little effect on the temperature distribution the results are not presented here.

As discussed earlier, the finite difference equations, Eqs. (4.15) through (4.17), can be easily adopted for different types of boundary conditions. Modification of the equations for the case of a constant bottom temperature boundary condition were made and sample calculations are presented in Figure 4.9. A comparison of the results in Figures 4.6, 4.8 and 4.9 shows that the temperature distribution in the surface layers is affected very little by the radiation characteristics of the bottom and the boundary condition.

4.4.3 Comparison of Analytical Predictions with Experiments

The laboratory experiments simulating heating of water by solar radiation were modeled analytically. At the surface, only the total incident radiation flux from the tungsten filament heaters was accounted for, and long-wave radiative heat exchange between the water surface and the surroundings, convective heat transfer, and latent transport of energy were neglected. For some experiments the observations and results showed a slight temperature reversal right below the surface indicating a heat loss from the surface. However, since the main region of interest was near the bottom, the inadequate modeling of the surface boundary condition did not affect the temperature distribution in that region and is therefore well justified. Experimental results showed that the bottom plate was not perfectly insulated but that the assumption of an insulated bottom was a reasonable one. Because of the relative insensitivity of results on the parameter ψ a constant value of 0.25 was used for all the calculations presented here. It should be pointed out that the insensitivity of temperature distribution to this parameter is due to precise modeling of total volumetric rate of radiant energy absorption and also choice of a very small grid at the surface, see Eq. (4.15). Due to the aging of the lamps which resulted in

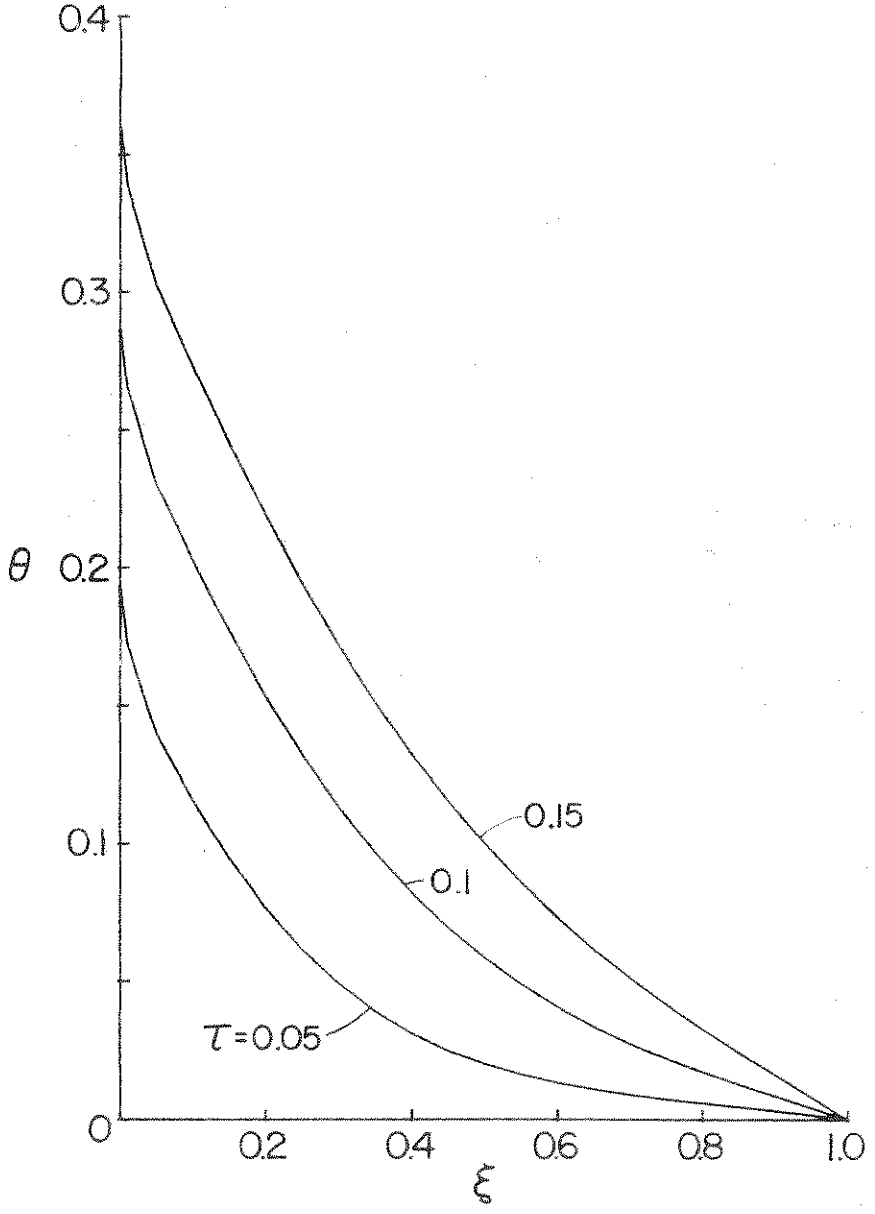

Figure 4.9 Predicted dimensionless temperature distribution during thermal stratification (constant temperature bottom boundary), D = 10 cm, α_b = 0.08, ψ = 0.25

formation of tungsten deposits on the quartz envelopes, the incident radiant flux F_{inc} decreased during the course of an experiment. The spectral characteristics of the radiation emitted by the tungsten filaments and transmitted through the quartz envelopes also changed as a result of the aging of the lamps. An average value of the total incident flux measured during the experiment was therefore used in the calculations.

A comparison of the measured and predicted dimensionless temperature distribution given in Figure 4.10 shows that the agreement between the analysis and experiment is excellent for all times. Results are presented for an experiment of relatively short duration to avoid significant aging of the lamps. The interferograms were recorded by photographing only the region near the bottom, and therefore the experimental results for the upper layers are not presented. The latter region has already been extensively studied by Snider and Viskanta (1974). The experimental results showed that because of intense heating, the fringe density near the water surface was very high which made the interpretation of the fringes impossible. The temperature distribution in the entire layer during intense radiant heating has been measured with thermocouples and will be reported in Chapter 6. In this experiment the bottom of the test cell was covered with highly reflective aluminum foil with an estimated total absorptivity of about 0.08. The total incident radiative flux reaching the air-water interface was measured to be 1350 W/m^2 at the start of the experiment and after 30 minutes this value decreased to 1230 W/m^2. In the predictions presented here an average value for $F_{inc} = 1286\ W/m^2$ was used. The radiant heaters were operating at a temperature of about 3000 K.

The comparisons between the measured and predicted temperature distribution for a different experiment is presented in Figure 4.11. In this particular experiment the water was irradiated for 50 minutes. The initial total incident radiative flux at the interface was measured to be 1350 W/m^2 which after 50 minutes dropped to 930 W/m^2. An average value of 1142 W/m^2 for the total incident flux

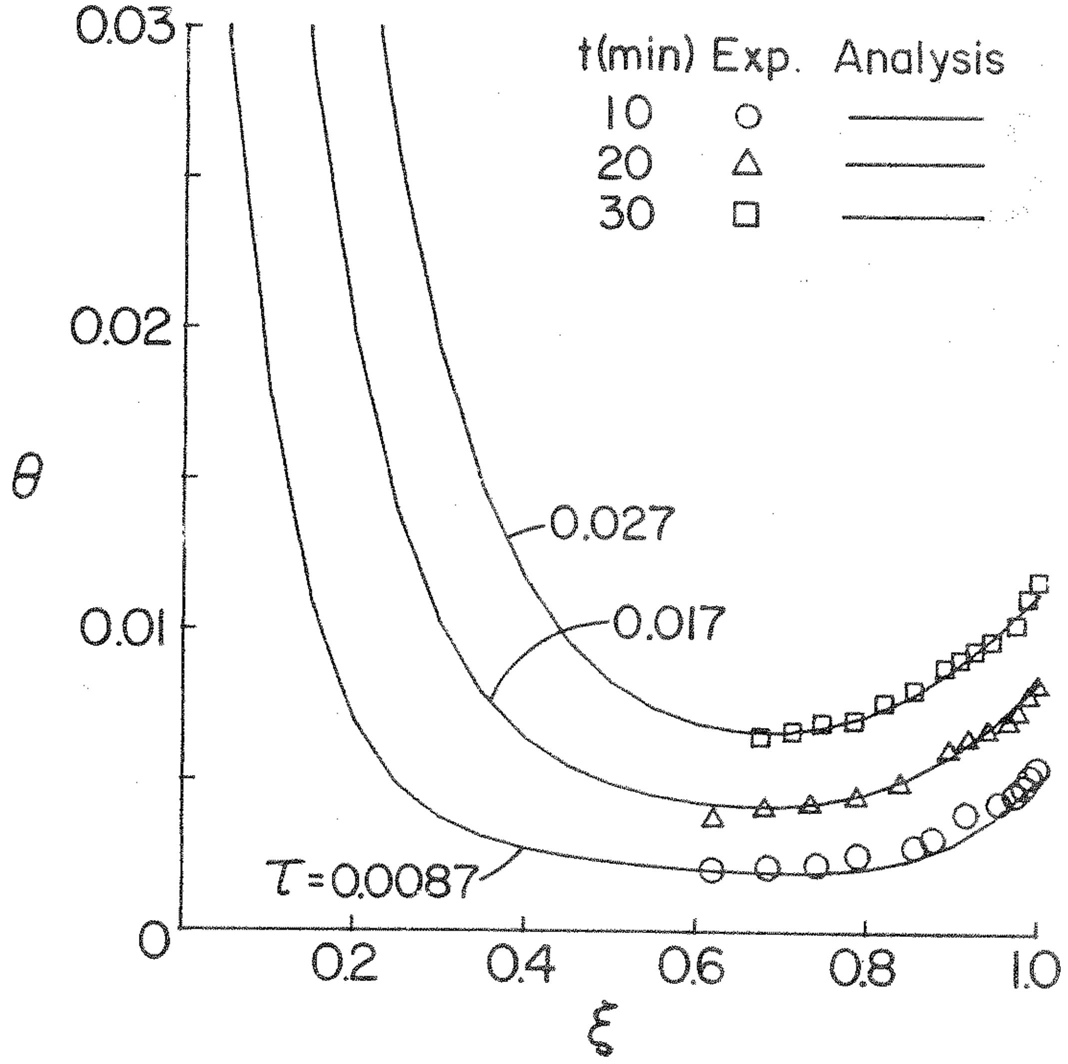

Figure 4.10 Comparison of measured and predicted dimensionless temperatures for experiment described in Figure 4.4: F_{inc} = 1286 W/m^2 (lamps at 3000 K), α_b = 0.08

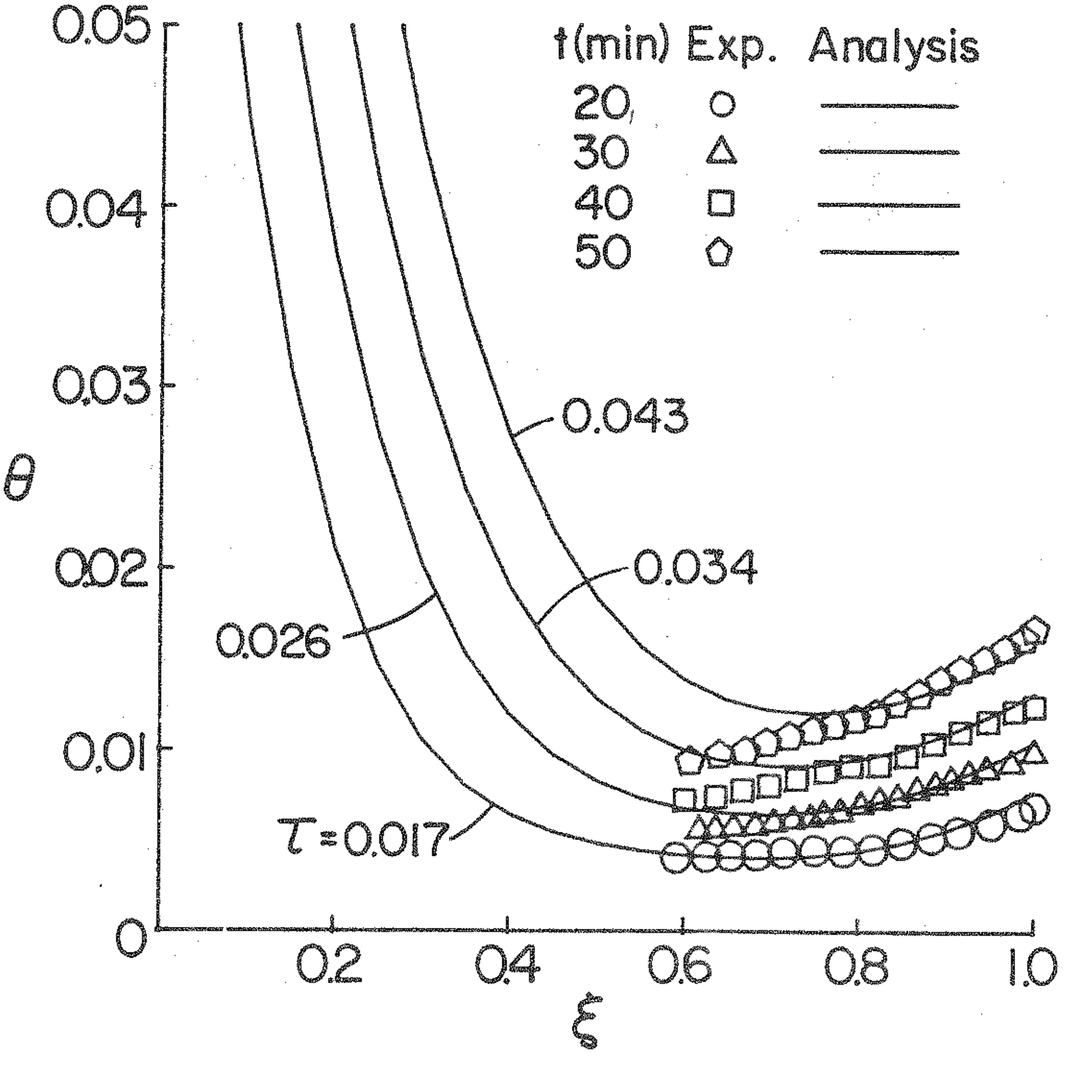

Figure 4.11 Comparison of measured and predicted dimensionless temperature: $D = 10$ cm, $\alpha_b = 0.08$, $T_o = 26°C$, $F_{inc} = 1142$ W/m^2 (lamps at 3050 K)

was used in the calculations. Figure 4.11 shows a reasonably good agreement between the experiment and analysis. However, at later times a discrepancy between the measured and predicted results are noted. The discrepancy is attributed to the natural convection heat transfer from the bottom and also to the change in magnitude and spectral characteristics of the incident flux due to the aging of the tungsten filament lamps during the experiment. The thermistor output provided evidence of temperature fluctuations and plume activity, and, as already noted, the degradation of lamps when operating at high (3050 K) temperature was also significant even in a short period of time.

The experimental and analytical results clearly demonstrate that absorption of radiation by the water and bottom can produce an unstable situation that may result in natural convection mixing and energy transport in the layer immediately adjacent to the bottom. Even though the spectral characteristics of incident solar radiation could not be simulated in the laboratory, the fact that a larger fraction of the solar energy is in the short-wave part of the spectrum suggests that the phenomena observed in the experiments is expected to occur in relatively shallow quiescent waterbodies. However, no field data or other detailed observational evidence of this particular phenomenon appear to have been reported in the literature.

5. HEATING OF A THERMALLY STRATIFIED LAYER OF WATER FROM BELOW

5.1 Introduction

This section reports on laboratory experiments intended to gain understanding of internal energy transport processes and mixing in nonuniformly stratified layers of water that may be cooled from above or heated from below. Such physical situations arise not only in geophysics, water resources but also in technology and include, for example: cooling of quiescent natural waterbodies by convection, latent energy transport and long-wave radiation after the water has been stratified by absorption of solar radiation, cooling of surface thermal discharges from electric power generating plants, heating of the atmospheric planetary boundary layer from below as a result of absorption of solar radiation by the ground, energy transfer and mixing in stratified, sensible energy storage tanks and many others. The specific objectives of the experiments and analysis are to:

- Produce nonuniform stratification in a shallow, quiescent layer of water and study the effect of stratification on internal energy transfer processes and mixing.
- Develop a simple analysis to predict mixed layer growth and mixed layer temperature under different stratification conditions and compare with experimental data.
- Apply and verify the K-ϵ turbulence model to predict the mixed-layer characteristics of a nonuniformly stratified shallow water layer.

The experiments in this phase of the study were performed with test cell A which allowed for a nonuniform thermal stratification and/or heating from below a shallow layer of water. This was desirable because the simple apparatus provided flexibility to study the basic physical processes and allowed to achieve different experimental conditions.

The experiments conducted are described, and observational data are discussed in some detail. A simple thermal model for predicting the mixed layer dynamics is developed, and results of sensitivity studies as well as comparisons between model predictions and data are reported. The K-ε turbulence model is used in the unsteady, one-dimensional energy equation to predict the temperature structure as well as the dynamics of a mixed layer and to establish the utility of the model by comparing experimental data with predictions.

5.2 Experimental Procedure

The test cell was cleaned and then filled with distilled water, covered, and left undisturbed for some time to eliminate all convective current which are normally present and to attain a uniform ambient room temperature. After it had been determined that convective currents in the test cell were absent, all the motors and compressors in the laboratory were turned off and the interferometer was adjusted to an infinite fringe (a single all-light or all-dark fringe).

In these series of experiments a thin sheet metal shield was placed approximately 30 cm above the test cell and covered the entire interferometer leg in which the test cell rested. A hole in the shield protected other components from radiant heating and reduced free convection within the interferometer leg.

After the interferometer was aligned to the infinite fringe, the optical windows of the test cell were covered with a 3 cm thick sheet of styrofoam to prevent heat losses/gains from the sides during heating and cooling. A few sheets of glass were placed above the test cell surface to reduce the long-wave infrared radiation from the tungsten filament lamps. The water was then simultaneously cooled from below (by circulation of coolant through the bottom plate) and heated from above (by radiant heaters) to achieve desired thermal stratification conditions. In some of the experiments, the water was stratified by heating from above and/or cooling from below.

After the desired stratification was achieved, the optical window covers were removed and the water was then heated from below by circulating coolant from a constant temperature bath at a prescribed temperature through the heat source/sink. The heating rate was adjusted by regulating the coolant flow in the circuit and the inlet temperature to the heat source/sink. At desired intervals, the interference fringe patterns or shadowgraph images were photographed and reference as well as other thermocouple readings and the coolant flow rate were simultaneously recorded. The calibrated thermistor was located approximately 0.6 cm above the bottom plate to detect temperature fluctuations caused by plumes departing from the vicinity of the plate. The output of the thermistor was recorded on a strip chart.

A heat sink was used to cool the water from above. The design and construction of the heat sink was very similar to that of the heat sink/source placed in the bottom of the test cell A. The sink fitted right into the test cell and its position could be adjusted by means of four threaded rods located on top. The sink was cooled by circulating ethylene glycol supplied from a constant temperature bath.

5.3 Discussion of Observational Data

Before discussing some observational data, it is desirable to review the general characteristics of the phenomena. Heating of an initially stagnant layer of water (stable thermal stratification or uniform temperature) produces a thin layer of warmer fluid adjacent to the heating surface. Since the warmer fluid has a smaller density than the fluid located right above it, the warmer fluid ascends. The parcels of warmer fluid are referred to as thermals.

As a result of the thermals breaking up from the thin conduction layer right above the heating surface, instability occurs which in turn causes the formation of a relatively uniform mixed layer. Howard (1966) has explained the generation of thermals by a phenomenological theory. According to his model, thermals are produced by a periodic process, each period of which consists of a conduction phase followed by a break-off and mixing phase. At the beginning of the conduction phase, the fluid adjacent to the plate is envisioned as having a uniform temperature which is different from that of the plate. As a result, a temperature front moves away from the plate into the fluid. When the thickness of the conduction layer contained between the moving front and the plate surface is such that the corresponding Rayleigh number exceeds a critical value, the layer becomes unstable and breaks up, thereby producing a thermal.

Figure 5.1 shows several photographs of the shadowgraph images taken 2 seconds apart. In this experiment the water was stratified by cooling an initially uniform layer of water from below for about 2 hours. Then the water was heated from below by circulating warm fluid through the heat source/sink. It took about 90 seconds before thermals were generated and started departing the heated surface. This was due to three different effects. First, the cool water in the bottom plate (which was used to stratify the layer) had to be replaced by the warm fluid. Second, the mass of the copper sink which did not allow the surface temperature of the plate to reach its steady value instantaneously. Third, initially the heat is transferred to the water adjacent to the plate by conduction and since this is a relatively slow energy transport process, it takes time to reach a critical value of the Rayleigh number. In these photographs the dark area near the bottom is the region where the activity of thermals was observed to be intense. This area appeared very dark because the shadowgraph technique has an averaging effect along the beam. The surface of the bottom plate can be seen

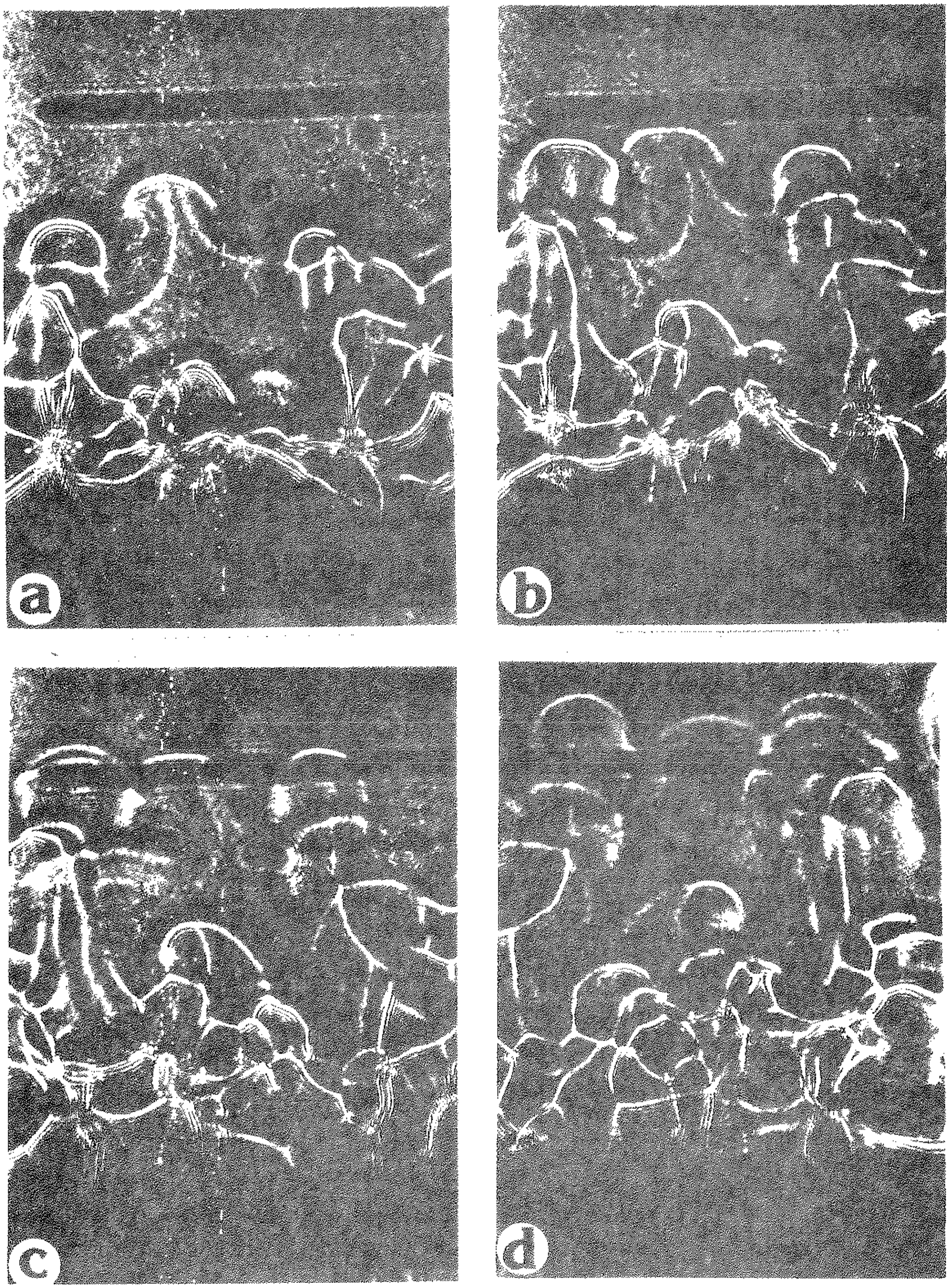

Figure 5.1 Shadowgraph images in a thermally stratified layer of water heated from below: (a) t = 120 s, (b) 122 s, (c) 124 s, (d) 126 s

right below this dark area (i.e., the gray line). In the photographs shown in Figure 5.1, the distance between the thermocouple and the bottom plate is about 3.5 cm which permits judgement of the actual distances. It should be noted that in these photographs only the lower part of the water layer is shown.

Although the shadowgraph technique has an averaging effect along the beam it is evident that the flow is three-dimensional, i.e., the thermals are generated not in one plane perpendicular to the beam on the surface of the bottom plate. This is also clearly evident in the photographs to be presented later. Figure 5.2 shows two shadowgraphs taken about two seconds apart for the same experiment. In these photographs a few thermals were isolated and magnified in order to show their deformation in greater detail. The pictures clearly indicate that as a thermal rises through the relatively quiescent fluid environment, its leading edge is blunted and folded back, producing a nearly hemispherical cap and giving a mushroom-like appearance to the thermal as a whole (see Figures 5.1 and 5.2). This is in close agreement with the observations of Sparrow et al. (1970). Figure 5.2a shows the mushroom-like convection elements with the middle thermal having a diameter of approximately 13 mm. Figure 5.2b shows the thermal about 2 seconds later which has grown to a diameter of about 15.7 mm. The center of this particular thermal has risen approximately 1.8 mm in 2 seconds. The trailing column of a thermal (i.e. the stem of the mushroom shape) is relatively cooler fluid entrained around the thermal. This entrainment is due to the motion of the thermal through relatively cooler surrounding fluid (see Figures 5.1 and 5.2).

A comparison between two experiments, one heating from below, and the other cooling from above, was made. Unlike experiments of Viskanta et al. (1977) who studied cooling of a thermally stratified layer of water from a free surface, in the cooling from above experiment the heat sink was placed in direct contact with the water, simulating the heating from the bottom experiment more closely.

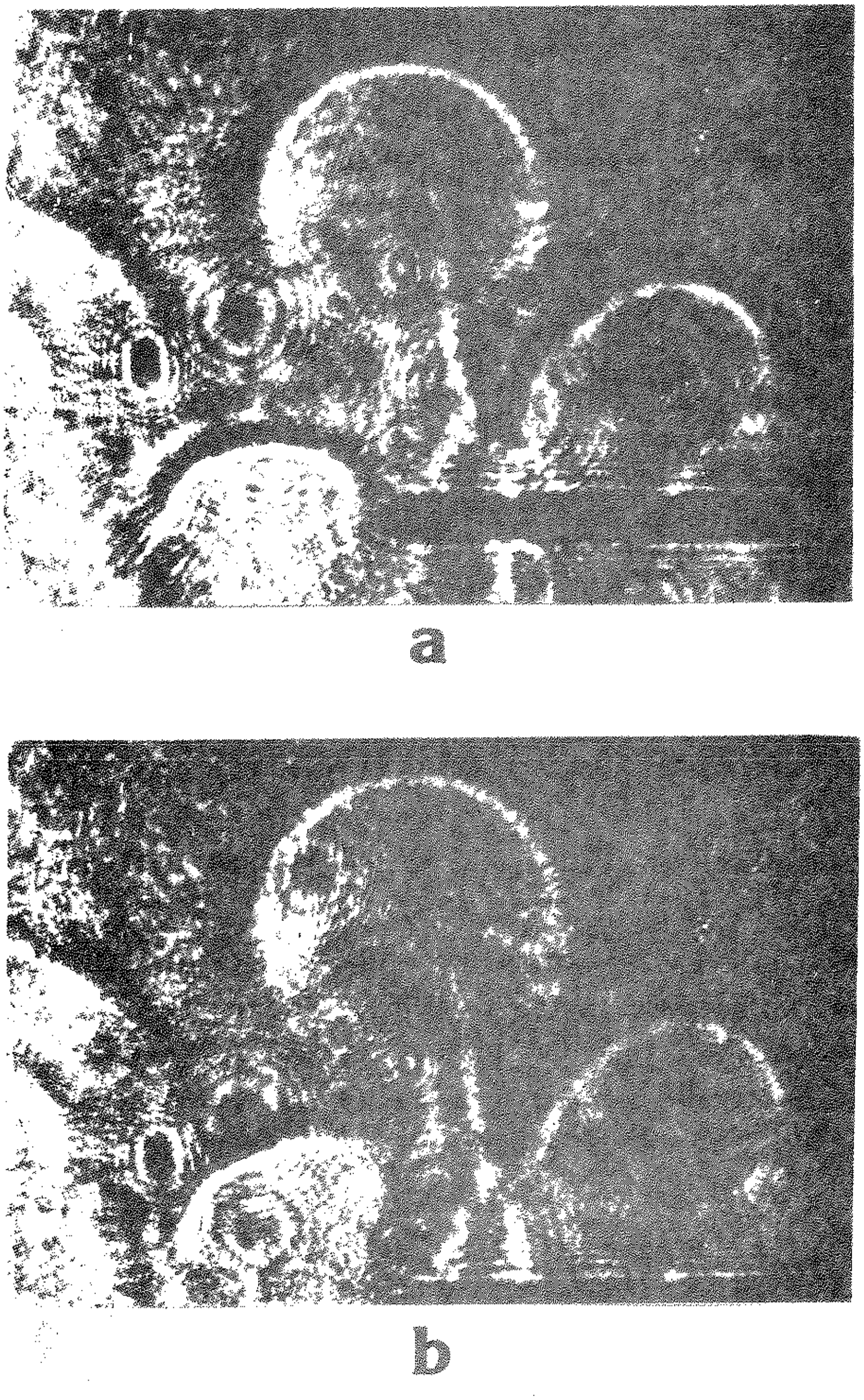

Figure 5.2 Shadowgraph images of typical thermal plumes during ascent in the layer: (a) $t = t_{ref}$, (b) $t = t_{ref} + 2$ s

Figure 5.3 shows the photographs for the two experiments side by side, which is intended to compare the general shape of the hot (or cold) parcels of water leaving the surface. The layer of water in both experiments was 10 cm deep with similar initial conditions. Photographs 5.3a and 5.3b are shadowgraphs for the heating from bottom, and photographs 5.3c and 5.3d are for the cooling from above experiments. The photographs were taken 2 seconds apart. Each square seen faintly in the photographs is 1 x 1 cm. It is evident from this figure that the thermals leaving the heated surface have a more blunt shaped leading edge than the plumes descending from the cooled surface. This is due to the fact that the thermals rise against the gravitational field, while the descent of the plumes is aided by the gravity.

Figure 5.4 shows the output of the thermistor for the heating from below experiment discussed in Figure 5.3. The strip chart recordings indicate very clearly that the amplitude and frequency of the thermals generated is not constant. However, Sparrow et al. (1970) reported a relatively constant spacial and temporal frequency of the thermals. The trace shows that temperature of the thermals were sometimes as high as about 1.5°C above the bulk temperature of the fluid around them. The output level of the thermistor is rising constantly (see Figure 5.4), because the thermistor measures the mean temperature of the fluid and not the fluctuations of the temperature. However, initially the thermistor was nulled with respect to the initial temperature surrounding it. Therefore, the steady rise in the output level indicates the heating of the fluid adjacent to the thermistor. The fluctuations from the instantaneous mean voltage level are the actual temperature fluctuations detected by the thermistor located about 0.6 cm above the bottom plate. The strip chart output indicates that at later times the amplitude of the fluctuations become smaller. This is due to the continued heating of the fluid which results in a smaller temperature difference between the plate and fluid adjacent to it.

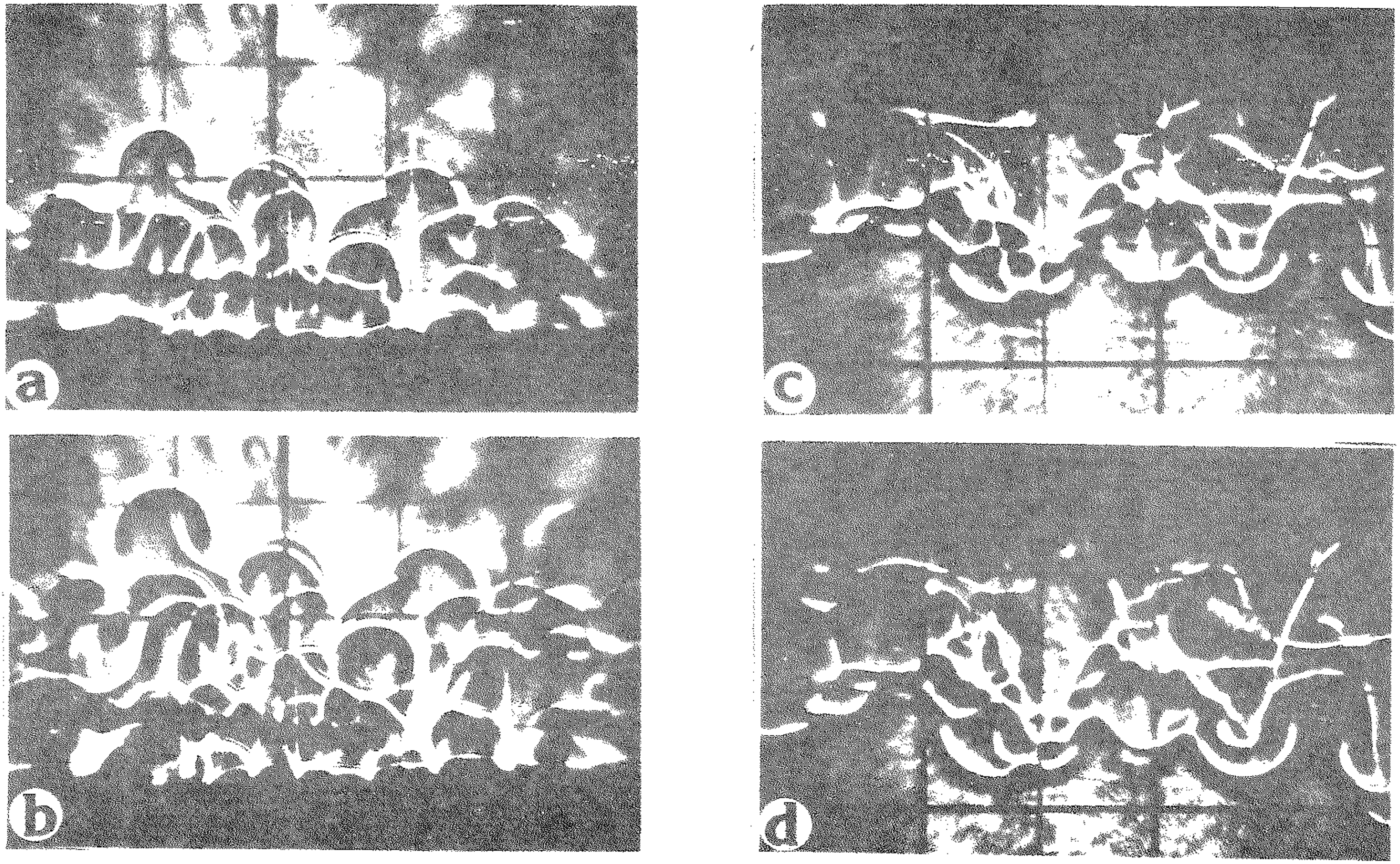

Figure 5.3 Comparison of shadowgraph images of typical heating and cooling experiments; heating from below: (a) $t = t_{ref}$, (b) $t = t_{ref} + 2$ s; cooling from above: (c) $t = t_{ref}$, (d) $t = t_{ref} + 2$ s

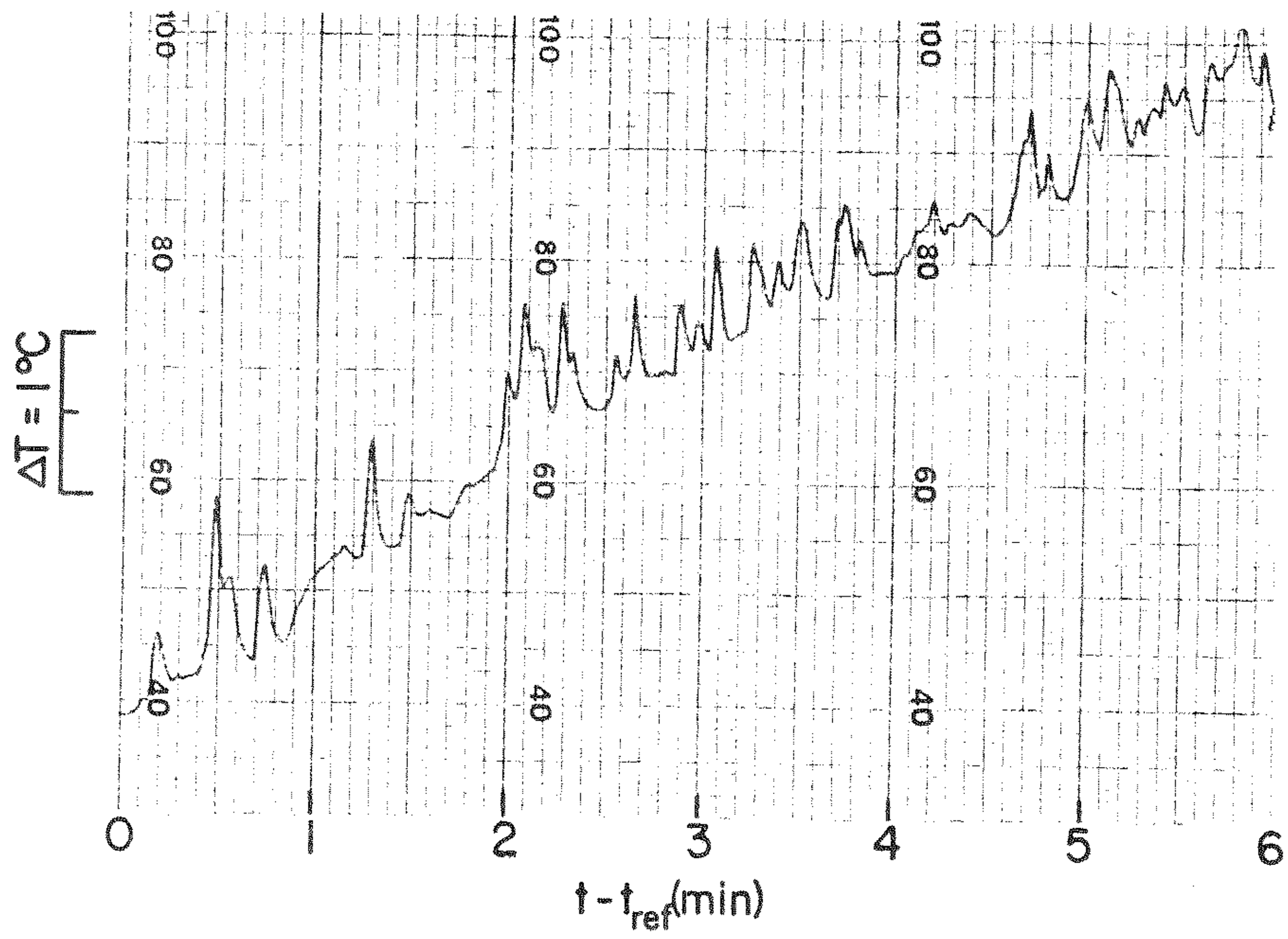

Figure 5.4 Sample thermistor output for heating of a thermally stratified layer of water from below, D = 10 cm

A qualitative comparison between uniform and thermally stratified layers of water heated from below was also made. The thermal characteristics in the two experiments were found to be very similar. Although the plumes had the same general shape, they moved at a greater velocity and penetrated to the surface. This was due to less resistance to their motion since the water was not stably stratified.

Several photographs illustrating the interference fringe pattern are shown in Figure 5.5. In this particular experiment the depth of the water was 14.8 cm. However, the interferograms shown do not cover the total depth of the layer. The reference thermocouple seen in the interferograms was located about 3.5 cm above the bottom of the test cell. Examination of the interferograms recorded earlier ($t < 45$ s) showed that the distance between the bottom few fringes increased, but they remained parallel indicating purely conductive heat transfer. Since the bottom plate was warmer than the fluid immediately above it, conduction of heat into the water produced a temperature reversal in the water just above the plate. This is clearly evident in Figure 5.5a which shows a layer about 3 mm deep across which the temperature reversal takes place. After about 1 minute from the start of circulation of water in the bottom plate, the lowest few fringes started to become wavy and moved very rapidly away from the plate. This indicated the onset of natural convection. After the onset of convection (i.e. Rayleigh number exceeding a critical value), the fluid layer adjacent to the plate became unstable and thermals broke away from the surface and plunged into the thermally stratified stable layer above (see Figure 5.5b). Figure 5.5b shows that the breaking away of thermals from the plate creates mixing and agitation which in turn creates a relatively uniform layer of about 2 cm deep.

As discussed earlier, the generation of thermals is due to the instability created in the layer adjacent to the heated surface. This is clearly evident from Figure 5.5b which shows that the thermals are at a different temperature than the bottom heating plate.

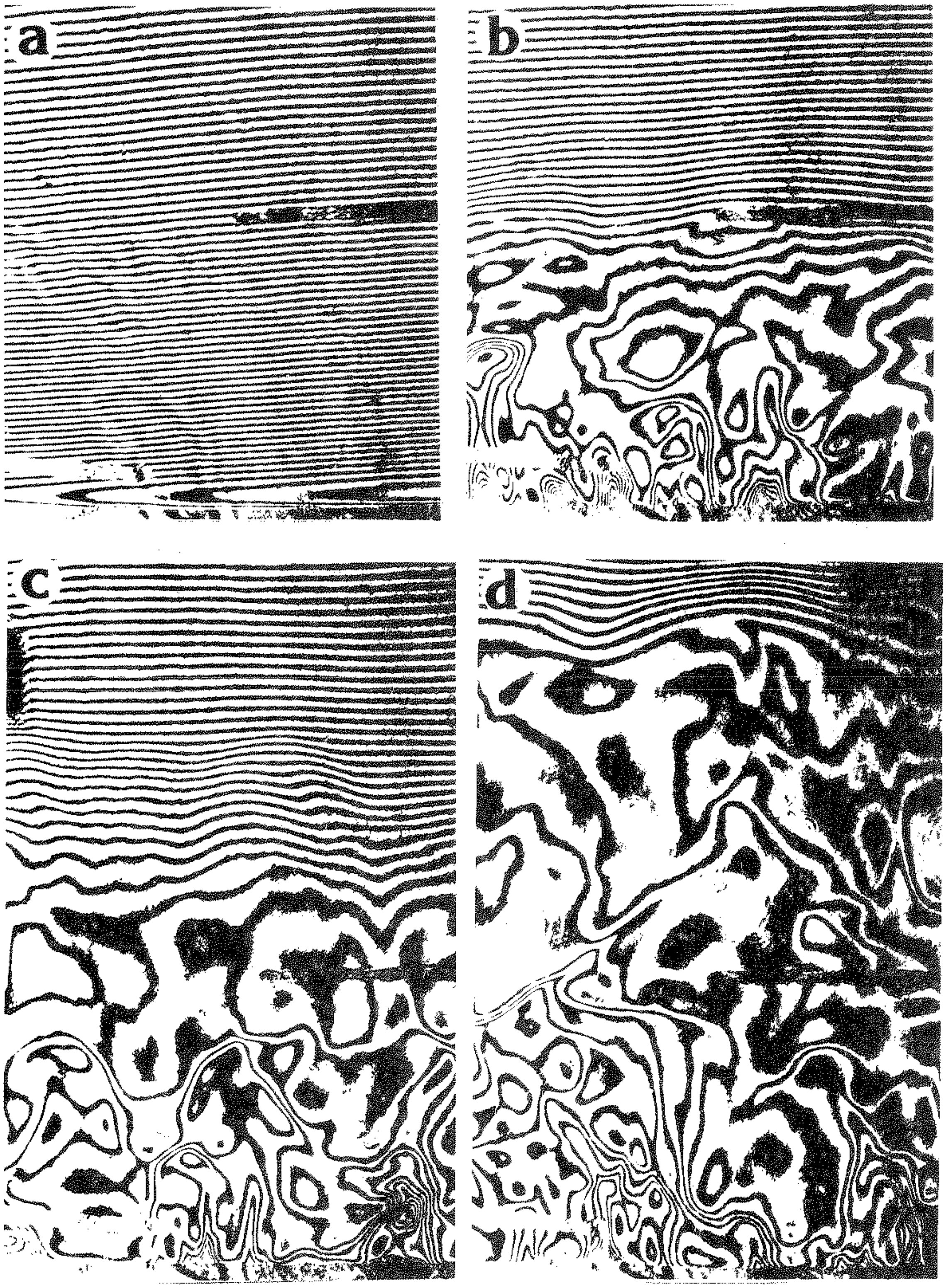

Figure 5.5 Photographs of interference fringe patterns for Experiment D (see Table 5.1 for conditions): (a) t = 1 min, (b) 2 min, (c) 3 min, (d) 5 min

The start of the ascending warm water appeared at random locations and no characteristic wavelength (wave number) could be defined for the process (see Figures 5.5b, 5.5c, 5.5d). The temperature of the thermals was not uniform across it and there was a considerable temperature difference between the center and the outer edge of thermals. For example, in Figure 5.5c across one of the thermals there are 10 fringes which correspond to roughly 1°C temperature difference. In this particular experiment, the voltage output of the thermistor located a few millimeters above the plate indicated that the upward moving thermals were approximately 0.4 to 2°C warmer than the surrounding bulk mean temperature.

The heating rate had a decisive influence on the generation of thermals. Both the spatial frequency of the sites and the temporal frequency of generation increased with an increase in the rate of heating. Even though the fringe density near the bottom is quite high and difficult to interpret, Figure 5.5c shows that as the thermal departs from the plate, a mass of relatively uniform cooler water rushes in and replaces the warmer water. The phenomena observed was similar to that reported by Sparrow et al. (1970) and Townsend (1959) who studied the rising of the thermals. However, unlike the findings of Sparrow et al. (1970), the shadowgraphs and interferograms indicated very clearly that the thermals are not spaced regularly on the heating surface and have no characteristic frequency of departure. The sites where the thermals originated were not fixed but wandered about the bottom plate. The difference between the findings of Sparrow et al. (1970) and this investigation can be due to several factors. Sparrow et al. have studied the rise of thermals in a uniform layer of water and not a thermally stratified layer. The test cell they used was larger than the test cell in the present experiments, and the electrically heated platform (8.9 cm square) was located about 8 cm above the bottom of the cell. This arrangement must have resulted in a much better circulation of water around the heated surface.

The relatively uniform layer of water right above the heated plate grew in depth as the heating continued. As it is evident from Figure 5.5, the initial growth rate of this layer was higher than at later times due to greater heat transfer as a result of a layer temperature difference between the plate and fluid adjacent to it.

As the ascending thermals reach the stratified layer, a parcel of this warmer fluid plunges into this stable layer and disturbs the interface between the uniform and stratified layers. As a result of this bombardment, the warmer fluid in the stable region is entrained into the mixed layer, and the layer grows at the expense of erosion of the bottom of the stably stratified region. This is clearly evident from the fact that the distance between the fringes in the stable layer increases as the heating continues. This means that heat is being transferred from this layer. The fringes at the bottom of the stable layer became wavy and distorted (see Figures 5.5c, 5.5d). This is due to the bombardment of the interface by the thermals which plunge into the stable region before spreading along the interfacial layer.

Figure 5.6 illustrates the initial temperature distributions prior to heating from below for several experiments. For example, the initial temperature distribution for experiment A clearly indicates that there is a temperature reversal in the immediate vicinity of the bottom plate. For experiment E the temperature varies almost linearly with the depth of the layer. Temperature distribution for experiment B clearly shows that the top surface of the water layer is effectively insulated and therefore a thin uniform temperature layer exists just below the free surface.

An attempt was made to measure the rise velocity of the thermals, and the velocity fluctuations due to the heating of the water from below. A calibrated hot-film anemometer was used to detect the velocity fluctuations caused by the thermal. However, because of low sensitivity of the anemometer (see Appendix D) even at high over-heat ratios, no meaningful results were obtained. There is some evidence that a Laser-Doppler-Velocimeter can be successfully

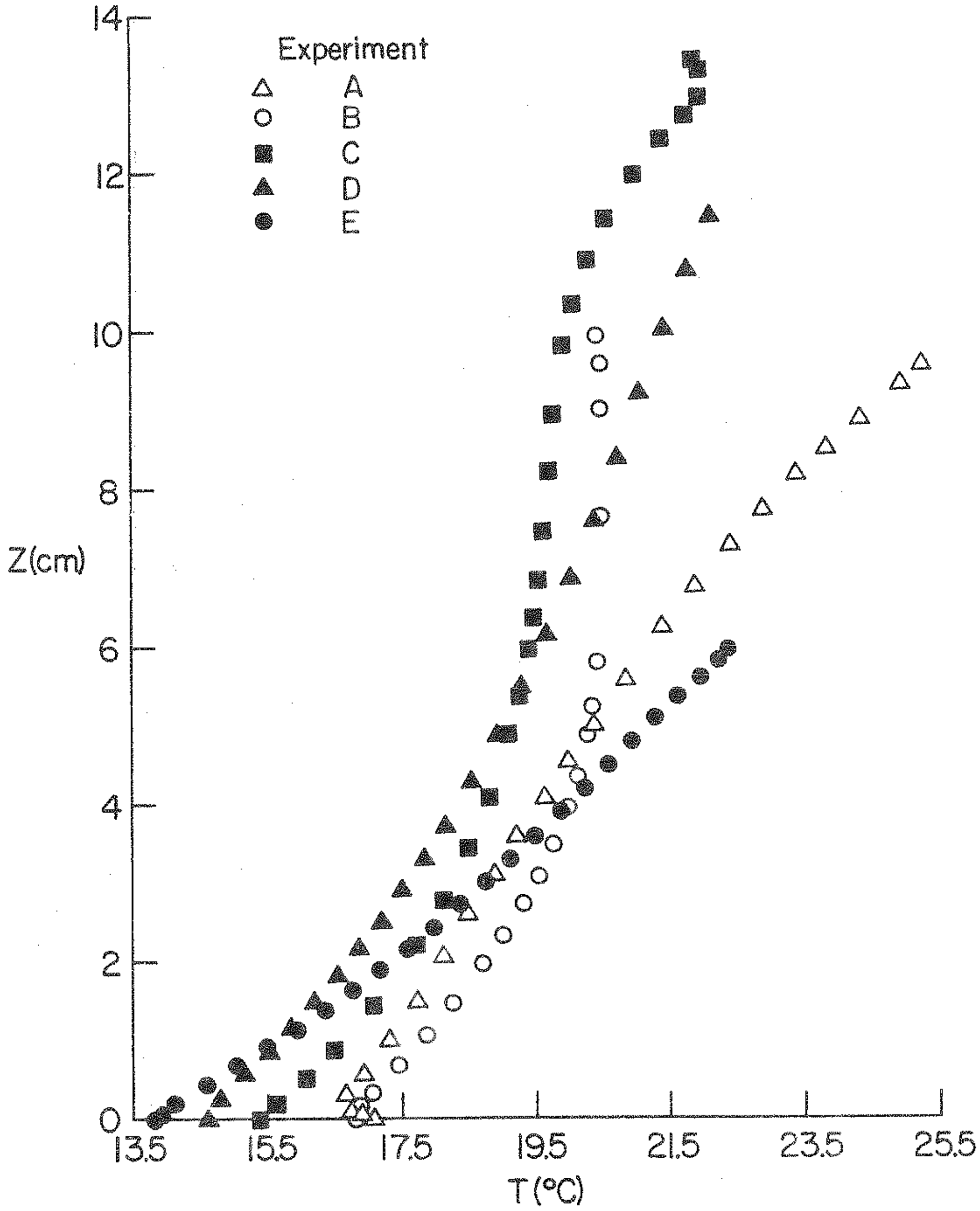

Figure 5.6 Initial temperature profiles in thermally stratified water before heating from below for different experiments (see Table 5.1 for conditions)

adopted to measure such small velocities.

5.4 Thermal Model

After the critical Rayleigh number has been exceeded, the temperature structure in a stratified layer of water heated from below can be considered to consist of four regions. A very thin thermal boundary layer in which relatively large temperature gradients are present in the fluid in contact with the bottom plate. The thermals (mushroom-like convection elements) create through turbulent mixing a practically homogeneous layer of water at temperature $T_m(t)$ above the thermal boundary layer. The temperature $T_m(t)$ and the height h(t) of the mixed layer increase with time. The strongly agitated region which lies between the mixed layer and the stable region, called the entrainment layer, is more and more eroded from below by the bombardment of the thermals. The main three factors which control the development of the mixed layer are the heat transfer rate at the bottom, the turbulent mixing processes which occur in the entrainment layer between the convective layer and the stable region above, and the vertical temperature gradient, $\partial T/\partial z = \gamma(z,t)$, in the stable region.

If the presence of the thin thermal boundary layer is neglected, an energy balance on the entire mixed (convective) layer extending from z = 0 to z = h gives

$$\rho ch \frac{dT_m}{dt} = -H(z,t)\Big|_{z=0}^{z=h} = H_0(t) - H_h(t) \tag{5.1}$$

where the local heat flux at any depth z is defined by

$$H(z,t) = -\rho c(\alpha \frac{\partial T}{\partial z} - \overline{w'T'}) \tag{5.2}$$

The entrainment of warm water from the stable region below into the mixed layer leads to a downward heat flux $H_h(t)$ at the top of the mixed layer which has an opposite direction (sign) of the heat flux

H_0 at the bottom wall. The heat flux at depth $h(t)$ is determined by the transport of warmer fluid at temperature $T_{mo} + \gamma h$ into the mixed layer of temperature T_m at a velocity dh/dt and can be expressed as

$$\rho c(T_{mo} + \gamma h - T_m)\frac{dh}{dt} = - H_h(t) \qquad (5.3)$$

To provide a closure condition for the problem it is assumed that the heat transported into the mixed layer H_h due to entrainment is proportional to the heat flux at the bottom of the layer H_0 such that

$$H_h(t) = - \kappa(t)H_0(t) \qquad (5.4)$$

where $\kappa(t)$ is a proportionality factor which is considered to depend on the height of the mixed layer h and therefore indirectly on time. The approach of taking the downward heat flux H_h at the top of the mixed layer to be proportional to upward heat flux at the bottom wall H_0 if the layer is in the state of natural convection is well established in the literature (Plate, 1971; Zeman and Tennekes, 1977). The proportionality factor κ lies between zero and unity and has been established by measurement (Heidt, 1977), and some experimental results obtained in this study will be presented.

Elimination of H_h from Eqs. (5.1) and (5.3) with the help of Eq. (5.4) and introduction of scaling parameters, yields the following two equations for the dimensionless mixed layer height η and temperature Θ, respectively,

$$\eta\frac{d\Theta}{d\tau} = H_0{}^*(\tau) - H_h{}^*(\tau) \qquad (5.5)$$

and

$$(\Gamma\eta - \Theta)\frac{d\eta}{d\tau} = - H_h{}^*(\tau) \qquad (5.6)$$

The simple physical model described is the same as for the convectively unstable planetary boundary layer in the atmosphere capped by a stable layer. The original development of the model has been reviewed by Plate (1971) and more recent contributions to the theory can be found in the papers of Zeman and Tennekes (1977) as well as of Venkatram and Viskanta (1977) together with up-to-date reviews of literature.

5.5.1 Sensitivity of Model Parameters

The analysis presented in the previous section has bypassed the tedious problem of modeling turbulence and predicting the eddy diffusivities, but this has been at the expense of generality. The temperature profile shape in the mixed layer had to be prescribed a priori and there is a loss of detail in the determined temperature distribution. The dimensionless model equations, Eqs. (5.4), (5.5) and (5.6), do not render a closed form analytical solution except in particular cases. Therefore, a 4th order Runge-Kutta numerical scheme was adopted to solve the two differential equations.

The model equations indicate that there are two dimensionless parameters and an empirical factor κ which control the dynamics of the mixed layer. The model is driven by the heat input to the layer from the bottom, and the dimensionless heat flux ($H_0{}^*$) is an important parameter. The other parameter, the normalized temperature gradient at the bottom of the stable layer (Γ), represents the resistance by the stable layer to the opposing buoyancy force from the mixed layer. The empirical factor κ will be determined from experimental data. Some experimental results for the heat flux ratio $-H_h/H_0$ as a function of time are presented in Figure 5.7. Results are included only after it was observed that vigorous mixing was established. The results obtained are within the range reported in the literature by Deardorff et al. (1969) and Heidt (1977), but cannot be directly compared because of different experimental conditions. The effects of the model parameters are systematically examined in the next few paragraphs.

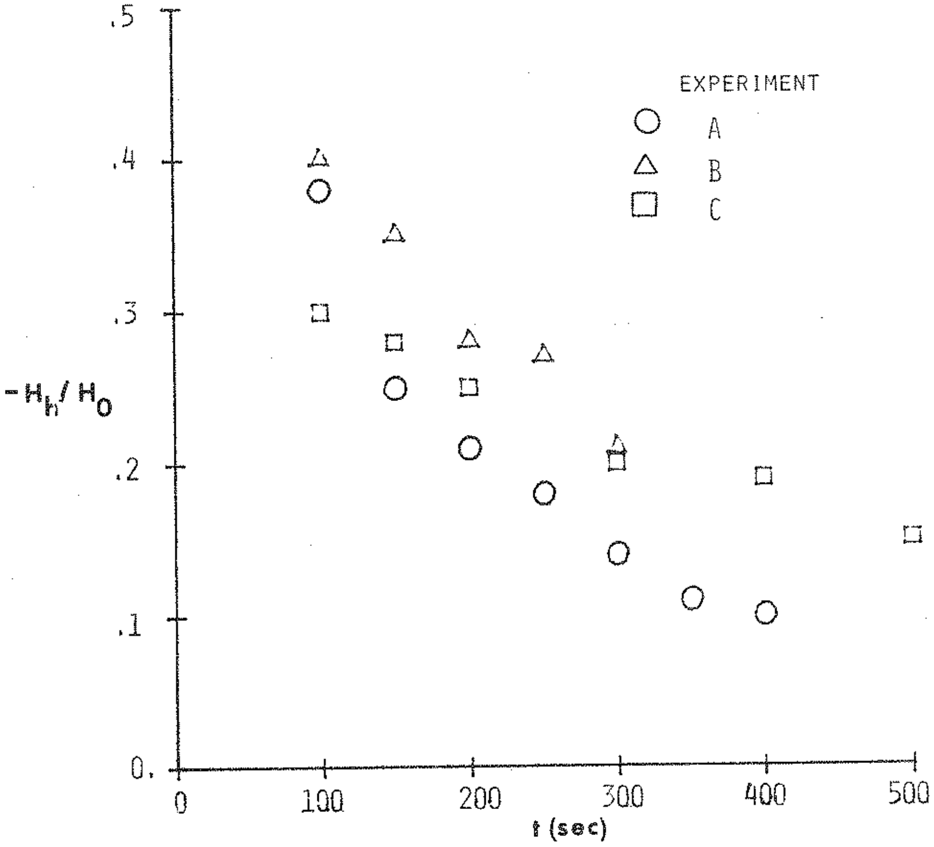

Figure 5.7 Variation of the heat flux ratio with time for different experiments; see Table 5.1 and Figure 5.6 for conditions

The effect of factor κ on the mixed layer growth is illustrated in Figure 5.8 for the case of time independent gradient Γ in the stable region and an exponentially decreasing dimensionless heat flux at the bottom, H_0. As expected from the model equations, the results show that a decrease in the value of κ decreases the growth rate of height and temperature of the mixed layer. However, it should be noted that the model is rather insensitive to the value of κ and an increase of 100 percent at most results in only about 10 percent increase in the value of the dimensionless mixed layer temperature and depth. This finding is in agreement with that of similar models (Behnia and Viskanta, 1979).

The effect of dimensionless bottom heat flux (H_0*) on the dimensionless mixed layer temperature and height is illustrated in Figure 5.9. It is noted from the figure that as the heat flux is changed from a constant to a time dependent decreasing input the rate of growth of mixed layer height and temperature decreases. This change is at most about 20 percent at $\tau = 3$. Although for curves (2) and (3) the heat flux at $\tau = 3$ has a value of about 40 percent of the initial flux, the mixed layer dynamics has not been changed significantly by the decrease in the heat flux. Figure 5.9 indicates that the higher the rate of heat input from the bottom, the more rapid is the growth of the mixed layer depth and an increase in temperature. This is in agreement with expectations and available results (Deardorff et al., 1969; Heidt, 1977). The results for cases (2) and (3) are practically indistinguishable from each other. This is due to the fact that the starting value of H_0* (i.e. at $\tau = 0$) is the same for both cases and also the value of H_0* at $\tau = 3$ is not much different from one to the other.

Figure 5.10 illustrates the effect of the dimensionless temperature gradient, Γ, on the dynamics of the mixed layer. As expected, the results show that a decrease in the parameter increases the growth rate of the mixed layer thickness considerably but decreases the rate of change of the mixed layer temperature [compare curves (1) and (4) for instance]. This indicates that the greater

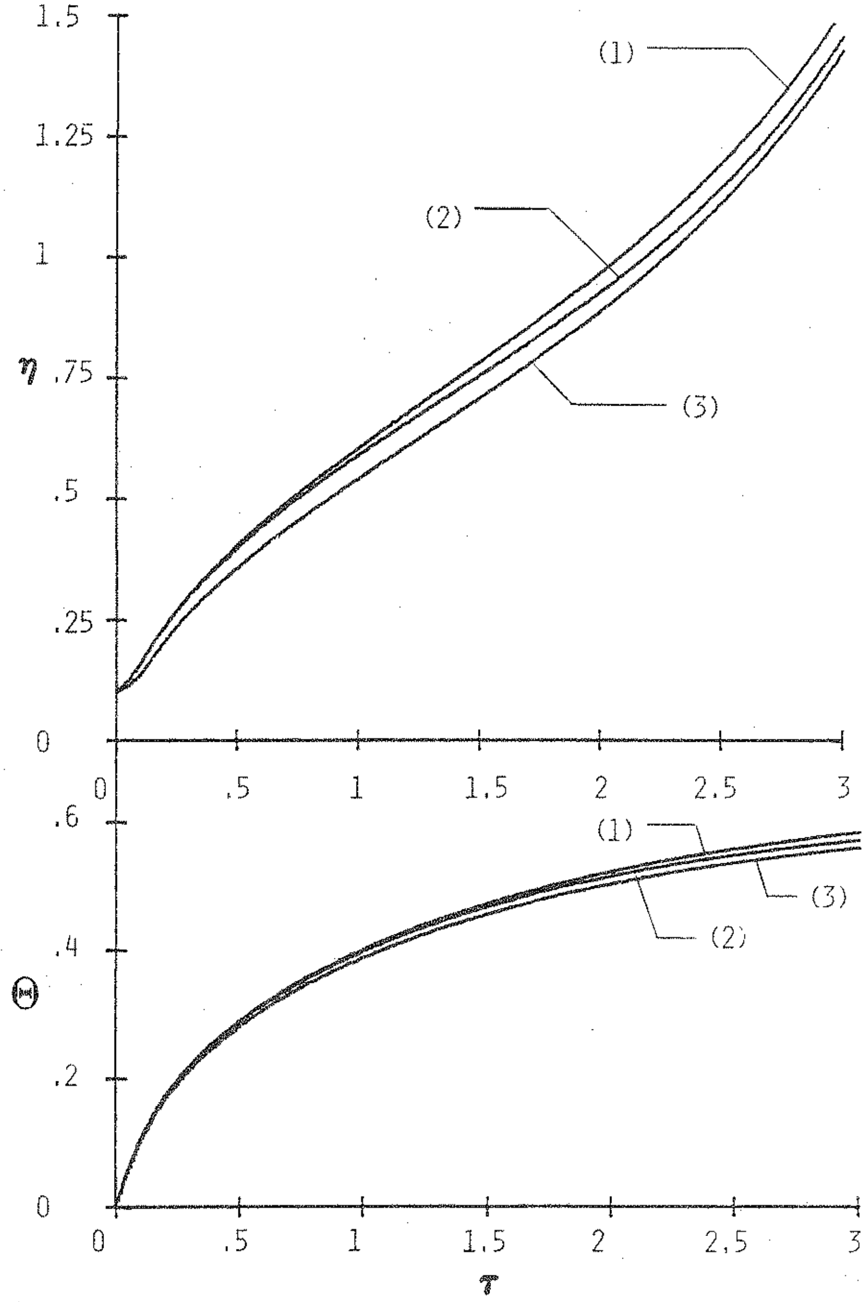

Figure 5.8 Effect of parameter κ on the dimensionless mixed layer depth and temperature for $H_0^* = 0.1 \exp(-\tau/4)$ and $\Gamma = 1.0$: 1) $\kappa = 0.4$, 2) $\kappa = 0.4 - 0.2\,\tau/3$, and 3) $\kappa = 0.2$

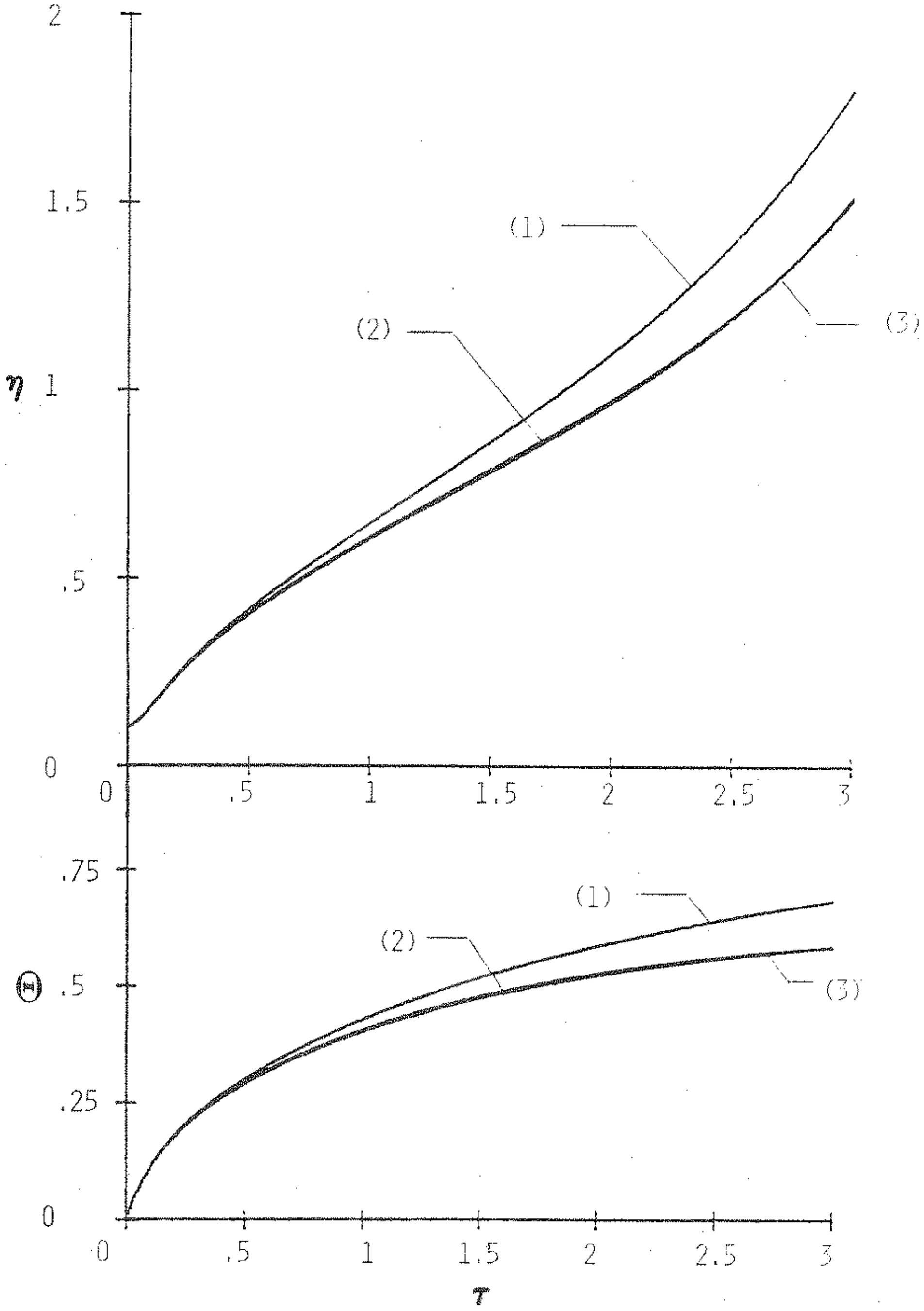

Figure 5.9 Effect of heat transfer H^* at the bottom on dimensionless mixed layer depth and temperature for $\kappa = 0.4$ and $\Gamma = 1 - 0.2\tau$: 1) $H_0^* = 0.1$, 2) $H_0^* = 0.1 \exp(-\tau/4)$ and 3) $H_0^* = 0.1 - 0.02\tau$

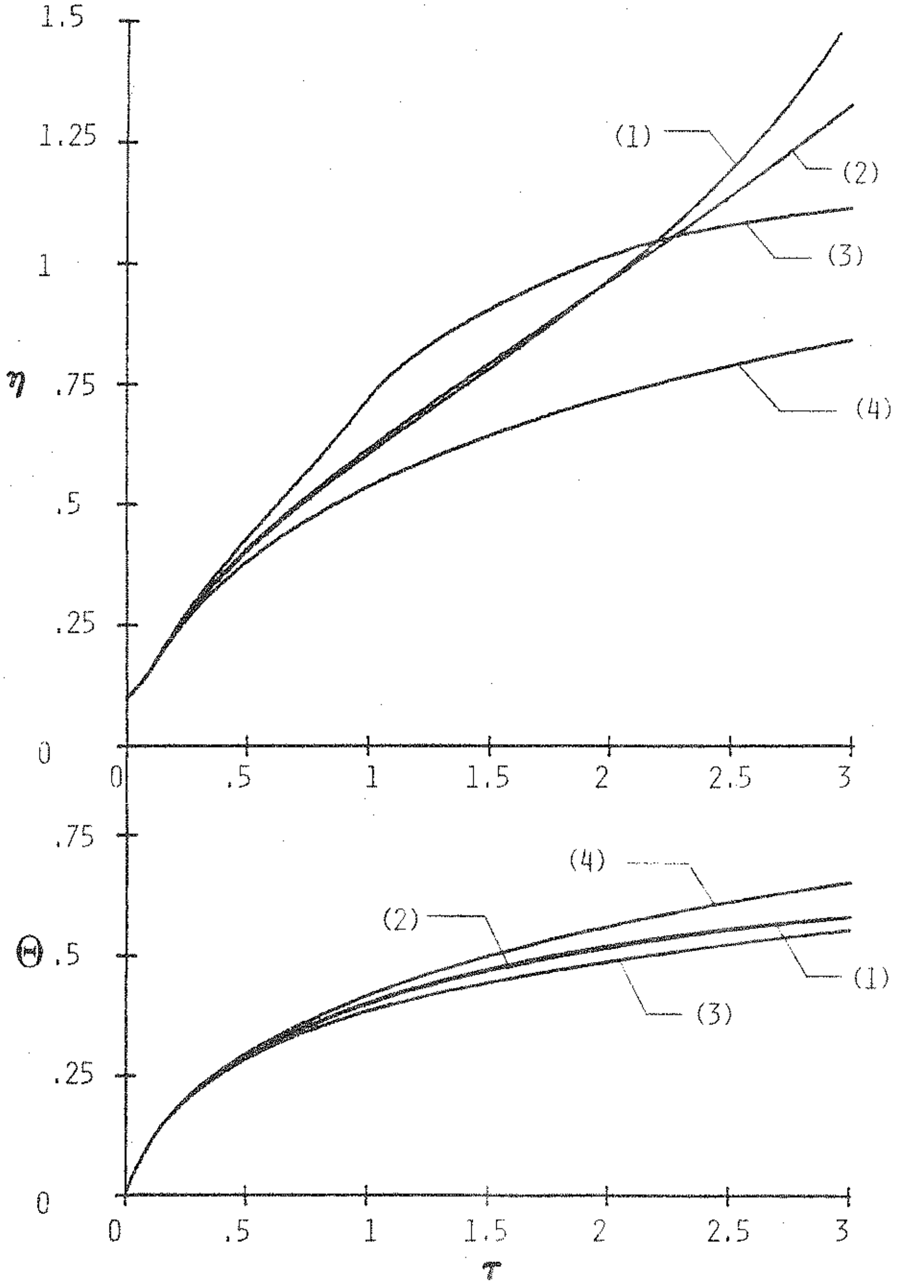

Figure 5.10 Effect of stratification parameter Γ on dimensionless mixed layer depth and temperature for κ = 0.4, and $H_0{}^* = 0.1 \exp(-\tau/4)$: 1) $\Gamma = 1 - 0.2\tau$, 2) $\Gamma = \exp(-\tau/4)$, 3) $\Gamma = 1 - 0.4\tau$ for $\tau < 1.0$, $\Gamma = 0.6$ for $1 \leq \tau \leq 2$, $\Gamma = 0.2 + 0.2\tau$ for $\tau > 2$ and 4) $\Gamma = 1$

the stratification in the stable region, the more it resists the growth of the mixed layer. Greater stratification results in more energy being entrained at the interface which in turn causes an increase in the mixed layer temperature. The results of the figure show that the depth of the mixed layer is more sensitive than the temperature to this parameter. It is evident from the model equations that the mixed layer height is directly related to this parameter; however, the temperature is related to it indirectly through dependence on height. Curve (3) corresponds to typical initial temperature profiles similar to that of experiment C (see Figure 5.6 and Table 5.1). Again, it should be noted that in this model unlike models discussed by Deardorff et al. (1969) and Heidt (1977) no assumption was made about the layer being uniformly stratified.

Table 5.1 The experimental conditions for different tests discussed

Experiment	Depth (cm)	T_{0o} (°C)	γ_o (°C/m)	T_{fo} (°C)	T_f (°C)
A	9.56	17.1	82	22.5	27.0
B	9.94	16.8	97	19.8	21.9
C	13.42	15.4	76	21.7	24.7
D	14.80	14.6	109	18.0	25.4
E	5.97	13.8	115	21.1	27.0

5.5.2 Comparison of Model Predictions with Experiments

In the experiments performed, after a short transient period the bottom plate reached a nearly constant temperature. Therefore, as mentioned before, the model equations could not be solved in closed form and numerical solution were obtained. The heat flux at the bottom and temperature gradient in the stable region were evaluated as discussed before. The proportionality factor κ which relates the heat flux at the bottom to the heat transported into the convective layer due to entrainment at the top of layer, see Eq. (5.4), was determined empirically using experimental data. The parameter is not constant during the development of the convective layer but varies with the depth of the mixed layer and, therefore, indirectly with time, see Figure 5.7. But in most of the calculations presented here a constant value of κ was used. Because of relative insensitivity of results on κ (see Figure 5.8) and significant uncertainty in its variation with time, a choice of constant κ is not likely to limit the range of applicability of the simple thermal model. Since the model is valid only after the mixed layer has become turbulent, the reference time ($t = t_{ref}$) was taken to be the time at which the layer depth has become sufficiently large for the flow to be turbulent.

Figure 5.11 shows the comparison of predicted and measured mixed layer height and temperature for experiment D. In these calculations (Figure 5.11) the dimensionless temperature gradient Γ was assumed to be constant even though the unsteady temperature profile showed slight variations with time. Curve (1) indicates that the predicted dimensionless mixed layer thickness is within 3 percent of experimental results. However, the dimensionless mixed layer temperature is overestimated by about 12%. This discrepancy is considered to be due to inadequate modeling of the entrainment process. Curve (2) shows that a time dependent linearly decreasing dimensionless heat flux at the bottom would bring the predicted mixed layer temperature closer to the experimental data, at least for later times, but this would result in an underestimation of the mixed layer depth for later times. A change of κ from a constant to a linearly decreasing function affects little the predictions of mixed layer temperature but underestimates the mixed layer height.

The value of $\kappa = 0.25$ is in the range of factors cited in the literature (Heidt, 1977) during growth of the convective layer. Deardorff et al. (1969) obtained time dependent values of κ ranging from 0.16 to 0.257. Heidt (1977) found that κ is nearly constant and recommended a mean value of 0.18. The fact that for some short time after the heating from below was initiated the buoyancy

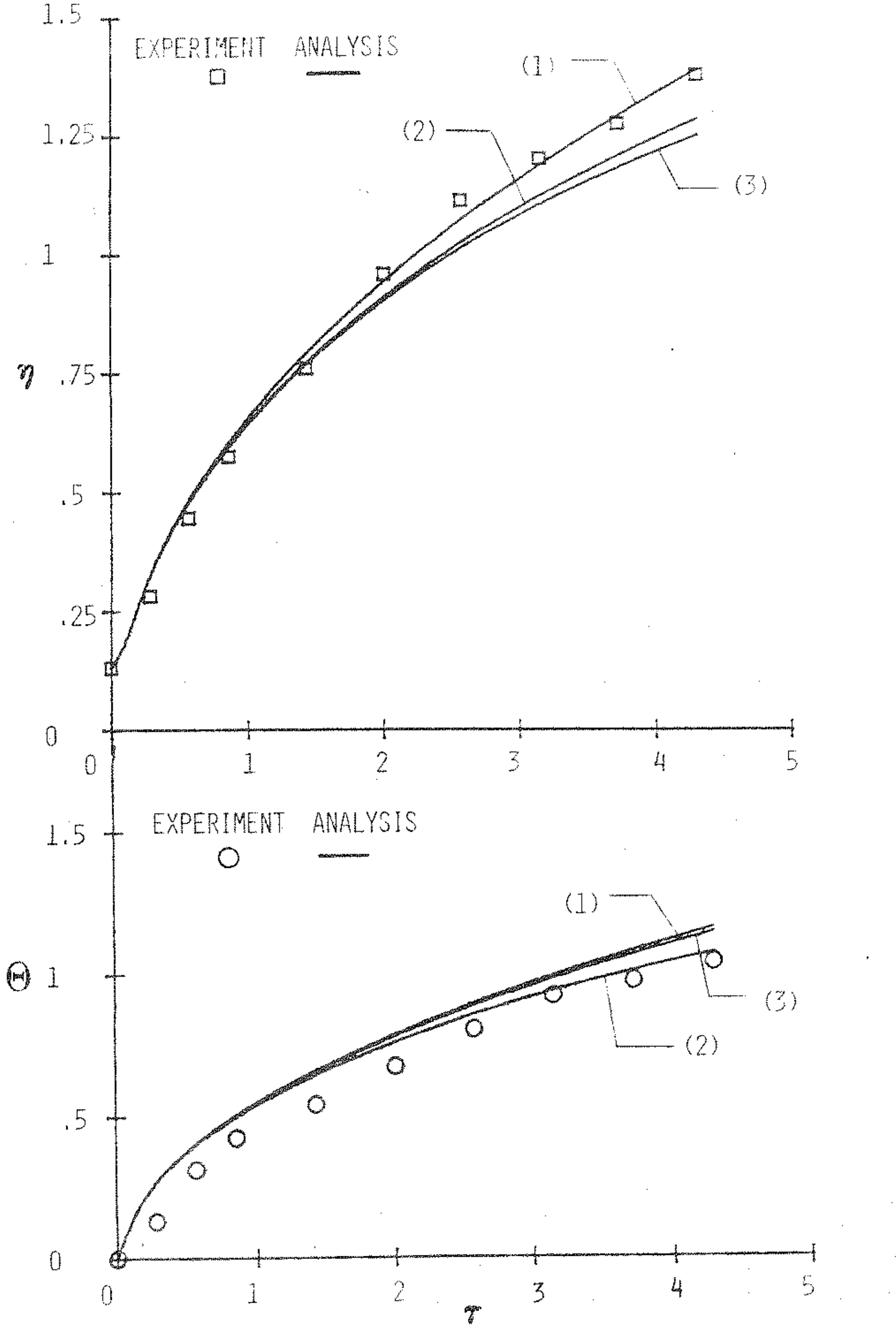

Figure 5.11 Comparison of predicted and measured mixed layer depth and temperature for Experiment D ($\Gamma = 1.0$): 1) $\kappa = 0.25$, $H_0^* = 0.15$, 2) $\kappa = 0.25$, $H_0^* = 0.15 - 0.01\tau$, and 3) $\kappa = 0.25 - 0.04\tau$, $H_0^* = 0.15$

induced motion was laminar may partly explain the discrepancy between results reported in the literature and those obtained in this study as well as the disagreement between data and the predictions of the model indicated in Figure 5.11 and 5.12. It should be pointed out again, for the present experiments the stratification was produced by radiation from above and cooling from below and in most experiments was not uniform with depth. In contrast, the stratification was nearly uniform throughout the layer in the experiments of Deardorff et al. (1969) and Heidt (1977).

Figure 5.12 shows the comparison between the measured and predicted dimensionless mixed layer depth and temperature for three different experiments. The experimental conditions for the tests discussed here are summarized in Table 5.1 and the initial temperature profiles are shown in Figure 5.6. It should be emphasized that the thermal stratification for the three experiments was different. The results indicate that on the average there is about a 5 percent discrepancy between the predicted dimensionless mixed layer depth η and the experimental data. For experiment D the agreement between the model predictions for η and data is excellent, but for Θ they are on the average about 15% higher than the experimental data. The discrepancy is due to the inability to model realistically the entrainment process. For all the three experiments an average value of 0.25 was used for the parameter κ. Due to the particular shape of the initial temperature profile for experiment C (see Figure 5.6), the initial local temperature gradient was different than the other experiments discussed here. In this experiment, initially Γ decreased with time. At later times the gradient started increasing with time, and a decrease in the growth rate of the mixed layer depth was observed (see Figure 5.12).

5.6 Predictions Based on K-ε Model

5.6.1 Model Characteristics

As discussed in Section 5.5, the simple thermal model developed is capable of predicting the dynamics of the mixed layer during

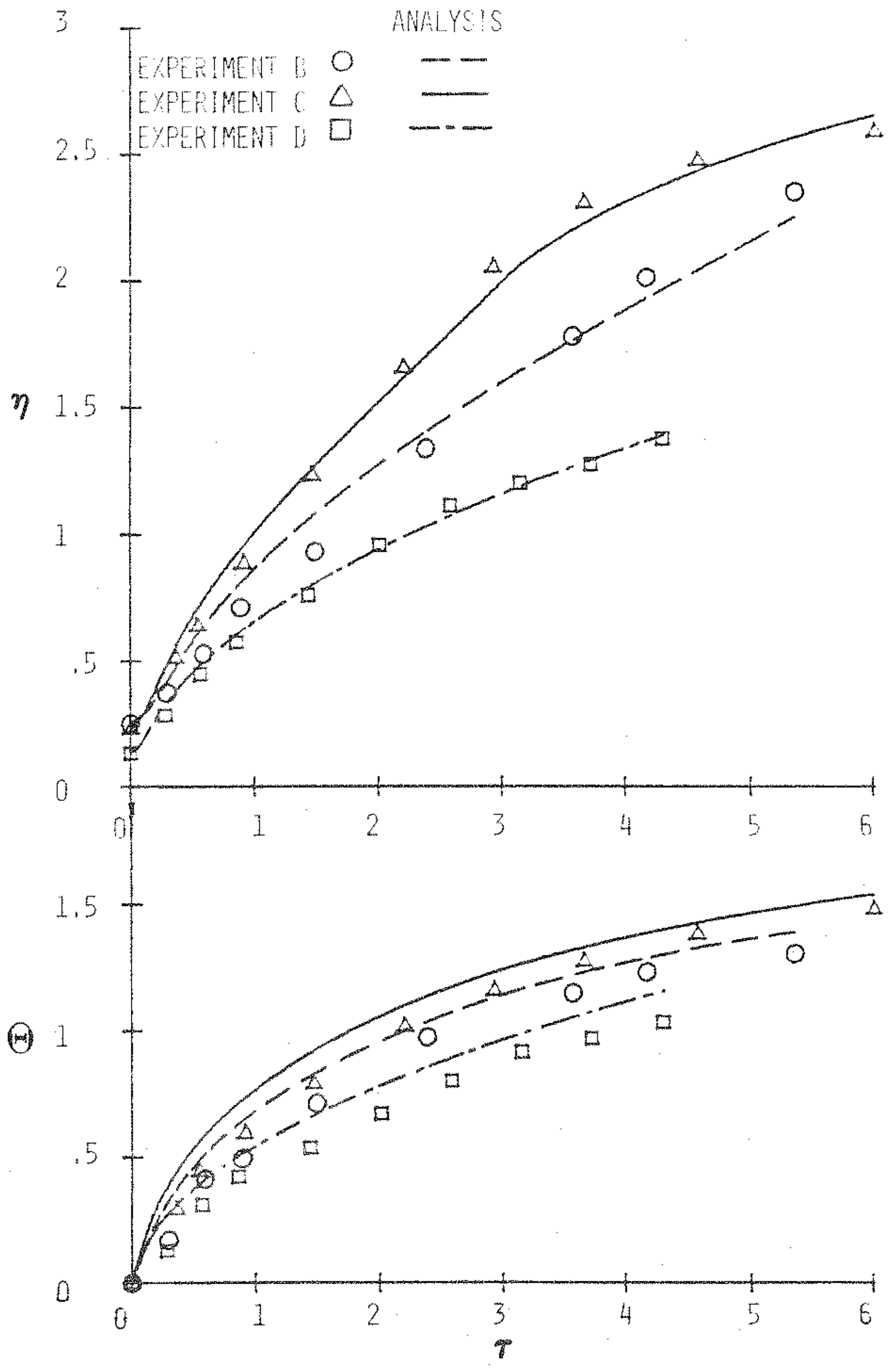

Figure 5.12 Comparison of predicted and measured mixed layer depth and temperature for different experiments: Experiment B ($\kappa = 0.25$, $H_0{}^* = 0.276 - 0.0276\tau$, $\Gamma = 1.0 - 0.062\tau$), Experiment C ($\kappa = 0.25$, $H_0{}^* = 0.34 - 0.034\tau$, $\Gamma = 1.0 - 0.105\tau$ for $\tau \leq 3$ and $\Gamma = 0.684$ for $\tau > 3$), and Experiment D ($\kappa = 0.25$, $H_0{}^* = 0.152$, $\Gamma = 1.0$)

heating from below of an initially thermally stratified layer of water, but cannot be used to predict detailed temperature profile. The temperature distribution in the layer of water can be determined through the modeling of turbulence in the one-dimensional energy equation.

The $K-\varepsilon$ model discussed in detail in Chapter 3 was employed, and the unsteady, one-dimensional energy equation was solved to yield the temperature profile. The effective eddy viscosity (e.g. eddy conductivity) distribution was also predicted in the layer of water. In adopting the turbulence model for this particular problem it was assumed: 1) no external shear stresses are present, 2) no pressure gradients exist, 3) the air-water interface is insulated, 4) the layer of water is heated only from below, 5) the turbulence is generated only by buoyancy induced by heating from below, and 6) the initial production and dissipation of turbulence is negligible.

It should also be noted that, although the model has been extensively tested and verified for several different problems (Launder and Spalding, 1974; Singhal and Spalding, 1975; Spalding and Svensson, 1976), no universality in the values of the model constants has been claimed. The values of the constants described in Chapter 3 were used in the calculations. No adjustments of these values were made to improve the agreement between experimental data and model predictions. The sensitivity of the model equations to these constants is discussed in detail in Chapter 3 and will not be repeated here.

5.6.2 $K-\varepsilon$ Model Predictions of Mixed Layer Dynamics

Figures 5.13 and 5.14 show the comparisons between the $K-\varepsilon$ model predictions and experiments for the mixed layer depth and temperature, respectively (for initial and experimental conditions, see Figure 5.6 and Table 5.1). It should be noted that the initial temperature profiles used in these model calculations were determined

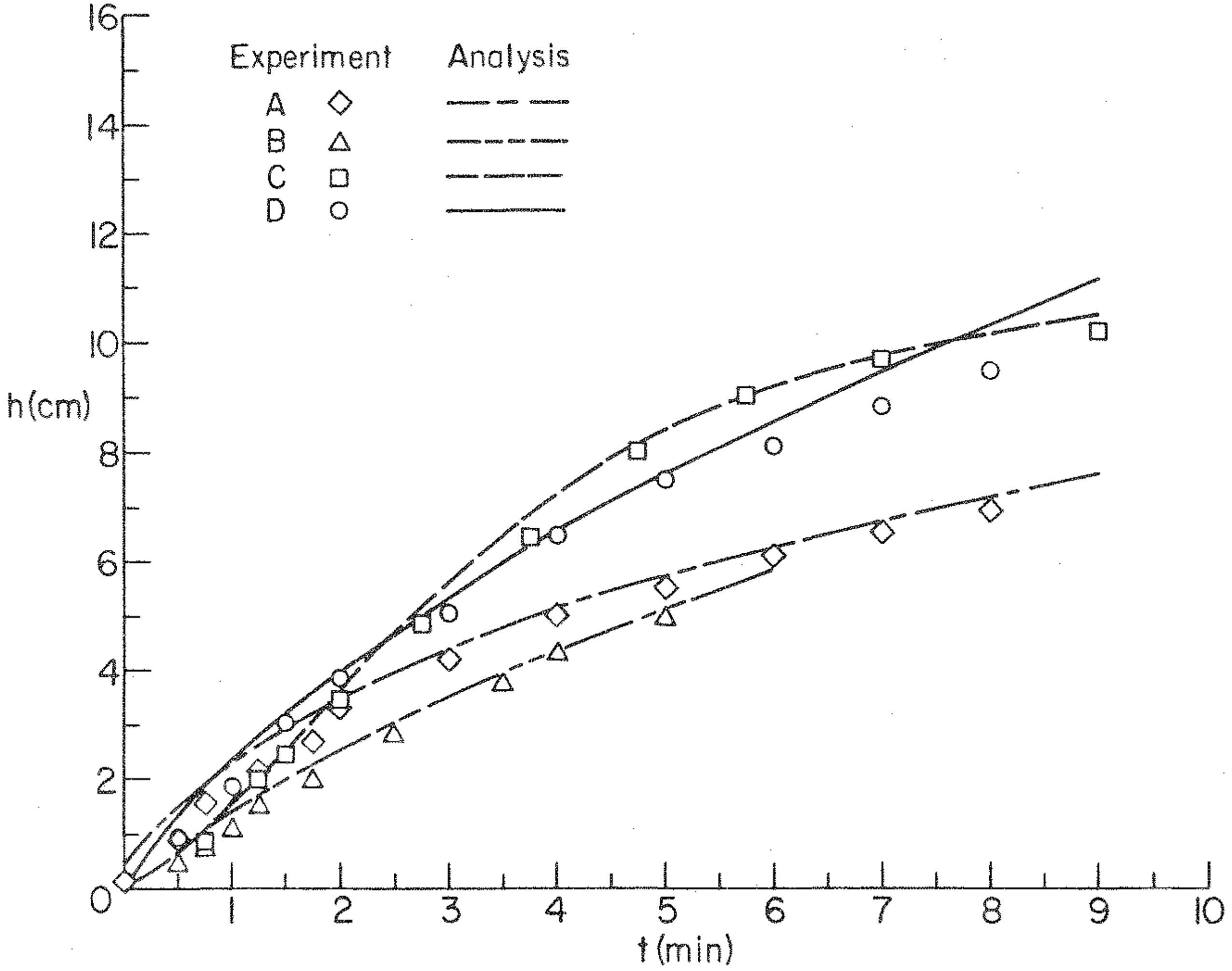

Figure 5.13 Comparison of measured and predicted mixed layer depths

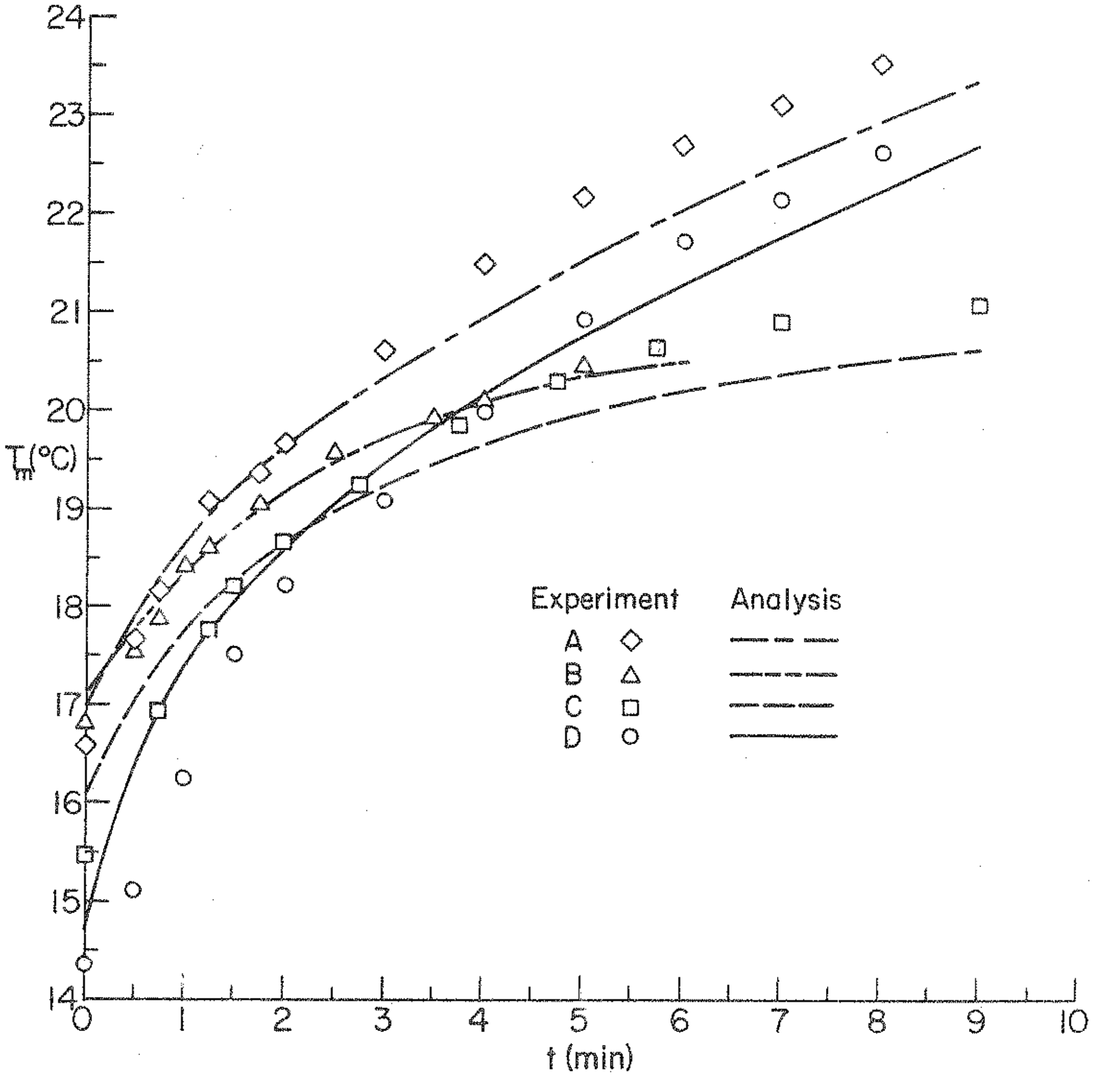

Figure 5.14 Comparison of measured and predicted mixed layer temperatures

experimentally. The agreement between experimental data and the model for both the mixed layer depth and temperature is very good for all experiments. The predictions are consistently higher for both the mixed layer temperature and depth at early times and also higher at later times. This is due to the fact that early in the experiments the turbulence is not yet fully developed, and therefore the model overpredicts the mixed layer height and temperature at early times. Although sufficiently small initial values of dissipation and production were used, the model equations at early times yielded a relatively rapid growth rate for both the dissipation and generation terms, and therefore resulted in overprediction of both the temperature and the depth of the mixed layer.

The relatively rapid initial growth of the dissipation term in the model equations results in a decrease of the total internal energy of the mixed layer which in turn causes a decrease in the time rate of change of the mixed layer temperature predicted by the model, and therefore results in underprediction at longer times (see Figure 5.14). As discussed earlier, the values of the model constants used were established in accordance with the experimental results of Deardorff et al. (1969). However, the experiments of Deardorff et al. were performed in a larger system with uniform initial stratification, but in the present study the stratification was not uniform and several different initial temperature profiles were considered. Use of the constants based on other investigations may partially account for the discrepancy between the model predictions and data.

5.6.3 Model Predictions of Temperature and Effective Viscosity Distributions

Although the K-ε model is more complicated than the simple thermal model developed, it has the advantage of predicting temperature and effective viscosity distributions. A comparison between the measured and predicted temperature distribution for experiment B is illustrated in Figure 5.15. The initial temperature profile used in the model calculations and shown in Figure 5.15 was determined experimentally. The agreement between data and analysis is excellent for all times. In this particular experiment a relatively uniform layer of warm water was overlying the stratified layer (see Figure 5.15). The experimental results indicate that the temperature of this uniform layer of water ($z > 6$ cm) increases slowly as heating continues. However, the model predicts no change in the temperature of this layer with time. This discrepancy can in part be due to modeling of the air-water interface as an insulated one. Within the first few millimeters of the bottom the analysis overpredicts the temperature. This is due to the inadequate modeling of the turbulence near the solid boundary particularly in the thin "conduction" layer a few millimeters in thickness right above the heated surface.

Figure 5.16 shows the predicted dimensionless effective viscosity as a function of depth for experiment B at several different times. No experimental determinations of the effective viscosities were made, but because of the good agreement between the predicted and measured temperature profiles (see Figure 5.15), it is believed that the predicted effective viscosities model the general trends and relative order magnitude of turbulence. As it is clearly evident from this figure, the peaks in the profiles move upward as time goes on. This is due to the growth of the mixed layer. The profiles are not symmetrical about the peak, and they are shifted towards the bottom. The upward heat flux decreases with the depth z, resulting in a small potential for the turbulence driving force at higher z. Therefore, there is a sharp increase in the effective viscosity near the bottom of the layer and the peak is shifted down. After five minutes of heating, the effective viscosity has a maximum value of about 22 at a depth of approximately 3 cm. At this particular time the minimum effective viscosity is 1 (i.e. $\mu_{eff} = \mu_{laminar}$) which occurs at the bottom ($z = 0$) and at a depth of about 7.2 cm. Note that the effective

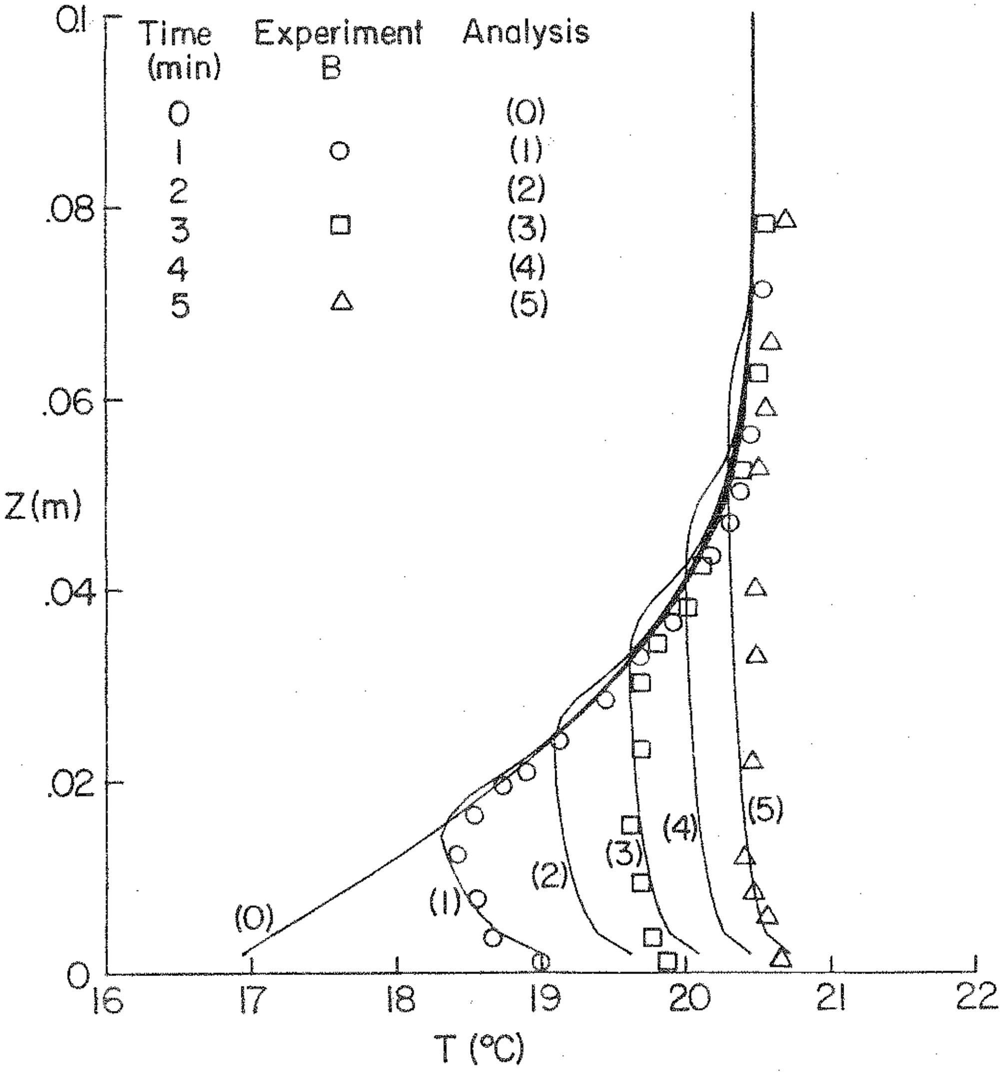

Figure 5.15 Comparison of measured and predicted temperature distributions in the mixed layer during heating from below for Experiment B

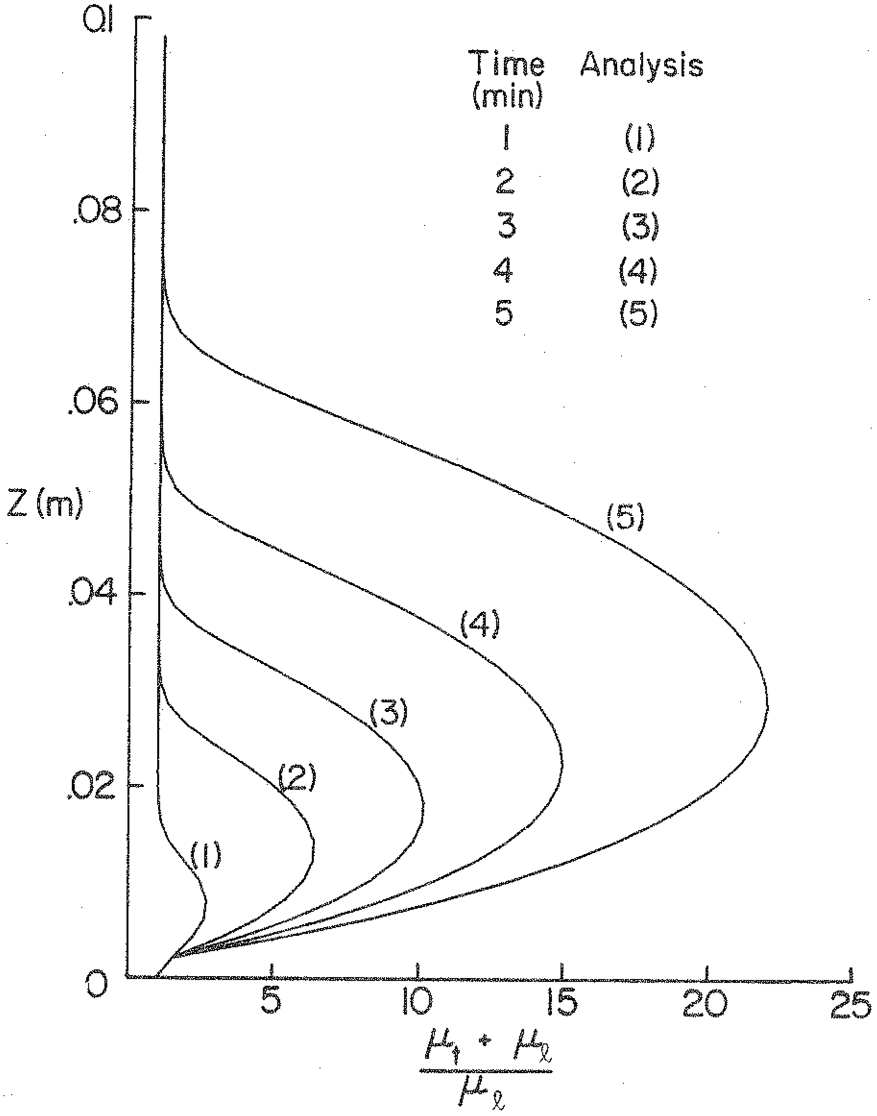

Figure 5.16 Predicted effective viscosity profiles for Experiment B

viscosity is always equal to 1 at the bottom and in the stable layer. The peak in the effective viscosity has increased from 2.5 at t = 1 min to about 22 at t = 5 min, indicating an increase in the level of turbulence of about one order magnitude in four minutes.

Figure 5.17 shows a comparison between the predicted temperature distribution and experimental data for experiment D. In this particular experiment the initial stratification was more intense than experiment B. The depth of the layer was also larger than in experiment B. The model predicts a clear "over-shoot" right above the mixed layer which has been observed and discussed by Deardorff et al. (1969) and in Section 5.2. The magnitude of the "over-shoot" increases as the heating continues.

Figure 5.18 presents the predicted effective viscosity profiles for experiment D and indicates a maximum value of 60 at t = 5 min. This is about 2-5 times higher than the value predicted for experiment B. This large difference between the predicted values for the two experiments is due to the larger bottom heat flux for experiment D. This finding indicates that the initial stratification of fluid is an important factor in modeling turbulence in buoyancy-driven flows.

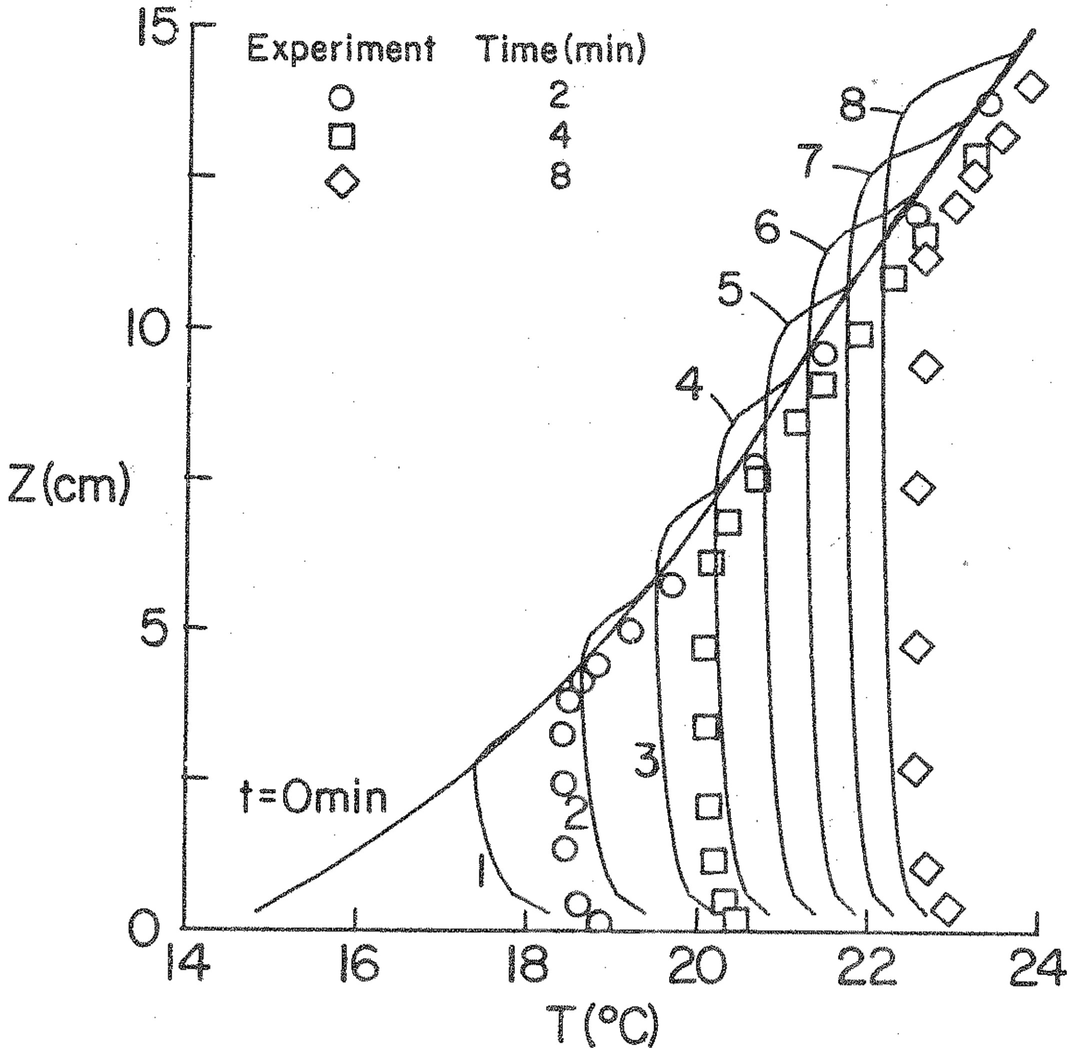

Figure 5.17 Comparison of measured and predicted temperature distributions in the mixed layer for Experiment D during heating from below

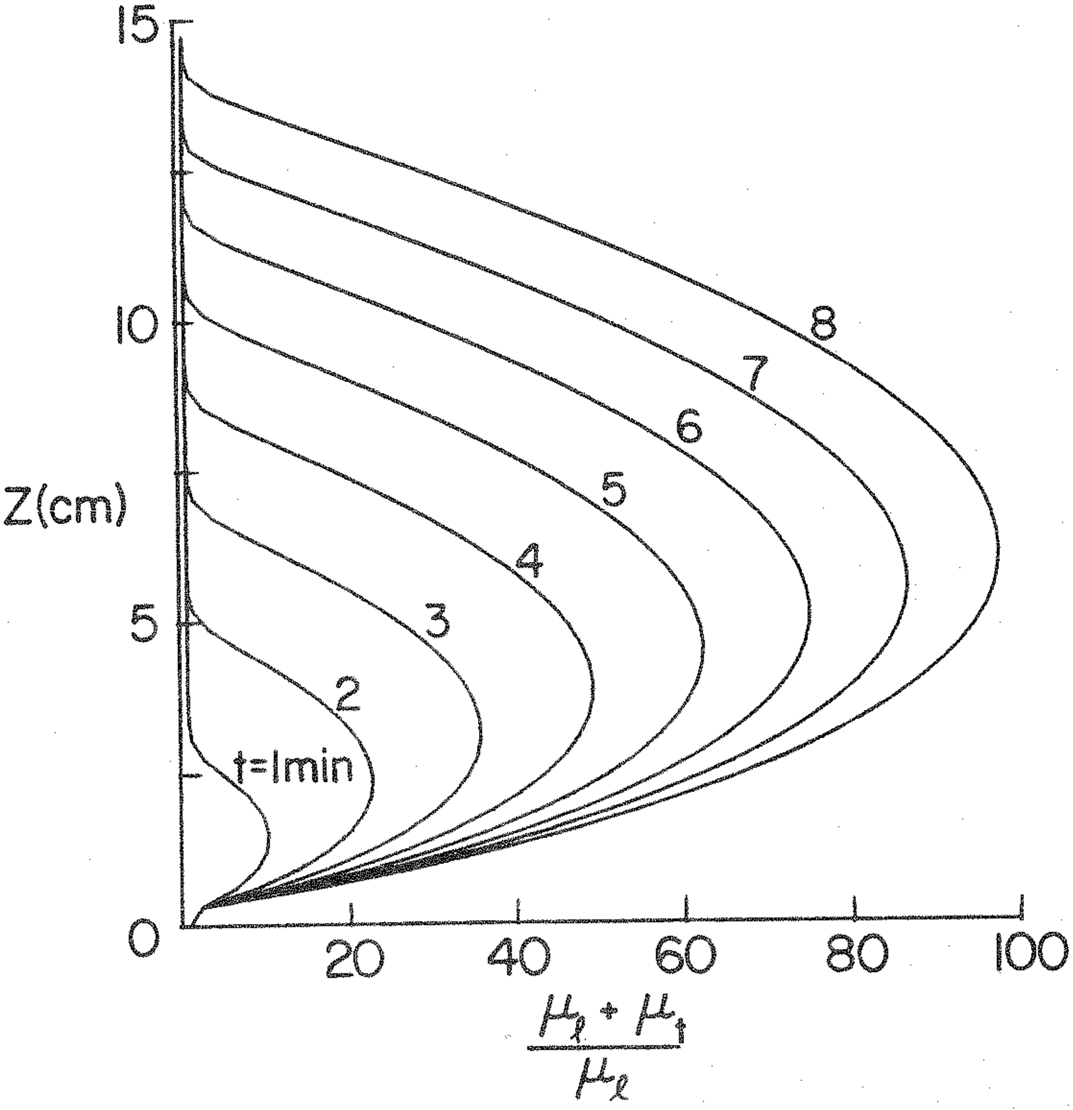

Figure 5.18 Predicted dimensionless effective viscosity profiles for Experiment D

6. HEATING AND/OR COOLING OF THERMALLY STRATIFIED LAYER OF WATER IN THE PRESENCE OF SURFACE SHEAR

6.1 Introduction

The temperature structure in a large body of water is determined by several different transport mechanisms. A detailed discussion of different processes controlling the thermal structure in water has already been given in the previous chapters. In this phase of the investigation internal energy and flow processes during transient heating of a thermally stratified layer of water by radiation and cooling by forced air flow over the water surface was studied. Controlled laboratory experiments were performed to determine the flow and detailed temperature structure in the surface layers of water due to simultaneous long-range heating and/or cooling with imposed shear at the interface.

The air channel was used to impose wind stress at the air-water interface. Both the interferometer and thermocouples were utilized to visualize and measure the unsteady temperature profile during cooling and/or heating by radiation of a thermally stratified layer of water. Several flow visualization techniques were adopted to visualize the flow field during the experiments. A mathematical model discussed in Chapter 3 is employed to predict the turbulent quantities and temperature distributions in the layer. The utility of the model is established by comparing the predictions with experimental data.

For ease of reference a summary of the typical experiments performed is listed in Table 6.1. Only a few of the experiments will be discussed in some detail, while the others will be only highlighted for the sake of brevity.

Table 6.1 Summary of some experiments performed

Experiment No.	Initial Temper-ature (°C)	Ambient Temper-ature (°C)	Center-line air speed (m/s)	Relative Humidity (%)	Heating Period Start Time (min)	Heating Period End Time (min)	Cooling Period Start Time (min)	Cooling Period End Time (min)	F_{inc} (W/m^2)	Remarks
I	24.0	23.3	4.8	67	-	-	0	17	-	Dye visualization
II	23.5	22.0	5.4	70	-	-	0	15	-	Dye visualization
III	23.25	22.2	3.8	71	0	40	40	67	845	Dye visualization
IV	22.0	22.1	4.8	73	0	30	30	55	2700	Dye visualization
V	23.5	22.0	3.8	65	-	-	0	20	-	Fish scales
VI	20.2	18.1	3.8	67	0	20	20	50	2540	Fish scales
VII	19.0	18.0	4.8	65	0,20	10,23	10	45	2370	Restratification
VIII	30.1	20.1	3.8	68	-	-	0	22	-	Shadowgraph
IX	28.0	18.9	4.8	60	-	-	0	23	-	Interferometer
X	28.1	20.0	4.8	65	-	-	0	17	-	Shadowgraph
XI	18.9	21.1	4.8	65	0,60	30,75	30	90	2370	Restratification
XII	17.3	18.9	4.8	64	0	40	0	60	2030	Intense heating
XIII	17.0	19.0	4.8	56	0	60	0	70	730	"Mild" heating
XIV	33.0	20.6	4.8	56	0	40	0	60	2200	Cooling continued

6.2 Experimental Procedure

All the experiments were performed with test cell B. Because of the special design of the air channel test cell it was not possible to mechanically clean the test cell. Therefore, it was flushed with distilled water several times before each experiment. Then it was filled with distilled water, covered, and left undisturbed for some time to eliminate all convective currents which are normally present and to attain a uniform ambient temperature. In some experiments the water was first heated by electric immersible heaters to a temperature above the ambient, mechanically stirred, and then pumped into the test cell. After it had been determined that all the convective motion in the tank was settled, the interferometer was adjusted to an infinite fringe.

A thermistor located about 1 cm below the water surface was used to detect temperature fluctuations in the vicinity of the surface. The thermistor bridge was nulled after the interferometer was aligned to an infinite fringe. Then, depending on the experiment, either the blower or the radiant heaters or both were adjusted to the desired setting and turned on. The top of the air channel test section which was made of 6 mm thick float glass acted as a filter for the radiation emitted by the heaters. In some experiments a stack of 12 sheets of glass was placed on top of the test cell before the heating was initiated.

During each experiment, at prescribed time intervals, the interference fringe patterns were photographed and the thermocouple emf readings were simultaneously recorded. The Graflex camera with Polaroid positive-negative film was used for the photography.

In the flow visualization experiments with the dye technique, an electronic flash was placed behind the test cell with the Bronica camera in front of it, and therefore it was not possible to use the interferometer during the flow visualization. The dye was injected constantly with a hypodermic needle from a syringe reservoir in which the level of dye was kept constant for a uniform flow through the needles. The exit velocity of the dye from the needles was adjusted to correspond to the velocity of water in the vicinity of the needle tips by varying the height of the dye level above the dye injectors. For high contrast photography a yellow filter was placed in front of the camera lens.

In the flow visualization experiments with the "fish scales" an 8 cm^3 of the Rheoscopic solution was injected through the water inlet of the test cell while the tank was being filled. After it was visually observed that the currents in the test cell were absent the multiple mirror scanner was started with the laser beam shining right at it. The photographs in these experiments were recorded by the Bronica camera on very fast film. Again, because of the experimental setup of the visualization technique, it was not possible to perform experiments in which both the interferometer and flow visualization technique could be employed simultaneously.

6.3 Qualitative Flow and Temperature Observations

In this section some observational data from the flow visualization experiments are presented, and some interferograms recorded during experiments are also discussed.

6.3.1 Dye Technique Observations

The Blue-Black dye technique described in Chapter 2 was used to visualize the flow. The dye was injected into the test cell by three hypodermic needles from a dye reservoir with a relatively constant head. Two series of dye visualization experiments under different conditions were performed, see Table 6.1. In both series air was forced over the water surface and the dye injected into the test cell. The trace of the dye was photographed at prescribed time intervals. Figure 6.1 shows several photographs of the dye streak during an experiment with an initially uniform temperature layer of water. In these photographs the distance between two large ticks on the scale shown is 2 cm, and the direction of the air flow

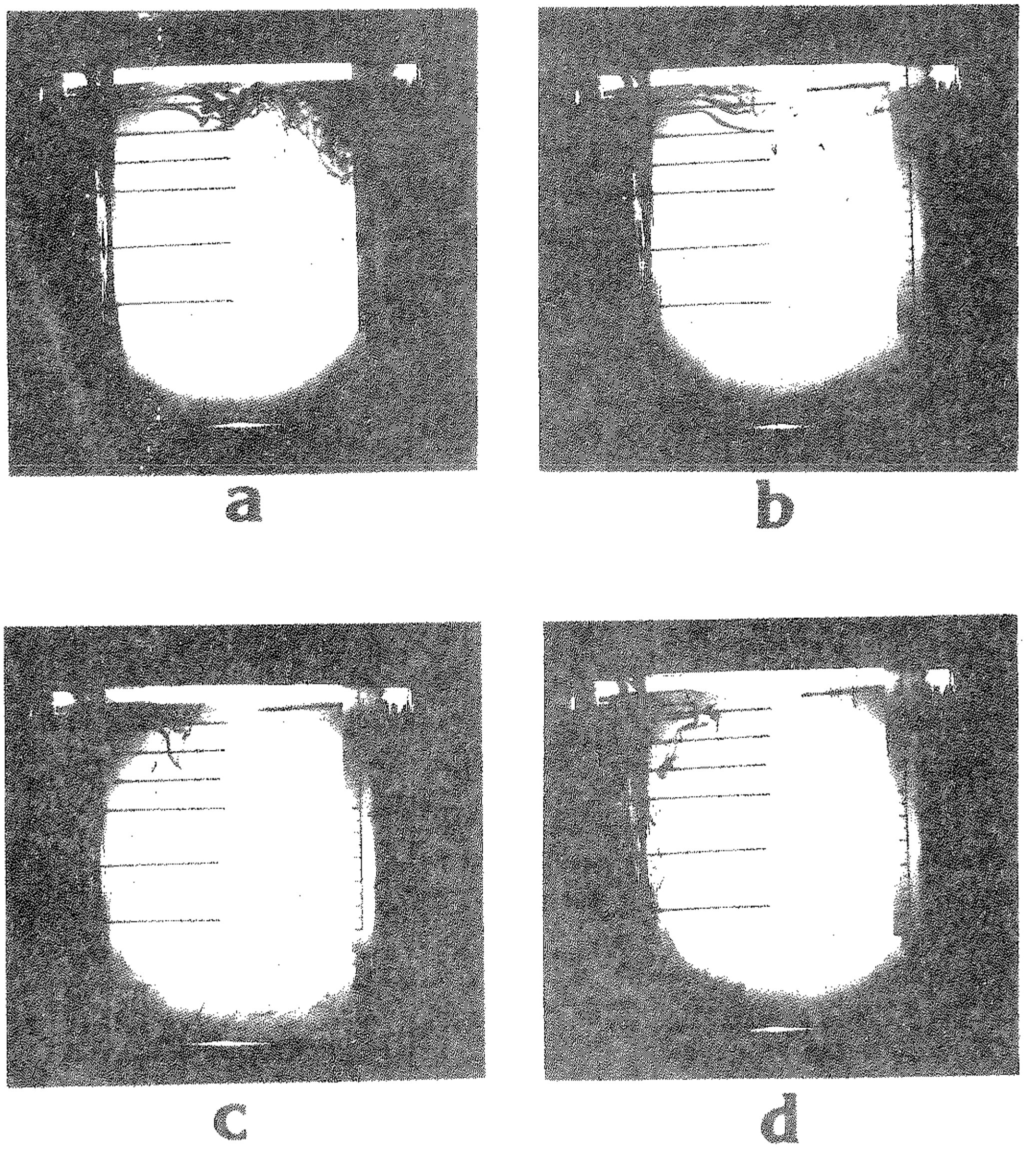

Figure 6.1 Photographs of dye visualization during cooling of an initially uniform layer of water (Experiment II): (a) t = 3 min, (b) t = 7 min, (c) t = 10 min, (d) t = 13 min, see Table 6.1 for conditions

over the water surface is from left to right. The results of this and several other experiments (e.g. Experiments No. I and No. V) indicated that the flow patterns are very complex. It was observed that initally the dye streaks from the needles were stretched and started to accelerate toward the upper right hand corner of the test cell and then turned downwards toward the bottom the cell. The downward moving dye indicates that the flow was decelerating. Upon reaching the bottom the dye turned upwards toward the middle of the tank, see Figures 6.1a and 6.1b.

The flow field indicated formation of a circulation pattern in the lower right and left hand sides of the tank. The continuous injection of the dye into the test cell at later times made it difficult to recognize and record the flow patterns; however, the overall flow field indicated four different circulation regions. The main circulation region which filled most of the tank was located in the upper right hand side of the cell, which as expected was due to acceleration of the flow to the right resulting from the imposed surface shear. In the bottom of the tank two circulation cells, one at the right and the other at the left hand corners were typical of those occurring in a corner. At the upper left hand side the acceleration of the upward moving flow that is turned around by the water surface, another circulation cell is developed. This is clearly indicated in photograph 6.1d by the dye streak moving towards the left wall.

An analytical study of circulation currents in a wind driven cavity has been reported by Oberkampf and Crow (1976). The unsteady, two-dimensional momentum and energy equations for laminar flow have been solved using a finite difference method. Although the thermistor output and the break-up of the dye indicates that the flow is turbulent, the laminar flow situation studied by Oberkampf and Crow is expected to have the same overall features. For this reason the computer program developed by Oberkampf and Crow (1976) was modified and the steady state solution was obtained for the test cell geometry. For a wind velocity of 5.4 m/s (centerline velocity of the air channel) the steady state streamlines are presented in Figure 6.2. In this figure the wind direction is from left to right. These results, although for a laminar flow at steady state, bear much similarity to the observations of the dye flow visualization.

The voltage output of the thermistor located about 1 cm below the water surface (see at the upper right hand side of the photographs in Figure 6.1) was recorded on a strip chart. During the experiment with an initially uniform and quiescent layer of water after the air was forced over the surface, the strip chart output indicated temperature fluctuations at the location of the thermistor. This suggested that the cooling of water at the surface by longwave radiation, forced convection, and evaporation generated parcels of denser water which plunged into the underlying layer in the form of thermal plumes. The thermistor output showed no fixed temporal frequency of plume departure. For the experiment discussed in Figure 6.1 it was found that the amplitude of the fluctuations was about 0.2°C which indicated that the mean temperature of a plume was 0.2°C lower than the bulk of the surrounding fluid in the vicinity of the thermistor. The plume activity died out after a few minutes of cooling. This was due to decrease in the temperature difference between the surface and the bulk fluid and was evidenced by the *emf* output of the thermocouples located in the water. A sample of the strip chart will be presented and discussed later in this chapter.

In another series of experiments (Experiment Nos. III and IV) in which the dye technique was adopted an initially uniform layer of water was thermally stratified in the absence of air flow over the water. After the desired degree of stratification was reached, the heaters were turned off and air was circulated in the channel, with the simultaneous injection of the dye. Typical photographs made during the experiment are presented in Figure 6.3. Initially, right after the air was blown over the water surface it was observed that the streak of dye from the top needle stretched horizontally and started to move upward. After reaching the right hand side wall

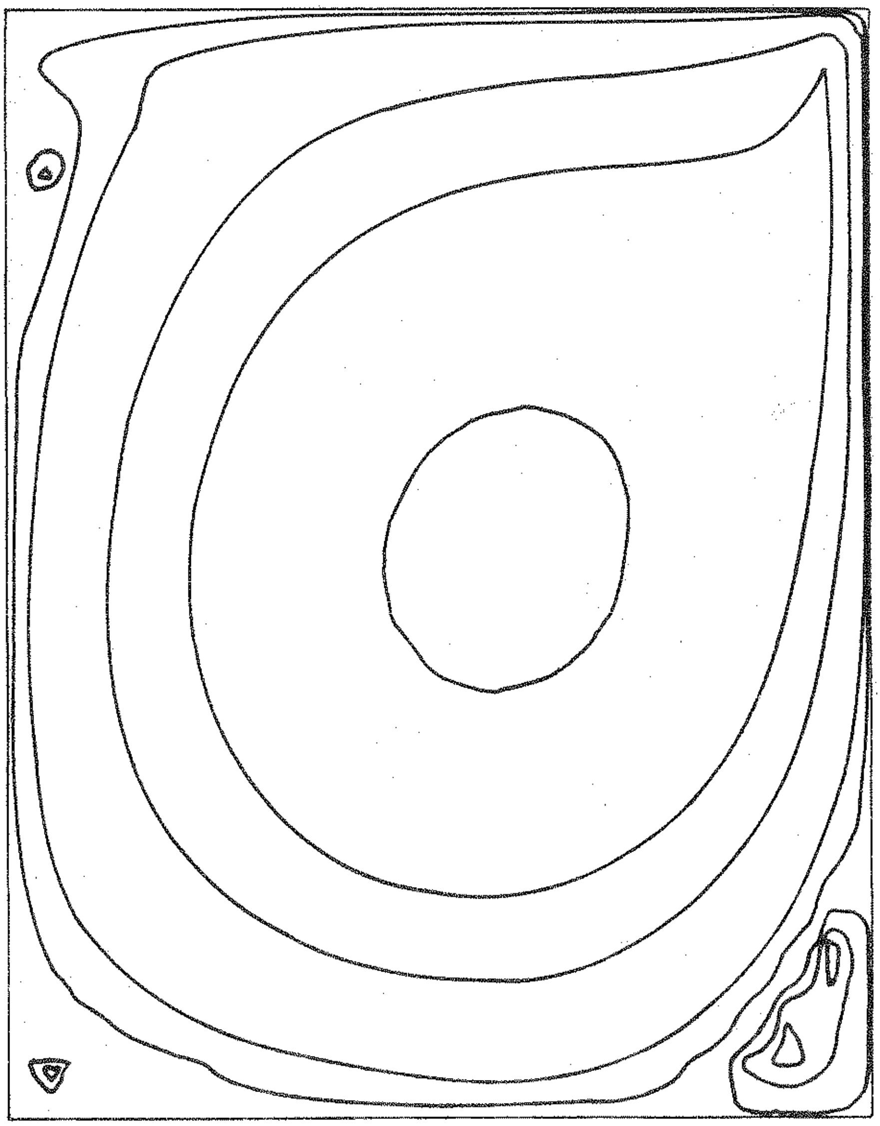

Figure 6.2 Steady state streamlines in a wind driven rectangular cavity, $V_{air} = 5.4$ m/s

it turned downward; however, the motion of dye was confined to the upper few millimeters of the water layer. The position of dye indicated that right below the surface there existed a well mixed layer which was separated from the underlying region by a contorted interface, see Figure 6.3. As the cooling continued the mixed layer grew at the expense of the stably stratified region below it. The stable stratification in the underlying layer caused a resistance to the flow, and, therefore, the flow field was well confined. It was observed that the flow circulation in the mixed layer was in a form of small cells. This is clearly evidenced by the position of the dye at the tip of the injectors in photograph 6.3b. The entrainment of warmer water from the stable into the mixed layer causes the contorted shape of the interface between the two layers. Also, as it is observed from Figure 6.3 the dye from the mixed layer penetrates the underlying layer in the form of parcels of water bombarding this interface. This was also indicated by the output of the thermistor which confirmed the small scale circulation patterns and the plume activities in the mixed layer.

The observations during the experiments performed with the dye technique confirmed that this method can only be adopted to visualize the main features of the flow. Because of the constant injection of dye into the test cell and its mixing with water, it became difficult to trace a streak of dye at later times as a result of the continuous decrease in the relative contrast of the dye. However, initially the high contrast of the dye yields useful information about the flow field which can be easily photographed.

6.3.2 "Fish Scale" Tracer Observations

The fish scale tracer technique discussed in Chapter 2 was also employed for flow visualization during similar experiments (Experiment Nos. V, VI and VII) to those discussed previously. The main features of the flow field were described in the previous subsection; therefore, the results of the fish scale technique will be presented

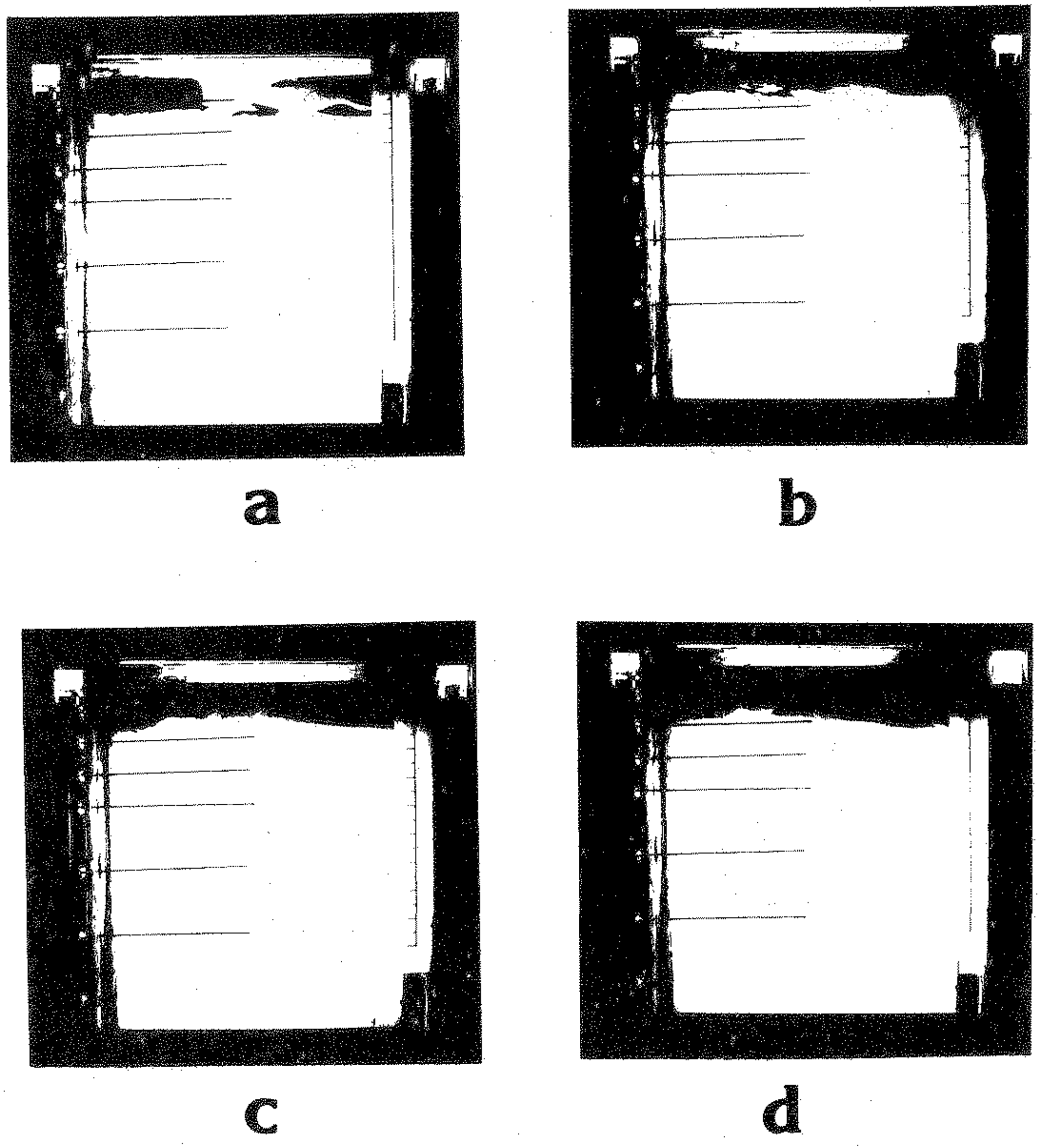

Figure 6.3 Photographs of dye visualization during cooling of a thermally stratified layer of water (Experiment IV, see Table 6.1 for conditions): (a) t = 39 min, (b) 43 min, (c) 47 min, (d) 55 min

without discussing in detail the main features of the flow field. Photographs of flow field in an initially uniform layer of water subjected to cooling and surface shear are shown in Figure 6.4. From these photographs it is clearly evident that there are two main regimes of flow. Figures 6.4a and 6.4b indicate that at early times the circulation patterns in the test cell have not yet penetrated to the bottom. It is seen from Figure 6.4d that the flow turns downward near the right hand side wall and that there is a relatively small cell in the lower right hand corner of the tank. This is also observed from Figure 6.4c which shows the fluid moving upward in the right cell towards the middle of the tank. A small circulation cell in the left bottom corner was also observed. In the vicinity of the surface plumes were seen to depart the air-water interface, e.g., Figure 6.4.

Selected photographs of flow pattern produced by fish scales during an experiment with initially thermally stratified layer of water are shown in Figure 6.5. In this particular experiment a uniform layer of water was thermally stratified by the radiant heaters in the absence of forced air flow over the water surface. After the heating was terminated the flow of air over the surface was initiated and continued for 20 minutes to establish mixing. At this time the heaters were again turned on to observe the effect of restratification of a layer of water undergoing mixing. Photographs 6.5a and 6.5b show the cooling phase of the experiment while Figures 6.5c and 6.5d were recorded during the restratification cycle. The photographs clearly indicate that there are two flow regions. In the upper region there exists intense mixing in the layer (see Photographs 6.5a and 6.5b) confined between the surface and the stratified region which resists the downward motion of the mixed layer. The interface between the two layers is contorted (non-planar) which can be distinguished in the photographs. The circulation in the mixed layer is made clear by the alignment of the tracer particles with the roll patterns (see Figure 6.5).

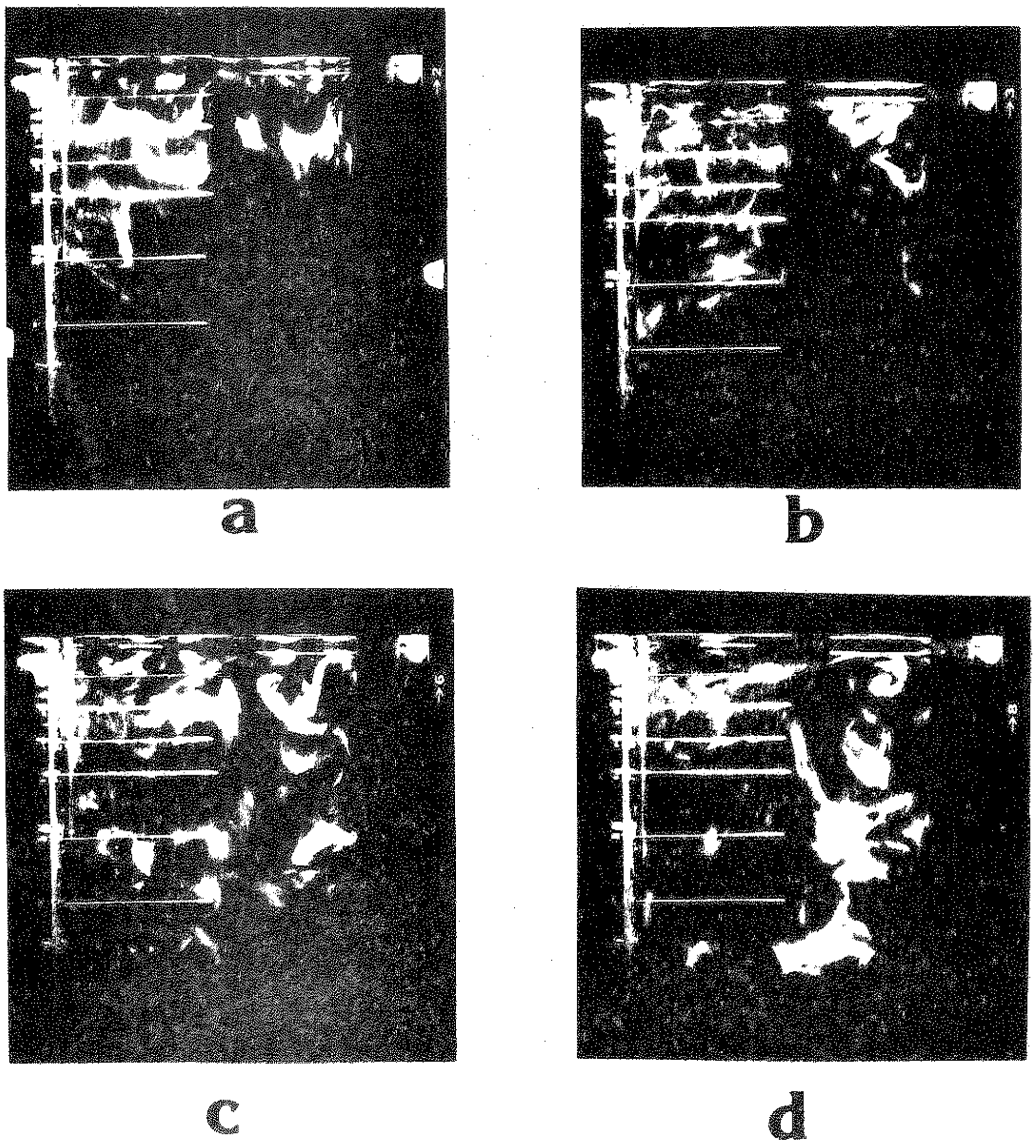

Figure 6.4 Photographs of "fish scales" visualization during cooling of a uniform layer of water (Experiment V, see Table 6.1 for conditions): (a) $t = 2$ min, (b) 3 min, (c) 7 min, (d) 10 min

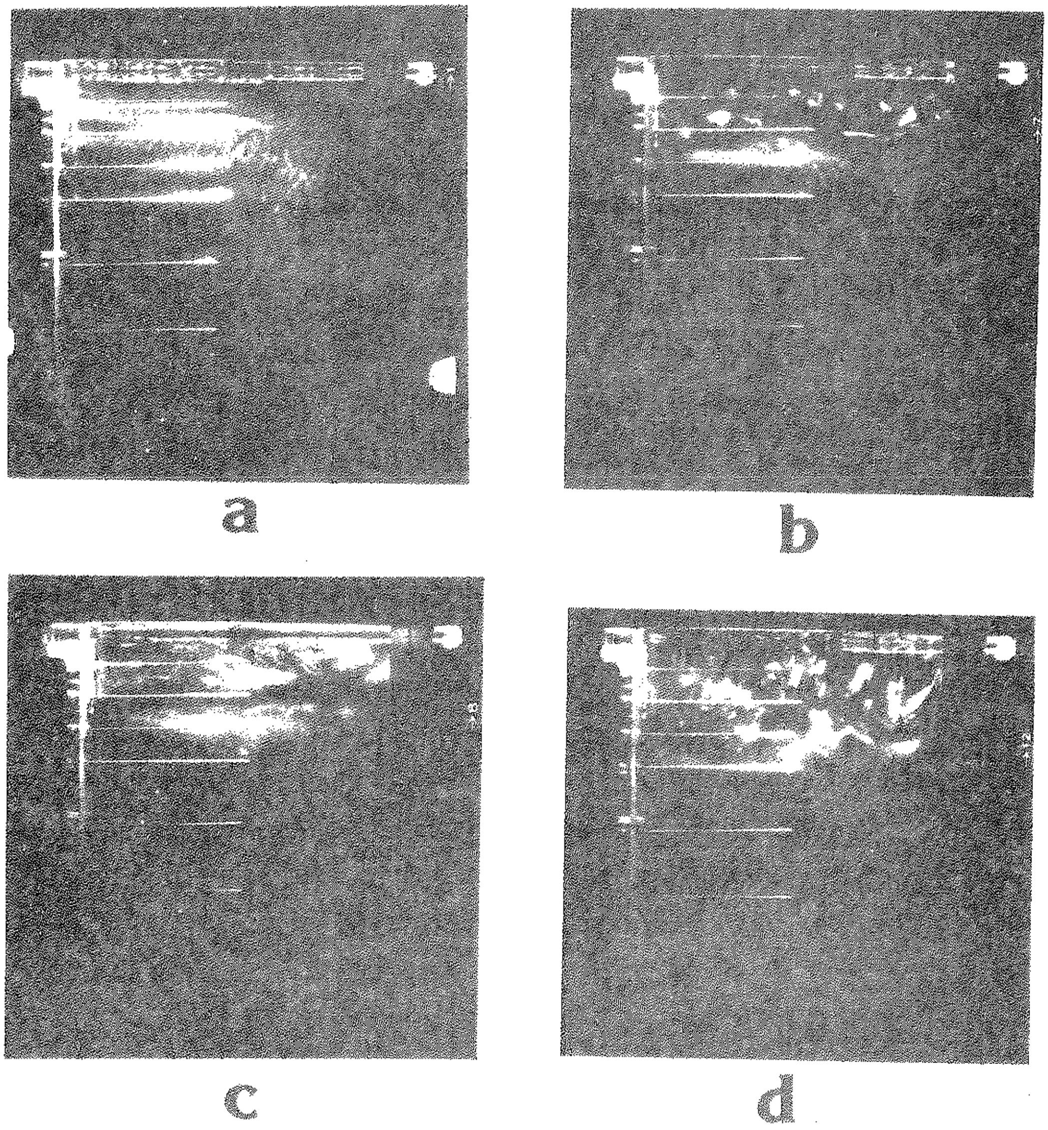

Figure 6.5 Photographs of "fish scales" visualization during cooling and restratification of a stratified layer of water (Experiment VII, see Table 6.1 for conditions): (a) t = 11.5 min, (b) 30 min, (c) 32 min, (d) 45 min

Photograph 6.5c was taken 2 minutes after the restratification was initiated. Although at this point in time mixing has not been completely suppressed by radiant heating, a comparison with Photograph 6.5b indicates that the stratification has a strong dampening effect on the circulation and that the roll pattern has already disappeared. A photograph recorded after about 3 minutes of restratification (not shown here) indicated that the flow was completely suppressed and the mixed layer disappeared. However, it should be noted that the water surface was still exposed to a forced air stream. At this time (after 3 minutes of restratification) the radiant heaters were turned off and the cooling of the surface continued with establishment of the same flow pattern and mixing as before (see Figure 6.5d).

A strip chart recording of the thermistor output provided evidence of plume activities near the surface in the first phase of the experiment. However, only several seconds after the radiant heaters were turned on the plume activities died out and thermistor output indicated a gradual increase in the temperature of the water in the vicinity of the probe. After the restratification was terminated and cooling continued thermistor output showed that it took only several seconds for the plume activity to resume. It should be noted that in the experiments discussed here the stack of glass sheets were not used to cut off some of the infrared radiation emitted by the tungsten filament lamps. As a consequence, the relatively high incident radiant flux (see Table 6.1) produced an intense stratification of water near the interface.

6.3.3 Shadowgraph Observations

The shadowgraph technique was also adopted for flow visualization. This was easily accomplished by blocking the reference beam of the interferometer. As discussed earlier, the shadowgraph is an ideal technique for visualization of the flow field resulting from the density differences. In the experiments of cooling of an initially uniform layer of water at ambient temperature the resulting density differences were not easily detectable. Also, because of the averaging effect of the shadowgraph technique along the optical path, the images did not have enough contrast for clear photography. For these reasons, an experiment was performed in which the water was initially preheated to about 10°C above the ambient room temperature and the tank was filled with preheated water. The larger temperature difference between water and air was expected to produce more intense cooling and flow. After the tank was filled with the preheated water, air was circulated in the channel. Several photographs of the shadowgraph images during this particular experiment (Experiment No. X) are shown in Figure 6.6 (photographs correspond to the actual size). During the experiment it was observed that the cooled water from the vicinity of the surface moved downward either in the form of sheets (Photograph 6.6b) or plumes (Photograph 6.6d). The plumes departing the interface did not descend downwards with the sideways motion in the direction of the wind. This was due to the circulation created by the wind shear at the surface. In Photograph 6.6d the plumes are moving down as well as to the right. The shadowgraph image provides conclusive evidence that the flow field is affected by buoyancy.

A strip chart recording of the thermistor output during this particular experiment is presented in Figure 6.7. The figure indicates that there is no fixed temporal frequency. However, the voltage peaks usually occur after a period of damped out fluctuations. The voltage peaks correspond to the downward moving plumes reaching the thermistor and the relatively "flat" voltage regions indicate a sheet of denser water following a plume (see Figure 6.7). The plumes are at times about 1°C cooler than the bulk of the surrounding fluid. The thermistor output can be characterized by a series of voltage "burst" periods followed by "flat" ones. Note that the gradually decreasing voltage level indicates that the local mean temperature of water surrounding the thermistor is decreasing, i.e. cooling of the bulk of the water.

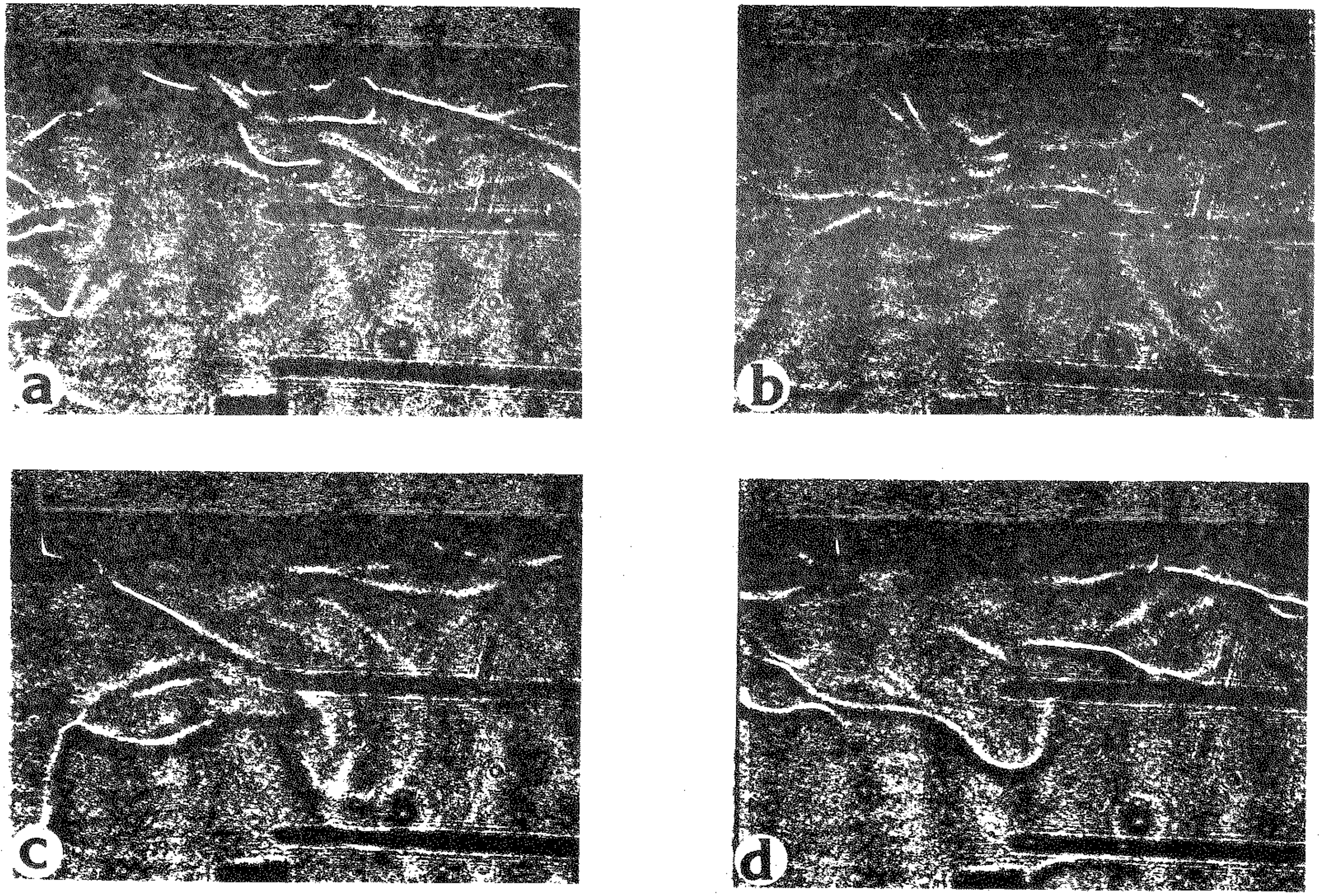

Figure 6.6 Shadowgraphs of a uniform layer of water being cooled from the surface (Experiment X, see Table 6.2 for conditions): (a) t = 5 min, (b) 7 min, (c) 9.5 min, (d) 12.5 min

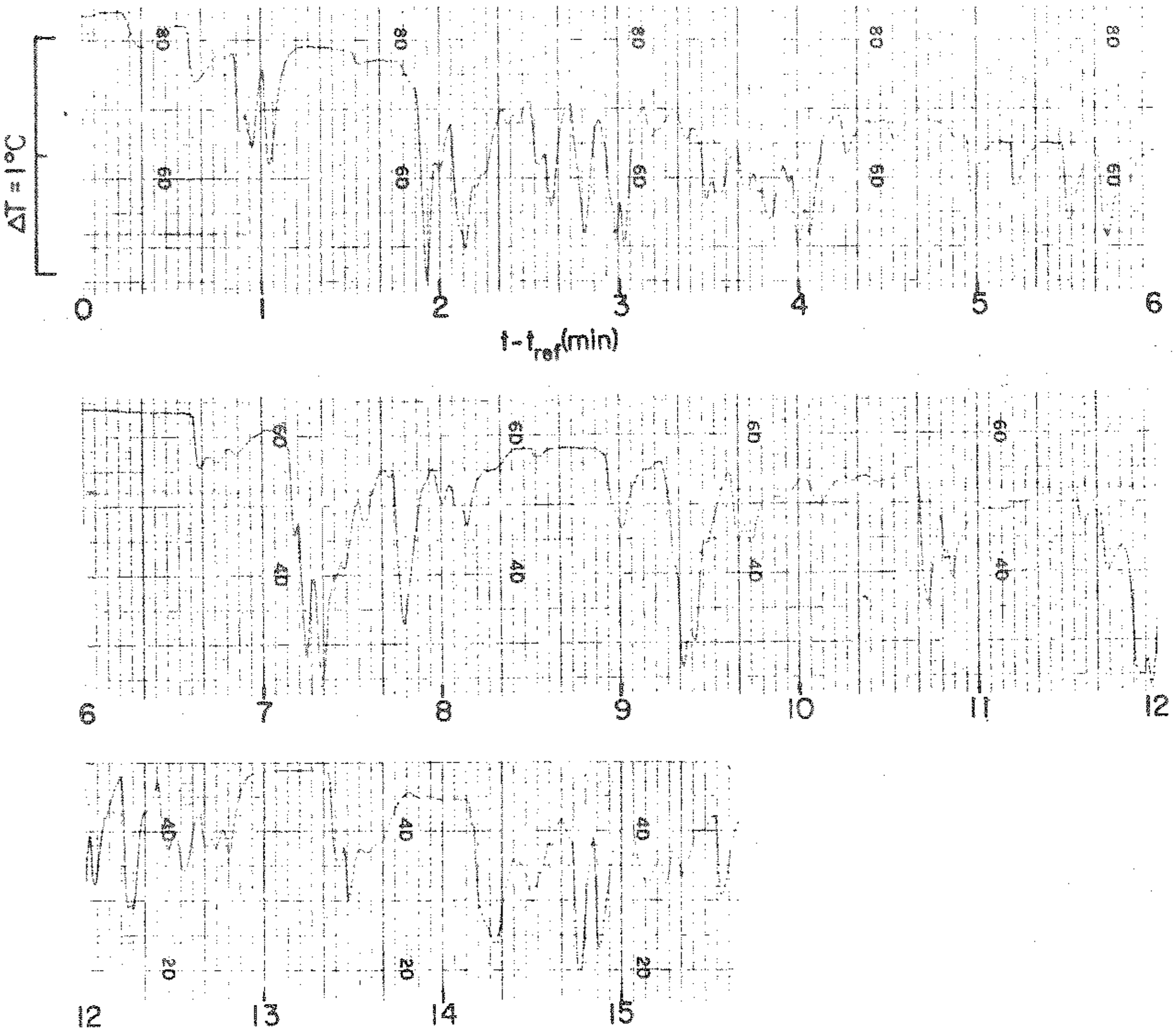

Figure 6.7 Sample strip chart recording of the thermistor output for Experiment X (see Table 6.1)

6.3.4 Interferometric Observations

In this subsection temperature distributions observed interferometrically during some typical experiments will be discussed. Because of the special setup of the flow visualization techniques, it was not possible to employ the interferometer and flow visualization simultaneously. An initially uniform layer of water at 28°C (Experiment No. IX) was cooled from above by forcing air over the surface. Two sample interferograms are presented in Figure 6.8 (photographs are actual size). It is observed that cooling of the surface produces plumes in the vicinity of the interface. The gray area just above the air-water interface is caused by evaporation of water from the surface which obstructs the interferometer beam. The few fringes closely spaced below the interface indicate that the surface is being cooled. Both interferograms indicate that the plumes plunge into the warmer uniform layer of water and after departure plumes are followed by a descending sheet of cool water. This behavior was also substantiated by the output of the thermistor. This is similar to the observations of Viskanta et al. (1975) who studied the cooling of an initially uniform layer of water from above in the absence of air flow over the surface. The plumes did not descend straight down and followed a pattern with a shift in the direction of air flow. Both the emf readings of thermocouples and the thermistor output indicated that the bulk mean temperature of the water continually decreased with time.

In a different experiment (Experiment No. XI) an initially uniform layer of water was thermally stratified by the radiant heaters for 30 minutes. Then the heating was terminated and surface was cooled by circulation of air over it. Three sample interferograms are presented in Figure 6.9 The photographs illustrated are actual size but do not show the entire layer of water. Photograph 6.9a gives evidence of such an intense thermal stratification that the fringes cannot be distinguished in the surface region. This is due to the fact that the stack of glass sheets for reducing a portion

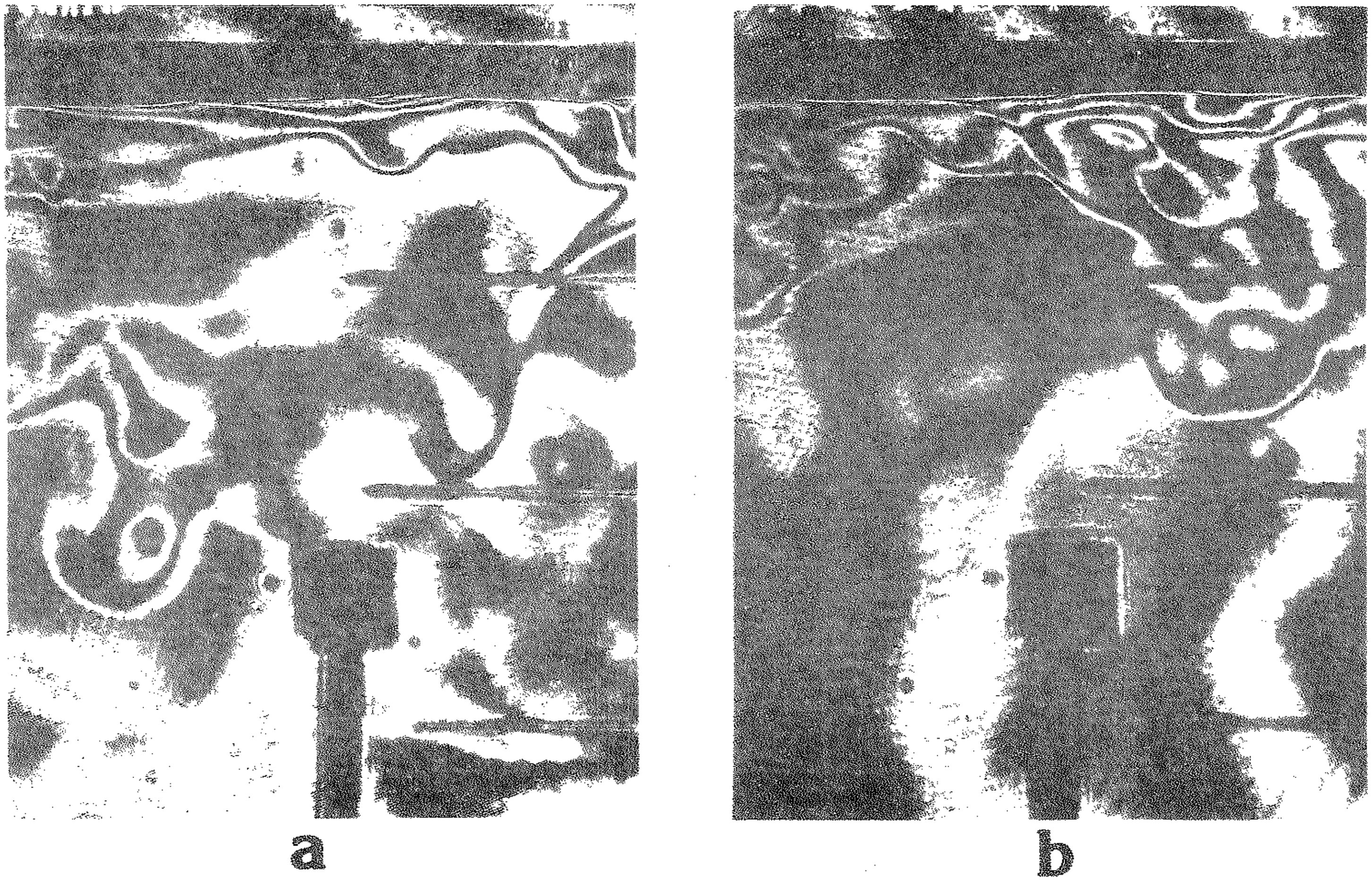

Figure 6.8 Selected interferograms during cooling of a uniform layer of water (Experiment IX, see Table 6.1 for conditions): (a) t = 5 min, (b) 15 min

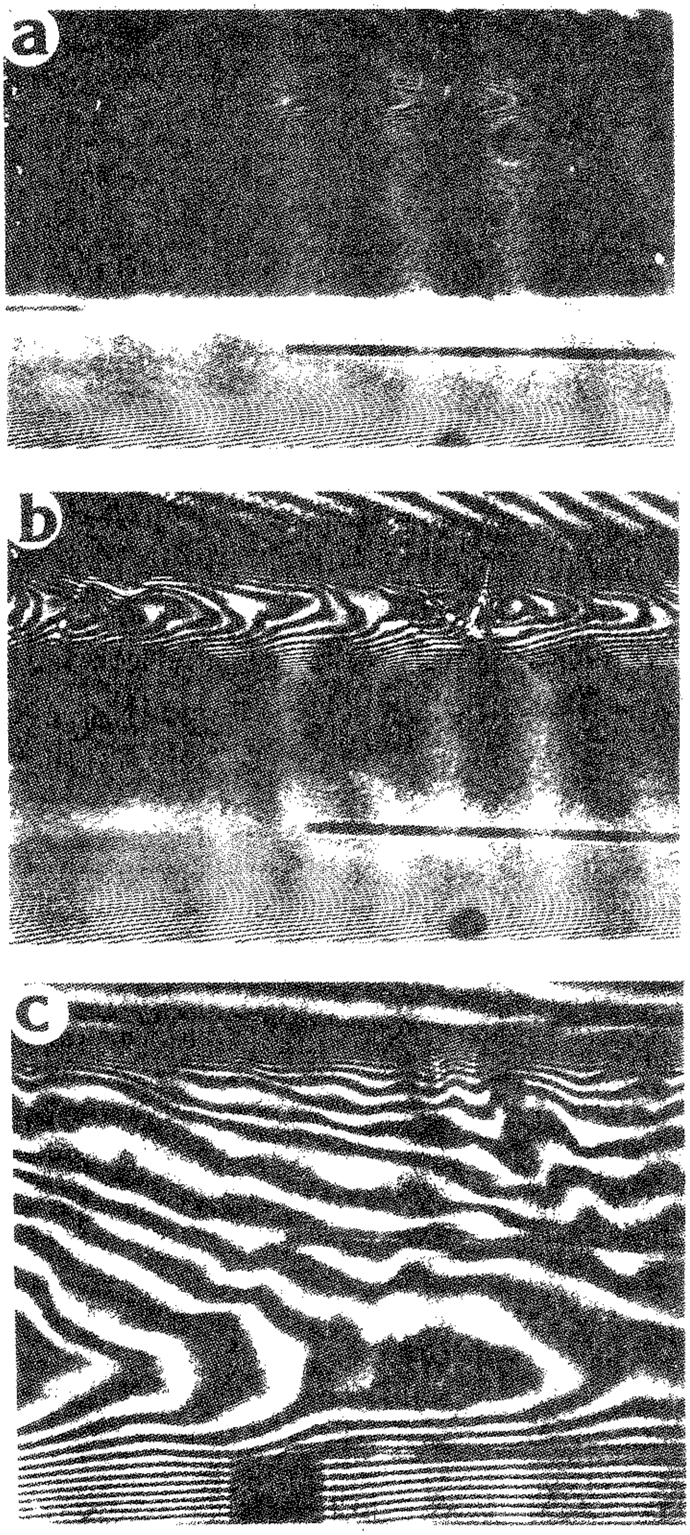

Figure 6.9 Selected interferograms during cooling of a thermally stratified layer (Experiment XI, see Table 6.1 for conditions): (a) t = 30 min, (b) 32 min, (c) 60 min

of the long-wave infrared radiation emitted by the tungsten filament lamps was not used. Photograph 6.9a clearly shows that there exists a temperature reversal a small distance below the interface indicating a net upward heat flux, i.e., the surface is being cooled. Photograph 6.9b illustrates the fringe pattern after 2 minutes from the start of forced cooling. Again, due to the intense evaporation from the surface the air-water interface cannot be clearly identified. The diagonal fringes indicate a temperature gradient in the air above the interface. Right below the interface there exists a thin layer a few millimeters in thickness in which temperature increases with depth implying a net upward heat flux. In this layer the closely spaced fringes are the result of large temperature gradients. Below the surface layer lies a relatively uniform temperature region which grows in thickness with time (see Photographs 6.9b, c). Mixing in this region is primarily induced by mechanical shear and heat losses at the surface. The flow structure in this layer is initially of the roll pattern (Figure 6.9b) which at later times breaks up into irregular motion (Figure 6.9c). This is similar to the flow structure which was observed during cooling from above of thermally stratified water in the absence of air flow over the surface (Behnia and Viskanta, 1979).

Below the mixed layer there exists a stably stratified region in which the temperature gradient is negative, i.e. temperature decreases with depth. As mixing in the layer continues its depth grows at the expense of the stably stratified underlying region. At the interface between the mixed stable layer relatively colder water at the top of the stable layer is entrained into the mixed layer and contributes to its growth. The process was similar to the one described in the previous chapter. During the experiment it was observed that the thickness of the mixed layer was not uniform across the width of the test cell but increased slightly in the direction of the air flow (Figure 6.9c). This was due to the build up of the surface pressure forces in the direction of air flow. This phenomenon has been previously observed by Wu (1977). Photograph 6.9c shows that the interference fringes in the surface and stably stratified layers is spaced further apart than those in Photograph 6.9b. This is due to the decrease in the heat flux at the surface as a result of the decrease with time of the surface temperature caused by the cooling of the mixed layer.

In the particular experiment discussed in Figure 6.9 after 30 minutes from the start of cooling the stratification was resumed and cooling continued. Figure 6.10 illustrates several photographs of the interference fringe pattern during the restratification period. The thermistor output indicated that the temperature fluctuations died out a few seconds after the stratification was reinitiated. Photograph 6.10a shows the fringe patterns after 1 minute of reheating (t = 31 min). Just below the surface layer there exists a temperature reversal indicating that although the body of water is being heated by the radiation from the heaters, the net surface heat flux is negative, i.e. net heat loss at the surface. Thermal stratification of the top of the mixed layer results in the confinement of the mixed layer by two stably stratified regions, both on top and bottom of this layer. Therefore, the fringes are formed in the shape of "S" in this layer which is similar to the temperature profile in the reheating experiments of Viskanta et al. (1977) in the absence of forced air flow over the surface. The "S" shape becomes less and less pronounced as the heating continues (Photograph 6.10b) and eventually disappears as clearly seen in Photograph 6.10c which is recorded a few seconds after the restratification has terminated. The results of this phase of the experiment indicate that the radiant heating of the water plays a very important role on the mixing processes in a layer of water during restratification.

The spectral distribution of solar radiation cannot be realistically simulated in the laboratory; therefore, in order to "cut off" some of the infrared part of the radiation emitted by the tungsten filament lamps in some experiments the stack of glass sheets was placed above the water surface on top of the air channel test section. As a result of this, the rate of thermal stratification of water was

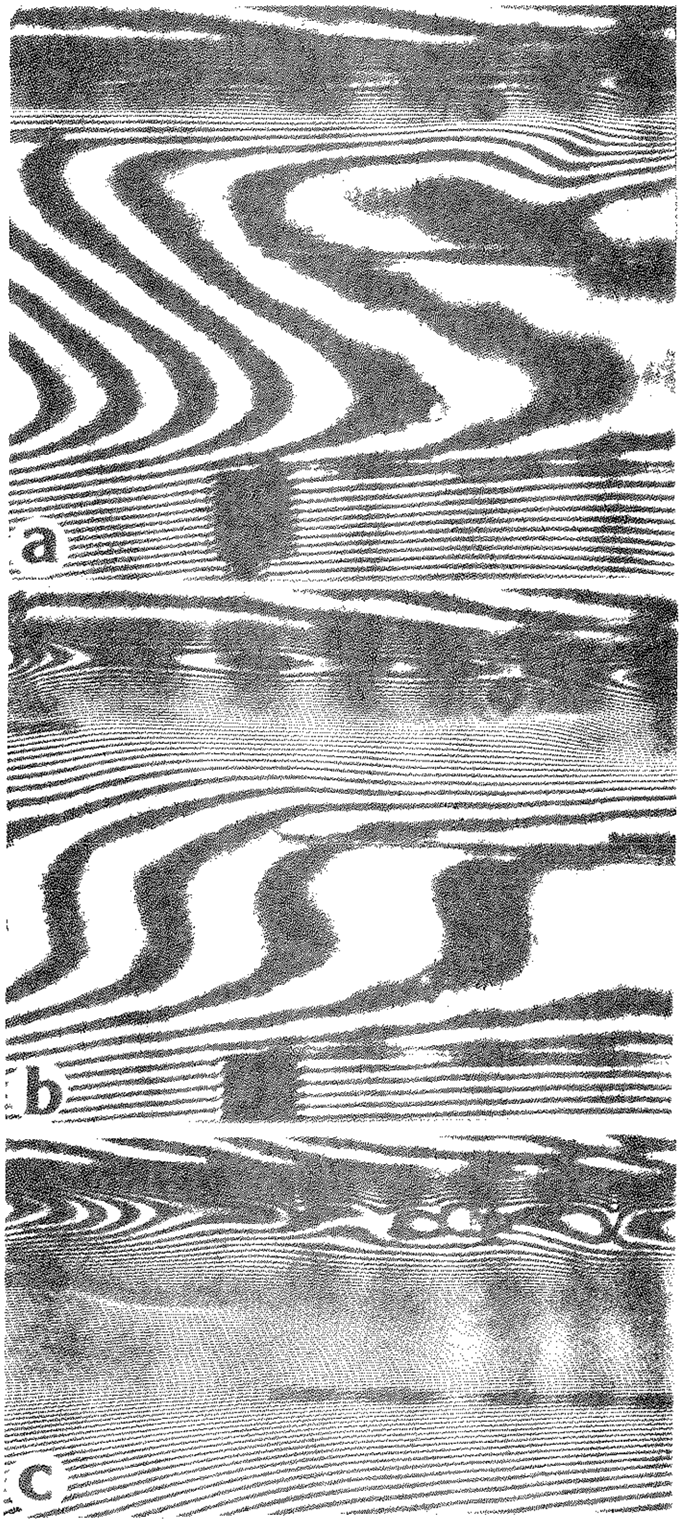

Figure 6.10 Selected interferograms of restratification period in Experiment X (see Table 6.1): (a) t = 61 min, (b) 63 min, (c) 75 min

decreased significantly, especially in the presence of simultaneous cooling of the surface. This required a long period of simulation, which due to the continuous deterioration of the lamps was not feasible. Therefore, most of the simulation experiments were performed without the use of the stack of glass sheets. Figure 6.11 shows two photographs from two similar experiments side by side. Both experiments were performed under simultaneous cooling and thermal stratification. The experimental conditions (Experiment Nos. XII and XIII) were similar, except that Photograph 6.11b belongs to the experiment in which the stack of glass sheets was used. Both photographs were taken after 40 minutes from the start of the stratification. Photograph 6.11a indicates a large degree of thermal stratification while Photograph 6.11b shows a very slight one even after 40 minutes. In both experiments the water was stratified in the presence of simultaneous cooling by forced air flow over the surface.

6.4 Analytical Model Predictions

In this section results obtained with the unsteady, one-dimensional energy-turbulence model are discussed. The emphasis in the sample results presented is on the predictions of turbulence. In order to understand the importance of the various terms and parameters controlling turbulence, a numerical experiment was considered. Figure 6.12 shows the conditions selected for the numerical simulation. The water was assumed to be at an initially uniform temperature of 20°C, and stratification was initiated and continued for 10 minutes in the absence of cooling from the water surface. At $t =$ 10 min the heating was terminated and air was circulated for 10 minutes. Stratification was resumed at $t = 20$ min, with the cooling from the surface continuing.

For this particular numerical simulation the different terms in the K-ϵ model equations, Eqs. (3.22) and (3.23), at $t = 15$ and 25 minutes are plotted in Figures 6.13 and 6.14, respectively.

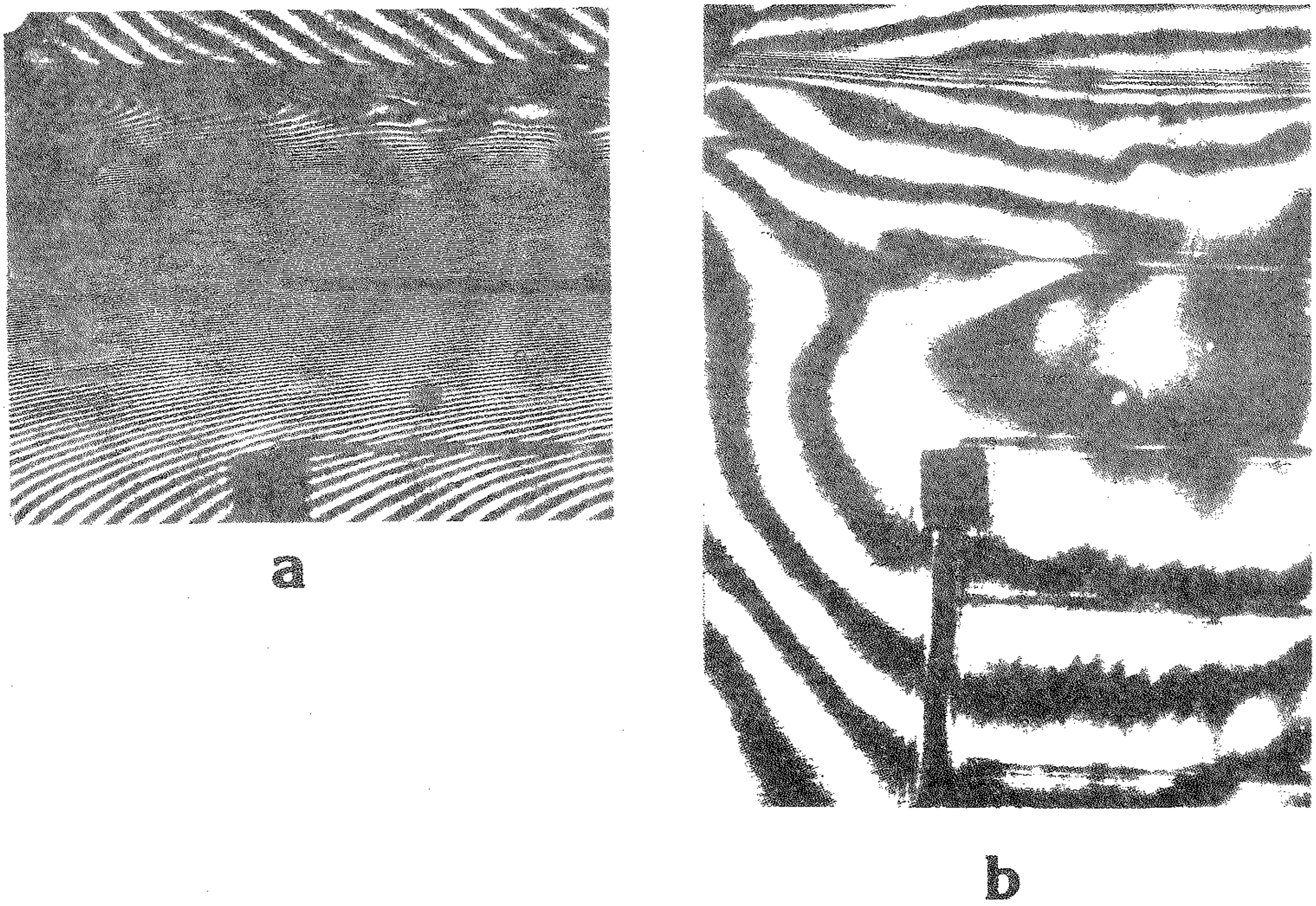

Figure 6.11 Comparison of interferograms for two experiments with different radiant heating conditions (t = 40 min): (a) Experiment XII, (b) Experiment XIII

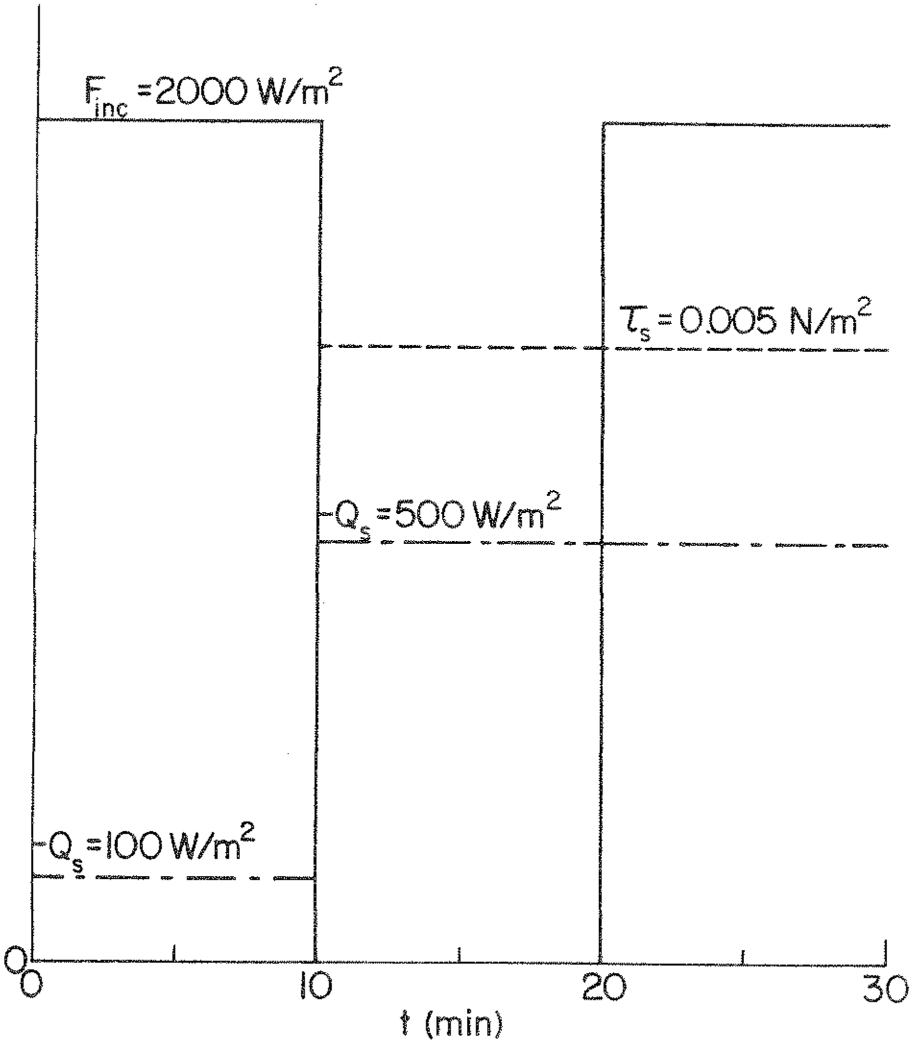

Figure 6.12 Conditions for the numerical experiment

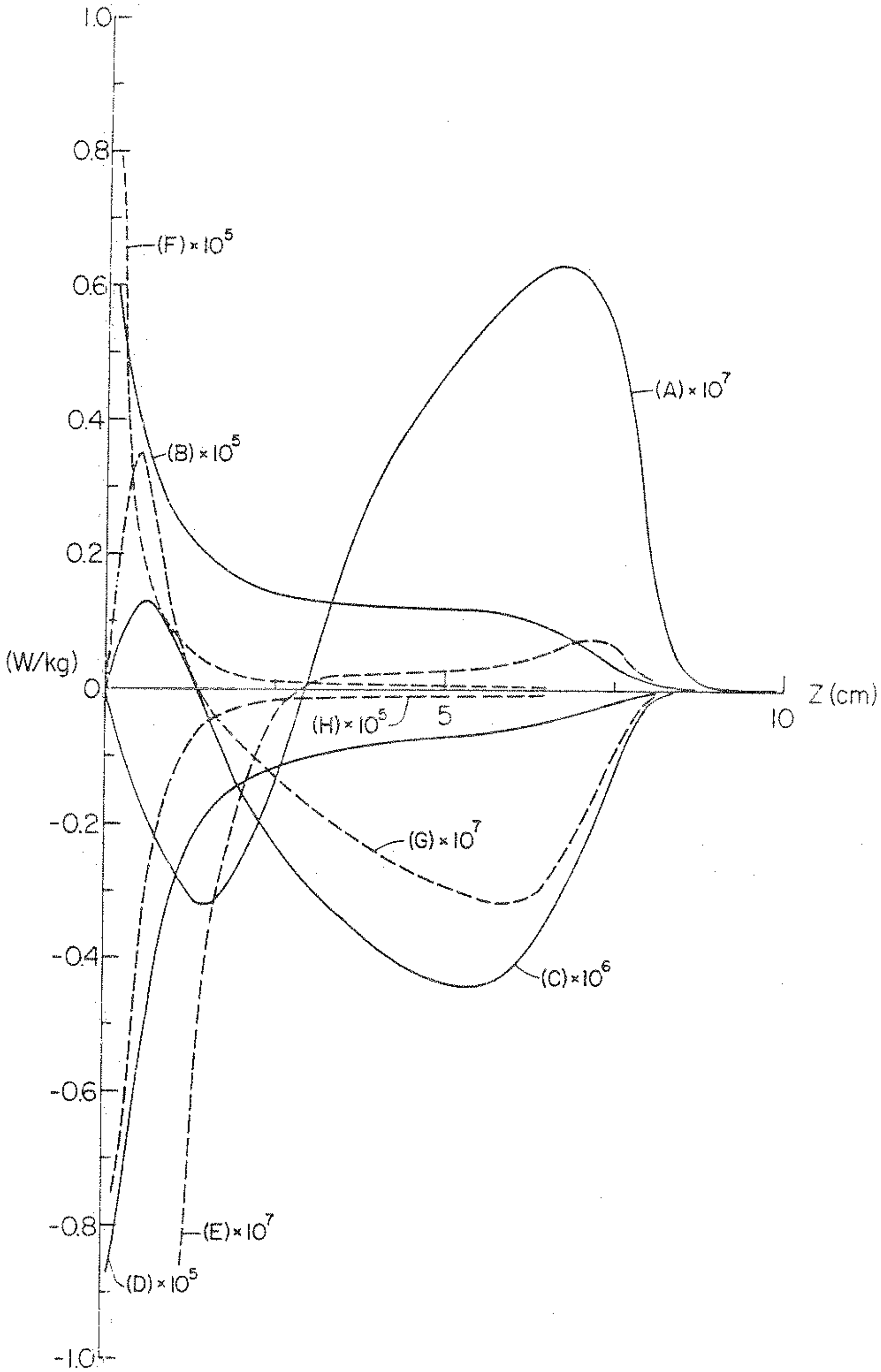

Figure 6.13 Predicted turbulent terms at t = 15 min (see Figure 6.12 and Table 6.2 for conditions and definition of terms)

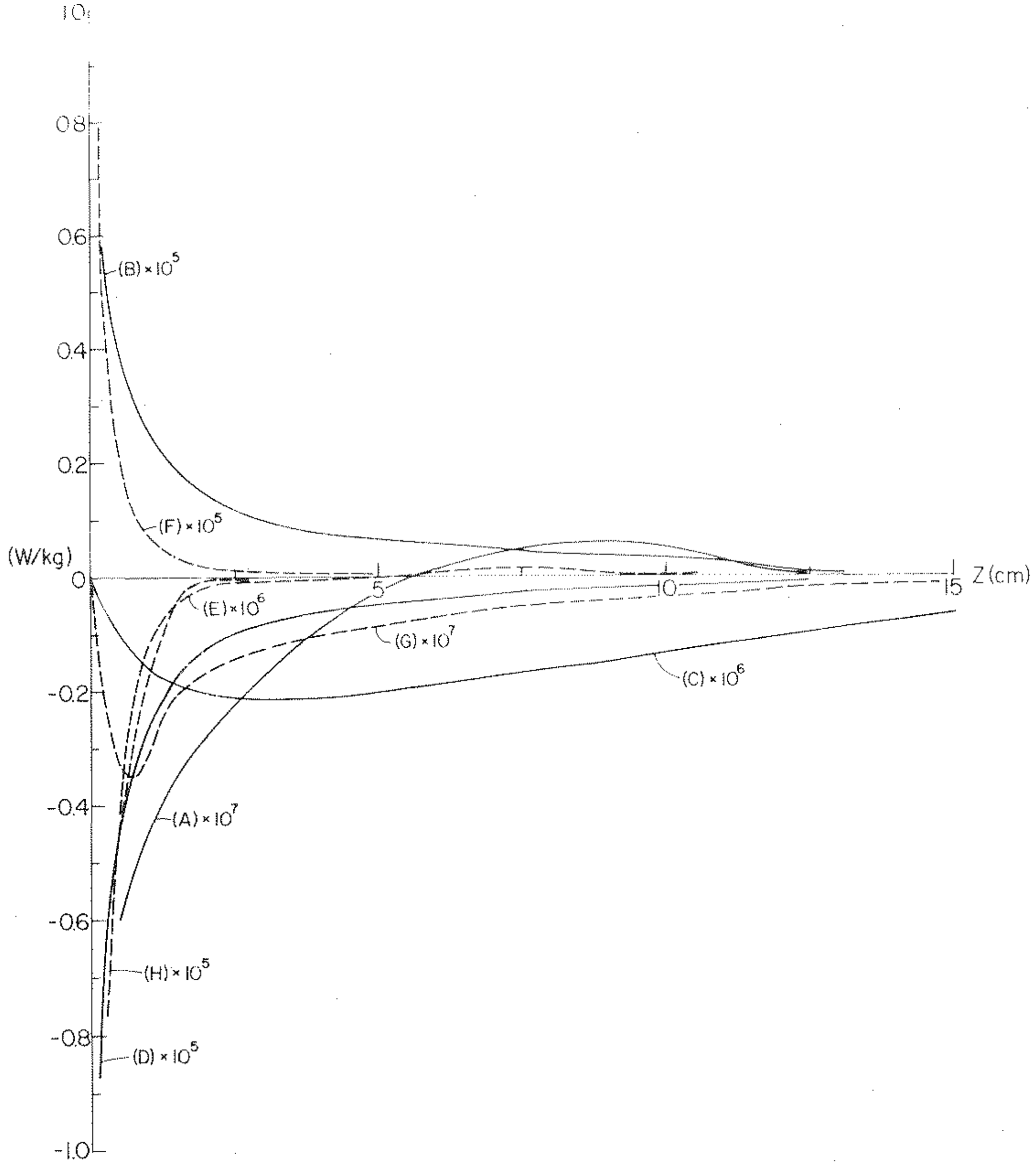

Figure 6.14 Predicted turbulent terms at t = 25 min (see Figure 6.12 and Table 6.2 for conditions and definition of terms)

Definitions of the quantities plotted in the figures are given in Table 6.2.

Table 6.2 Definitions of turbulence quantities plotted in Figure 6.13 and 6.14, see Eqs. (3.22) and (3.23)

(A)	$\frac{1}{\rho}\frac{\partial}{\partial z}(\frac{\mu_{eff}}{\sigma_K}\frac{\partial K}{\partial z})$
(B)	$\frac{\mu_t}{\rho}[(\frac{\partial u}{\partial z})^2 + (\frac{\partial v}{\partial z})^2]$
(C)	$-\frac{\mu_t}{\rho}\frac{g\beta}{Pr_t}\frac{\partial T}{\partial z}$
(D)	$-\varepsilon$
(E)	$\frac{1}{\rho}\frac{\partial}{\partial z}(\frac{\mu_{eff}}{\sigma_\varepsilon}\frac{\partial \varepsilon}{\partial z})$
(F)	$C_{1\varepsilon}\frac{\mu_t}{\rho}\frac{\varepsilon}{K}[(\frac{\partial u}{\partial z})^2 + (\frac{\partial v}{\partial z})^2]$
(G)	$-C_{3\varepsilon}\frac{\mu_t}{\rho}\frac{\varepsilon}{K}\frac{g\beta}{Pr_t}\frac{\partial T}{\partial z}$
(H)	$-C_{2\varepsilon}\frac{\varepsilon^2}{K}$

Figure 6.13 indicates that in the presence of surface shear even for a thermally stratified layer of water the production of turbulence due to shear, term B, is the most important term. In the K-ε equation, Eq. (3.22), this term is balanced out mainly by the dissipation of turbulent kinetic energy term D. In the ε-equation, Eq. (3.23), the production term F due to shear is also the most important one which is nearly balanced out by the dissipation term H. The results show that the diffusion of turbulent kinetic energy, term A, and

the diffusion of dissipation of turbulent kinetic energy, term E, are significant near the surface. The buoyancy terms in K- and ε-equations, terms C and G, respectively, are positive near the surface which implies production and then become negative away from the interface indicating dissipation. The effect of the buoyancy on the turbulent kinetic energy is more pronounced than on the dissipation of turbulent kinetic energy and is evident from the results which indicate that the absolute value of term C is an order magnitude higher than that of term G. The negative temperature gradient away from the surface, which corresponds to a thermally stable stratification, retards development of turbulence in this region. This is in accordance with experimental observations discussed previously. It should be noted that for a short duration simulation considered the turbulent mixing has penetrated only the upper 10 cm of the total depth of the water layer ($D = 33$ cm).

The turbulent quantities at $t = 25$ minutes are plotted in Figure 6.14. At this time the water is being thermally stratified by radiation in the presence of surface cooling and shear (see Figure 6.12). The figure also shows that the production of turbulent kinetic energy and its dissipation by shear are the most significant terms in the development of turbulence. However, it should be noted that in this case where the water is being thermally stratified by radiation the buoyancy (terms C and G) always opposes the development of turbulence in the stable region. Again, as in Figure 6.13 the absolute value of the buoyancy term C in the K-equation is an order magnitude larger than the term G in the ε-equation. The results show that at this time these terms are only significant in the upper 15 cm of the layer.

The temperature and effective viscosity profiles at different times for this particular numerical simulation are presented in Figures 6.15 and 6.16, respectively. At the end of the initial heating period ($t = 10$ min) the surface layer is seen (Figure 6.15) to be strongly stratified, and within the first few centimeters there exists a sharp temperature gradient which is due to internal absorption

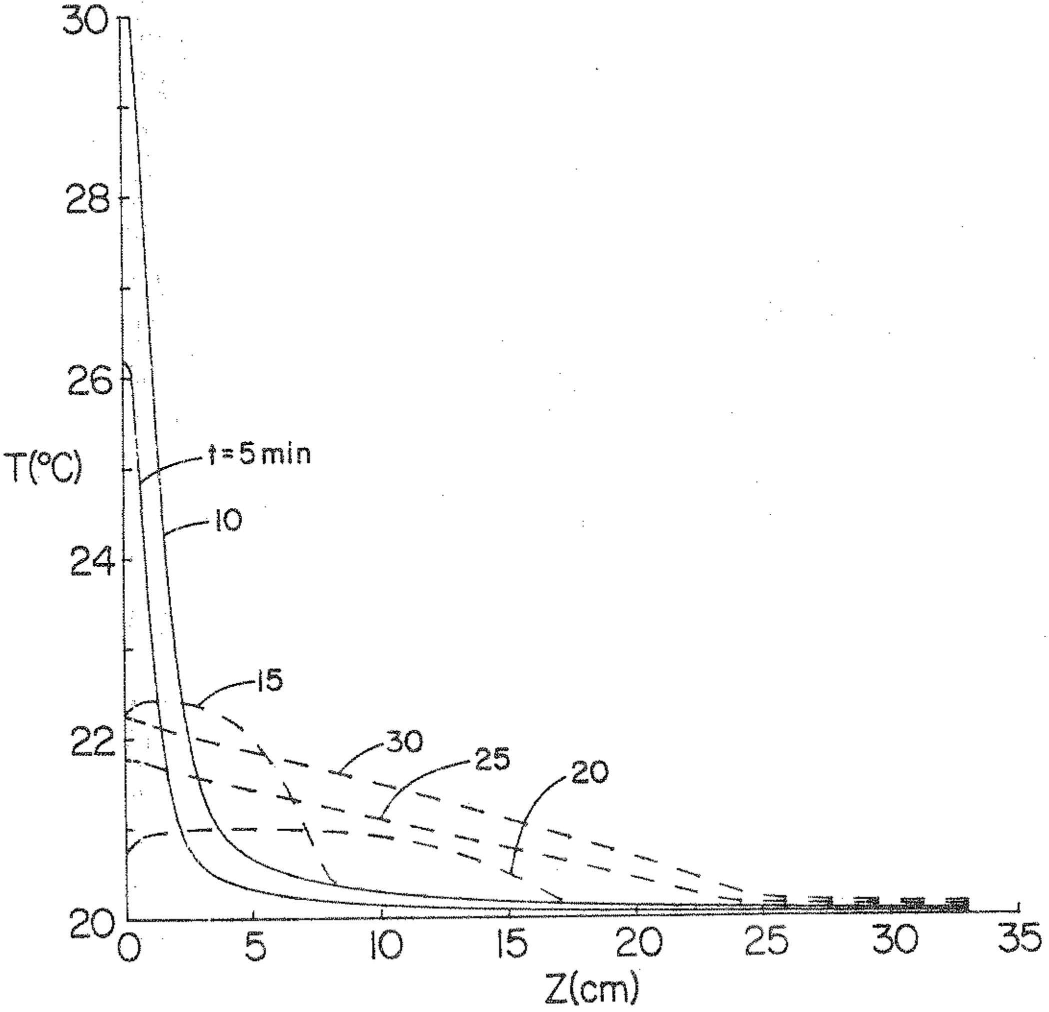

Figure 6.15 Predicted temperature distributions for numerical experiment (see Figure 6.12 for conditions)

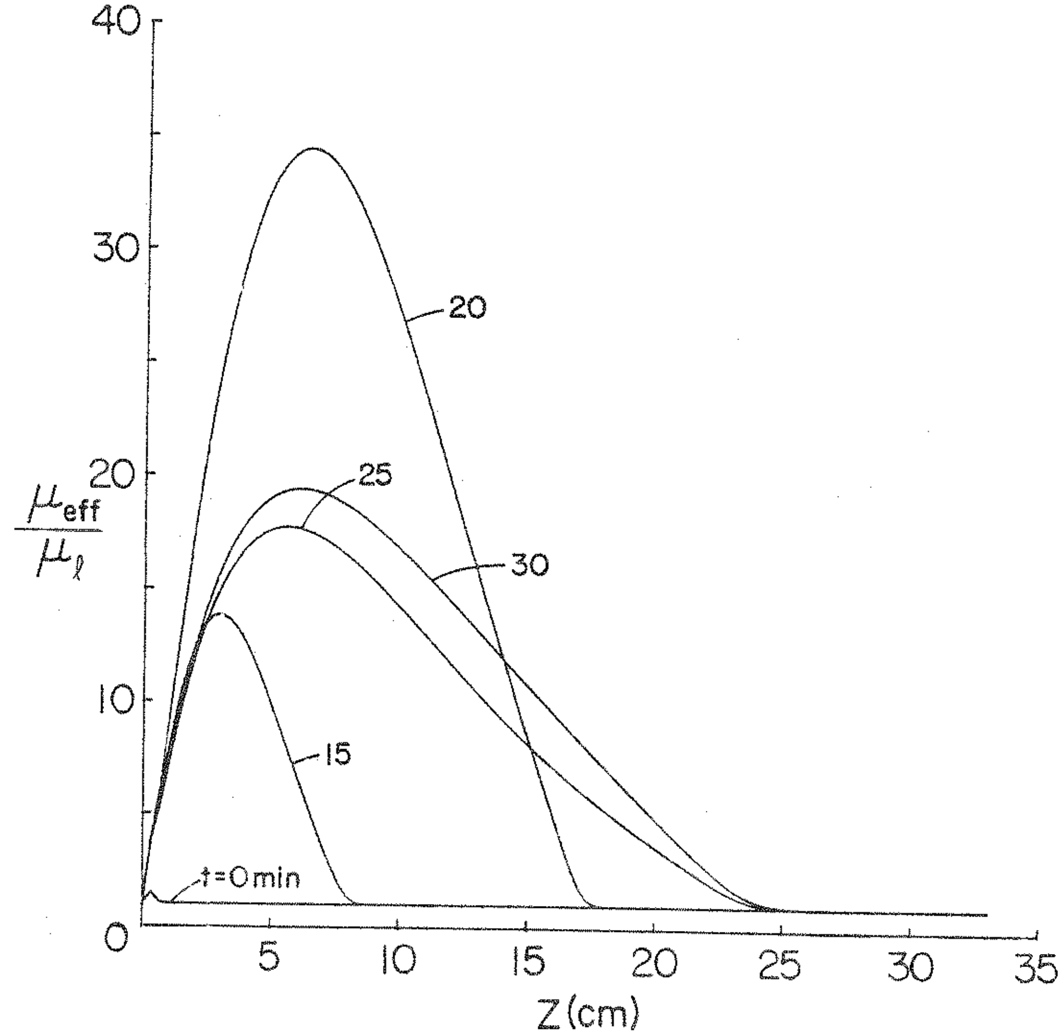

Figure 6.16 Predicted effective viscosity distributions for numerical experiment

of radiation in the upper layers of water. Once the radiant heating is terminated and surface cooling and shear are imposed by forced air flow, mixing starts in the upper layers ($t = 15$ min) and the depth of the mixed layer grows with continued cooling. At this time the stratification of the water is resumed and surface cooling is continued (see Figure 6.12). The radiant energy absorbed by water is distributed more effectively by turbulent mixing than in the absence of surface shear, e.g. compare temperature profiles at $t = 10$ min and $t = 25$ min. As the simultaneous heating and cooling continue, the local temperature increases throughout the layer.

The dimensionless effective viscosity profiles at different times are presented in Figure 6.16. It is evident that during the initial heating period in the absence of forced air flow over the surface ($t < 10$ min), the effective viscosity is equal to the laminar viscosity. At $t = 15$ min, which is five minutes after the termination of radiant heating and start of surface cooling, the dimensionless effective viscosity has a peak of 13 at a depth of 3 cm. The maximum reaches a value of 35 at a depth of 7 cm and $t = 20$ min. Once the reheating cycle is initiated at $t = 20$ min and cooling is continued, turbulence is damped and a decrease in the peak value of effective viscosity results, but sustained circulation of air over the water surface results in a slow increase in the level of turbulence during radiant heating. In a period of 5 minutes (from 25 to 30 minutes) peak value of viscosity increases by about 8%, while in the same length of time (from 15 to 20 minutes) in the absence of heating by radiation the increase is about 170%.

In all the numerical calculations presented an equally spaced 100 grid point mesh and 0.5 sec time increment was used. The numerical results were checked and verified to be independent of the grid spacing and time step.

6.5 Comparison of Model Predictions with Experimental Data

Experimental conditions for several different experiments were simulated numerically and the model equations were solved. The predictions for Experiment No. XI discussed in Figure 6.9 are presented in Figures 6.17, 6.18, and 6.19. In this experiment the water was thermally stratified for 30 minutes. The heating was then terminated and immediately the circulation of air over the water surface was started. A comparison between predicted and measured temperature distributions is given in Figure 6.17. Because of intense stratification and high fringe density the temperature distribution could not be determined interferometrically, and therefore temperature profiles were measured by means of thermocouples. The agreement between the experiment and analysis during stratification of water by radiation is excellent. This reaffirms the reliability and accuracy of the radiation model for laboratory experiments with distilled water. The predicted temperature profiles show a temperature reversal a small distance below the water interface. This indicates that the surface layer is being cooled, i.e., net heat flux at the surface is upward, while the bulk of the water is heated. This was also observed in the interferograms.

A comparison between measured and predicted temperature distribution during the cooling phase (e.g., after the surface was exposed to forced air flow) is presented in Figure 6.18. Inspection of the figure reveals that there is good agreement between the data and predictions. The model predicts that in the presence of cooling and shear at the surface a mixed layer develops. The depth of the layer grows and its temperature decreases with continued cooling. This trend was also verified by thermocouple readings. At later times (t = 45 min) the model overpredicts the depth and temperature of the mixed layer. The discrepancy is partially due to inadequate modeling of the heat transfer processes at the air-water interface. At this time, the predicted total thermal energy content of the water is higher than measured experimentally. This suggests

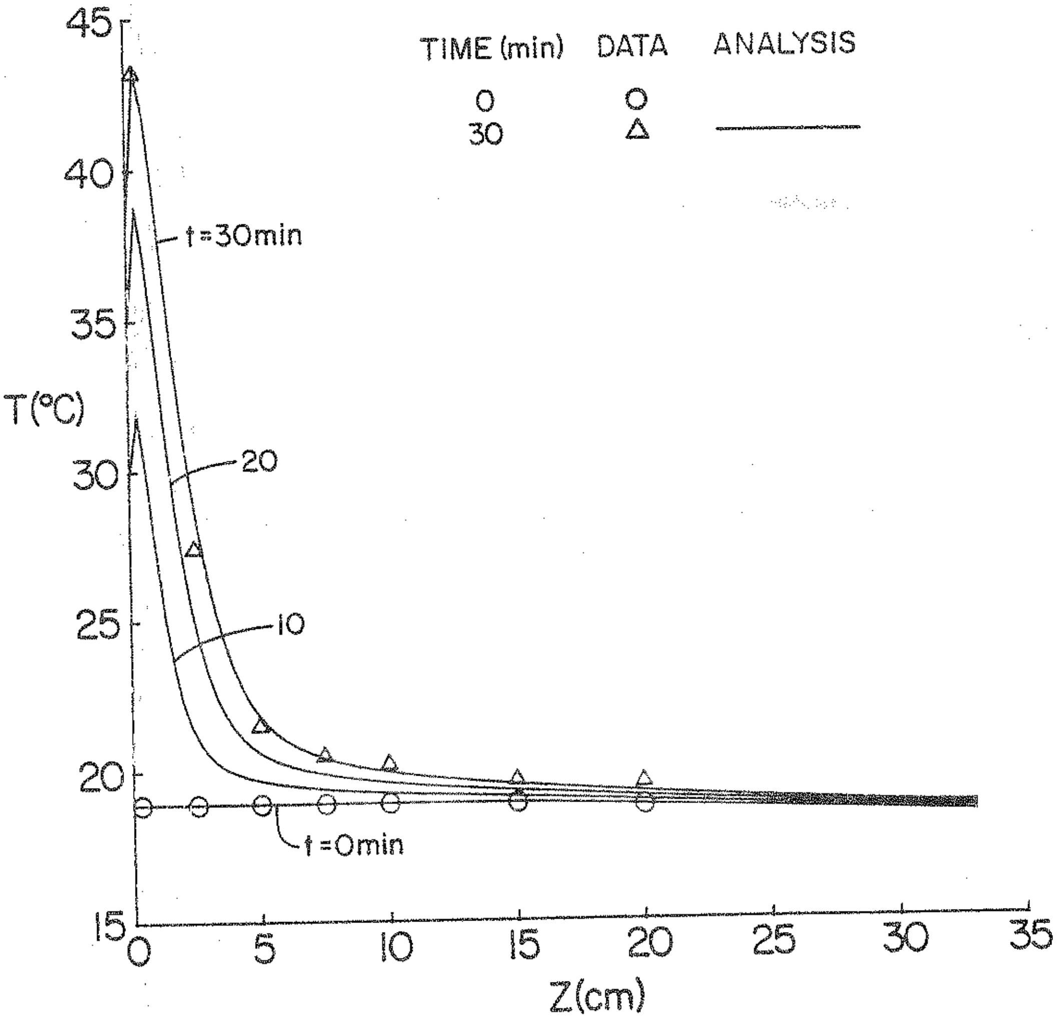

Figure 6.17 Comparison of measured and predicted temperature distributions during heating cycle for Experiment XI (see Table 6.1 for conditions)

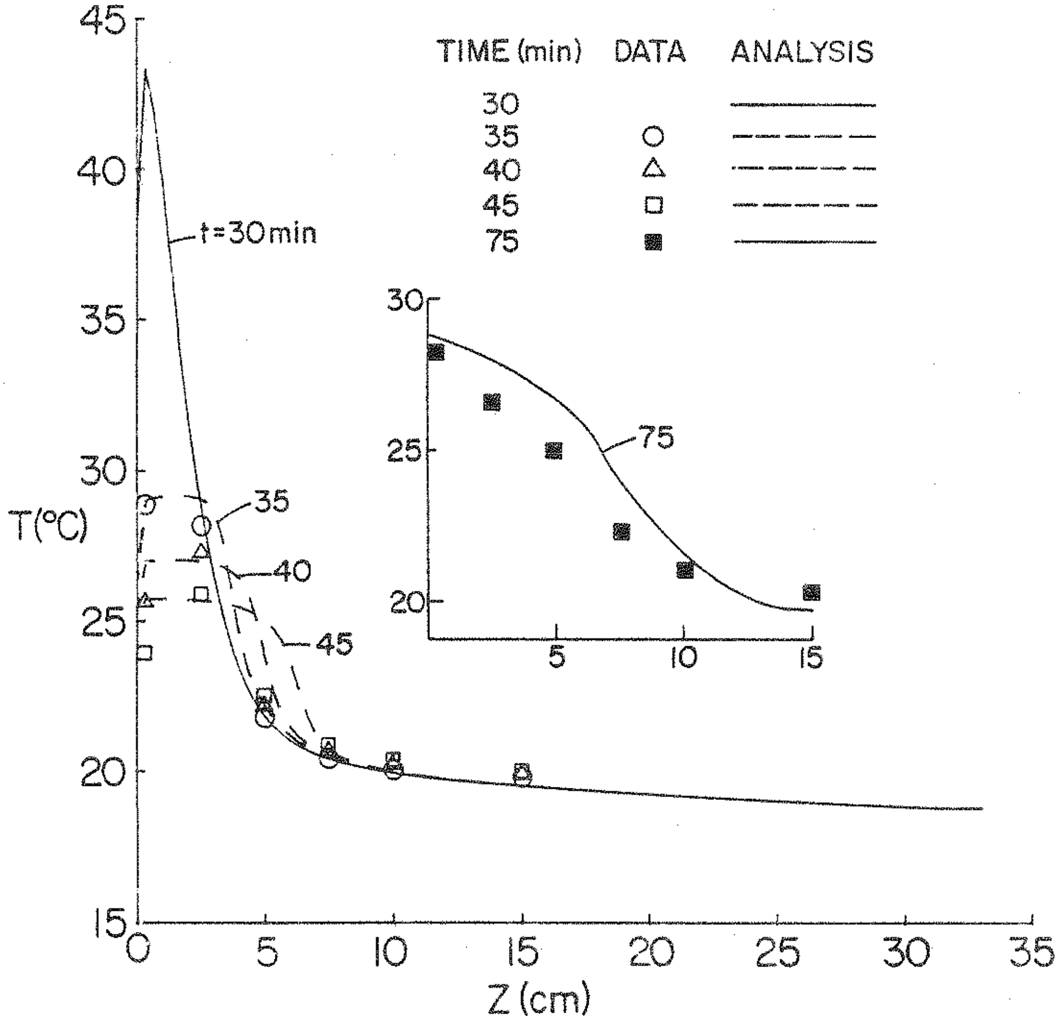

Figure 6.18 Comparison of measured and predicted temperature distributions during cooling and restratification periods for Experiment XI (see Table 6.1 for conditions)

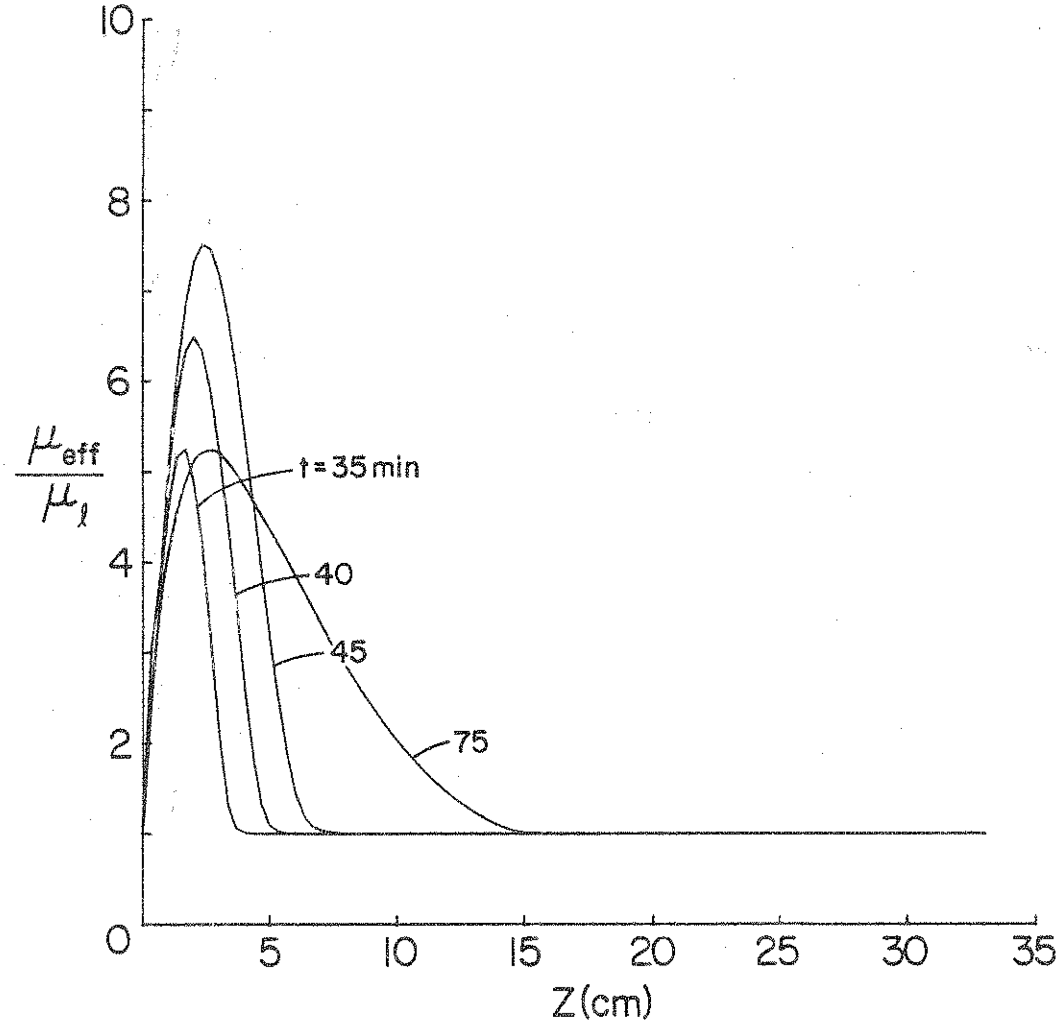

Figure 6.19 Predicted dimensionless effective viscosity distributions for Experiment XI (see Table 6.1 for conditions)

that the model equations underpredicted the surface heat flux. Another contributing factor to the discrepancy between calculations and experiment is the uncertainty in the turbulence model constants, which were established for a physical problem where surface shear was absent (Chapter 3), and are not adjusted for this situation where cooling and shear are simultaneously present at the water surface. Note that both the experimental and numerical results indicate that the temperature distribution at depths greater than 10 cm do not change during the experiment.

The calculated temperature distribution at t = 75 min also agrees reasonably well with the experimental data. This suggests that the model is capable of fair predictions during the restratification cycle. For the sake of clarity, the temperature distribution at the end of the reheating period (see Table 6.1) is given as an insert in Figure 6.18. The temperature trends at this time are similar to those obtained for the numerical experiment (Figure 6.15) during the restratification by radiant heating and simultaneous cooling by circulating air over the water surface.

The calculated dimensionless effective viscosity profiles at different times are given in Figure 6.19. After 5 minutes from the termination of the radiant heating period and start of surface cooling (t = 35 min), the dimensionless effective viscosity was a peak value of 5.2 at a depth of 2 cm. With continued cooling and application of shear at the surface turbulence intensifies and the mixed layer grows in depth. This is evidenced by the effective viscosities presented in the figure. At t = 75 min the peak value of the effective viscosity is 30% lower than at t = 45 min. This is due to suppression of turbulence level by radiant heating during the restratification phase. Although at this time the turbulence level is lower, but the mixed layer deepens as a result of surface cooling and turbulent entrainment of water from the stable region.

A comparison between the model predictions and experiments for a different experiment (Experiment No. XII) is given in Figure 6.20, 6.21, and 6.22. In this particular experiment the water was

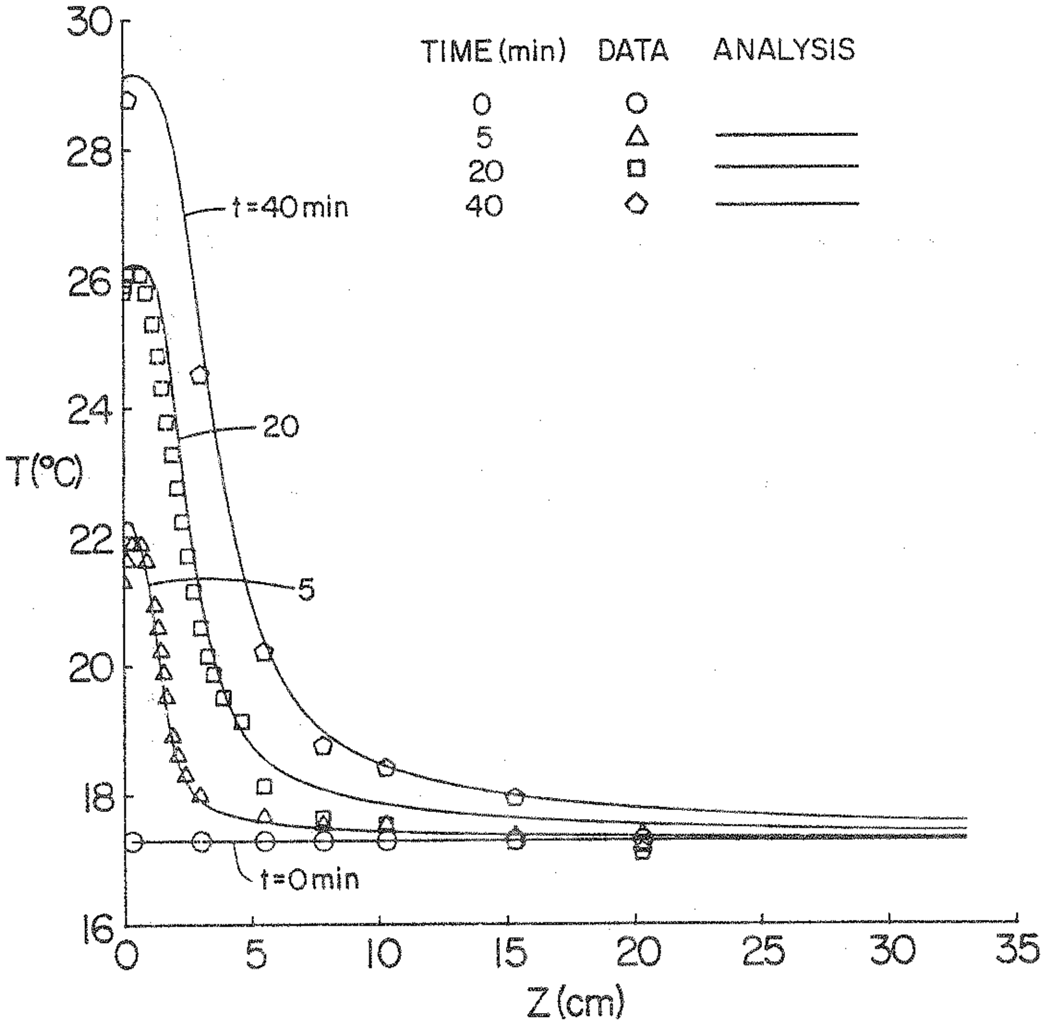

Figure 6.20 Comparison of measured and predicted temperature distributions during heating by radiation and surface cooling for Experiment XII (see Table 6.1 for conditions)

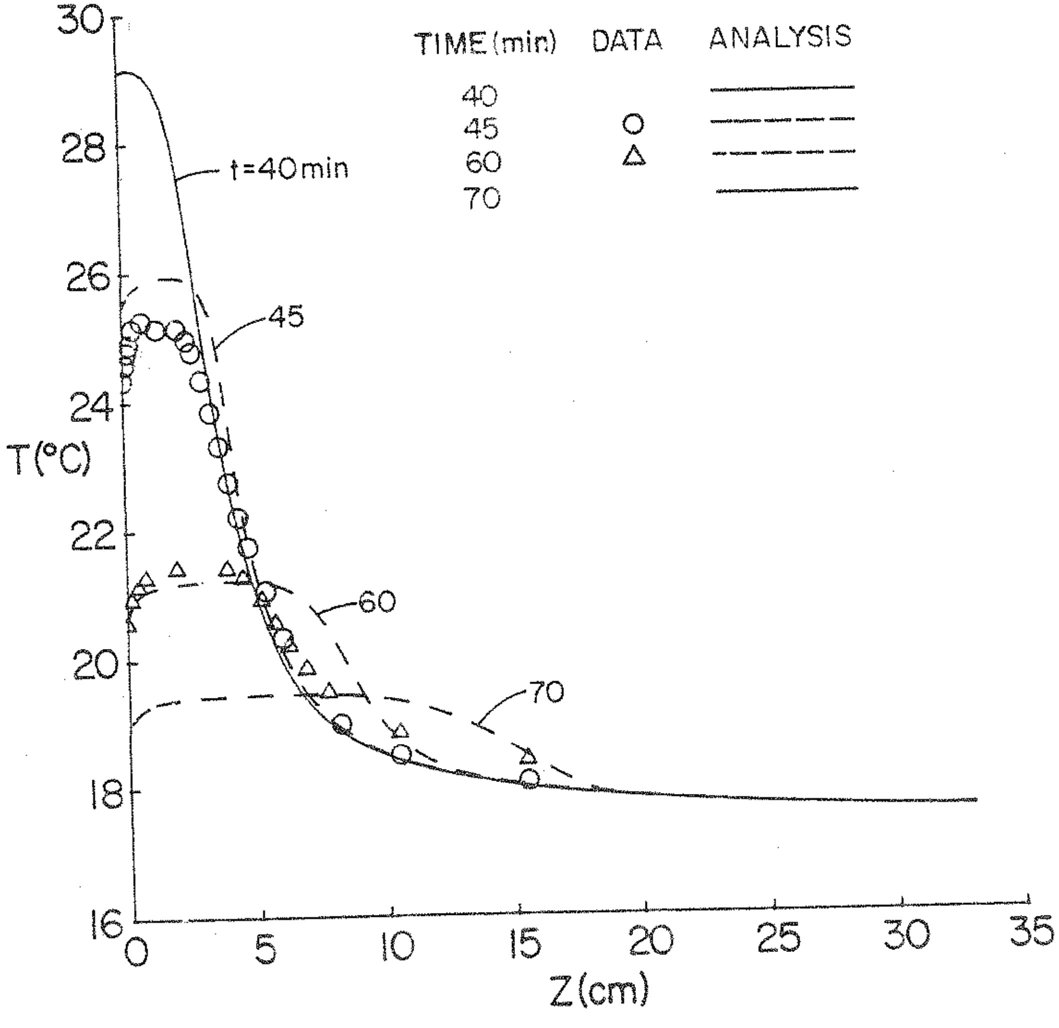

Figure 6.21 Comparison of measured and predicted temperature distributions during cooling of a thermally stratified layer of water (Experiment XII, see Table 6.1 for conditions)

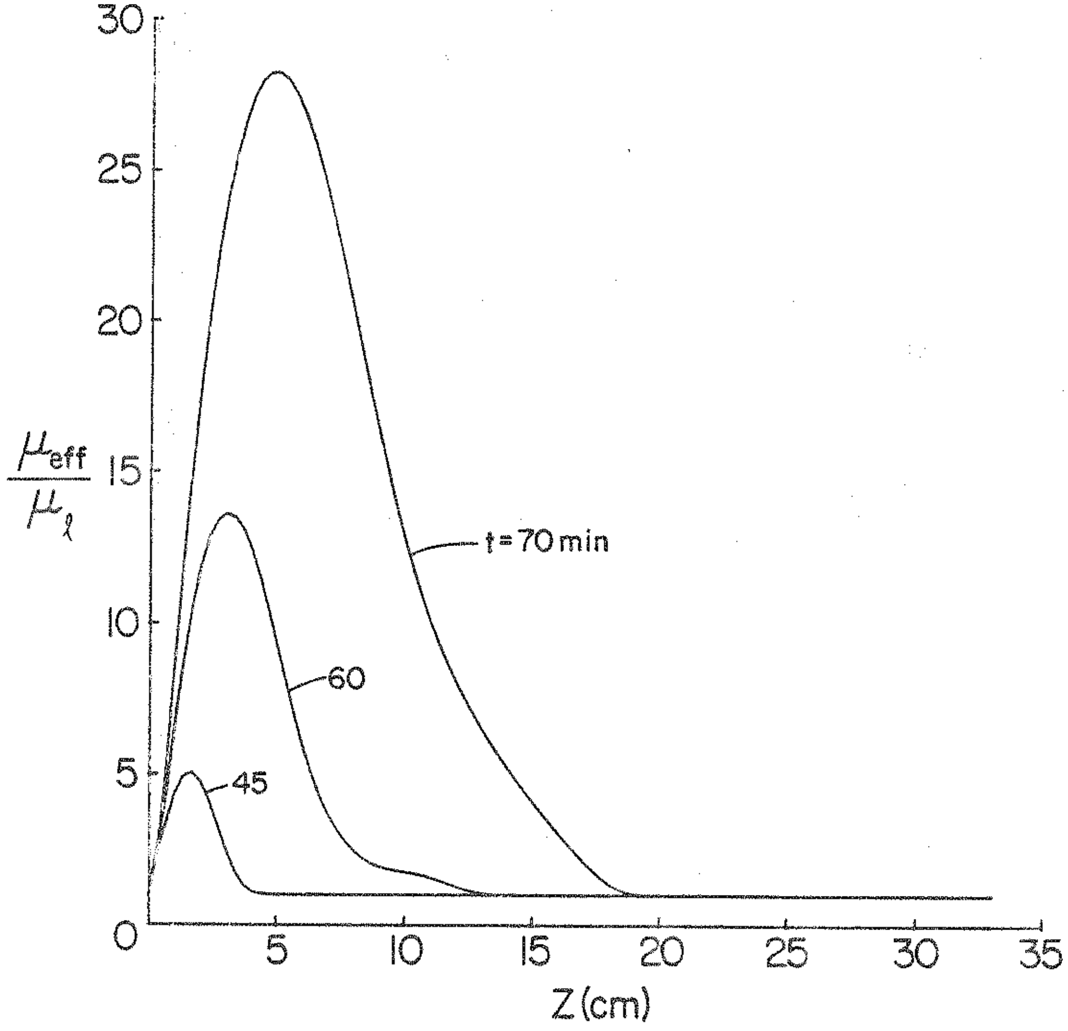

Figure 6.22 Predicted effective viscosity distributions for Experiment XII (see Table 6.1 for conditions)

simultaneously heated by radiant heaters and cooled by forcing air over the surface. Then after 40 minutes have elapsed, the heating was terminated, but the cooling of the surface persisted. Figure 6.20 gives a comparison between the interferometrically measured and predicted temperature distribution at different times during the simultaneous heating and cooling phase of the experiment. The agreement between data and predictions is very good at all times. A comparison of this figure and Figure 6.17 clearly indicates that the temperature increase in the surface layer ($z < 2$ cm) is not as large as in the case with no cooling; however, the presence of cooling and shear at the surface cause a deeper but less intense penetration of the thermal stratification. A comparison between predicted and measured temperature distributions during the second phase of the experiment, i.e., in the presence of surface cooling but the absence of radiative heating, is presented in Figure 6.21. Inspection of the figure reveals generally good agreement; however, the mixed layer temperature at $t = 45$ min is overestimated, while at $t = 60$ min it is slightly underestimated. The model overpredicts the depth of the mixed layer. The discrepancy between the data and predictions in the temperature distribution and the depth of the mixed layer is attributed to inadequate modeling of the sensible and latent heat transfer at the water surface and the entrainment process between the mixed and stably stratified regions. It should also be emphasized that the constants used in the turbulence model were not adjusted and were identical to those determined for the problem of heating from below a thermally stratified layer of water (see Chapter 3). The effective viscosity distributions calculated by the model during the cooling phase presented in Figure 6.22 show similar trends as those described in Figure 6.19. The magnitudes of the effective viscosity and the depth of the mixed layer are greater for Experiment XII than for Experiment XI, because the surface was exposed to air flow even during the radiant heating phase in the former.

The temperature distribution in the water depends strongly on the surface boundary conditions and turbulence level in the mixed layer. The overall validity of the model predictions is examined in Figure 6.23 where the calculated mixed layer depth is compared with the measurements. Good agreement is obtained between the calculated and measured mixed layer depth at all times. Since it was not possible to determine the surface temperature due to the large interference fringe density, the temperature measured with a thermocouple 3 mm below the interface was used for comparison purposes with the calculations at that location (Figure 6.24). The agreement is generally better than 6%, thus verifying the overall predictive capabilities of the model. It should be noted that in this figure the decrease in the temperature after t = 40 min is due to the continued cooling of water in absence of radiant heating.

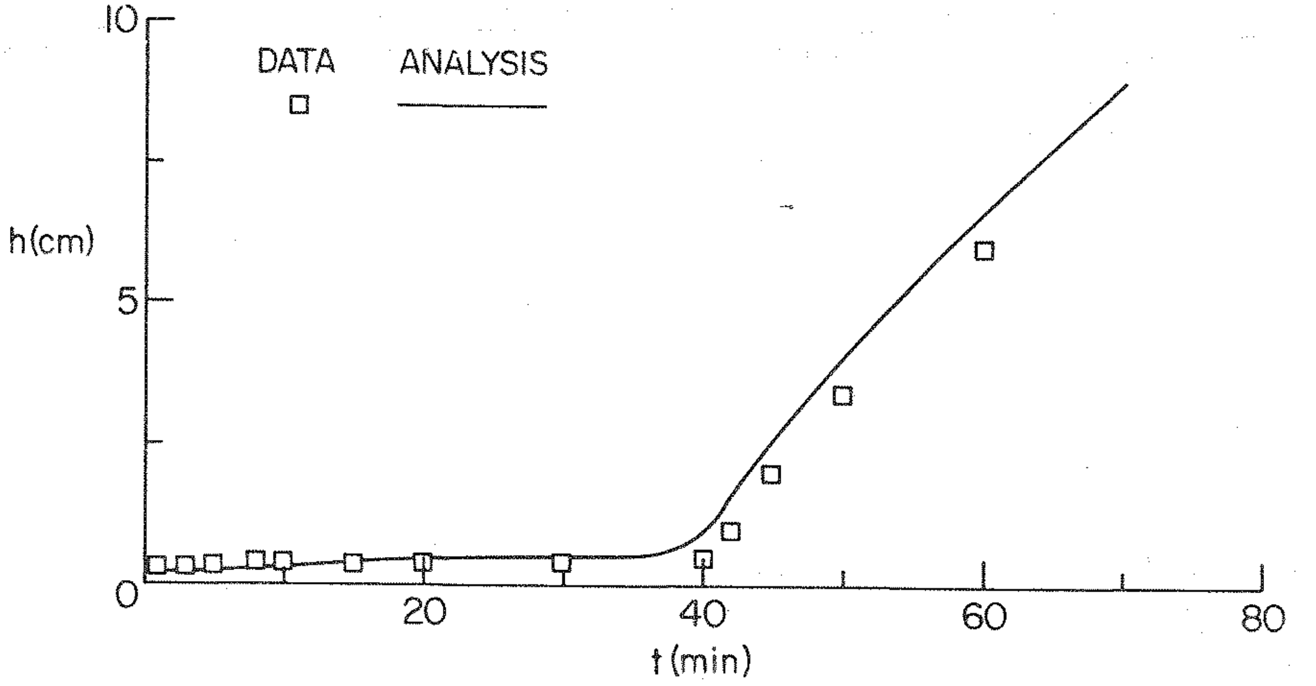

Figure 6.23 Comparison of measured and predicted mixed layer depths (Experiment XII, see Table 6.1 for conditions)

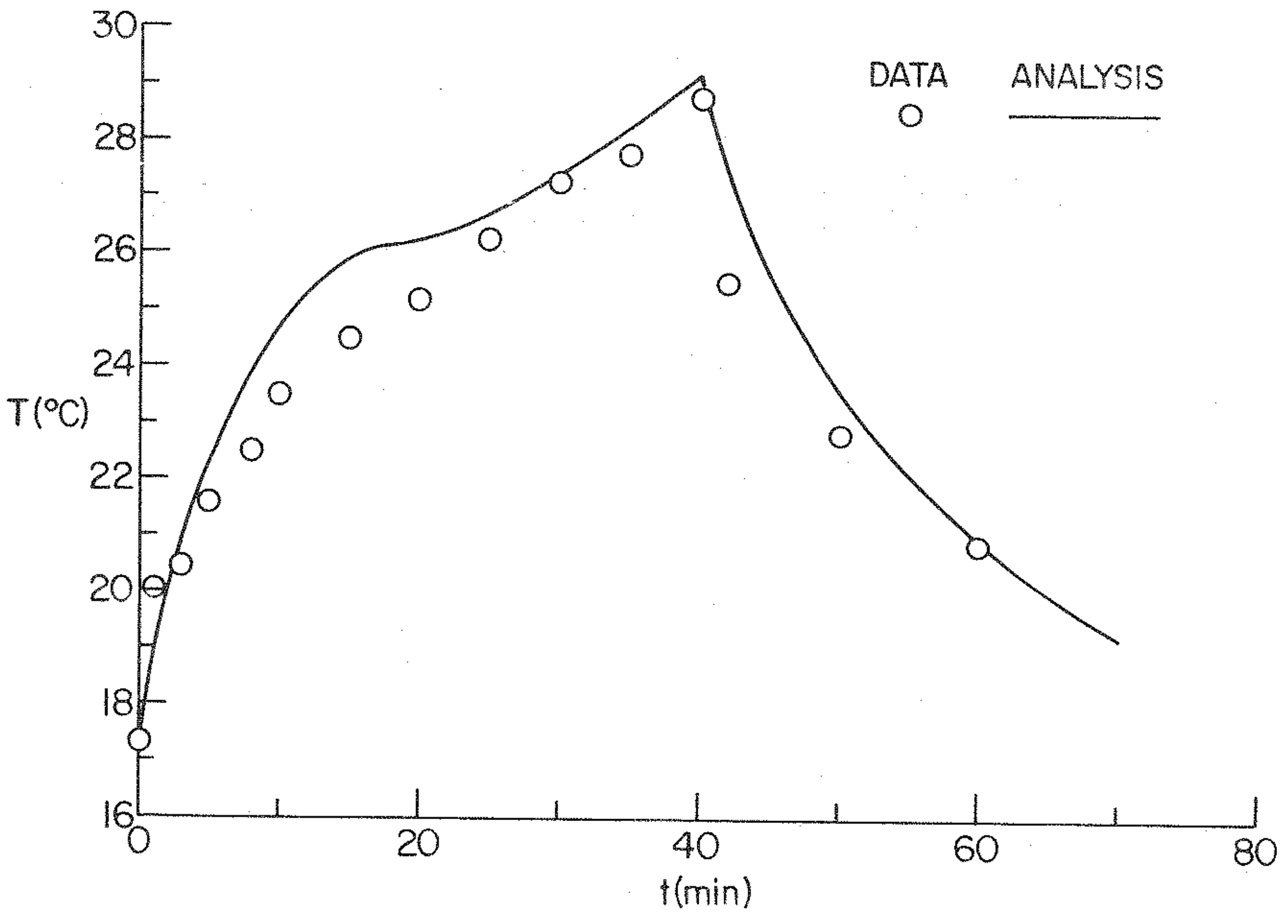

Figure 6.24 Comparison of measured and predicted temperatures at z = 3 mm (Experiment XII, see Table 6.1 for conditions)

7. CONCLUSIONS

This chapter highlights the conclusions that have been reached on the basis of the particular experimental and analytical studies conducted which are described in the report. It should be emphasized that the remarks, strictly speaking, are appropriate only for the specific experiments performed and their generality must be validated by future studies under different conditions.

Conclusions which may be drawn from the laboratory experiments are as follows:

1. In a shallow layer of water undergoing thermal stratification by radiant heating, the internal absorption of radiation near the bottom can produce an unstable situation with a subsequent generation of thermal plumes which transport heat from the bottom and cause mixing of water. Formation and departure of such plumes were detected in the experiments by a thermistor located a few millimeters above the bottom.
2. When a nonuniformly stratified layer of water is heated from below (or cooled from above), fluid motion is produced by buoyancy. A very complex natural convection mixing phenomena takes place in the water, especially above the heater surface and at the bottom of the stable region. The plume (thermal) departure from the vicinity of the heated surface causes mixing in the fluid layer above. The temperature of the thermals is at times about 1°C higher than the surrounding fluid. At the top of the mixed layer entrainment of warmer water into the layer takes place at the expense of the erosion of the stable overlying region.
3. Cooling of an initially uniform layer of water by forcing

air over the surface results in a complex fluid motion throughout the layer. Several circulation cells are developed, and cooled water at the surface plunges into the underlying, nearly uniform temperature region. The circulation of water produced was influenced by the size of the test cell. Therefore, it is concluded that the tank was too small for simulation during cooling of nonstratified water in the laboratory.

4. Internal absorption of radiation plays a very decisive role in the flow and the thermal structure in water heated by radiation and cooled by forced air flow over the surface. The flow in a thermally stratified layer of water being cooled is confined and mixing occurs only in the upper regions. Interaction of radiation and turbulent mixing in a layer of water which is cooled from the surface has important bearing on the rate of the mixed layer growth.

The good agreement between experimental data and the analytical predictions of different analyses indicates that the temperature distribution in water being heated and/or cooled can be modeled with some confidence. Based on the comparison between numerical results and experimental data the following conclusions can be drawn:

1. For accurate prediction of the temperature distribution during radiant heating of water the volumetric rate of radiant energy absorption must be modeled realistically.
2. The temperature distribution as well as mixed layer depth and temperature are very sensitive to the boundary conditions at the air-water interface. This means the convective, latent and radiative energy transfer as well as wind shear must be properly modeled. There is still considerable uncertainty and the range of applicability of the semiempirical correlations available in the literature.

3. Accurate determination of the local volumetric rate of radiant energy absorption near the bottom is not crucial for calculating the temperature distribution in a deep layer of water being stratified by radiation; however, accurate specification of the radiation characteristics of the bottom in shallows waters is important.
4. The K-ε turbulence model is not completely satisfactory for predicting temperature structure in the mixed layer and its dynamics. The entrainment processes at the interface between the mixed and stable regions to not appear to have been modeled properly.
5. Knowledge of the spectral absorption and scattering characteristics of natural waters are required for modeling radiation transfer.

LIST OF REFERENCES

Abraham, G., 1975: "Methodologies for Temperature Impact Assessment," in European Course on Heat Disposal from Power Generation in Water Environment, Delft Hydraulics Laboratory, June 23-27, 1975, Chapter 3.

Annonymous (Editor), 1969: Eutrophication: Causes, Consequences, Corrections, National Academy of Sciences, Wasnington, D.C.

Baker, D. J., 1966: "A Technique for the Precise Measurement of Small Fluid Velocities," J. Fluid Mech. 26, 573-575.

Behnia, M., and Viskanta, R., 1979: "Free Convection in Thermally Stratified Water Cooled from Above," Int. J. Heat Mass Transfer 22, 611-623.

Berg, J. C., Acrivos, A., and Boudart, M., 1966: "Evaporative Convection," in Advances in Chemical Engineering, T. G. Drew, J. W. Hoopes, Jr. and T. Vermenten, Editors, Academic Press, New York, Volume 6, pp. 61-123.

Bloss, S. und Grigull, U., 1978: "Temperaturverteilung in tiefen und flachen Seen," Wärme-und Stoffübertragung 11, 119-130.

Carnahan, B., Luther, H. A., and Wilkes, J. O., 1969: Applied Numerical Methods, John Wiley and Sons, New York.

Carroll, J. J., 1971: "The Structure of Turbulent Convection," Ph.D. Thesis, Dept. of Met., Univ. of Calif., Los Angeles.

Carson, D. J., and Smith, F. B., 1974: "Thermodynamic Model for the Development of a Convectively Unstable Boundary Layer," in Turbulent Diffusion in Environmental Pollution--Advances in Geophysics, F. N. Frankiel and R. E. Munn, Editors, Academic Press, New York, Volume 18A, pp. 111-124.

Chu, T. Y., 1972: "Thermal Convection in Horizontal Liquid Layers," Ph.D. Thesis, University of Minnesota, Minneapolis, Minn.

Chu, T. Y. and Goldstein, R. J., 1973: "Turbulent Convection in a Horizontal Layer of Water," J. Fluid Mech. 60, 141-159.

Coantic, M. F., 1978: "An Introduction to Turbulence in Geophysics, and Air-Sea Interactions," North Atlantic Treaty Organization, Technical Report AGARD-AG-232.

Dake, J. M. K., and Harleman, D. P., 1969: "Thermal Stratification in Lakes: Analytical and Experimental Studies," Water Resour. Res. 5, 484-495.

Daniel, K. J., Laurendeau, N. M., and Incropera, F. P., 1979: "Prediction of Radiation Absorption and Scattering in Turbid Water Bodies," ASME J. Heat Transfer 101, 63-67.

Davies, J. A., Schertzer, W., and Nunez, M., 1975: "Estimating Global Solar Radiation," Boundary Layer Meteorology 9, 33-52.

Deardorff, J. W., and Willis, G. E., 1967a: "Investigation of Turbulent Thermal Convection Between Horizontal Plates," J. Fluid Mech. 28, 675-704.

Deardorff, J. W., and Willis, G. E., 1967b: "The Free-Convection Temperature Profile," Quart. J. Roy. Meteor. Soc. 93, 166-175.

Deardorff, J. W., Willis, G. E., and Lilly, D. K., 1969: "Laboratory Investigation of Nonsteady Penetrative Convection," J. Fluid Mech. 35, 7-31.

Denman, K. L., 1973: "A Time-Dependent Model of the Upper Ocean," J. Phys. Ocean. 3, 173-184.

Denman, K. L., and Miyake, M., 1973: "Upper Layer Modification at Ocean Station 'Papa': Observation and Simulation," J. Phys. Ocean. 3, 185-196.

Dunchel, M., Hasse, L., Krugermeyer, L., Schriever, D., and Wucknitz, J., 1974: "Turbulent Fluxes of Momentum, Heat and Water Vapor in the Atmospheric Surface Layer at Sea During Atex," Boundary Layer Meteor. 6, 81-106.

Eddington, D. N., and Robbins, J. A., 1976: "Records of Lead Deposition in Lake Michigan Since 1880," Environ. Sci. & Technol. 10, 266-274.

Eichhorn, R., 1961: "Flow Visualization and Velocity Measurement in Natural Convection with the Tellurium Dye Method," ASME J. Heat Transfer 83, 379-381.

Eskinazi, S., 1975: Fluid Mechanics and Thermodynamics of Our Environment, Academic Press, New York.

Fischer, H. B., 1973: "Longitudinal Dispersion and Turbulent Mixing in Open-Channel Flow," in Annual Review of Fluid Mech., M. Van Dyke et al., Editors, Annual Reviews Inc., Palo Alto, Calif., Volume 5, pp. 59-78.

Fischer, H. B., 1976: "Mixing and Dispersion in Estuaries," in Annual Review of Fluid Mech., M. Van Dyke et al., Editors, Annual Reviews Inc., Palo Alto, Calif., Volume 8, 107-133.

Fitzjarrald, D. E., 1976: "An Experimental Study of Turbulent Convection in Air," J. Fluid Mech. 73, 693-719.

Foster, T. D., 1965: "Onset of Convection in a Layer of Fluid Cooled from Above," Fluids 8, 1770-1774.

Gerald, C. F., 1978: Applied Numerical Analysis, Addison-Wesley Publishing Co., Reading, Mass.

Gibson, N. M., and Launder, B. E., 1976: "On the Calculation of Horizontal Turbulent, Free Shear Flows Under Gravitational Influence," ASME J. Heat Transfer 96, 81-87.

Ginzburg, A. I., and Fedorov, K. N., 1978: "Cooling of Water from the Surface Under Free and Forced Convection," Izv. Atm. Ocean. Phys. 14, 57-62.

Gold, V., 1956: pH Measurements, Wiley, New York.

Goldstein, R. J., 1976: "Optical Measurements in Heat Transfer," in Measurements in Heat Transfer, E. R. G. Eckert and R. J. Goldstein, Editors, Hemisphere Publishing Corp., Washington, D. C., pp. 241-293.

Goldstein, R. J., and Chu, T. Y., 1969: "Thermal Convection in a Horizontal Layer of Air," Progress Heat and Mass Transfer, Pergamon Press, London, Volume 2, pp. 55-75.

Hamelnik, J. L., and Waybrant, R. D., 1973: "Factors Controlling the Dynamics of Non-Ionic Synthetis Organic Chemicals in Aquatic Environments," Purdue University, Water Resources Research Center, Technical Report No. 44.

Harleman, D. F., Editor, 1972: "Engineering Aspects of Heat Disposal From Power Generation," Dept. Civil Eng., Mass. Inst. of Technology, Cambridge, Mass.

Harleman, D. R. F., and Stolzenbach, K. D., 1972: "Fluid Mechanics of Heat Disposal from Power Generation," in Annual Review of Fluid Mech., M. Van Dyke et al., Editors, Annual Reviews Inc., Palo Alto, Calif., Volume 4, pp. 7-32.

Hauf, W., and Grigull, U., 1970: "Optical Methods in Heat Transfer," in Advances in Heat Transfer, J. P. Hartnett and T. F. Irvine, Jr., Editors, Academic Press, New York, Volume 6, pp. 191-362.

Heidt, F. D., 1977: "Comparison of Experiments on Penetrative Convection with Measurements in Nature," in Heat Transfer in

Turbulent Buoyant Convection, D. B. Spalding and N. Afgan, Editors, Hemisphere Publishing Corp., Washington, D. C., Volume 1, pp. 199-210.

Hicks, B. B., and Hess, G. D., 1977: "On the Bowen Ratio and Surface Temperature at Sea," J. Phys. Ocean. 7, 141-145.

Hill, M. N., Editor, 1962: The Sea, Volume 1, Physical Oceanography, Interscience Publishers, New York.

Holm-Hansen, O., Goldman, R., Richards, R., and Williams, P. M., 1976: "Chemical and Biological Characteristics of a Water Column in Lake Tahoe," Limnol. Oceanogr. 21, 548-562.

Hossain, M. S., and Rodi, W., 1977: "Influence of Buoyancy on the Turbulent Intensities in Horizontal and Vertical Jets," in Heat Transfer in Buoyant Turbulent Convection, D. B. Spalding and N. Afgan, Editors, Hemisphere Publishing Corp., Washington, D. C., Volume 1, pp. 39-51.

Howard, L. N., 1966: "Convection at High Rayleigh Number," Proc. Eleventh Int. Congress Applied Mechanics, H. Görtler, Editor, Munich, Germany, pp. 1109-1115.

Hutchinson, G. E., 1957: A Treatis on Limnology, Volumes I and II, John Wiley, New York.

Iribane, A., Frantisak, F., Hummel, R. L., and Smith, J. W., 1972: "An Experimental Study of Instabilities and Other Flow Properties of a Laminar Pipe Jet," AIChE Journal 18, 689-698.

Jerlov, N. G., 1976: Marine Optics, Elsevier Scientific Publishing Co., Amsterdam.

Jirka, G. H., Ryan, P. J., and Stolzenbach, K. D., 1975: "Physical Processes in Heat Transport," in European Course on Heat Disposal from Power Generation in the Water Environment, Delft Hydraulics Laboratory, June 23-27, 1975, Chapter 5.

Jones, W. P., and Launder, B. E., 1972: "The Prediction of a Laminarization with a 2-Equation Model of Turbulence," Int. J. Heat Mass Transfer 15, 301-314.

Katsaros, K. B., Lin, W. T., Businger, J. A., and Tillman, J. E., 1977: "Heat Transport and Thermal Structure in the Interfacial Boundary Layer Measured in an Open Tank of Water in Turbulent Free Convection," J. Fluid Mech. 83, 311-335.

Kraus, E. B., and Roth, C., 1968: "Temperature and Steady-State Vertical Heat Flux in the Ocean Surface Layers," Tellus 13, 231-238.

Kraus, E. B., and Turner, J. S., 1967: "A One-Dimensional Model of the Seasonal Thermocline: (I) A Laboratory Experiment and Its Interpretation, (II) The General Theory and Its Consequences," Tellus 19, 88-97.

Lai, R. J., 1977: "Evaporation from a Warm, Wavy Surface: A Laboratory Study," J. Phys. Ocean. 7, 431-435.

Launder, B. E., 1975: "On the Effects of a Gravitational Field on the Transport of Heat and Momentum," J. Fluid Mech. 67, 569-587.

Launder, B. E., and Spalding, D. B., 1972: Lectures in Mathematical Models of Turbulence, Academic Press, New York.

Lee, S. S., and Sengupta, S., Editors, 1977: Proceedings of the First Conference on Waste Heat Management and Utilization, University of Miami, Coral Gables, Florida.

Lee, S. S., and Sengupta, S., Editors, 1979: Proceedings of the Second Conference on Waste Heat Management and Utilization, University of Miami, Coral Gables, Florida.

Mahrt, L., and Lenschow, D. H., 1976: "Growth Dynamics of the Convectively Mixed Layer," J. Atm. Sci. 33, 41-51.

Mamayer, O. I., 1975: Temperature-Salinity Analysis of World Ocean Waters, Elsevier Scientific Publishing Co., Amsterdam.

Mangarella, P. A., Chambers, A. J., Street, R. L., and Hsu, E. Y., 1971: "Energy and Mass Transfer Through an Air-Water Interface," Tech. Rept. No. 134, Department of Civil Engineering, Stanford University, Stanford, California.

Mangarella, P. A., Chambers, A. J., Street, R. L., and Hsu, E. Y., 1973: "Laboratory Studies of Evaporation and Energy Transfer Through a Wavy Air-Water Interface," J. Phys. Ocean. 3, 93-101.

Matisse, P., 1973: "A Flow-Indicating Fluid," Manuscript from Kalliroscope Corp., Cambridge, Mass.

Merzkirch, W., 1974: Flow Visualization, Academic Press, New York.

Moore, F. K., and Jaluria, Y., 1972: "Thermal Effects of Power Plants on Lakes," ASME J. Heat Transfer 94, 163-168.

Niiler, P. P., and Kraus, E. B., 1977: "One-Dimensional Models," in Modelling and Prediction of the Upper Layers of the Ocean, E. B. Kraus, Editor, Pergamon Press, London.

Noller, C. R., 1957: Chemistry of Organic Compounds, W. B. Saunders, Philadelphia, p. 699.

Paily, P. P., Macagno, E. O., and Kennedy, J. F., 1974: "Winter-Regime Surface Heat Loss from Heated Streams," IIHR Report No. 155, Institute of Hydraulics Research, The University of Iowa, Iowa City, Iowa.

Parker, F. L., and Krenkel, P. A., 1969: "Thermal Pollution: Status of the Art," Report No. 3, Department of Environmental and Water Resources Engineering, Vanderbilt University, Nashville, Tenn.

Parker, F. L., and Krenkel, P. A., 1970: Physical and Engineering Aspects of Thermal Pollution, Chemical Rubber Co., Cleveland, Ohio.

Patankar, S. V., and Spalding, D. B., 1970: Heat and Mass Transfer in Boundary Layers, 2nd edition, Intertext Books, London.

Payne, R. E., 1972: "Albedo of the Sea Surface," J. Atm. Sci. 29, 959-970.

Phillips, O. M., 1966: The Dynamics of the Upper Ocean, Cambridge University Press, Cambridge.

Plate, E. J., 1971: "Aerodynamic Characteristics of Atmospheric Boundary Layers," U. S. Atomic Energy Commission, Oak Ridge, Tenn.

Plumb, O. A., and Kennedy, L. A., 1977: "Application of K-ε Turbulence Model to Natural Convection from a Vertical Isothermal Surface," ASME J. Heat Transfer 99, 79-85.

Popovich, A. T., and Hummel, R. L., 1967: "A New Method for Non-disturbing Turbulent Flow Measurements Very Close to a Wall," Chem. Eng. Sci. 22, 21-25.

Powe, R. E., Yin, S. H., Scanlan, J. A., and Bishop, E. H., 1973: "A Technique for Visualization of the Very Slow Motion of Water in Enclosed Spaces," ASME J. Heat Transfer 95, 408-409.

Preisendorfer, R. W., 1971: "General Theory of Radiative Transfer Across the Random Atmospheric Ocean," J. Quant. Spectros. Radiat. Transfer 11, 723-737.

Rabl, A., and Nielsen, C. E., 1975: "Solar Ponds for Space Heating," Solar Energy 17, 1-15.

Raithby, G. D., 1976: "Prediction of Dispersion by Surface Discharge," Basin Investigation and Modelling Section, Canada Center for Inland Waters, Burlington, Ontario, Canada.

Reed, R. K., 1977: "On Estimating Insolation Over the Ocean," J. Phys. Ocean. 7, 482-485.

Roache, P. J., 1976: Computational Fluid Dynamics, Hermosa Publishers, Albuquerque, New Mexico.

Ryan, P. J., 1974: "Temperature Distribution in Lakes and Reservoirs," in Engineering Aspects of Heat Disposal from Power Generation, Summer Short Course Notes, Chapter 2, pp. 2-1 to 2-80, Department of Civil Engineering, Massachusetts Institute of Technology, Cambridge, Mass.

Ryan, P. J., Harleman, D. R. F., and Stolzenbach, K. D., 1974: "Surface Heat Loss from Cooling Ponds," Water Resour. Res. 10, 930-938.

Salvadori, M., and Baron, M., 1961: Numerical Methods in Engineering, Prentice-Hall, Inc., Engelwood Cliffs, New Jersey.

Schindler, D. W., and Fee, E. J., 1973: "Diurnal Variation of Dissolved Inorganic Carbon and Its Use in Estimating Primary Production," J. Fish. Res. Bd. Can. 30, 1501-1510.

Schöll, G., 1974: "Wärmewasser-Grosswärmespeicher," Z. Ver. Dt. Ing. 223, 33-38.

Shaw, C. Y., and Lee, Y., 1976: "Wind-Induced Turbulent Heat and Mass Transfer Over Large Bodies of Water," J. Fluid Mech. 77, 645-664.

Snider, D. M., and Viskanta, R., 1974: "Combined Conduction-Radiation Energy Transfer in Stagnant Water," Water Resour. Res. 10, 939-946.

Snider, D. M., and Viskanta, R., 1975: "Radiation Induced Thermal Stratification in Surface Layers of Stagnant Water," ASME J. Heat Transfer 97, 35-40.

Spalding, D. B., 1977: "GENMIX: A General Computer Program for Two-Dimensional Parabolic Phenomena," Report No. HTS/77/9, Mechanical Engineering Department, Imperial College, London.

Spalding, D. B., and Afgan, N., Editors, 1977: Heat Transfer and Turbulent Buoyant Convection: Studies and Applications for Natural Environment, Buildings, Engineering Systems, Hemisphere Publishing Corp., Washington, D. C.

Spalding, D. B., and Svensson, U., 1977: "The Development and Erosion of the Thermocline," in Heat Transfer and Buoyant Turbulent Convection, D. B. Spalding and N. Afgan, Editors, Hemisphere Publishing Corp., Washington, D. C., Volume 1, pp. 113-122.

Spangenberg, W. G., and Rowland, W. R., 1961: "Convection Circulation of Water Induced by Evaporative Cooling," Phys. Fluids 6, 743-750.

Sparrow, E. M., Husar, R. B., and Goldstein, R. J., 1970: "Observations and Other Characteristics of Thermals," J. Fluid Mech. 41, 793-800.

Stevenson, W. H., 1965: "An Investigation of Diffusional Processes in Binary Gas Mixtures," Ph.D. Thesis, Purdue University, West Lafayette, Indiana.

Sundram, T. R., and Rehm, R. G., 1973: "The Seasonal Thermal Structure of Deep Temperature Lakes," Tellus 25, 157-168.

Svensson, U., 1978: "Examination of the Summer Stratification," Nordis Hydrology 9, 105-120.

Tennekes, H., 1973: "A Model for the Dynamics of the Inversion Above a Convective Boundary Layer," J. Atm. Sci. 30, 558-567.

Tichenor, B. A., and Cawley, W. A., 1969: "Research Needs for Thermal Pollution Control," in Engineering Aspects of Thermal Pollution, F. L. Parker and P. A. Krenkel, Editors, Vanderbilt Undersity Press, Nashville, Tenn., 320-339.

Tilton, L. S., and Taylor, J. K., 1938: "Refractive Index and Dispersion of Distilled Water for Visible Radiation at Temperatures 0 to 60°C," U. S. National Bureau Standards J. Res. 20, 419-477.

Townsend, A. A., 1959: "Temperature Fluctuations Over a Heated Horizontal Surface," J. Fluid Mech. 5, 209-241.

Turner, J. S., 1973: Buoyancy Effects in Fluids, Cambridge University Press, Cambridge, Mass.

Venkatram, A., and Viskanta, R., 1977: "Effects of Aerosol-Induced Heating of the Convective Boundary Layer," J. Atmos. Sci. 34, 1918-1933.

Viskanta, R., Behnia, M., and Karalis, A., 1977: "Interferometric Observations of the Temperature Structure in Water Cooled or Heated from Above," Advances in Water Resources 1, 57-69.

Viskanta, R., Karalis, A., and Behnia, M., 1978: "Effects of a Barrier on Temperature Structure and Mixing in Thermally Stratified Water Cooled from Above," Wärme-und Stoffübertragung 11, 229-239.

Viskanta, R., Snider, D. M., and Behnia, M., 1975: "Laboratory Modeling of Thermal Structure in Stagnant Water," Purdue University, Water Resources Research Center, Technical Report No. 62.

Viskanta, R., and Toor, J. S., 1972: "Radiant Energy Transfer in Waters," Water Resour. Res. 8, 595-608.

Viskanta, R., and Toor, J. S., 1973: "Effect of Multiple Scattering on Radiant Energy Transfer in Waters," J. Geophys. Res. 78, 3538-3551.

Viskanta, R., and Toor, J. S., 1978: "Absorption of Solar Radiation in Ponds," Solar Energy 21, 17-25.

Weisman, R. N., 1975: "Comparison of Warm Water Evaporation Equations," Proc. ASCE, J. Hydraulics Div. 101, 1303-1313.

Werlé, H., 1973: "Hydrodynamic Flow Visualization," in Annual Review of Fluid Mech., M. Van Dyke et al., Editors, Annual Reviews Inc., Palo Alto, Calif., Volume 5, pp. 361-382.

Wieringa, J., 1974: "Comparison of Three Methods for Determining Strong Wind Stress Over Lake Flevo," Boundary Layer Meteorology 7, 3-19.

Willis, G. E., and Deardorff, J. W., 1967a: "Development of Short Period Temperature Fluctuations in Thermal Convection," Phys. Fluids 10, 931-937.

Willis, G. E., and Deardorff, J. W., 1967b: "Confirmation and Renumbering of the Discrete Heat Flux Transition of Malkus," J. Appl. Meteor. 14, 1861-1866.

Wortmann, F. Y., 1953: "Eine Methode zur Beobachtung und Messung von Wassertrömungen mit Tellur," Z. Angew. Phys. 5, 201-206.

Wu, J., 1977: "A Note on the Slope of a Density Interface Between Two Stably Stratified Fluids Under Wind," J. Fluid Mech. 81, 335-339.

Zaric, Z., Editor, 1977: Thermal Effluent Disposal from Power Generation, Hemisphere Publishing Corp., Washington, D. C.

Zeman, O., and Tennekes, H., 1977: "Parameterization of the Turbulent Energy Budget at the Top of the Daytime Atmospheric Boundary Layer," J. Atmos. Sci. 34, 111-123.

APPENDIX A

THERMISTOR CIRCUITRY AND CALIBRATION

A YSI44201 (Yellow Springs Instrument Co.) thermistor was used to detect temperature fluctuations near the cooled surface or the heated bottom. The output of a thermistor alone varies nonlinearly with the temperature. This nonlinearity causes difficulty in evaluation of temperature fluctuations. Therefore, the thermistor is usually placed in an electronic circuit consisting of other resistors in order to produce a nearly linear total impedence change with temperature. Figure A.1 illustrates the circuit suggested by the manufacturer in which the thermistor was placed. The circuit was wired into one arm of an Ellis Amplifier Bridge for nulling the voltage output of the bridge under different operating conditions for easy interpretation of the temperature fluctuations. In this circuit the output of the thermistor had a maximum of ± 0.2°C deviation from linearity, see Figure A.2. The maximum error at any given temperature is the algebraic sum of the thermistor tolerances plus the deviation. However, since the deviation from linearity is known, it may be accounted for at any given temperature.

The thermistor was calibrated by placing it in a regulated constant temperature bath. The bath temperature was measured by a calibrated Type T thermocouple and the output of the Ellis Bridge recorded at several different temperatures. The calibration curve for the bridge excitation of 4 volts is given in Figure A.3. From the calibration curve a sensitivity of 0.68 V/°C was determined. Due to small linearity deviation of the thermistor output in the range of interest this average value of sensitivity is expected to be independent of the fluid temperature.

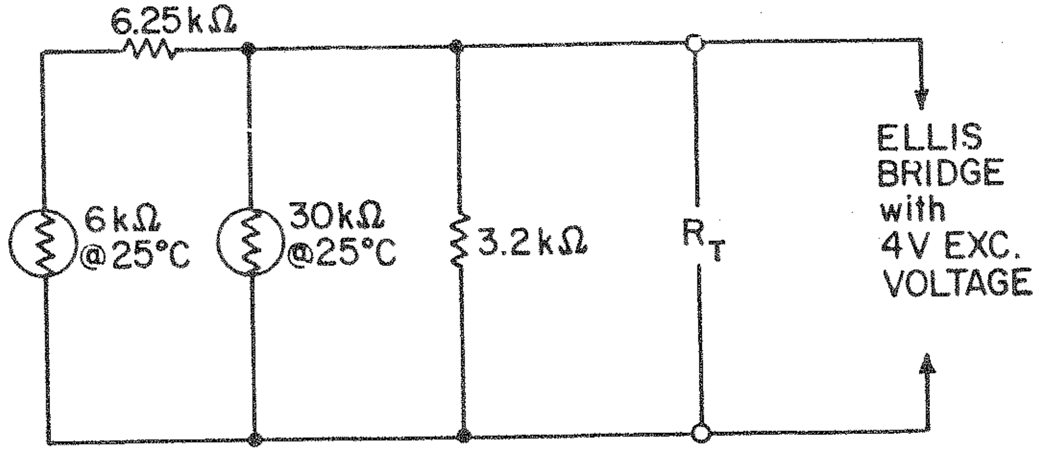

Figure A.1 Thermistor electrical circuit

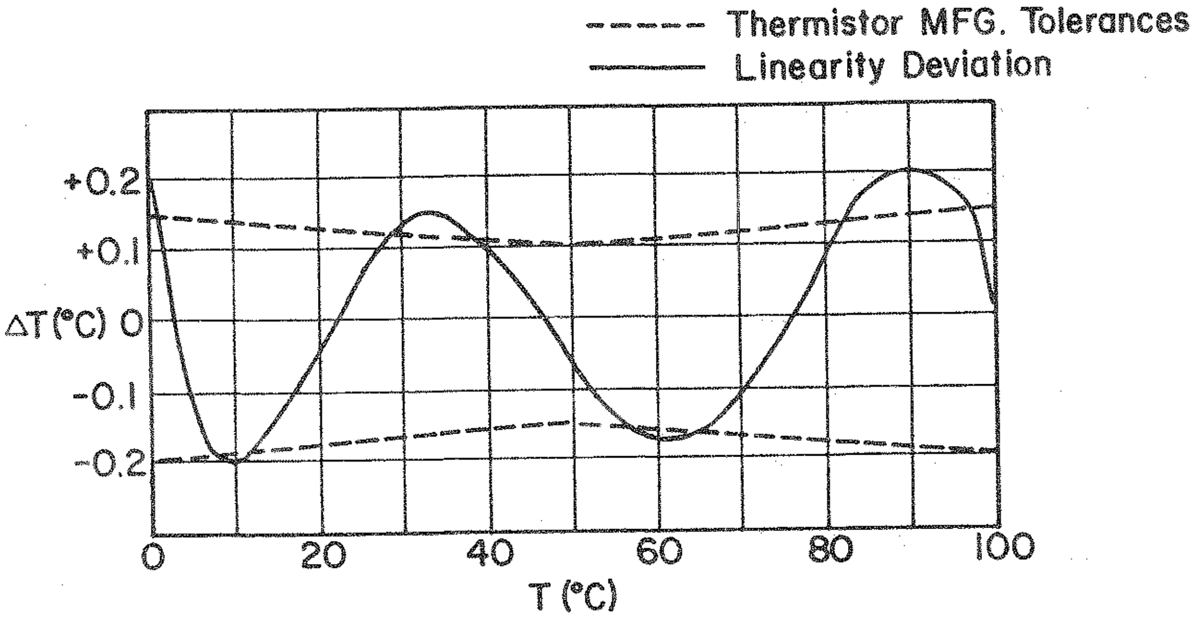

Figure A.2 Thermistor nonlinearity and tolerance curve

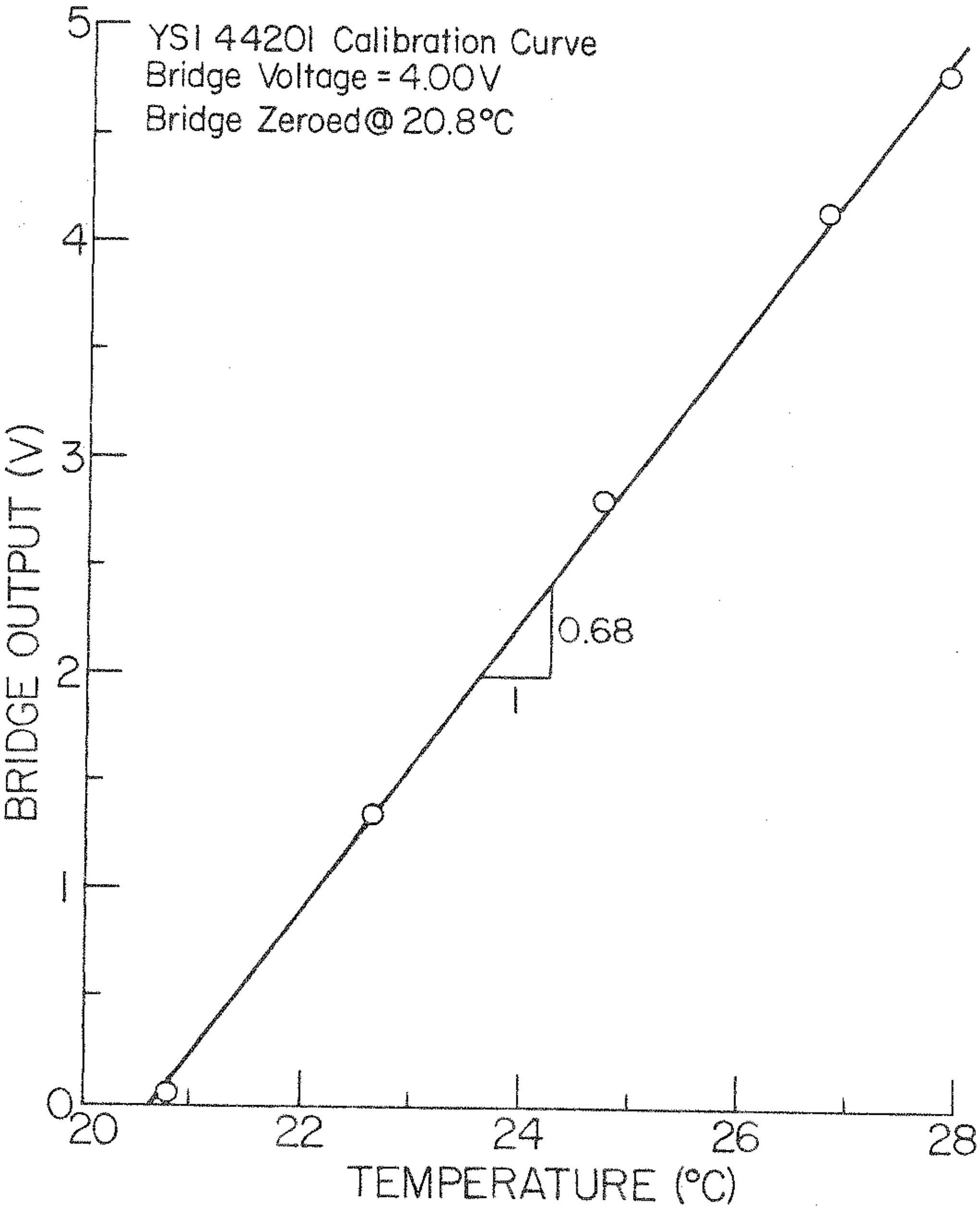

Figure A.3 Thermistor calibration curve

The time constant of the thermistor was not checked. However, the manufacturer specified that the time required for the thermistor to indicate 63% of a new impressed temperature was about 1 second in "well stirred oil" and 10 seconds in still air.

APPENDIX B

DETERMINATION OF INCIDENT RADIATION FLUX

The spectral incident radiation flux must be accurately determined in order to predict the volumetric rate of internal radiant energy absorption. The total radiation flux incident on the air-water interface was measured by an Eppley Radiometer (Model 8-48). The output voltage of the radiometer was a linear function of the total radiation incident on it. The proportionality factor was 11.82×10^{-6} V/(W/m^2).

For determination of the spectral distribution of the incident flux the effective brightness temperature of the radiant heater was measured with an optical pyrometer (Instrument Development Laboratories Model Pyro 650). The tungsten filament temperature was determined from the brightness temperature by correcting for the emissivity of tungsten, and a relationship between the tungsten filament temperature and voltage applied to the lamps was established. The filament temperature of the lamps was measured for several different settings of the Variac and was related to the voltage of the lamps, see Figure B.1. The input power vs. filament temperature was also measured. The results presented in Figure B.1 indicate that once a desired filament temperature is selected, the corresponding voltage can be determined from the voltage vs. Variac curve and then the powerstat transformer setting is chosen.

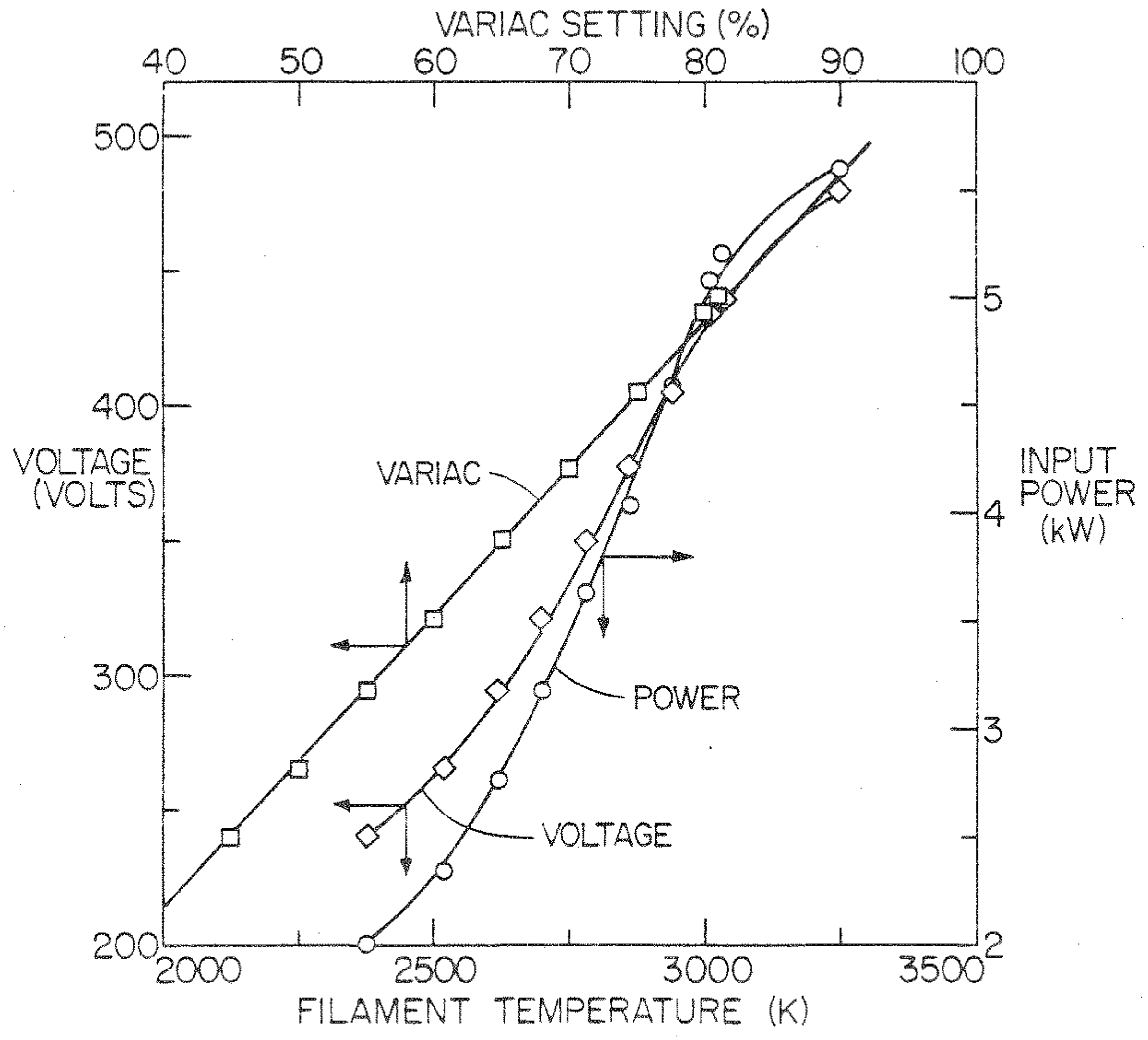

Figure B.1 Tungsten filament lamp characteristics

APPENDIX C

MEASUREMENT OF VELOCITY PROFILE IN THE AIR-CHANNEL

The air velocity profile in the air-channel was measured by means of a traversing Pitot-type probe and a static pressure tap. The dynamic pressure (stagnation minus static pressure) was measured by connecting the two pressure probes to a micro-manometer (CGS Scientific Corporation Model MM3) with N-Butyl Alcohol (specific gravity of 0.8076) as the working fluid. Once the dynamic pressure is known the local velocity can be calculated from the Bernoulli's equation,

$$V_{air} = \sqrt{\frac{2\ P_{dynamic}}{\rho_{air}}} = \sqrt{\frac{2\ \rho_{alcohol}\ g\Delta h}{\rho_{air}}} \qquad (C.1)$$

where Δh is the manometer displacement in centimeters of alcohol. The velocity profiles in the air-channel were measured and are plotted in Figure C.1 for three different blower speeds. The fan speed was determined by means of a calibrated strobe light. The velocity profile was measured some distance upstream of the water filled test cell. As a result of free air-water interface the profiles are non-symmetrical about the centerline of the channel ($z = 5$ cm).

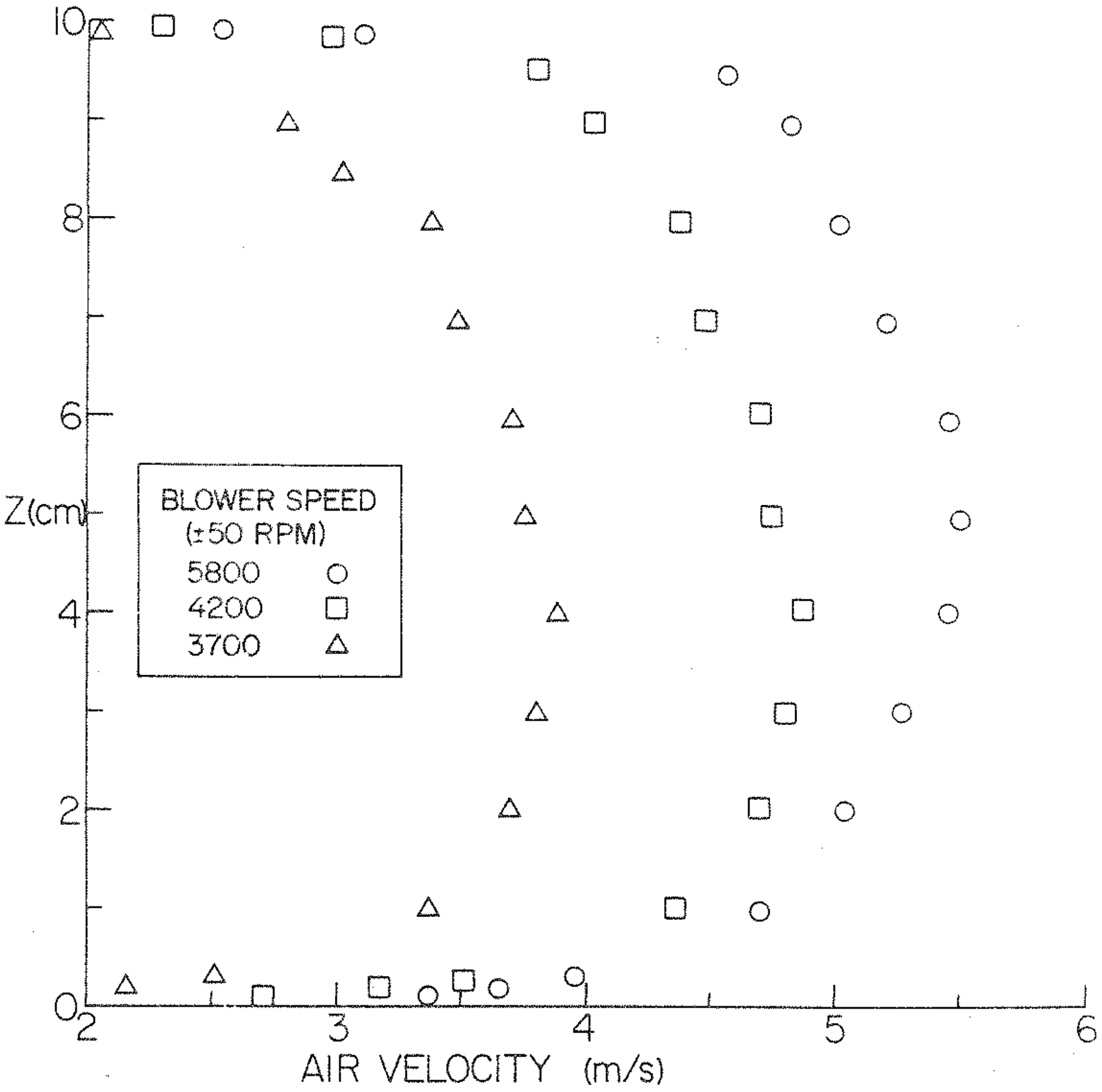

Figure C.1 Measured air velocity distribution in the air-channel

APPENDIX D

ANEMOMETER CALIBRATION

The velocity and temperature fluctuations in a fluid can be measured with a hot-film anemometer. A DISA 55M anemometer system with temperature compensator bridge and hot film dual probe was calibrated at low velocities. The probe was installed in a channel of a closed loop deionized water system, and the water velocity was accurately measured. The calibration curve for an overheat ratio of 1.05 is presented in Figure D.1.

It is clearly evident from this figure that at low velocity the anemometer is rather insensitive. This is due to the fact that the free convection velocities induced by heating of the probe are of the same order of magnitude as the imposed forced convection velocities, and therefore this part (< 0.2 cm/s) of the curve is rather flat. This suggests that accurate velocity measurements cannot be made using the anemometer probe in the low velocity range ($0 < V < 0.4$ cm/s) due to the lack of adequate sensitivity. For low velocity buoyancy driven flows a Laser Doppler Anemometer may be suitable for absolute velocity measurement.

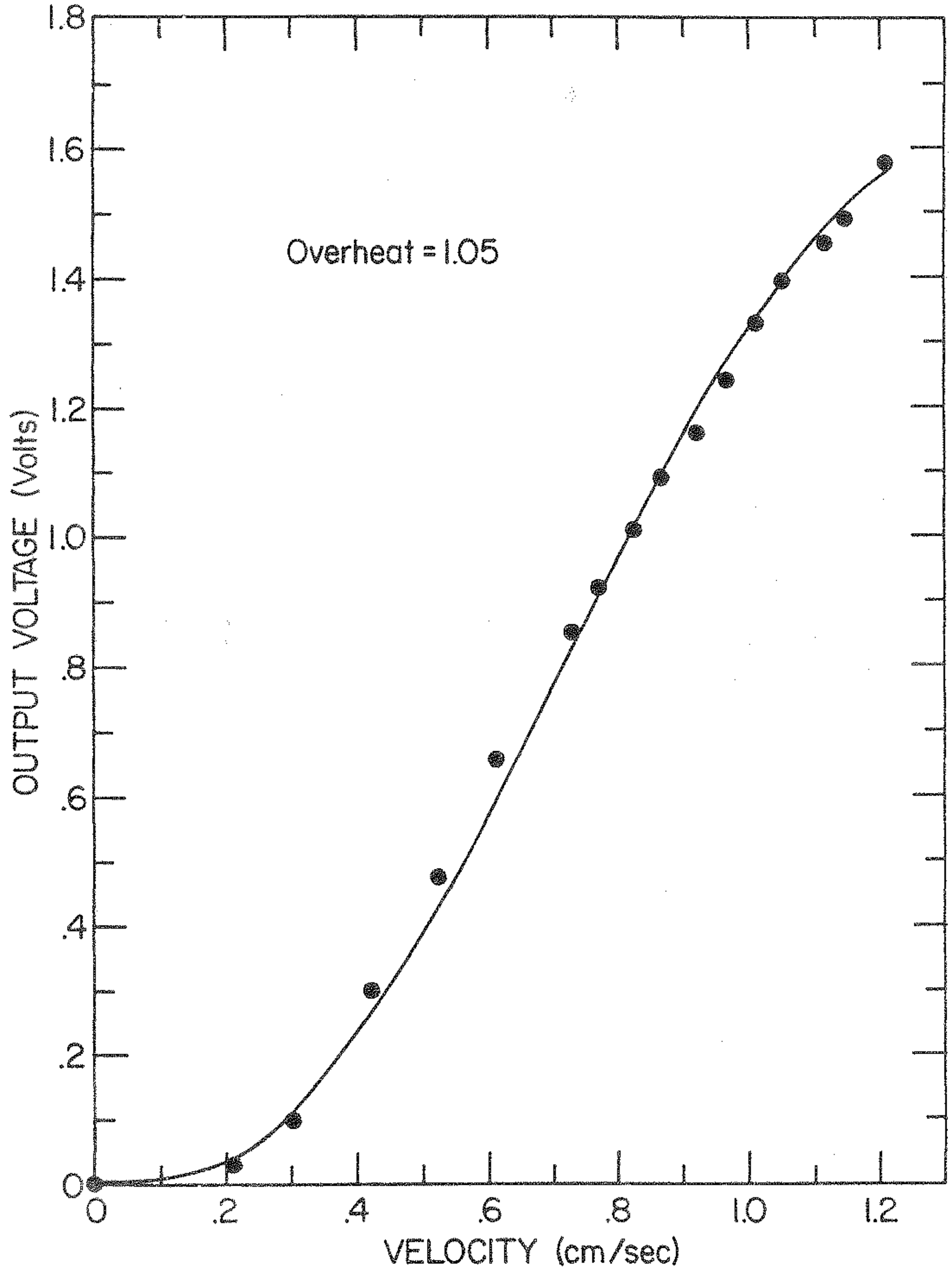

Figure D.1 Anemometer calibration curve

APPENDIX E

RADIATION FILTERS CHARACTERISTICS

The spectral characteristics of solar radiation cannot be simulated precisely in the laboratory without great difficulty. The high temperature tungsten filament radiant heaters were operated at temperatures much less than that of the sun's effective temperature. Therefore, compared to solar radiation a larger fraction of total flux emitted by the lamps was in the long-wave infrared part of the spectrum. Since the water is highly absorbing in this region a large fraction of the flux incident on the water would be absorbed at and near the surface. This is undesirable as far as simulation of stratification by solar radiation is concerned.

In order to "cut-off" some of the incident radiant energy in the infrared part of the spectrum two different glass "filters" were used. A 6 mm thick float glass covered the top of the test section in the air channel and acted as a radiation filter. For more effective reduction of the incident radiation flux a stack of 12 glass plates (8 sheets of float and 4 sheets of Pyrex) was used. The glass plates did not touch each other and were placed in a plexiglass frame with equally spaced grooves machined in it. A spectral scan of the float glass and the stack of 12 glass plates was made with a Carey Model 12 spectrophotometer, and the transmission characteristics are presented in Figure E.1. The spectral transmittance of the float glass measured was compared to spectral transmission curve reported by the glass manufacturer and agreed very well with each other. This provided some confidence in the measured spectral transmittance of a stack of glass plates.

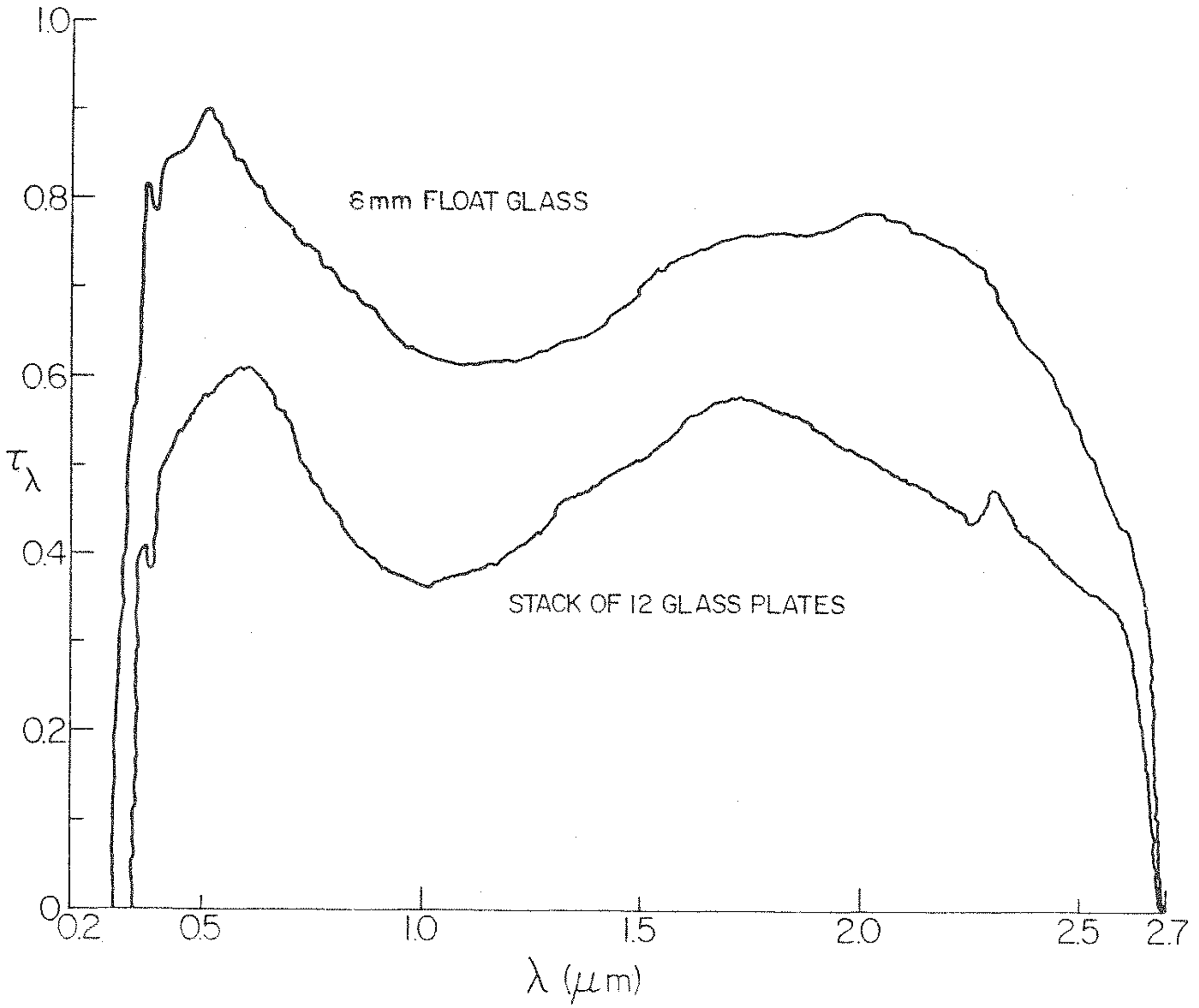

Figure E.1 Spectral transmission characteristics of the glass filters

APPENDIX F

ESTIMATES OF MEASUREMENT ERRORS

The purpose of this appendix is to briefly examine the measurement errors and to estimate their magnitude. For interferometric temperature measurement only one absolute (reference) temperature was required in the entire field. This temperature was measured with a thermocouple calibrated against an NBS standard. Other temperature measurements were made with calibrated Type T (Copper-Constantan) thermocouples. Comparison of temperatures determined with the interferometer and with thermocouples indicated that the thermocouples were far more accurate than the ANSI stated limits. At each time, depending on the type of the experiment, several thermocouple readings were recorded and the corresponding interference fringe pattern photographed. The emf readings were printed-out in approximately 5 seconds, and the photograph was taken during this period. A slight time difference could exist between the reference thermocouple emf reading and the interferogram; however, the temperature transients were relatively slow and are not likely to result in any significant time lag.

A scale factor was determined by comparing the known distance between two points visible in an interferogram with the actual distance between the points. The accuracy of the coordinate microscope was ± 0.01 mm which corresponded to approximately ± 0.01 or 0.02 mm actual distance depending on the size of the negatives of the interferograms.

A detailed discussion of the measurement errors associated with the Mach-Zehnder interferometer is given by Hauf and Grigull (1970) and will not be repeated here. In interpreting the temperature distribution from interference fringe shifts, only index of refraction change of water with temperature was considered. A comparison of temperature differences between two different points measured by thermocouples with those interpreted from interferograms for several experiments indicated a discrepancy of less than 3% of the total temperature difference. During heating or cooling the test cell assembly deforms due to thermal expansion or contraction. The deformation changes the optical path length which in turn produces temperature errors (Hauf and Grigull, 1970). The glass windows, each 2.5 cm thick, will expand approximately $1.37(10)^{-5}$ cm for a 1.0°C temperature increase, and this expansion produces negligible error. For the same temperature increase the differential thermal expansion of plexiglass spacers is estimated to produce approximately 0.01°C error in the interpreted temperature. The overall accuracy of the interferometric temperature measurement is estimated to be ± 0.1°C.

In the air velocity measurements the position of the pitot-type tube could be determined to within ± 0.005 mm, and the dynamic pressure (stagnation minus static) could be measured to ± 0.005 cm of manometer fluid (N-Butyl Alcohol). This uncertainty is estimated to result in an error of approximately ± 0.1 m/s in the air velocity measurements.

OTHER PUBLICATIONS

Viskanta, R. and Parkin, J. R., 1976: Laboratory Study of Unsteady Energy Transfer in Surface Layers of Water. Water Resour. Res. 12, 1277-1288.

Viskanta, R., Behnia, M. and Karalis, A., 1977: Interferometric Observations of the Temperature Structure in Water Cooled or Heated From Above. Adv. Water Resour. 1, 57-69.

Viskanta, R., Karalis, A. and Behnia, M., 1978: Effects of a Barrier on Temperature Structure and Mixing in Thermally Stratified Water Cooled From Above. Thermo- and Fluid Dynamics 11, 229-239.

Behnia, M. and Viskanta, R., 1979: Free Convection in Thermally Stratified Water Cooled From Above. Int. J. Heat Mass Transfer 22, 611-623.

Behnia, M. and Viskanta, R., 1979: Mixed Layer Growth and Heat Transfer in Stratified Fluid Heated From Below. ASME Paper No. 79-HT-107, 18th National ASME/AIChE Heat Transfer Conference, August 6-8, 1979, San Diego, California.

Water Resources Research Center
Lilly Hall of Life Sciences
Purdue University
West Lafayette, Indiana 47907